The implications of shale geomechanics and pressure diffusion for 4D interpretation

Yesser HajNasser

Submitted for the Degree of Doctor of Philosophy.
Heriot-Watt Institute of Petroleum Engineering
Heriot-Watt University,

October 2012

ACADEMIC REGISTRY
Research Thesis Submission

Name*:*	**YESSER HAJNASSER**		
School/PGI:	Institute of Petroleum Engineering		
Version: *(i.e. First, Resubmission, Final)*	**FINAL**	Degree Sought (Award **and** Subject area)	**Ph.D.** **RESERVOIR GEOPHYSICS**

Declaration

In accordance with the appropriate regulations I hereby submit my thesis and I declare that:

1) the thesis embodies the results of my own work and has been composed by myself
2) where appropriate, I have made acknowledgement of the work of others and have made reference to work carried out in collaboration with other persons
3) the thesis is the correct version of the thesis for submission and is the same version as any electronic versions submitted*.
4) my thesis for the award referred to, deposited in the Heriot-Watt University Library, should be made available for loan or photocopying and be available via the Institutional Repository, subject to such conditions as the Librarian may require
5) I understand that as a student of the University I am required to abide by the Regulations of the University and to conform to its discipline.

* *Please note that it is the responsibility of the candidate to ensure that the correct version of the thesis is submitted.*

Signature of Candidate*:*		Date:	08/10/2012

Submission

Submitted By *(name in capitals):*	
Signature of Individual Submitting:	
Date Submitted:	

For Completion in the Student Service Centre (SSC)

Received in the SSC by *(name in capitals):*			
3) Method of Submission (Handed in to SSC; posted through internal/external mail):			
4)** E-thesis Submitted (**mandatory for final theses)			
Signature:		Date:	

Abstract

Shales in the reservoir and the surrounding rocks are often regarded as mechanically active for stress deformation and inactive barriers for fluid flow transportation. In clastic reservoirs experiencing pressure depletion due to production, the sands naturally compact to some degree. Consequently, the much lower permeability intra-reservoir and non-reservoir shales may experience mechanical tension. It is well documented that the dilation in the overburden and underburden shales leads to a detectable time shift in the seismic (Hatchell et al., 2003; Tura et al., 2005; Sayers, 2010). Less well know is that the combined effect of stress deformations and pressure diffusion in the non-reservoir and intra-reservoir shales may alter the predicted effective seismic response of the reservoir interval and the surrounding rocks. In this thesis, the combined effect of geomechanics and pressure diffusion process in the reservoir and non-reservoir shales is examined. The integration of these coupled mechanisms into forward seismic modelling is performed to assess the 4D seismic implications. For this, both; synthetic and field data are used in this thesis.

It is commonplace to regard shales as barriers in the simulation of reservoir fluid flow induced by hydrocarbon production. Whilst this appears correct for fluid exchange, this is not the case for the fluid pressure component of this process. Based on this work, I observe that pore pressure reduction due to reservoir depletion can propagate significant distances into the intra-reservoir and non-reservoir shale over the production time scale. This diffusion process opposes the geomechanical effects. Numerical computation for a range of shale permeabilities suggests that intra- reservoir shales of 1m to 10m thickness should be considered as active when quantitatively assessing the 4D seismic signature with frequent acquisitions of 3 to 12 months. The critical set of parameters required to carry out accurate calibration of these predictions is not yet fully available from published literature. Also it is observed that pressure depletion in the reservoir can ‘propagate’ distances of as much as 50m into the shale over/under burden during the production time scale. Consequently this could leads to different polarity of time shift above and below the reservoir.

In this thesis, I consider two field case studies. In the first case study I focus on the Schiehallion field. Here, the coupled mechanisms of geomechanics and pressure diffusion is integrated into the forward modelling of time lapse seismic. It is found that the polarity of the

P-wave acoustic impedance changes and the corresponding synthetic 4D amplitude changes obtained from the coupled mechanisms are different from those modeled using geomechanics alone. Remarkably the synthetic 4D seismic amplitude generated using the coupled mechanisms is in agreement with the observed 4D amplitude. The second field case study is the HPHT Erskine field from the UK central North Sea. Here, 4D seismic data have been used to investigate the combined effects of geomechanics and pressure diffusion on the intra-reservoir and non-reservoir shales. Modelling of synthetic seismic time shifts capturing these effects allow a quantitative evaluation of the observed 4D seismic time shifts. In particular, the comparison between synthetics and observations helps to calibrate the range of permeability for the Heather formation and the Erskine shale units. This calibration gives rise to a model which should more reliably predict the pore pressure and stress tensor changes, allowing more confidence in selecting safe well paths, mud weights, and casing schemes. For this particular case, the results suggest that the Heather formation undergoes pressure diffusion and consequently the trapping mechanism at the Heather shale is highly uncertain. The Erskine shale, however acts as an effective pressure barrier, and hence it is overpressured relative to the surrounding formations and could be a high-risk formation for future drilling programs.

The results of this work strongly indicate that the understanding of shale geomechanics and pressure diffusion is essential to adequately understand the elastic wave stress sensitivity of the reservoir and the surrounding rocks. Based on the field case studies, the observed time-lapse seismic data are consistent with the combined effects of shale geomechanics and pressure diffusion, and are preferable to taking into account only the geomechanical effects. In addition to the above, the results suggest that the need for shale properties should be recognized and measurement become more common practice in order to calibrate the predictions made in this study.

Acknowledgements

Firstly, I sincerely thank my advisor, Prof. Colin MacBeth, for being supportive and understanding right from the beginning; he inspired and motivated me. He not only helped me in every aspect of this project but also made me a better person, and scientist by setting high standards. His support on doing a PhD and MSc at the same time is very much appreciated, as it turned out it was the best approach to rapidly expand my knowledge and finish two degrees at the same time.

I express my gratitude to Prof. Eric Mackay, Dr. Karl D. Stephen, Dr. Andy Gardiner, and Dr. Asghar Shams for their valuable ideas and support in developing this project. Also I would like to thank Prof. Patrick Corbett for his constructive discussions and guidelines in my research. Special thanks to my officemates: Dr. Weisheng He, Dr. Rossmary Villegas, Dr. Ludovic Ricard, Dr. Amran Benguigui, Dr. Mehdi Paydayesh, and Dr. Nader Kooli, for being helpful and for providing a good environment for research and their social relations.

Thanks also go to all at Heriot-Watt Institute of Petroleum who helped me out or were just a friendly face. I am also grateful for the financial support of the Edinburgh Time Lapse Project, Phase III and IV ETLP sponsors: BG, BP, Chevron, ConocoPhillips, EnCana, ENI, ExxonMobil, Hess, Hydro, Ikon Science, Landmark, Maersk, Marathon, Norsar, Petrobras, Shell, Statoil, Ohm, Total and Woodside. Also I thank Schlumberger-Geoquest for use of their Petrel and Eclipse software (TM Schlumberger). Additional financial support was gratefully received from the SEG Foundation, which awarded me the Leon Thompson/BP Scholarship. Special thanks go to Jeremy Zimmerman from Chevron (Houston), John Fletcher from BP (Aberdeen), and Peter Schutjens form Shell (Aberdeen) for being supportive and for providing field data and valuable feedback.

I have great memories of my time at Heriot-Watt in Edinburgh. I was very lucky to have the opportunity to meet and share great moments with really nice, smart people during that time. Dr. Alejandro, Dhiman, Hamed, Dr. Reza, Valeriy, Dr. Yi, and Sean, are great friends and have been a source of encouragement.

At the end of my PhD, I did an internship with ConocoPhillips in Houston, USA. This internship opportunity was a turning point in my career. After finishing this internship I got my first job. I would like to express my deepest gratitude to Ali Tura, Roy Baishali and Arcangelo Sena for their advice, support, and encouragement.

Whenever this PhD seemed like hard work I have drawn endless inspiration from my Father Khalifa. I watched him work hard to provide us with the best for life and education. Your love, encouragement, support and guidance over the years have been invaluable. Thanks also go to my dear mother Hallouma, brother Badri, and sister Najla for everything. I could not have done this without such a supportive family.

Yesser HajNasser, October 2012

Publications

Part of this work is presented in the following publications:

1. Ricard L., MacBeth C., **HajNasser Y.**, and Schutjens P. 2012. An evaluation of pressure diffusion into a shale overburden and sideburden induced by production-related changes in reservoir fluid pressure. *Journal of Geophysics and Engineering* **9**, 345-358.

2. **HajNasser Y.** 2011. Application of the "Active Shale" Concept to the Erskine field. Presented at Chevron Upstream Europe Reservoir Management Forum **'The Resource Factory – Enhancing Value'**, Aberdeen, UK.

3. **HajNasser Y.** and MacBeth C. 2011. The effect of intra-reservoir and non-reservoir shales on 4D seismic signatures. 81st SEG meeting, San Antonio, Texas, USA, Expanded Abstracts.

4. MacBeth C. and **HajNasser Y.**, Stephen K., and Gardiner A. 2011. Exploring the effect of meso-scale shale beds on a reservoir's overall stress sensitivity to seismic waves. *Geophysical Prospecting* **59**, 90–110.

5. **HajNasser Y.** and MacBeth C. 2010. The effect of intra-reservoir shales on effective stress sensitivity. 72nd EAGE meeting, Barcelona, Spain, Expanded Abstracts.

Contents

List of Figures

List of Tables

CHAPTER

ONE

1 Introduction

This chapter gives the main topics discussed in this thesis. First, I illustrate examples where shale is introduced into the time-lapse seismic interpretation. Here I review the use of time-lapse seismic in understanding shale effect in reservoir management and reservoir geomechanics. Next I discuss the Shale understanding from geophysical and engineering prospective. For this I examine Shale understanding in different disciplines; petrophysics, reservoir geomodelling, and reservoir simulation. Finally I give an overview about the main challenges of the thesis.

1.1 Introduction

Shales make up a large proportion of most sedimentary basins and form the over/under/side burden and source rocks of many hydrocarbon reservoirs. In addition most clastic reservoirs contain shales, which either divide the reservoirs into separate hydraulic units, or, if the shales are discontinuous, set a tortuous environment in which fluid transport occurs. Shales have been considered in the past literature, mainly in association with problems for fluid flow simulation and hence reservoir production. Several studies have shown that the presence of these shales could have a significant impact on the fluid flow behavior and the pressure development within the reservoir units. For example Jackson et al., (2001) conducted a numerical simulation of fluid flow behavior in 2D and 3D models of specific depositional environments derived directly from the outcrop. The studies suggest that shales could have significant effects on the reservoir performance and water flooding.

Shale is often the most troublesome of all the formations to handle when drilling for oil and gas. In the petroleum industry, shales cause billions of dollars in losses annually. The drilling of shale or shaley sequences often needs constant interruption to solve problems such as a tight hole or unstable wellbore. On average, drilling problems due to wellbore instability are responsible for about 10 to 20% of the total drilling cost of a well. Further extensive statistical analysis reveals that 80 to 90% of quoted instabilities occur when drilling through shales (Da Fontoura, Rabe, and Lomba, 2002). Time and money spent on this problem, together with overall reduced profit margins, has led the oil industry to assign considerable time and effort to assess shale properties and try to solve the problem of an unstable borehole in shale sequences.

In addition to the above, shales are often not cored or if so, not preserved properly. Despite their obvious importance, there have been few laboratory or field studies of shale behavior, and properties remain poorly defined (Sayers, 2008). This knowledge void is a problem because improved understanding of static and dynamic properties of shale would benefit several geophysical areas such as fluid identification and lithology determination, anisotropy quantification, pore pressure prediction, seal evaluation, rock strength modelling, and time lapse seismic interpretation. More recently, there is the start of a new era of shale-gas resources (also known as unconventional reservoirs), where the shales act as both the source

rock and the reservoir. This has emphasized further the need for a better understanding of shale properties and behavior.

In this chapter I give an overview of knowledge of shales from both a geophysical and engineering perspective. First, I illustrate examples where the presence of shales has led to detectable time-lapse seismic anomalies. I review some of the reported studies of shale geomechanics and time-lapse seismic interpretation. Next, I present the understanding of shales from a petrophysical, reservoir geomodelling, and reservoir simulation point of view. Finally I present the main challenges and thesis outlines.

1.2 Shale and time lapse seismic

1.2.1 Time lapse seismic

The 1990's brought new life to seismic attributes analysis primarily because the industry had embraced 3D technology – which was by far the most successful new exploration technology of several decades (Chopra and Marfurt, 2007). Interestingly this technology has been very beneficial for the reservoir imaging, by providing a better understanding of spatial distribution of the physical and structural properties of the reservoir. Furthermore, introducing time lapse seismic to the oil industry has brought a new approach to monitor the dynamic behaviour of the reservoir. Time-lapse seismic, commonly known as 4D seismic, is the practice of repeating two seismic measurements at different times and comparing them. The very first application of 4D was performed by ARCO. The application aimed to monitor the oil recovery using 4D seismic (Greaves and Flup 1987). In 1995, that 4D seismic technology was implemented on a oil field – Gullfaks in the North Sea– as part of a Statoil-Schlumberger joint project. Since then, time lapse seismic has been applied to many fields as a reservoir-monitoring tool (Tura et al., 1999 and Landrø 2001). More recently, fluid movements and pressure changes (Alsos, 2009) have been detected using 4D seismic. This information is of particular benefit in adjusting the reservoir model, and in planning the locations of wells or completions.

Furthermore these new sets of data were found to be of value to both the geologists in preparing the geological model and also the reservoir engineer. To optimize the value of time-lapse seismic data and to be able to attribute 4D seismic signal to specific reservoir flow units

and stratigraphic margins or faults, it is essential to understand the reservoir architecture and structure.

Shales are the most abundant of all lithologies, constituting some of the sedimentary basin. Their complex geometry and distribution present a source of uncertainty in the true positions of seismic events. Therefore shales are challenging geophysical interpretation issues that could lead to incorrect structural concepts, unresolved geometries or inaccurate velocities used for the pre-stack depth migrations. This is outside the scope of this thesis however further research on resolving the shale effect on the seismic processing is recommended.

As the shales in and around the hydrocarbons reservoir are known to be among the main parameters that define the reservoir architecture, they could therefore have a significant impact on the time-lapse seismic interpretations. To support this point, in the next section, I present a two field examples where shales plays a major role in the time lapse seismic interpretation.

1.2.2 Example 1: Nelson Field

Nelson is a simple dip closed structure and is one of a series of Palaeocene sandstone oil accumulations situated on the Forties-Montrose High (Kunka, et al., 2003). The reservoirs are predominantly channelized submarine turbidite sands of the Forties Sandstone Member of the Sele Formation (Whyatt, et al., 1992). In this particular field, shale is a dominant lithology within the reservoir and in the surrounding rocks. Nelson has a history of 4D seismic, the pre-production 3D survey was shot in 1990, with one of the first dedicated marine 4D surveys in 1997 (Harris and Henry 1998, Boyd-Gorst et al. 2001). Acquisition of further 4D monitor datasets was in 2000 and 2003, giving roughly an equal spacing of three years production between each survey. MacLellan et al., (2006) has conducted a study on the 4D seismic interpretation of the Nelson Field. He suggested that the time lapse signal is mainly driven by the fluid contact movements, however the lithological heterogeneity associated with turbidite deposition complicates the interpretation. To have a better understanding, the study suggests that it is necessary to consider the reservoir heterogeneity that contributes to producing variability of water sweep, and to show how these can be explained through the joint interpretation of 3D and 4D seismic data. Preliminary interpretation recommended that the absence of the signal could either be due to unswept sand or to poor quality reservoir with inter-bedded shales below the seismic resolution.

Figure 1.1 displays different time-lapse seismic data in the same environment. Figure 1.1(a) shows the seismic difference data 2000-1990 in green and 2003-2000 in blue, the negative values are made transparent. Figure 1.1(b) shows the elastic impedance (EI) generated from 3D near-stack seismic data. The good quality sand bodies have high elastic impedance. With integration of the well data it was possible to identify the intra-reservoir shales, and hence a better understanding of the seismic response was achieved.

Figure 1.1(c) highlights the variation in the OWC between isolated sand units subject to different drive mechanisms. Such contact variation indicates the development of baffles or barriers during a production timeframe in what was considered to be highly connected reservoir. Combined 3D/4D interpretation is used to identify and account for OWC movement and locate regions of bypassed oil. The 4D signal demonstrates flushing from different contacts during the period 2000 to 2003. Combined interpretation with the 3D EI data reveals flushing from distinct sand units isolated by low net-to-gross (NTG) regions, thus explaining the different edge and basal drive mechanisms. Well results and 4D time lapse seismic data point towards a uniform basal drive mechanism with massive channel fairway sand bodies open to aquifer support. Laterally extensive sand units drape and incise earlier channels, with basal drive when in vertical communication with the aquifer. Conversely, where separated by a laterally extensive intra-reservoir shale barrier, edge drive becomes the dominant mechanism. For this particular field, fluid contact variation indicates the development of baffles or barriers during a production timeframe.

This study highlights the importance of lithological heterogeneity (shales) associated with the turbidite depositional system in developing a complex fluid tortuosity within the reservoir and hence a complicated time lapse signature. The intra-reservoir shales are essential to improve stratigraphic imaging and seismic interpretation and to identify bypassed and down dip reserves. The 4D signal associated with the fluid movement was used to verify the presence of intra-reservoir shales where 3D EI interpretation is ambiguous.

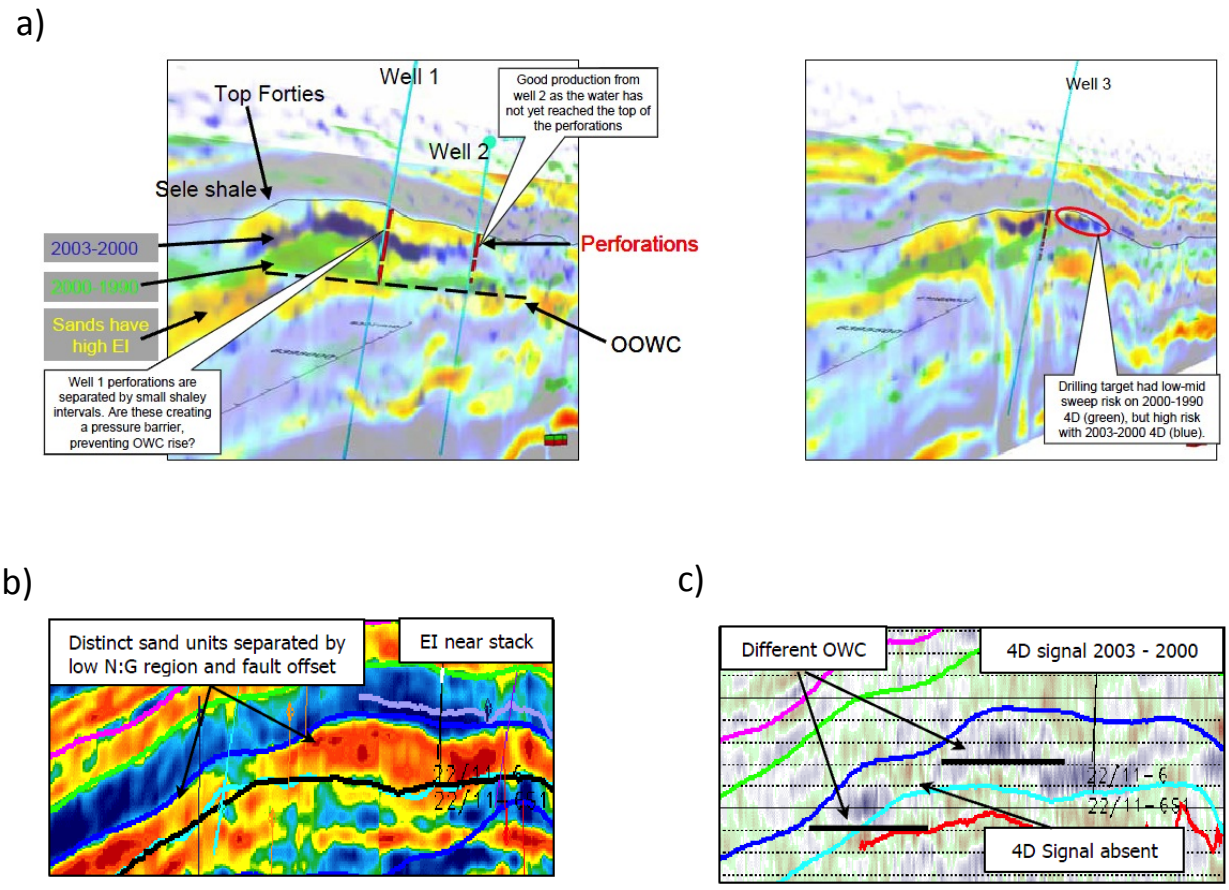

Figure 1.1: (a) Different time-lapse seismic data for the Nelson Field. (b) Elastic impedance (EI) generated from 3D near-stack seismic data. The good quality sand bodies have high elastic impedance. (c) highlight variation in OWC between isolated sand units subject to different drive mechanisms. The 4D signal demonstrates flushing from different contacts during the period 2000 to 2003. Combined interpretation with the 3D EI data reveals flushing from distinct sand units isolated by shale barriers or baffles, thus explaining different edge and basal drive mechanisms.

1.2.3 Example 2: The Gannet Field.

The use of 4D seismic data on the Gannet field gave new insights into the structure and dynamic behavior of the oil and gas field (Staples et al., 2006). Differences between these time-lapse seismic datasets have been interpreted in terms of changes in reservoir fluid movement. These interpretations have proven useful for reservoir management by identifying swept and unswept zones. Gannet (C and B) is a ring-shaped structure formed by the salt diapir growth. In the southern part of the field, the initial 4D seismic interpretation revealed major extensions of reservoir units previously presumed to be absent or thin over much of the reservoir. However further evaluation of the 4D seismic difference volume indicated differential fluid contact rise in this part of the field. Thin intra-reservoir shales are thought to be the reason for the differential contact rise.

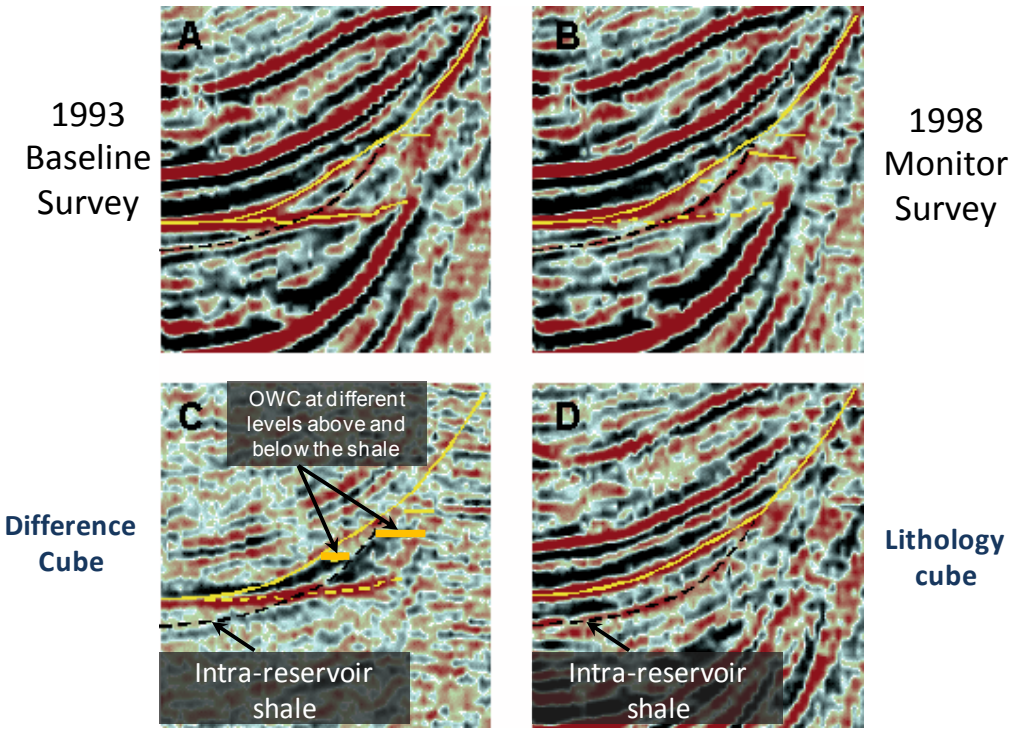

Figure 1.2: Seismic data at the Gannet C Field. (A) Base line seismic surveys, (B) monitor seismic survey. (C) difference seismic cube (D) lithology cube. The intra-reservoir shales are shown as a dashed yellow line. The bold yellow lines in (C) highlight the variable OWC induced by the presence of intra-reservoir shales. After Staples et al. (2006)

In the eastern part of the field a markedly different effect was observed. Here, a thin intra-reservoir shale layer mapped on the lithology cube appears to separate the Forties reservoir into a top and base unit. The difference volume between the 1993 and 1998 data shows different OWC levels for both units (Kloosterman et al., 2003).

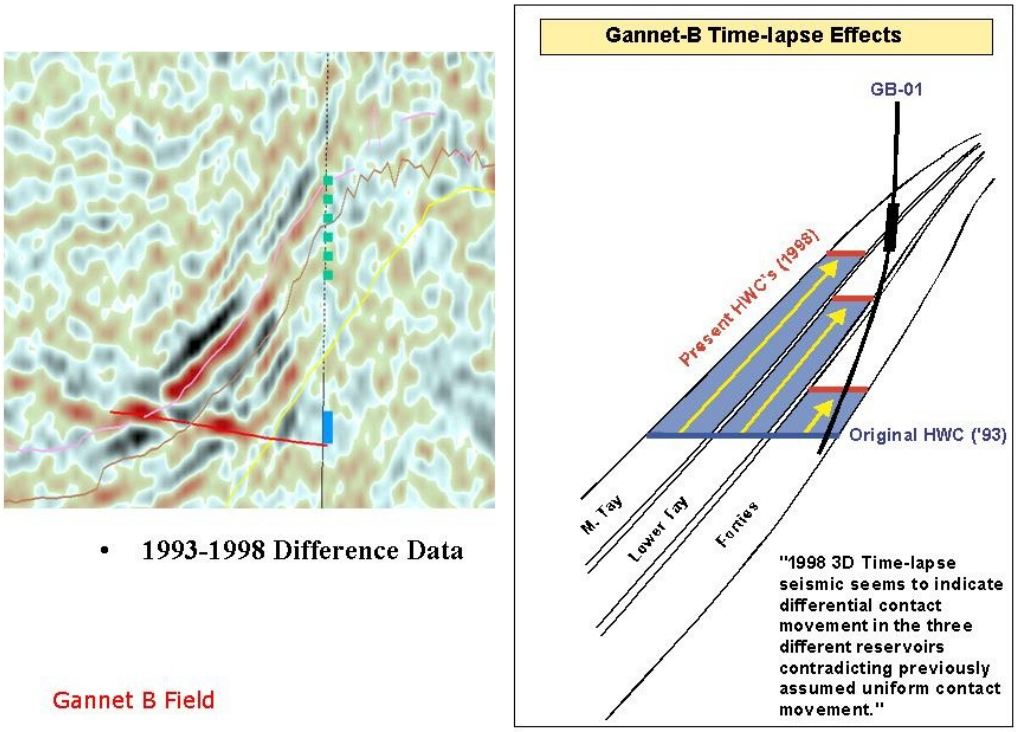

Figure 1.3: Time-lapse seismic data at the Gannet B field. The 4D amplitude difference between 1993 and 1998 indicates strongly different saturation changes. 4D seismic seems to indicate differential contact movement in three different reservoirs, contradicting the previously assumed uniform contact movement.

Gannet B is a small gas field developed by depletion through two subsea wells. A 3D seismic survey shot in 1998 allow a time-lapse comparison to be made with the pre-development Gannet B survey. A section through the amplitude difference cube in Figure 1.3 indicates strongly differential saturation changes from layer to layer. This image of differential gas depletion was opposite to the expected response.

In the west–east section over Gannet B, through the 1993/1998 seismic amplitude difference cube, the apparent water movement signature is anomalously high in the Lower Tay

(Kloosterman et al. 2003) There are strong differential saturation changes between the producing units due to laterally persistent and sealing shales.

Based on the observation illustrated above, intra-reservoir shales are observed to have a significant impact on the fluid flow behavior and the pressure development within the reservoir units. Indeed, another study by Al-Najjar et al. (1999) shows that the presence of laterally persistent shale in the basal Ness formation has effectively limited the pressure communication between the Lower and Upper Brent reservoirs. The two reservoirs have therefore been developed separately.

1.3 Shale geomechanics and 4D seismic monitoring

Production of hydrocarbons changes reservoir pore pressure and hence alters the stresses acting on the reservoir and the surrounding rocks (Addis, 1997; Hettema, et al., 2000; Hatchell, et al., 2003; Sayers, 2005b). Strong evidence for altered stress in and around reservoirs undergoing depletion is provided by seismic events resulting from production (Segall, 1989; Grasso, 1992) and by time shifts observed by using time lapse seismic data (Hatchell et al., 2003). Time-lapse time shifts for near vertical travelling P-waves are, at present, the most widely reported geomechanically induced time-lapse seismic signal. A literature review found that geomechanically induced overburden shale time-lapse time shifts have been reported for at least 15 fields (Herwanger and Horne, 2009). Overburden time-lapse time shifts have been observed predominantly above hydrocarbon fields that can be classified into three different geologic regimes: deepwater turbidities in the Gulf of Mexico; chalk fields in the North Sea; and high-pressure, high-temperature (HPHT) fields in the North Sea.

Most of the clastic reservoirs contain shales and the majority of the layers between the free surface and the reservoir are shales. Therefore the overburden/underburden shales have been the focus of several geomechanical studies of the depleted reservoir. Recently, attention has focused on shale properties because of the time shifts observed in the shales surrounding producing reservoirs which now can be monitored with time-lapse seismic. For example, in the high porosity, poorly consolidated turbidities of the deepwater Gulf of Mexico, 4D time shifts are observed due to the alteration of the stress state inside and outside the reservoir (Tura et al., 2005).

Due to compaction in the reservoir sand units, the overburden shales experience vertical expansion; consequently a large positive time shift is detected (Figure 1.4). The figure compares time lapse time shifts observed from stacked field data (Figure 1.4(a)) with time shifts calculated from a geomechanical model for reservoir depletion (Figure 1.4(b)). In Figure 1.4, the positive time shifts that result from the velocity decrease in the shales are clearly seen. In addition, the anticipated decrease in two-way travel time as a result of a compaction-induced increase in velocity in the reservoir is apparent.

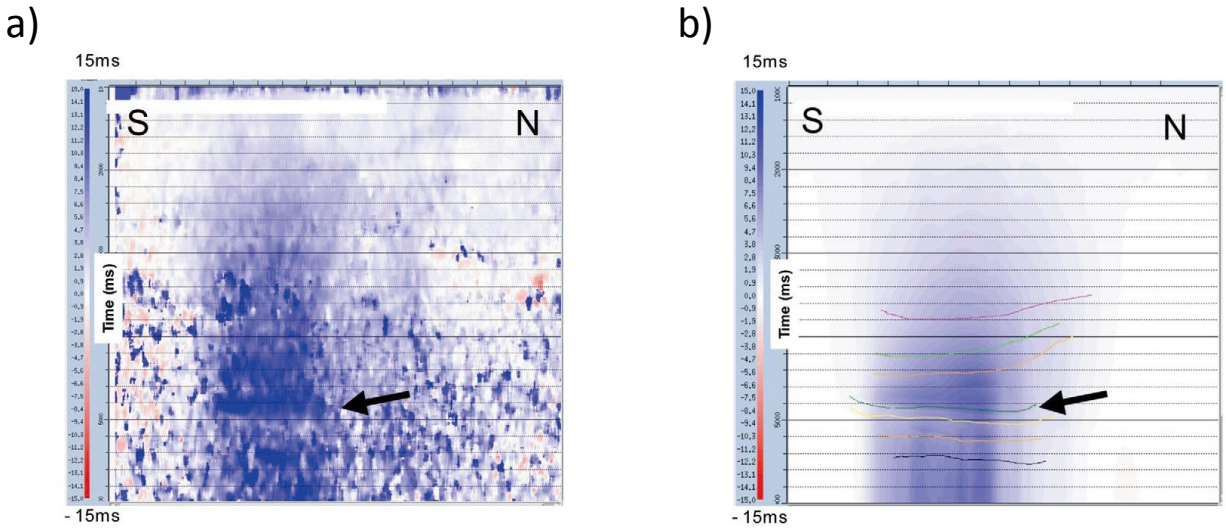

Figure 1.4: Measured time shifts for a deepwater Gulf of Mexico turbidite field. Comparison of time-lapse time shifts (a) observed from stacked field data and (b) calculated from an a priori geomechanical model for reservoir depletion. The producing reservoirs, indicted by the arrow, lie between 4000 and 6000 m with the porosities between 25% and 35%. After Tura et al. (2005).

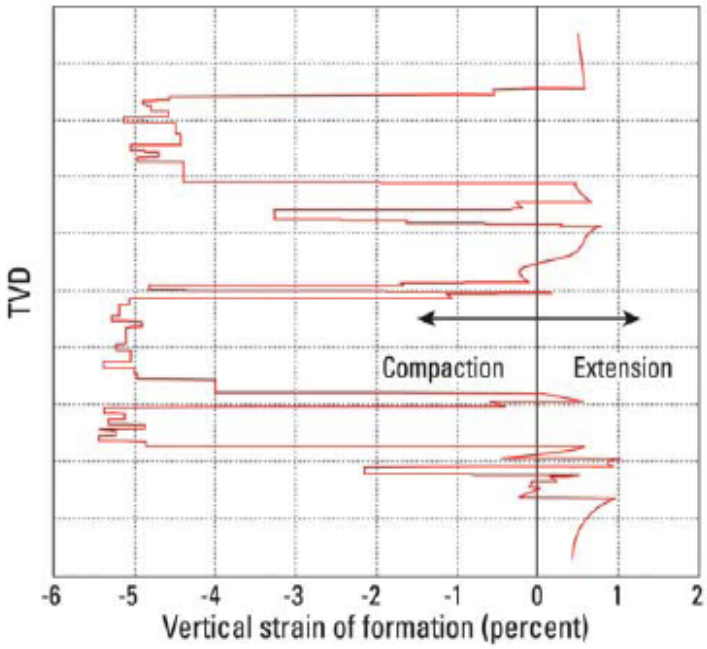

Figure 1.5: Vertical strain in the formation at one of the wells as a function of depth. Compressive strains are negative in this figure. After Sayers et al. (2006)

Pressure drop of 6000psi has been reported for deepwater Gulf of Mexico turbidite fields (Sayers 2006 a & b). The geomechanical response of the reservoir and the surrounding rocks at one of the wells is shown in Figure 1.5. Sayers, (2006) shows that although the reservoir sands are undergoing compaction (compressive strains are negative in Figure 1.5) the overlying, underlying, and the interbedded shales are undergoing extension (extensional strain are positive in Figure 1.5). Several other studies by Hatchell et al. (2005b) and Staples et al. (2007) have reported similar observations. They have concluded that an understanding of such effects requires knowledge of the geomechanical and the elastic properties of shales. This subject is introduced in this thesis, and the implications for the time-lapse seismic are examined.

In the following section I give an overview of shales from the perspective of the petroleum community. Firstly I will give a definition of the shale from a petrophysical point of view and the way the shale units are identified in log data, and then show how these shales are generated and implemented in reservoir geomodelling. In a similar way, I review the understanding of shale in the reservoir simulation and their effects on the fluid flow simulation. The aim of this section is to look at the shale from a different perspective and to

show a cross disciplinary definition of shale, which could lead to better understanding of its dynamic and static properties.

1.4 Shales treated in the Petrophysical domain

The objective of petrophysical analysis is to identify lithologies, and in particular the main reservoir units. For a reliable lithological reconstruction, two independent sources of lithology data available from oil wells are essential (Rider, 1996). One set of data comes directly from drilling and another from wireline logging. The drilling data consists of cuttings, cores and all the recorded drilling parameters. The log data consist of the wireline, geophysical log suite and sidewall cores. The identification of shale formations/units is conducted based on these two sets of data. For the drilling data, the mud log is the first to be recorded during drilling of a well. This log provides basic information about the lithology. The lithology examination is achieved through assessment of the cuttings, which are small chips broken off the formation as the drill advances. Because of smearing and mixing of the cuttings while traveling to the surface, interpretation of the mud log will yield only a percentage of each cuttings type. Therefore the mud-log interpretation of lithology should not used to interpret shale boundaries on the well logs. Clearly the limitation of the mud log to identify the main lithologies raises the requirement for more drilling data such as the drilling rate which could help to identify shales (where the drilling will be slower). In addition, the core / physical sample of the formation collected during the drilling could also help to identify the shale and non-shale units. The log data provide a series of quantitative values derived for the formation. These set of data help to conduct a precise petrophysical analysis, rather than a subjective interpretation through cores and cuttings. For the wireline logs there are several methods to identify shale units. The two most common are the gamma ray (GR) and the spontaneous potential (SP) logs. Also, density neutron separation is another common method for visual analysis of the shale volume.

Figure 1.6(a) illustrates the use of SP to identify shales units. A base line for the SP is shown on the right hand side of the SP track. This line is called the shale base line or the shale line (SPl00). The SP deflects to the left in clean sand. In the cleanest sand, the maximum SP reading to the left of the shale base line represents the clean SP line (SP0).

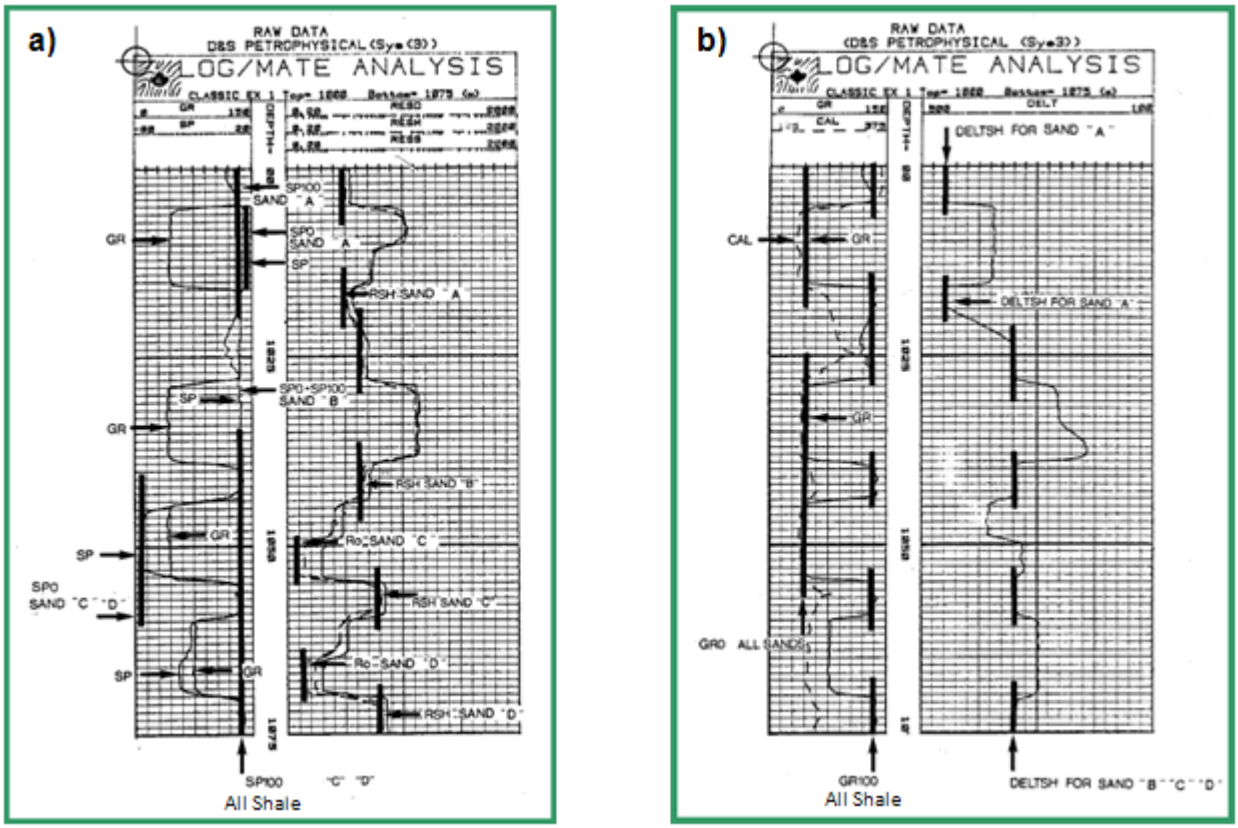

Figure 1.6: a) Spontaneous Potential and b) Gamma Ray Logs at a North Sea field wellbore (Rider, 1996).

However other formations may not develop an SP response of the same degree as the cleanest sand. Therefore, they are either shaley sands or else they have fresher water (salinity < 0.5 ppt) in them. The proportion of shale can be estimated by observing the SP deflection with respect to the clean sand and shale base lines (Rider, 1996). The gamma ray, like the SP, has a shale base line and a clean sand line. Estimation of shale content is performed by observation of the gamma ray log with respect to the clean line (GR0) and the shale base line (GRl00). The base lines for the gamma ray log are shown in Figure 1.6(b). Having chosen the calibration for both the SP and GR, it is possible to scale logs in units of shale content (V_{sh}). This is done by defining the clean line $V_{sh} = 0.0$ and the shale base line $V_{sh} = 1.0$ as shown above.

For a more quantitative interpretation of lithology interpretation, a wells log grouping is recommended. This quantification may be made at several levels of sophistication by using several or many logs. The simplest way to group well-log values is by using a histogram. For

example, a histogram of the gamma ray can be used to identify sand and shale. Another approach is cross plots of compatible or incompatible logs, which could lead to a better lithology identification. For example, the neutron-density cross plot shown in Figure 1.7.

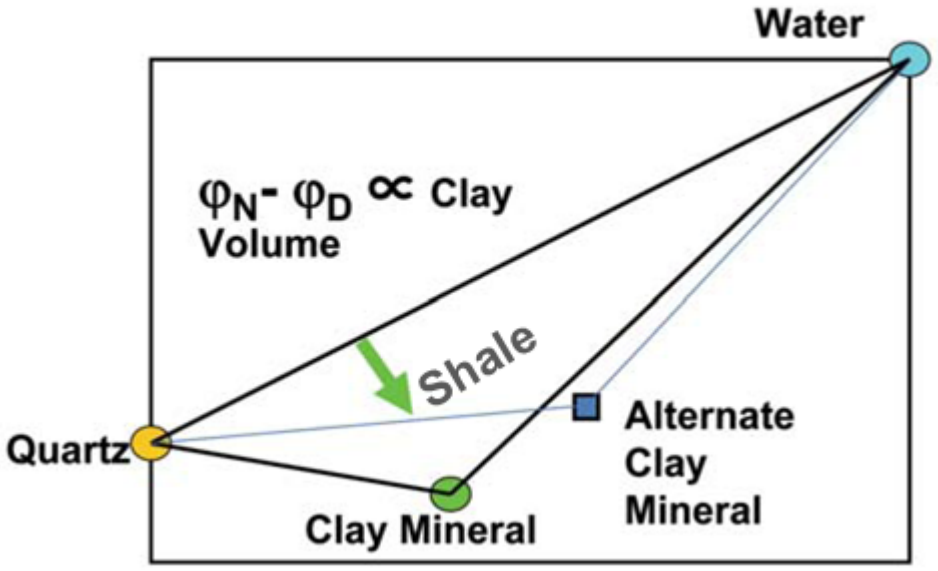

Figure 1.7: Schematic neutron-density crossplot with neutron porosity on the horizontal axis and density-derived porosity on the vertical axis. A very simple model of shale composition where the only components are quartz, water, and a clay mineral, is assumed. Then the shale will fall within the triangle bounded by those three end points, (after Katahara, 2008)

In Figure 1.7, clean, wet sands are on the line connecting the quartz and water endpoints. Shales or clay-mineral matrix formations fall below the clean sand line. For a given clay mineral, lines of constant clay volume are parallel to the clean, wet-sand line. Therefore the shale volume is proportional to difference between the neutron-derived porosity and density-derived porosity.

Heslop, (1972) give a very simple and effective definition of shale. Figure 1.8, (reproduced by Katahara, (2008), from the Heslep's paper) illustrates schematically what happens as clay content is increased from clean sandstones on the left to clay-rich shales on the right. In the sands on the left, rigid sand grains and grain contacts support stresses. With increasing clay, the sand and silt grains cannot form a continuous network with stresses supported by grain-grain contacts. The grains then float in a clay-mineral-matrix that is load bearing. This definition suggests that there is threshold clay content separating sand at the lower clay content, from shales with a higher clay content. Interestingly a cross plot of density versus the difference between neutron porosity and density porosity shows the same behavior that Heslop found (Figure 1.9).

Petrophysical studies use a practical definition of shale in shale-sand sequences. Several log properties such as density, neutron derived porosity, density derived porosity, and gamma ray show a change in slope when plotted against clay content. The change in slope is at the boundary between grain-supported sands and clay-matrix supported shales. Thus, the slope discontinuity can be used to distinguish shales from other lithologies. After trying different cross plots of different log data, Katahara, (2008) recommended that the neutron-density difference is a better measure of clay content and hence shale identification for geophysical purposes.

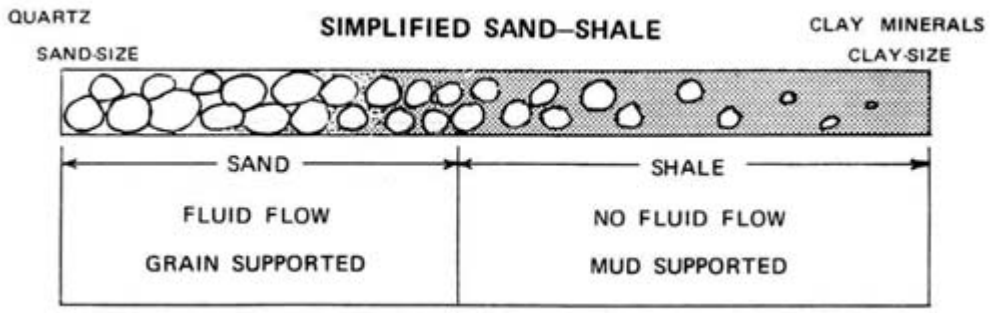

Figure 1.8: Schematic diagram of the variation of sediment with clay mineral content increasing from left to right. In sands on the left, external stresses are supported by sand grains and their contacts; clays occupy the inter granular space. Sand and silt grains float in a clay-mineral matrix (right), (Heslop 1972)

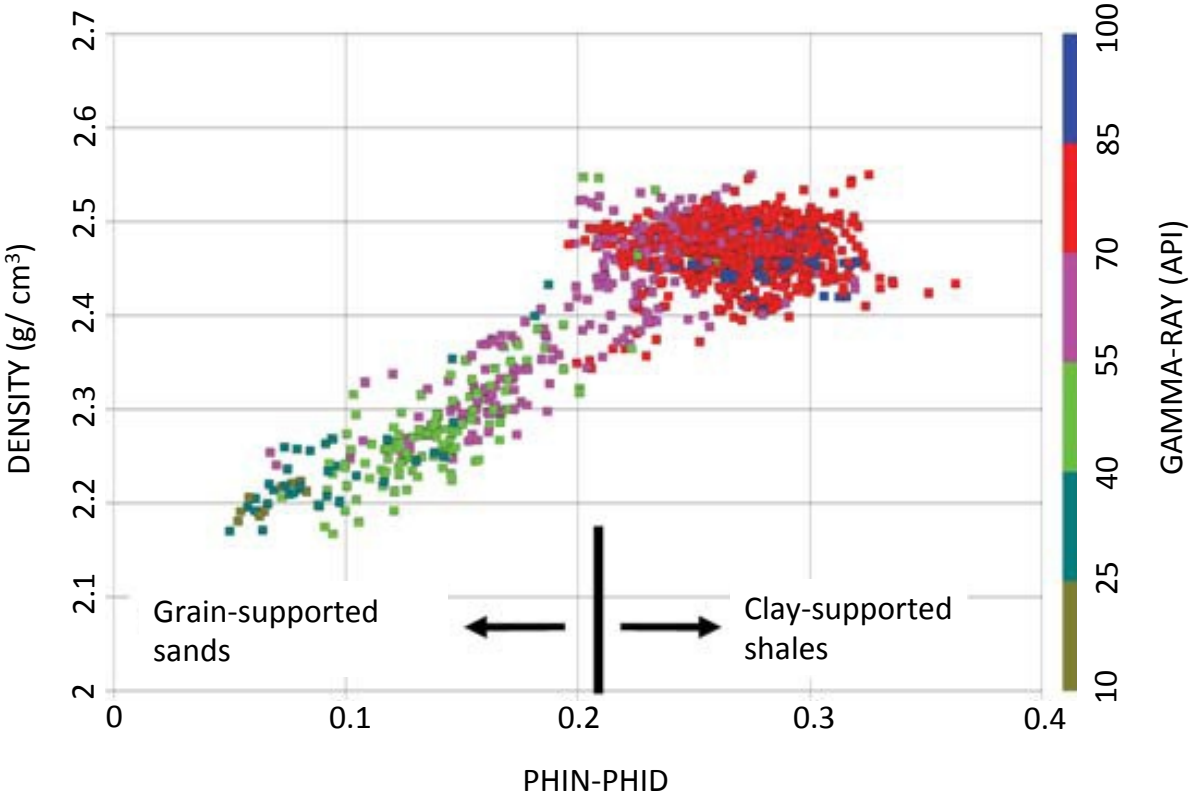

Figure 1.9: Density versus the difference between neutron-derived porosity and density-derived porosity. The difference is a measure of shale volume. The gamma-ray log is shown in colour, and there is clearly a discontinuity in slope of the response at the point shown by the vertical bar. Grain supported sands are to the left and clay matrix-supported shales are to the right of the slope break (after Katahara, 2008).

1.5 Shale in reservoir geomodelling

Identification of shales and other lithologies from the log data is a very important task to be able to build a geological model and then to construct a simulation model to evaluate the reservoir performance. In this section I examine the techniques used in the discipline of reservoir geomodelling to populate shale in the geological and the simulation model.

Most clastic reservoirs contain shales which are either continous correlatable shales or discountinous shales (Figure 1.10). While the continous correlatable shales are handled with ease in reservoir geomodelling, discountinous shales present a source of uncertainty. These shales cannot be correlated between wells, and their likely location within the reservoir can be modelled using geostatistical techniques conditioned to core and outcrop data. In addition, an understanding of the geological background of the depostional enviroment for a given reservoir is a prerequisite for geomodelling. Further geological analysis provides several insights that are useful for statistical model-building: categorization of petrophysical dependencies, identification of large-scale trends, interpretation of statistical measures, and quality-control on generated models (Corbett, 2009).

Depending on the complexity of the reservoir structure, different geostatistical techniques could be used to populate the model with discontinous/stochastic shales. In fields where the variation between the elements is not clearly defined and distinct objects cannot be measured, the shale distribution is determined using Sequential Indicator Simulation (SIS) (Figure 1.11(a)). For this method, variograms of shale length and thickness are required. Vertical, major, and minor direction variograms are usually prepared on the basis of analogue and well test data (Corbett, 2009 and Rossini et al., 1994).

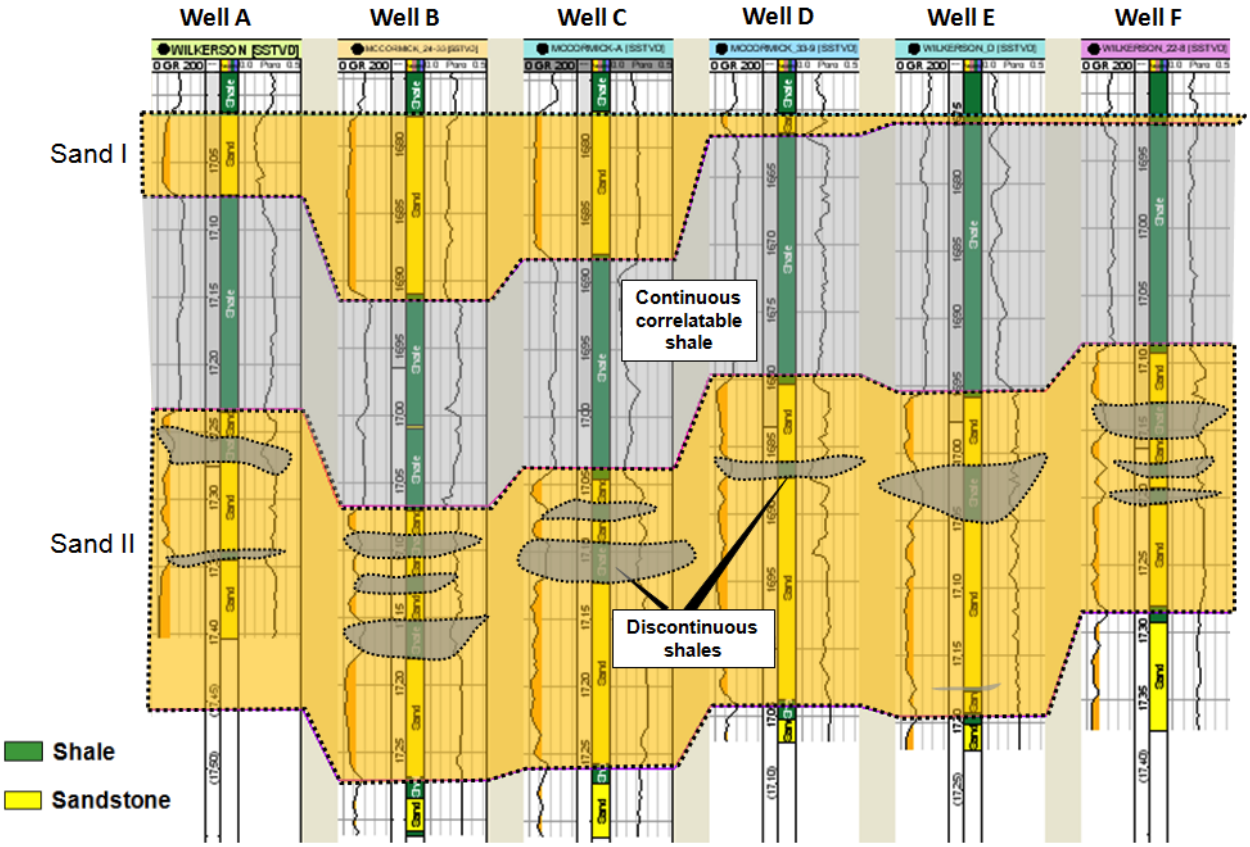

Figure 1.10: Shale distribution across different wells in a North Sea Field. There are continuous shales that can be correlated between the wells and there are discontinuous shales that cannot be correlated between wells (course given by Questiaux, 2010).

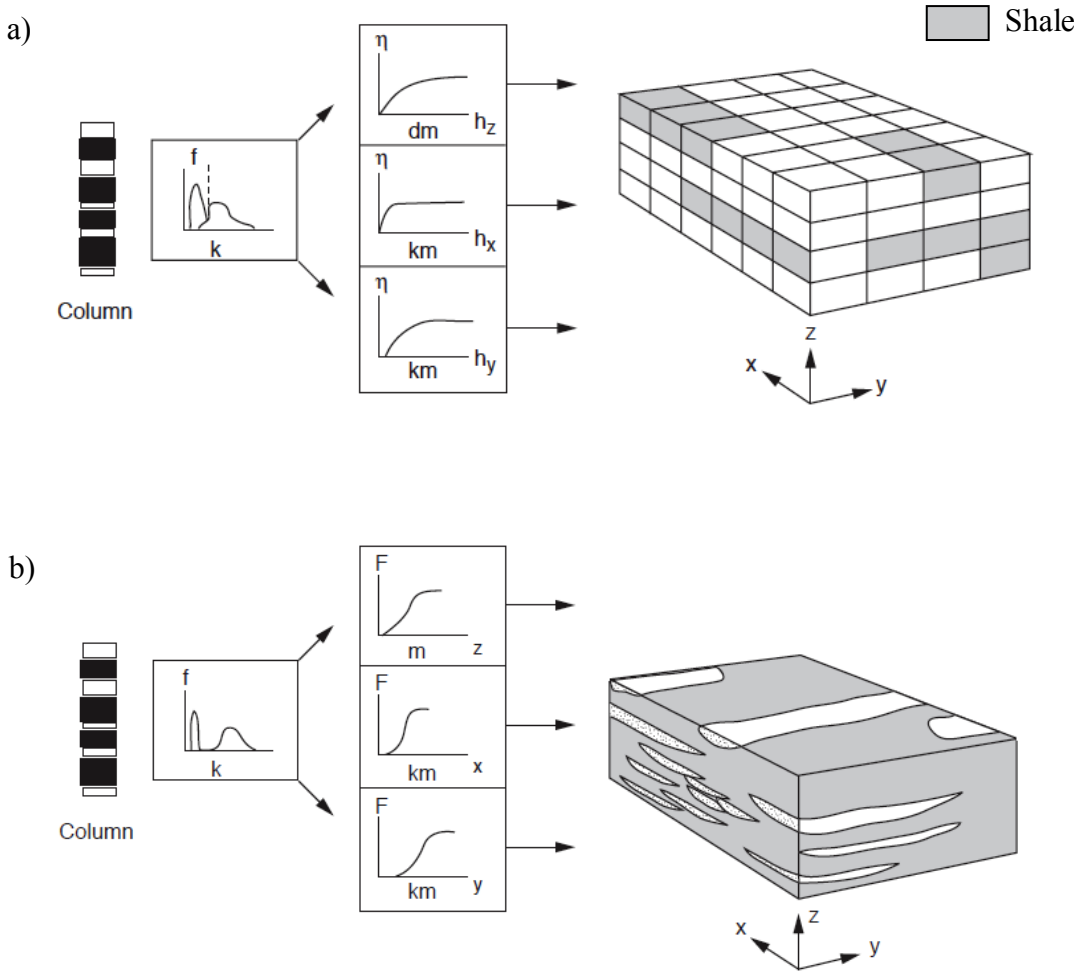

Figure 1.11: Techniques used to populate shales in the geological and the simulation model; a) Sequential Indicator Simulation (SIS) method b) Object based modelling method

However in a field where the para-sequences contain distinct rock types and dimensions, the object based modelling is recommmended (Figure 1.11(b)). For this geostatistical technique there are more sophisticated rules to follow to define objects and their interaction (e.g. erosion or aversion). The stochastic shale objects are defined depending on the depostional environment. For example for a braided fluvial environment, the shale objects are populated in a sand background, however in a turbidite system the sand channels are inserted as objects in a shale background. These models are the most realistic for handling low net-to-gross fluvial reservoirs; however, they require a good association between the petrophysical properties and the cumulative distribution function (CDF) of the objects geometry. Tyler et al. (1994) give a good example of this application. The shale geology will be discussed further in Chapter 2. After an extensive petrophysical analysis of the well data, the reservoir properties distribution is normally controlled by the facies distribution. Therefore the sequential simulation methods is normally implemented to populate the properties. Generally the reservoir and non reservoir shales are assumed to be impermeable and not part of the flow units.

1.6 Shale in reservoir simulation

In the previous sections, I examined the identification of shales from the petrophysical data, and then I presented the techniques used to populate these shales in the geological and the simulation model. Here, to close the loop of reservoir modelling, I give an overview about the understanding of shales in the reservoir simulation.

1.6.1 Shale and Net to Gross

Reservoir simultion aims to predict the reservoir performance and to estimate the fluid flow behaviour and pressure evolution. In most cases, available computers are usually memory-limited and are not fast enough to simulate the detailed geologic models derived from reservoir characterization. This has given rise to the need for upscaling techniques. Averaging, one of the key components of upscaling, calculates the effective properties for a coarse simulation grid that preserves fine-grid fluid-flow dynamics (including pressure and flow rate) within the coarse gridblock. This technique leads to an average of the shale and sand dimensions within the coarse grid block. Proportional to the volume of shale and sand

averaged per coarse grid cell, a Net to Gross ratio, also known as NTG, will be assigned to each cell of the upscaled model. NTG is therefore defined as the ratio of the bulk volume of sand to the total bulk volume. In the reservoir simulation, this is done by defining the clean sand as NTG=1.0, and the pure shale NTG=0.0. However for a shaley formation the NTG will vary between 0 and 1. The fluid flow simulation between the adjacent cells will be calculated using the effective properties derived from the upscaling techniques.

1.6.2 Shale and fluid flow simulation

In fluid flow simulation, the pressure equation that governed the fluid flow behaviour is solved only within the active cells. The active cells are those with non-zero NTG. In other words, because of the low permeability of the shales, the cells with 0 NTG, are known as inactive cells and are excluded from the fluid flow simulation. However for the active cells with non-zero NTG, the pressure and saturation changes are calculated within the effective volume of the adjacent cells. Figure 1.12 illustrates the way the fluid flow simulator solves the pressure equation. For a given NTG of two adjacent grid blocks, the fluid flow simulator (in this case Eclipse (TM Schlumberger)) considers the effective volume of each cell to solve the pressure and saturation changes. The effective volume of each cell is the volume of the grid block multiplied by NTG (Figure 1.12). Using the notation in Figure 1.12, the effective area of each cell is given by the following equation:

$$, A_i^{eff} = A_i \cdot NTG_i \tag{1.1}$$

$$A_{i-1}^{eff} = A_{i-1} \cdot NTG_{i-1} \tag{1.2}$$

Where A_{i-1}^{eff} and A_i^{eff} are the effective areas of the $(i-1)^{th}$ and i^{th} blocks.

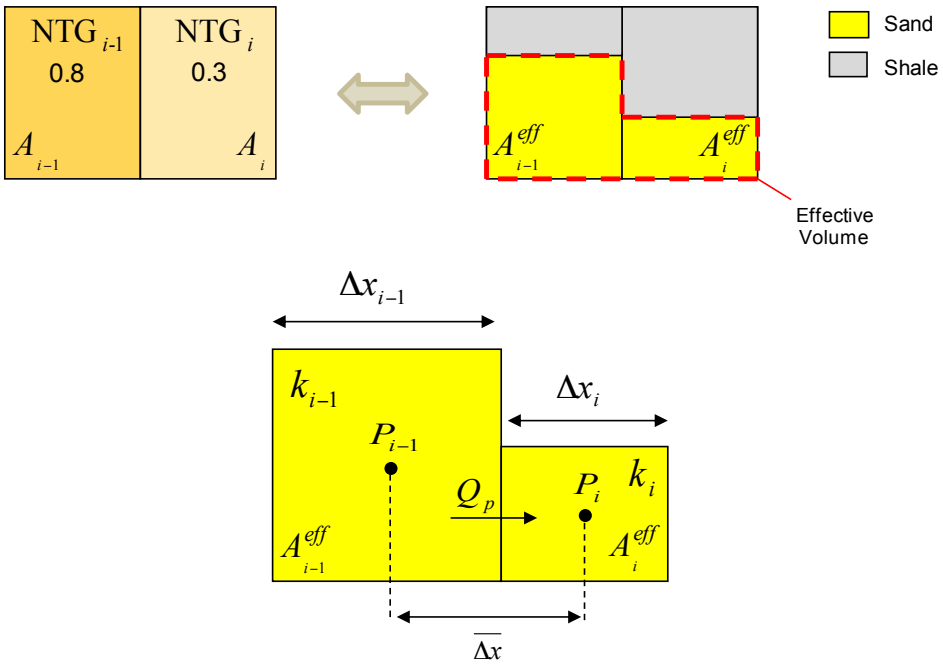

Figure 1.12: Illustration of the inter block volumetric flow for a single fluid flow scenario. The effective area of each cell is equal to the original grid block area multiplied by NTG.

The volumetric flow between the two blocks is derived from Darcy's law and in the case of single fluid flow the inter block volumetric flow; Q_p is given by:

$$Q_p = -\overline{KA}\left(\frac{\overline{\lambda_p}}{\overline{B_p}}\right)\left(\frac{P_i - P_{i-1}}{\left(\frac{\Delta x_i + \Delta x_{i-1}}{2}\right)}\right), \tag{1.3}$$

Where the permeability-area product KA is given by

$$\overline{KA} = \left(\frac{\Delta x_{i-1} + \Delta x_i}{\frac{\Delta x_{i-1}}{\left(kA^{eff}\right)_{i-1}} + \frac{\Delta x_i}{\left(kA^{eff}\right)_i}}\right) \tag{1.4}$$

Where:

$\Delta x_{i-1}, \Delta x_i$ are the sizes of the (i-1)th and ith blocks;

k_{i-1}, k_i are the permeabilities of the (i-1)th and ith blocks;

$P_i - P_{i-1}$ is the pressure drop between grid block centres;

λ_p is the mobility of the phase p;

B_p is the formation volume factor of phase p.

In terms of fluid flow behaviour several studies have looked at the effect of reservoir shales. Haldorsen and Lake, (1984) studied shales with no permeability. Their study mainly focused on stochastic shales that had zero permeability and variable length within 2D numerical grid blocks. Studies of simple "genetic" shale models suggest that the presence of shale will clearly increase the tortuosity of fluid flowpaths, and hence decrease the effective single-phase permeability of the reservoir (Martin and Cooper, 1984), (Figure 1.13(a)). Furthermore another study by Stephen et al., (2001), has examined the effect of shale on two phase flow by conductiong Monte Carlo realizations of 2D cross-sections at the genetic sedimentary unit scale. Results demonstrate that the flow is strongly dependent on the balance of viscous, capillary and gravity forces, which can vary according to the distribution of amalgamation surfaces. Another study by Thomas (1990) suggests that, during immiscible displacements, oil in the vicinity of shale is initially bypassed by the displacing fluid, and subsequently drains from around the shale driven by viscous and gravitational forces, (Figure 1.13(b)). The initial

bypassing of oil leads to early breakthrough of the displacing fluid, and if many shales are present, to disruption of the displacement front. Other studies by White and Barton, (1999) of specific outcrops suggest that oil located in the junction where shales intersect is bypassed by the displacing fluid and remains unswept (Figure 1.13(c)).

Jackson and Muggeridge (2000) have investigated quantitatively the effect of inclined, intersecting, and discontinous shales on horizontal waterfloods, and whether these shales alter the sweep efficiency. They use generic, dimensionless two- and three- dimensional models. The results shows that these shales have a significant effect only if they are continuous over a large area and are steeply inclined. In addition the study showed that two-dimensional simulations can significantly overestimate the effect of shales. Therefore a better understanding of the shale distribution, length, width, and orientation is very important to evaluate fluid flow behaviour.

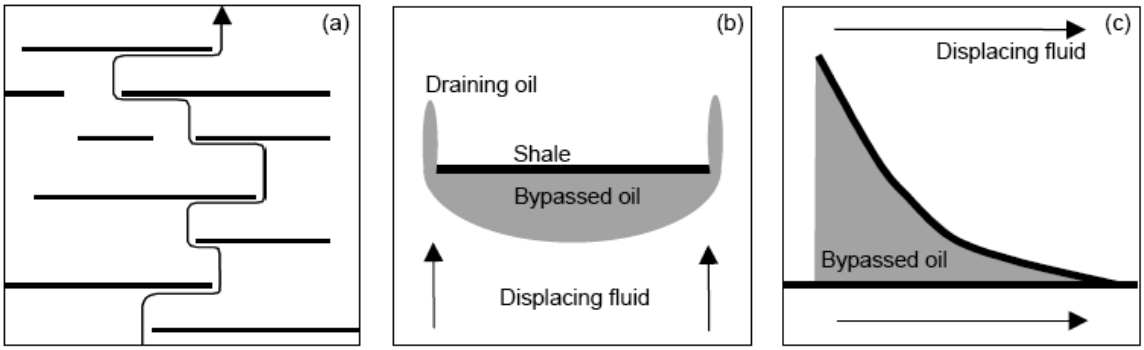

Figure 1.13: Schematic illustration showing the effects of discontinuous shales; (a) increase the tortuosity of fluid flow paths and hence decrease the single-phase permeability; (b) cause bypassing of oil behind individual shales; (c) causes bypassing of oil in the junction between intersecting shales.

In the area of carbon capture and storage, shales have been investigated as a geological parameter for the CO_2 storage. Compositional simulations of CO_2 injection suggest that the presence of thin shale layers has radically affected the CO_2 distribution in the reservoir, with CO_2 migrating laterally for several hundred metres beneath the intra-reservoir shales. Time

lapse seismic data have provided insight into the geometrical distribution of the injected CO_2 at different time steps and show the different migration pathways indicated in Figure 1.14. The seismic data have revealed at least temporary barriers (very thin shale layers) to vertical migration of the CO_2 that could not be resolved on the pre-injection baseline data alone. Due to the pronounced effect of the CO_2 on the amplitude of the time lapse seismic signal, these barriers have been mapped locally, and markedly increased the understanding of the CO_2 migration within the reservoir.

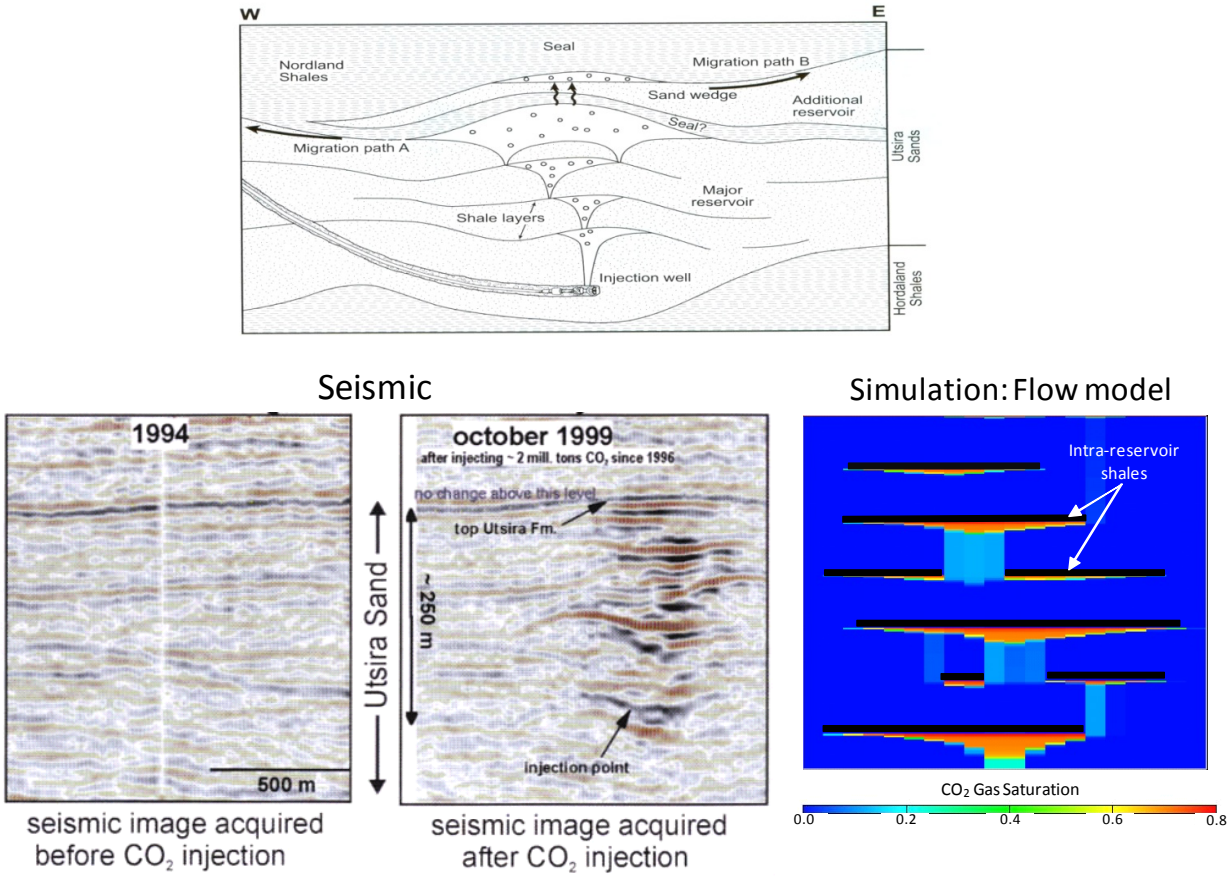

Figure 1.14: Seismic and fluid flow simulation for CO_2 storage. Strong seismic reflection amplitude observed at the location of the intra-reservoir shales. The seismic data have revealed at least temporary barriers (very thin shale layers) to vertical migration of the CO2 that could not be resolved on the pre-injection baseline data alone (Arts et al., 2002)

From the seismic and simulation data, at various locations, chimneys have been observed where CO_2 passes through the thin shale layers. Also in similar study, HajNasser (2010), has conducted a study of the effect of discontinuous intra-reservoir shales on CO_2 storage in realistic 3D geological model of fluvial dispositional environment. The results suggest that discontinuous reservoir shales have a significant impact on CO_2 injectivity. The existence of intra-reservoir shale necessitates additional wells to maintain the necessary injection rate.

Moreover the presence of discontinuous intra-reservoir shales shows a significant effect on fluid tortuosity and the CO_2 dissolution in brine. In the case of high density intra-reservoir shales, the CO_2 will be in contact with larger amount of unsaturated brine causing more CO_2 to be dissolved. Also by varying the shale length, the compositional fluid flow simulation shows that the more extensive the shales the higher the free CO_2 trapped benath these shales. Long term compositional simulation has shown that the shale length could enhance the solubility trapping mechanism. However shale length alone does not affect the injectivity of CO_2.

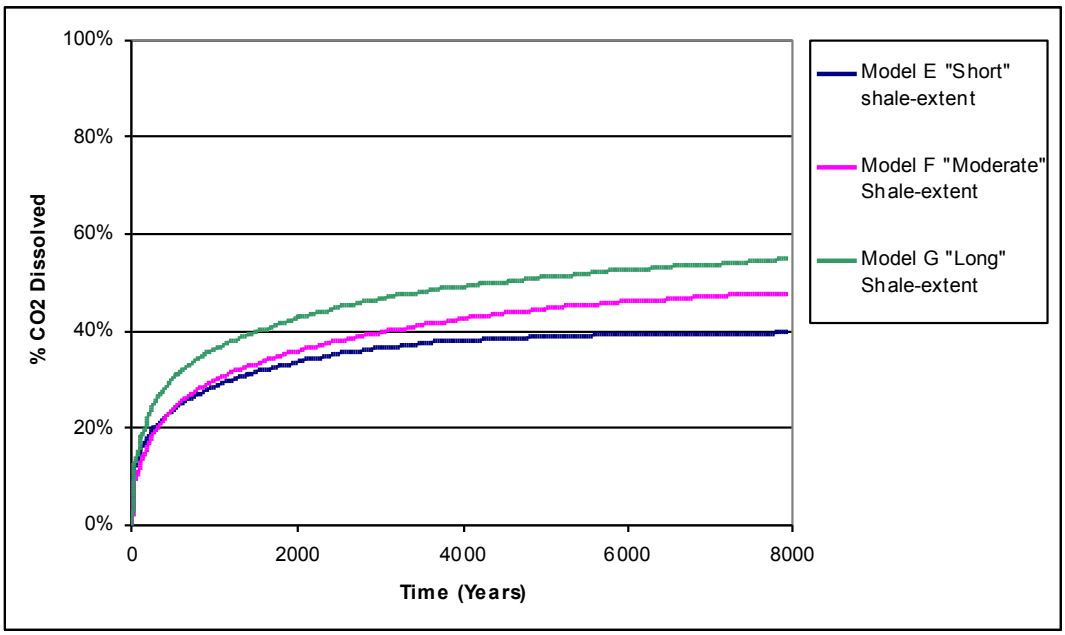

Figure 1.15: Percentage of CO_2 dissolved over time for different intra-reservoir shales length. (HajNasser, 2010)

The amount of CO_2 dissolved in brine increases as intra-reservoir shale length increases (Figure 1.15). In the case of "long" intra-reservoir shales (100m), simulation results show that more than 55% of the CO_2 injected is dissolved in brine. However, in the case of "short" intra-reservoir shale (10m), only 40% is dissolved.

1.7 Main challenges of the thesis

The main focus of the thesis is to identify the combined effect of geomechanics and pressure diffusion on shales, and to assess the implications for time lapse seismic. The ultimate objective of this analysis to be able to identify the reservoir and non-reservoir shale formations of high risk for future drilling directly from time-lapse seismic data. In order to achieve a reliable understanding of the impact of shales on seismic response, an extensive literature review on shale properties is conducted. Numerical coupled geomechanical and fluid flow simulation is performed. The findings of the simulation are integrated into seismic forward modelling and then the resulting seismic is compared to the observed data. For this, two field case studies: the Schiehallion field and the Erskine field are examined in this thesis.

1.8 Thesis outlines

The remainder of this thesis consists of six chapters:

Chapter 2 Provides an overview of various aspects of shale characterization and an understanding of their key properties. The chapter begins by giving a definition of what I consider shale. Next, the origin and their depositional environment are discussed. In addition, shale structure and geometry, such as thickness and lateral extension, is examined against the depositional environment. Next fluid flow transport and mechanical properties are presented and discussed. For this, several examples of laboratory measurement of fluid flow transport, elastic, and geomechanical properties are presented. A very brief overview of the implication of shale rock physics on the seismic analysis is given.

Chapter 3 Focuses on the physics of pressure development in shales. Based on the fluid flow transport properties of shales, and properties gathered from the literature, analytical calculation of the pressure diffusion in shales is performed. The predictions are based on different scenarios of pressure drop and different boundary conditions that reflect realistic cases. Finally a 3D numerical analysis of pressure diffusion and its effect on 3D realistic heterogeneous reservoirs is carried out. This case study is achieved by using a models supplied by Shell (Aberdeen).

Chapter 4 Presents the use of the nucleus of strain method in the stress analysis of shales.

Firstly numerical simulation of stress changes is performed for impermeable and mechanically active shales. Next, permeable and mechanically active shales are considered. The findings of the simulations are used to examine the changes of elastic wave properties for both types of shales.

Chapter 5 Shows the implementation of the coupled geomechanics and pressure diffusion simulation on seismic modelling. For this the theoretical background of the coupled fluid flow and geomechanical simulation. is presented. Next, the workflow that integrates these coupled mechanisms into the forward modelling of time lapse seismic is obtained. Finally the integrated workflow of seismic forward modelling is applied to a synthetic case and then to the full field simulation model of the Schiehallion field from the North Sea.

Chapter 6 Presents the second field application of the HPHT Erskine field. The aim of this field application is to implement my previous findings into the quantitative interpretation of time-lapse 4D seismic data from the Erskine field. For this, a 3D finite element based geomechanical and fluid flow simulation is performed for the Erskine field. To be able to assess the stress and pressure development in the sand rock and the reservoir and non-reservoir shales, the concept of active shale (permeable and mechanically active shale) is implemented. The geomechanical modelling and conversion of model results to synthetic seismic time shifts is used to perform a quantitative comparison of the models with the observed 4D seismic time shifts. This study aims to calibrate the shale properties and to identify the geohazerds and the formations with high risk for the future development of the Erskine field.

Chapter 7 Presents a summary of the thesis. In addition, recommendations for the further development of the ideas presented in this thesis are made.

CHAPTER

TWO

2 Shale properties

This chapter provides an overview of various aspects of shale characterization, and an understanding of their key properties. The chapter begins by giving a definition for what I consider *Shale*. Next, the origin and depositional environment are discussed. In addition, structure and thickness and lateral extent, are examined against the depositional environment. Finally, shale fluid flow transport and mechanical properties are presented and discussed.

2.1 Introduction

Shales are the most abundant of all lithologies, constituting some 45 to 55% of sedimentary rock sequence (Tucker, 1981). However it has been the experience of many sedimentologists that shales are hard to work with: they are very fine grained and lack the well-known sedimentary structures that are so useful in sandstones. Much more is known about sandstones, carbonates, and even evaporates than shale. However several recent studies including this thesis show that shale deserves much more attention and, when properly studied, can yield valuable additional insight into the dynamic characterisation of the reservoir. To address this, the current chapter provides an overview of various aspects of shale characterization and an understanding of their key properties. The chapter begins by giving a definition of what I consider shale. Next, the origin and depositional environments are discussed. In addition, shale thickness, lateral extension, and geometry are examined in the context of the depositional environment. Finally shale fluid flow transport and mechanical properties are discussed.

2.2 Shale definition

Here I define 'shale' as a clastic sedimentary rock which is fine–grained and composed of mud with a mix of silt and other minerals such as calcite and quartz. Despite a difference in definitions from the geomechanical, petrophysical, geophysical scale and geological literature (including a suggested change of name to mudstones – Potter et al. 2005), here I describe shale as fine-grained rock and sediments having more than 50% terrigenous clastic components less than 0.0625mm in size. Shales are a major component of the sedimentary basins (Sayers , 2010), and we may find such shales in the reservoir, but also acting as the overburden, underburden and the sideburden. In unconventional reservoirs, shales are the reservoir. For the purpose of this study, I define the intra-reservoir shales or sub-seismic shales as thin 1m to 10m thick shales interbedded within the reservoir. Generally, intra-reservoir shales are thinner than the size of a typical massive sand body (10m to 20m) and the seismic wavelength (50 to100m). Figure 2.1 is a picture of an outcrop of a deepwater channel system in Ainsa II, Spain. This provides a perspective for the scale of such shale deposits. In this thesis, I use the term 'shale' for these intra-reservoir shales, but also for overburden and underburden sediments. I focus on brine-saturated shales with no hydrocarbon potential.

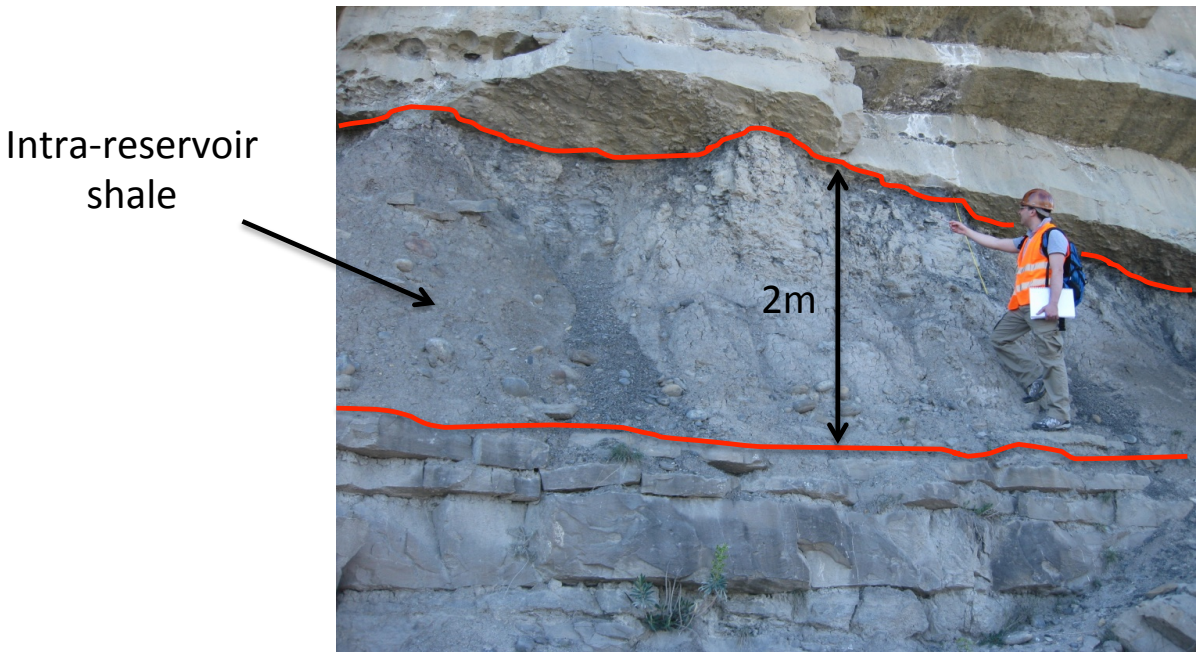

Figure 2.1: An outcrop from the Ainsa II basin. The red lines show the boundaries of what I call intra-reservoir shale. For scale, I am standing next to the intra-reservoir shale. The photo is taken by Prof Patrick Corbett during a field trip to Ainsa II in Spain in 2010.

2.3 Origin and depositional environment

2.3.1 The origin of shale sediments

The depositional environment for shales has very weak currents, and is likely to be lakes, ponds, swamps or the deep ocean floor (Schieber et al. 1998). Depending on the origin of the sediment three major groups can be distinguished (Potter, Maynard, and Pryor, 1980). The first shale group is known as the residual shales, this group is mainly formed by the weathering and soil formation acting on pre-existing sediments. The second group is from volcaniclastic, and are formed through in-situ weathering and/or later alteration of volcaniclastic deposits. This group is the most difficult shale to be distinguished. The third group is known as the detrital shale. This includes the most common shale that is formed through the normal sedimentary processes of erosion, transportation, and deposition. The majority of shale minerals (clay, silts, quartz…) are derived from the erosion of contemporary land masses. These fine terrigenous particles are largely transported in suspension, with deposition taking place in quiet, low energy environments (Mutti and Normark, 1987). Figure 2.2 illustrates the differences for transportation in high and low energy flows.

There are many transportation mechanisms. Rivers in particular, transport vast quantities of clay and silts in suspension for deposition in floodplains, lakes, deltaic environments and nearshore and offshore marine environments. Wind is another major agent of transportation, carrying shale sediments up to thousands of kilometres from source areas which are typically deserts and glacial outwash plains. The sediment may be deposited on land as loess (Aeolian shale/silt) or carried into the oceans (Potter, Maynard, and Pryor, 1980). On continental shelves and slopes mud can be re-suspended by storms to form clay- and silt rich clouds, which are thought to be an important mechanism for transporting fine sediment to ocean floors and abyssal plains. On alluvial fans and submarine fans shale sediment can be transported in viscous, sediment-rich, water-poor flows known as mudflows.

High efficiency flows

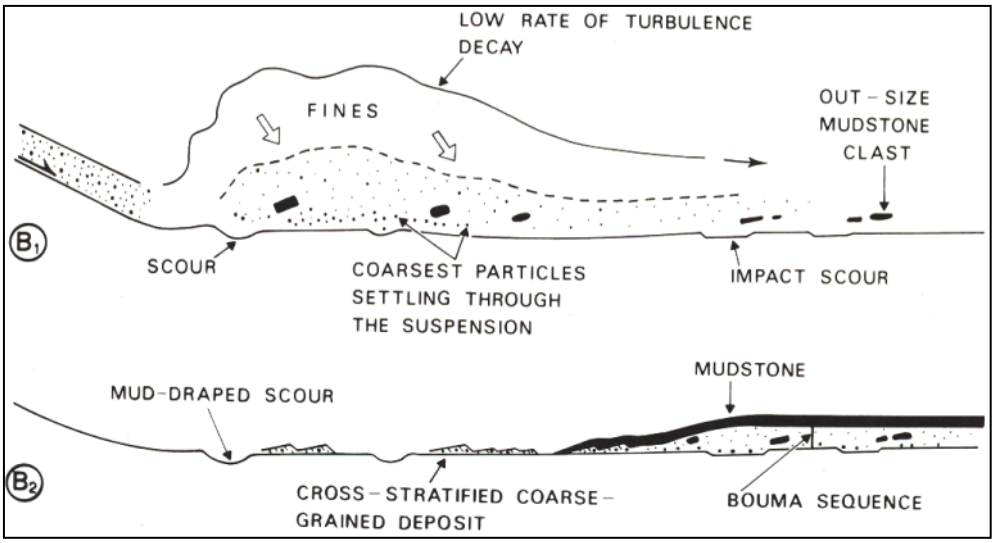

Low efficiency flows

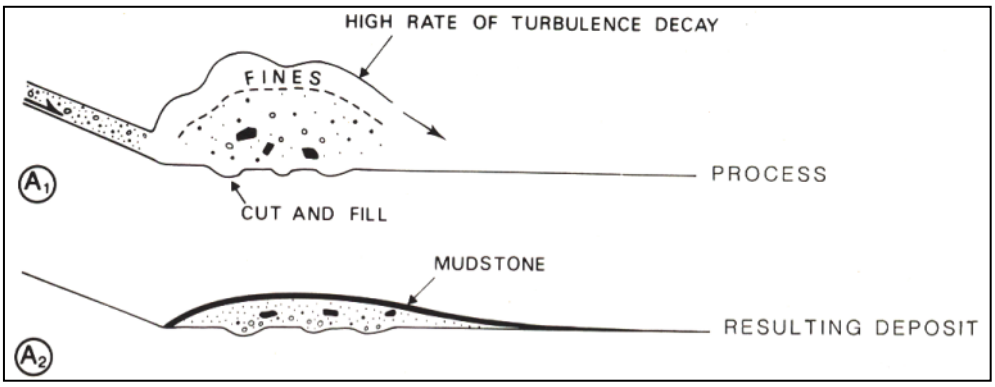

Figure 2.2: Schematic illustration of the transportation of fine terrigenous particles in high and low energy flows (Mutti and Normark, 1987).

2.3.2 Depositional environment

The depositional environment of shales has been the topic of several studies. Here I summarize shale characteristics for typical marine, non-marine, and loess environment.

2.3.2.1 Marine Shales (shelf, deep water, lagoons)

Here the marine environment includes shelf, deep water, and lagoon environments. The typical shales of the marine open shelf are various shades of grey and rich fossils. These are mainly deposited below wavebase, at depths in excess of 20 to 50 m. They are a major component of the entire shelf platforms (see Figure 2.3) and epeiric-sea sequences of the geological record, and so frequently pass laterally (shorewards) or vertically into limestones or sandstone of the shallower water, near shore zones. Shales deposited in deeper water largely from suspension, are termed hemipelagic. They consist of detrital clay and silt, clay minerals and zeolites derived from alteration of volcanic ash, and radiolarians, diatoms and sponge spicules. These types of shale cover the abyssal plains of the central Pacific. Shales of shoreline environments such as lagoons, tidal flats, deltaic inter-distributary bays and coastal swamps can be identified by their fauna sedimentary structures, and associated coarser classic deposits such as channel, beach or barrier sandstones.

2.3.2.2 Non-marine Shales (fluvial: channel, lacustrine)

Shales from river floodplains are best identified by their association with fluvial channel sandstones. In many cases, these shales are overbank deposits and constitute the upper part of fining upward sequences generated through lateral migration of the river channel or by channel abandonment. Shales deposited in lakes vary considerably depending on the chemistry of the lake waters, organic productivity and climate. In the majority of cases the clay minerals are detrital, but clay minerals can be precipitated in the lake. In the Lacustrine environment, as a result of the poor circulation and organic matter preservation, organic rich shale can be deposited. The importance of organic-rich shales, lies in their potential as a source rocks for petroleum, if buried to suitable depths and subjected to appropriate temperatures. Figure 2.3 summarizes the shale stratigraphy for deltaic and fluvial settings. In addition, the stratigraphy of shale in clastic marine and deep sea environment is illustrated.

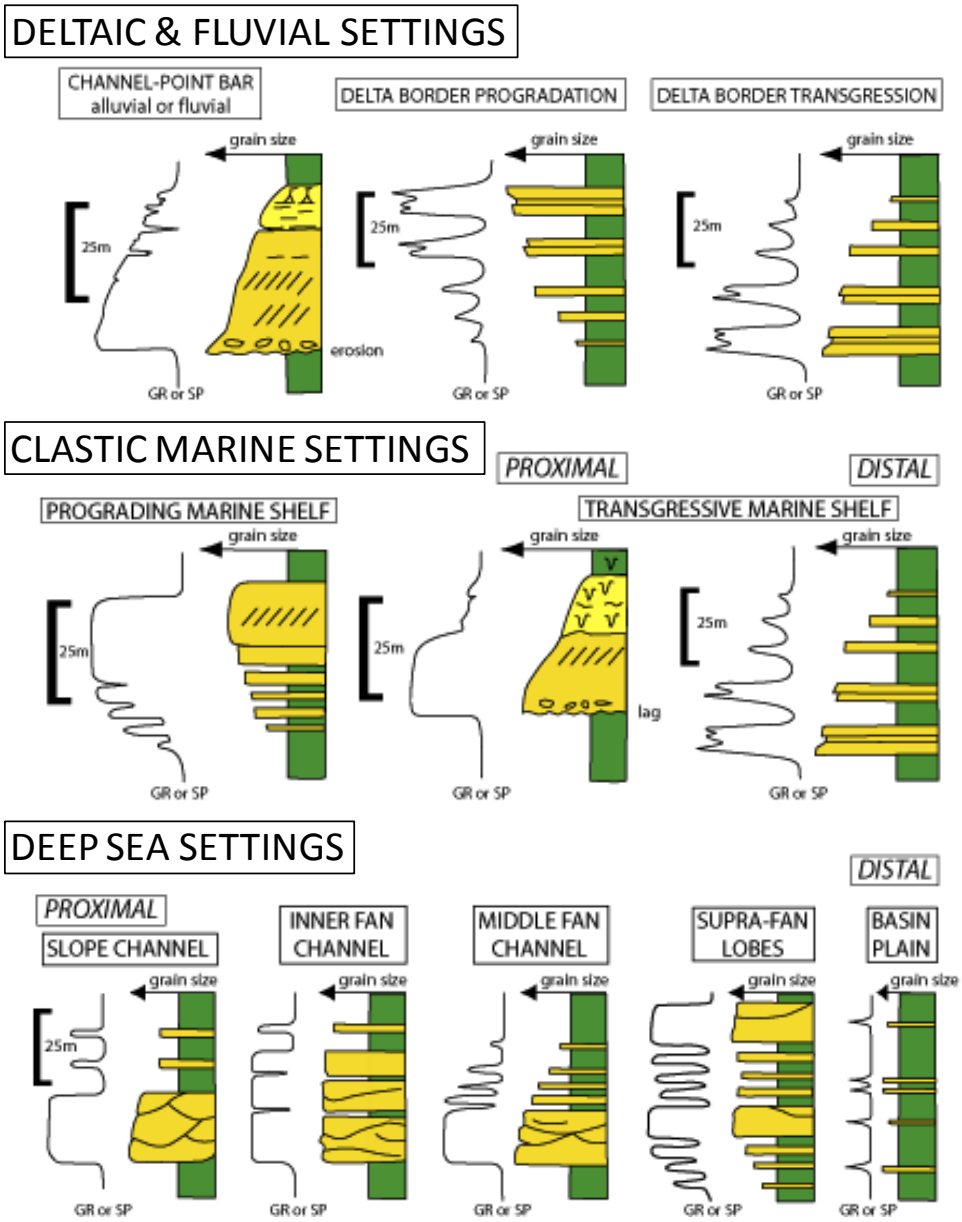

Figure 2.3: Shale (green) stratigraphy for different depositional environments. High Gamma Ray (GR) and Spontaneous potential (SP) are associated with shale units (course given by Questiaux, 2010).

2.4 Geometry

From a structural point of view there are two well-known shale types. The definitions are based on whether the dimensions and spatial deposition of the shales are known. Stochastic shales or shales break cannot be correlated between wells and appear to be scattered randomly within the sand matrix. Deterministic shales are continuous between observation points. There is no uncertainty associated with their existence and lateral continuity. Most reservoirs are a hybrid with respect to shales in that both deterministic and stochastic shales coexist; however, the occurrence of stochastic shales clearly becomes more prevalent with large well spacings.

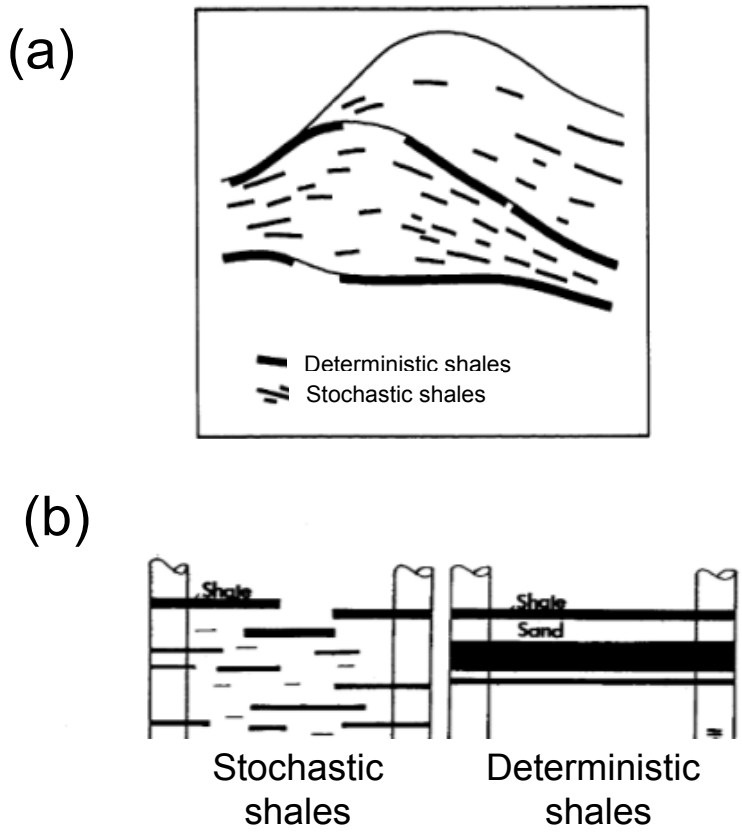

Figure 2.4: In this work thin sub-seismic shales are considered, similar in character to that shown above. (a) Example of intercalcating shales from the turbiditic Frigg field (Skaug and Gunesø 1986). (b) Thin sub-seismic shales can be distinguished as laterally continuous 'deterministic' shales or the more laterally discontinuous 'stochastic' shales.

For the purpose of this thesis, a quantitative understanding of shale lateral continuity and shale thickness is very important. For this, published studies are examined.

2.4.1 Lateral continuity

Shale breaks in reservoirs generally can be detected on logs, but their continuity and petrophysical properties are often unknown. Outcrop studies have shown that the geometry, frequency and lithology of shale and silt intercalations are determined largely by the environment of deposition of the rock. Thus, detailed studies of suitable outcrops of various deposition types should provide a better understanding of subsurface shale properties. Only a few such detailed studies have been reported, the best examples are by Zeito (1965) and Verrien et al. (1967) who analyse closely drilled wells in recent sediments. Also providing useful data on shale continuity is Pryor and Fulton, (1978), and these and other more general outcrop studies indicate that the geometry and distribution of shale in clastic formations show considerable similarities in the rock deposited in depositional enviroments.

Zeito, (1965), made visual observations of shale dimensions in various depositional environments. Weber, (1982), enhanced and systematized Zeito's findings, and presented possibly the first quantitative relationship between shale continuity and the type of depostional enviroment (Figure 2.5). Based on Weber's study, in a marine environment shale beds extending for several hundred meters are common. For coastal barriers, the shales are also quite continuous and are generally concentrated in the lower half of the sandy interval. Delta-fringe and delta-plain sediments contain shale breaks, which are usually less extensive than those of the above depostional environments mainly because of erosion by migrating and nonmigrating rivers, and tidal channels. Zeito, (1965) found that in deltaic environments, shales commonly joined other shales rather than being isolated.

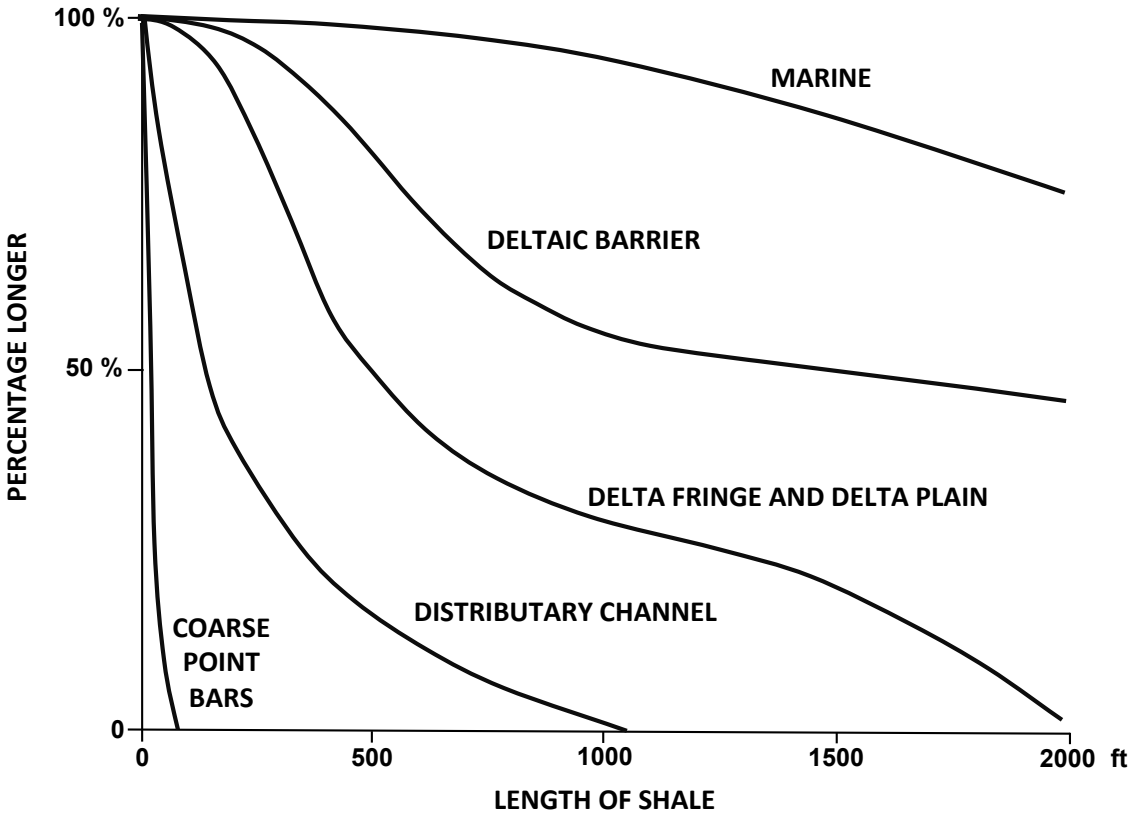

Figure 2.5: Lateral shale continuity as function of depositional environment (Weber, 1982)

Distributary channel fills possess shale breaks which are often less than 10m, where their most common occurrence is related to festoon cross-bedding and where they often merge. Point bars of meandering rivers possess, in addition to the shale-break types found in distributary channel fills, more continuous shale beds occuring along accretion planes. Coarse-grained point bars and braided rivers generally have very short shale and silt intercalations. Several studies confirm a significant confidence in the findings of Weber. Skaug and Gundeso, (1986) who present data on the geometry and occurrence of shales on the Frigg Field. Potter et al., (1980) present data on the geometry and occurrence of shales in modern enviroments. LeBlanc, (1977) Sneider et al., (1978) and Richardson, (1978) discuss shales in ancient environments. Their discussion reinforces the hypothesis that certain depositional environments exhibit distinguishable shale characteristics.

2.4.2 Thickness

Most studies tend to focus on the lateral continuity of shale and the impact of shale breaks or clay/silt intercalations on the fluid transport properties, especially the vertical flow. Unfortunately, published numerical data specifically on shale thickness are generally scarce, although statistics from outcrops or general summaries for shale length and their variation are readily available (Weber 1982). Unfortunately, the lateral dimensions of the intra-reservoir shale are not a reliable way of evaluating its thickness. This point is highlighted by Haldorsen and Lake (1984) in a modelling-based study based on data from a Cambrian reservoir in Algeria. This is due to the fine material that composes the shale being deposited in the non-uniformities of topography in areas of weak turbulence. As a consequence the thickness of the deposits is related to the local topography prevailing at the time of deposition and is independent of depth.

Here, my approach in evaluating shale thickness is to define a broad qualitative classification of depositional environments against thickness (Figure 2.6). This is based on the principles of sediment deposition guided by knowledge acquired from an understanding of the outcrop geology and sedimentary architecture. As shales represent deposition under lower energy conditions than the sandstones and may relate to either lower energy locations within the depositional system or periods of lower energy. Sediments deposited in different depositional environments generate different patterns of sandstone and shale and the degree of preservation of shale within sandstone dominated intervals will vary from environment to environment. A sudden change in process or energy may allow the temporary accumulation of some thin shales. Thus, the top end members of Figure 2.6 are those reservoirs that are commonly dominated by shales as their depositional processes are mostly low energy. For example, deep-sea slopes have thick sections of shale with almost no sand. Shale is transported to these areas easily, whereas sand is regarded as being a more localized input spatially and temporally. Indeed, even the sand-prone portions are likely to include some zones with thick shale – Figure 2.7(a) gives an outcrop example of such a system. Systems that deposit essentially sheet-like sandstones (such as unconstrained deepwater turbidite systems) often produce interbedded sandstones and shales, so that extensive shale-dominated intervals may be preserved within the reservoir. For the low end member environments, the reverse is true – they are generally sand and gravel dominated, characterized by erosion as well as deposition, with most finer grained sediments washed or blown away by high energy

processes. For example, shales are very rare in the Aeolian systems (Figure 2.7(b)), where generally only thin playa lake shales exist. It is usually the fluvial incursions that will generate the shales. Also, in fluvial systems individual channel sandstones within a shale-dominated floodplain succession may stack vertically and horizontally to form thicker and more extensive sand-dominated sheets. Discontinuous shale bodies may then be preserved within the sandstone dominated channel complex and their shapes will be irregular, reflecting the shape, size and stacking pattern of the channel sandstones. In other cases, the shape of the shales preserved within a sandstone dominated interval reflects the sub-environment in which they were deposited. For example, in a braided river environment, sections of a river channel may be abandoned and may become filled by shale. In this case, the preserved shales will reflect the shape and size of the channels and will tend to be elongated parallel to the channel sandstones. The different clastic depositional environments above can provide the necessary range of shale dimensions anticipated and examined in this study. Thus, for example, in reservoirs created by the deep-sea slope environment such as in the Girassol field (Navarre et al. 2002) or the Schiehallion field (Leach et al. 1999), the shales may be sufficiently thick (5–10 m)

In addition to the shale geometry, shale composition is very important parameter to take into account for a dynamic characterisation of the shale. However a detailed shale composition is beyond the objective of this study, therefore a very brief description is presented in the next section.

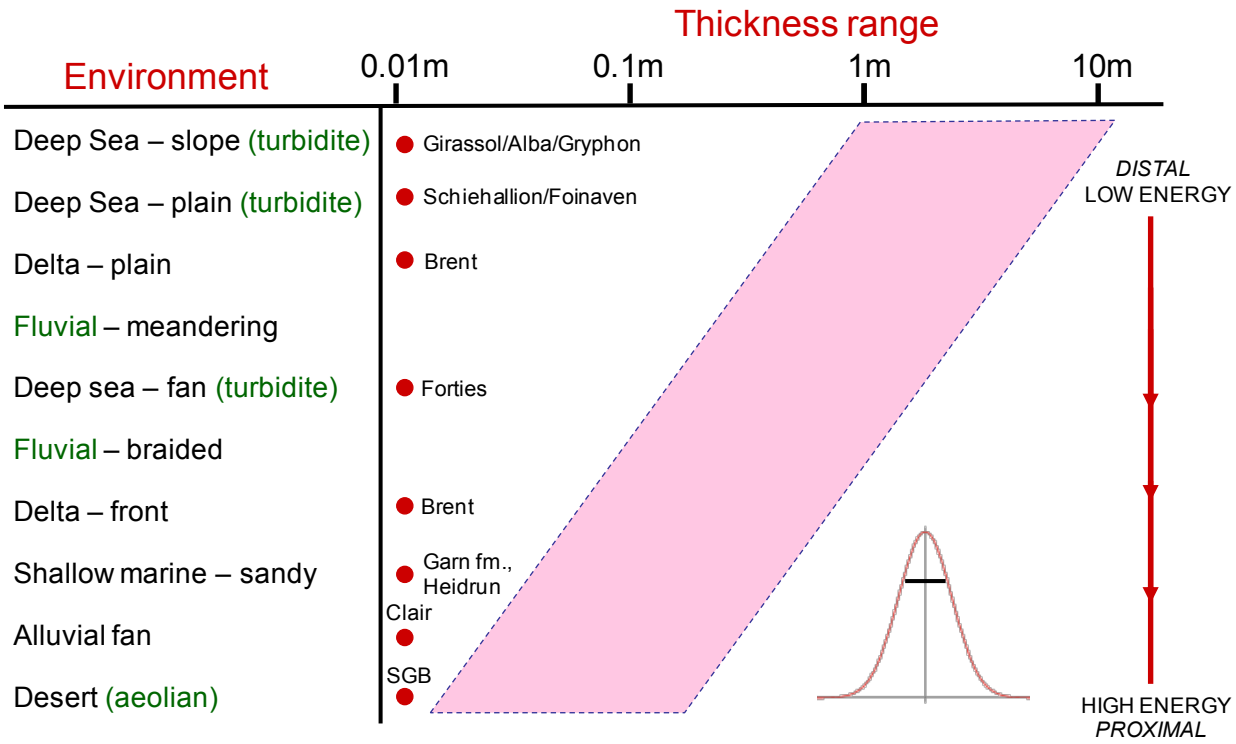

Figure 2.6: An order of magnitude estimate of intra-reservoir shale thickness range for various depositional environments. Note that these are for parts of the depositional system in which only sands dominate. Values are defined for the most typical (frequently occurring) shale units. Drawn from contributions by Dorrik Stow (personal communication). Field names are shown for reference purposes. The acronym SGB stands for the southern gas basin.

a)

b)

Figure 2.7: Outcrop photographs of two depositional systems from my hierarchy. Preserved shale thickness can be clearly seen in the Deepsea fan/basin plain example (a) from the Annot sandstone, SE France, but is mostly absent in the Aeolian dune sandstones of (b) from the Navajo sandstone, Zion national Park, US – highlighted by the white arrows in both cases. Photographs are sourced from Dorrik Stow (personal communication).

2.5 Mineralogy

Shales contain a wide range of clay minerals and non clay minerals. Clay minerals are the most abundant materials in shales. The most common are kaolinite, illite, chlorite, and smectite which are found in various amounts in shale. The depositional environment was once thought to exert considerable influence on the clay mineralogy through early mineral transformations in the basin of deposition. In addition other constituents such as quartz, feldspar and zeolites are generally present in low concentration. Organic materials such as kerogen are present in almost all shales, and it is an indicator by the gas potential of the basin and the thermal history.

2.6 Maturity and petrology

The understanding of the organic chemistry of shales has made rapid progress in recent years, largely as a result of the interest in shales as source rocks for petroleum (Vanorio et al. 2008). The capacity of shale to generate hydrocarbons is governed by the amount of organic matter present, and its state of thermal maturity. The minimum amount of organic matter for the generation of significant amounts of hydrocarbons seems to be about 0.5% organic carbon. The thermal maturity of shales affects the type of hydrocarbon produced, consequently the determination of temperature history is an extremely important part of shale maturity analysis. Shales exist in both unconventional and conventional reservoirs.

Shale in unconventional Oil and Natural Gas resources:

Some shales are considered to be self –contained petroleum systems where this source rock is both the reservoir and the seal. These quartz rich shales are organic-rich units of unconventional oil and natural gas resources.

Shale in conventional Oil and Natural Gas resources:

In the case of a conventional reservoir, hydrocarbons are produced from organic rich shale and have migrated to reservoir rocks that are interbedded with further shales. These clay rich shale units are less mature and have less organic maturity and high water saturation. For the purpose of this thesis, only shales with no hydrocarbon potential: less organic maturity and high water saturation are of interest.

The maturity of organic mater in the shale is mainly controlled by heat and time. Heat gradually increases over millions years as the organic matter continues to be buried deeper under increasing sediment load. Through increasing temperature and pressure during burial, clay composition, the maturity of the organic matter is altered. This geological process can be summarized in three broad steps. It starts with diagenesis, then catagenesis and finally the metagenesis. The last two steps are mainly associated with hydrocarbon generation. However since I am only interested in shales with no hydrocarbon potential, only the diagenesis process will explained in the next section.

2.6.1 Diagenesis

The term diagenesis is used to refer to all physical and chemical changes which affect the minerals consisting the sediments from the time of deposition. For shale, the most prevalent and dramatic diagenetic changes involve the conversion of smectite to illite in the clay portion. As the level of diagenesis increases the amount of smectite decreases while the illite content increases (Gutierrez et al., 1996). Shale diagenesis is often characterized by low-temperature alteration of organic matter, typically at temperature below 50 °C (Peters, Walters, and Moldowan, 2004). During this stage, oxidation and other chemical processes begin to break down the material. Biological processes will also alter the amount of organic material. At this point bacterial decay may produce biogenic methane with increasing temperatures. The organic matter is gradually converted to kerogen and lesser amounts of bitumen. Further sedimentation increases the depth of burial over time. The organic matter slowly cooks as pressure and temperature increase with greater burial depths. Kerogen formed by degradation of organic matter is the primary ingredient in the generation of hydrocarbons. Kerogen has been classified into four broad groups, each of which has distinct bearing on what type of hydrocarbons, if any, will be produced (Makhous and Galushkin, 2005) (Figure 2.8).

Type I kerogen is generated predominantly form lacustrine environments and, in some cases marine environments. It is rich in hydrogen and low in oxygen, and it is prone to oil production. (Klemme and Ulmishek, 1991).

Type II kerogen is typically generated in reducing environments found in moderately deep marine settings. It is rich in hydrogen and low in carbon. It can generate oil and gas (Vandenbroucke, 2003).

Type III kerogen is derived primarily from terrestrial plant debris that has been deposited in shallow to deep marine or non-marine environments. This type of kerogen has low hydrogen and higher oxygen content than type I and II. Consequently it generates mostly dry gas.

Type IV kerogen, is typically derived from older sediments redeposited after erosion. This type of kerogen consists of residual organic matter with high carbon content and no hydrogen. It is considered a form of dead carbon with no potential for generating hydrocarbons.

2.6.2 Shale maturity and seismic response

Earlier works have attempted to establish a relationship between seismic properties of shale and their maturity. Parker (1968) showed that density and P-wave velocity were inversely correlated with maturity. Mraz et al., (1983) also found an inverse relation between P- and S-wave velocities (V_P and V_S) and organic content in the green river oil shale formation. In an attempt to compile data and to understand and quantify the velocity-kerogen content correlation, Vernik and Nur, (1994) measured shale from various formations and found that a good correlation exists between velocity and kerogen content in all the samples. The change in impedance with maturity of a shale is shown in Figure 2.9. The acoustic impedance of the microstructural image is plotted agianst the hydrogen index (HI) for all samples. Both impedances are plotted in Figure 2.9 from the analysis of the microstructure and from ultrasonic experiments.

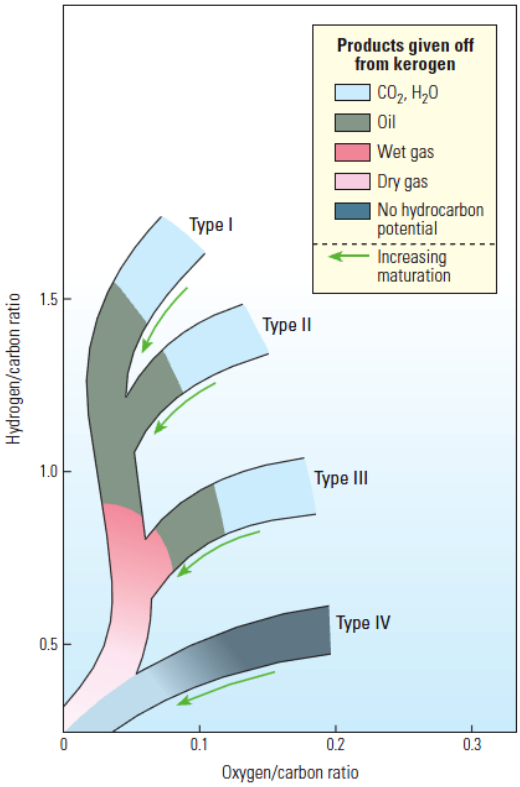

Figure 2.8: Different types of kerogen as function of hydrogen/carbon ratio and oxygen/carbon ratio (Makhous and Galushkin, 2005)

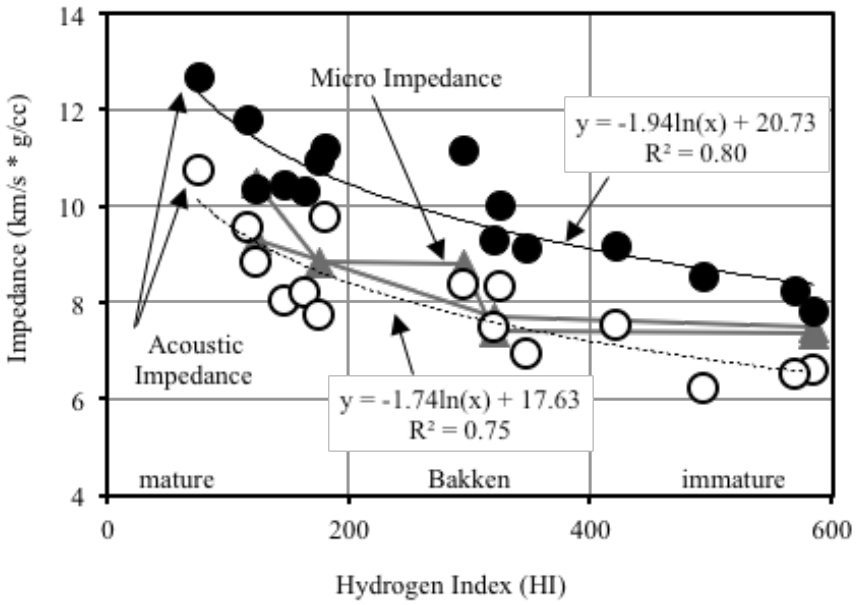

Figure 2.9: Correlation between the hydrogen index (HI) and acoustic impedance (kg/s*g/cc) in Bakken shale of varying maturity. Open and solid black circles represent impedance measured by ultrasonic wave propagation perpendicular and parallel to bedding planes, respectively. Solid lines are best fits with a correlation coefficient of 0.75 or larger. The microstructural impedances (grey triangles) match the ultrasonic impedances obtained from wave propagation data; both increase with maturity. The correlation between these properties measured at two different scales is significant if we constrain the samples to one formation, (Prasad et al., 2009).

The analysis of the data above highlights major differences in the impedance microstructure and in elastic propeties of oil shale as a function of maturity:

- There is an inverse linear relation between velocity and kerogen content in shales with low porosity;
- Low velocity in low maturity shales is due to the frame-softening effect of kerogen;
- The overall impedance of the samples increase as maturity progresses
- Grain size increase with maturity;

If we wish to have better understanding of the dynamic behaviour of shales, fluid flow and mechanical properties need to be considered. This will be discussed in detail in the next section.

2.7 Fluid flow properties of shales

Investigating the fluid flow propeties of shales was one of the challenging tasks in my research. Unfortunately so little was published about the shale fluid properties. My approach in this topic is to perform an extensive literature research in order to have a better understanding of porosity and permeability of the shale.

2.7.1 Porosity

Horsrud, Sønstebø, and Bøe (1998) have looked at the fluid flow transport properties of different North Sea shales from different geological periods. Tertiary, Cretaceous, and Jurassic shales have been tested and characterized in this study. For Tertiary shales the porosity is generally high. As expected the porosity decreases with increasing depth and age, down up to 3% for the deepest shale. The porosity of the shales has been estimated from the determination of free water content. The free water content has been determined by drying 20 to 40 g of each sample until a constant weight is reached. For this method of porosity determination, it is necessary that the sample has been well preserved. In addition, the study suggests that it is difficult to draw a definite limit between bound water and free water in the shale, which has a range of pore sizes down to a nanometer.

Howard, (1991) conducted a quantitative study on shale porosity. The measured porosity is defined as the void space large enough to promote fluid flow. Massive and laminated shale from the lower Frio Formation of south Texas are used. The original 60 m section of core from a well in south Texas was stored for several years, exposed to fluctuations in room temperature and humidity. Drying occurred during this time, but there was no large-scale shrinkage or cracking of the core. Plugs 2 cm in diameter and 3.75 cm in length were cut from the core. Samples were oven dried at a temperature of 80 °C in order to remove as much interstitial water as possible without inducing severe desiccation effects. The sample plugs exhibited no shrinkage or cracking after this drying. Porosity was measured by standard buoyancy methods on the shale plugs saturated with Isoparaffin fluid (Isopar-M). Also in another experiment, porosity measurement was done by mercury injection porosimetry.

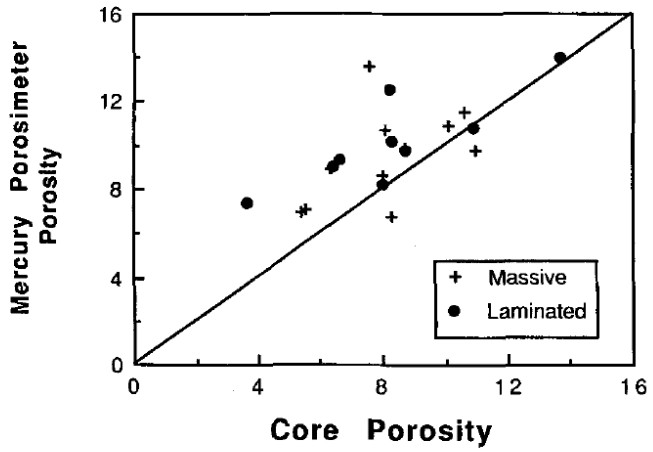

Figure 2.10: Porosity values for Frio shale samples as determined by standard buoyancy methods and the total intrusion volume of mercury Neuzil (1994).

Porosity measured for the shale samples ranges from 3.6% to 13.7%. Both laminated shale and massive shale have a mean porosity of 8.2%. These values fall within the range of shale pore sizes observed in shales older than 50 million years and buried to greater than 1200m (Borst, 1982). Also this range of porosity is within that reported by Neuzil (1994). For this particular study silt-sized quartz was dispersed throughout the massive shale, while in the laminated shales the silt was found in thin 0.1 to 1.0mm thick laminae. It was suggested that the concept of silt laminations served to create greater pore surfaces. This concept of silt

enhancing the fluid flow in shale was observed in the Devonian shales where a positive correlation between rate of production and number of silt lamination (Nuhfer et al. 1979).

2.7.2 Permeability

In addition to porosity, permeability is very important factor in fluid flow transportation in shales. Intuitively one would think that the permeability of shale is so low that it can be regarded as zero. However, laboratory measurement showed that is not the case. It has been shown that the low permeability of shale can be an important contribution in explaining the time delayed failure often experienced during drilling of shales (Horsrud et al., 1994) and (Charlez and Heugas, 1994). The permeability of shales can vary over several decades and may be very low. Permeability below 10^{-21} m^2 (1nDarcy) have been measured, Katsube and Mudford (1991), Chenevert and Sharma (1991), Van Oort (1994). Because of the low shale permeability, steady-state type measurement techniques are not usually applied. Instead, techniques based on transient measurements are used (Figure 2.11). In this technique, a disk shape shale samples is placed in a pressure cell, where pore pressure and lithostatic confining pressure is applied. After loading to pre-determined levels of pore pressure and confining pressure, the pore pressure is increased by a certain amount of pressure on one side of the sample and reduced by the same on the other side. The decay of this pressure difference is then recorded by a differential pressure transducer and the permeability is calculated for this time response.

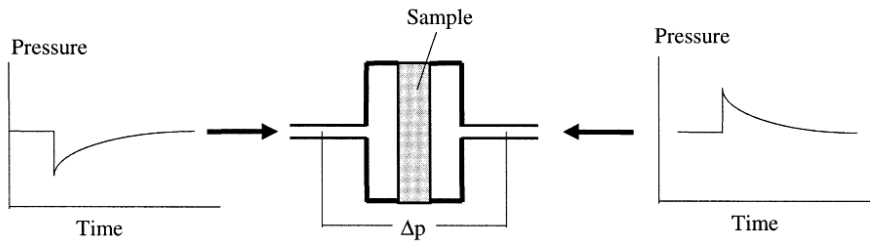

Figure 2.11: Illustration of the pressure transient method used for permeability estimation

An extensive literature review of different laboratory measurement of shale permeability is summarized in Figure 2.12. The figure gives a general qualitative measure of permeability for different rock types such as sands, silts, claystone and their intermediate rocks. The permeability ranges are derived from published data by Howard (1991), Katsube (2000), Best and Katsube (1995), and Schlomer and Krooss (1997).

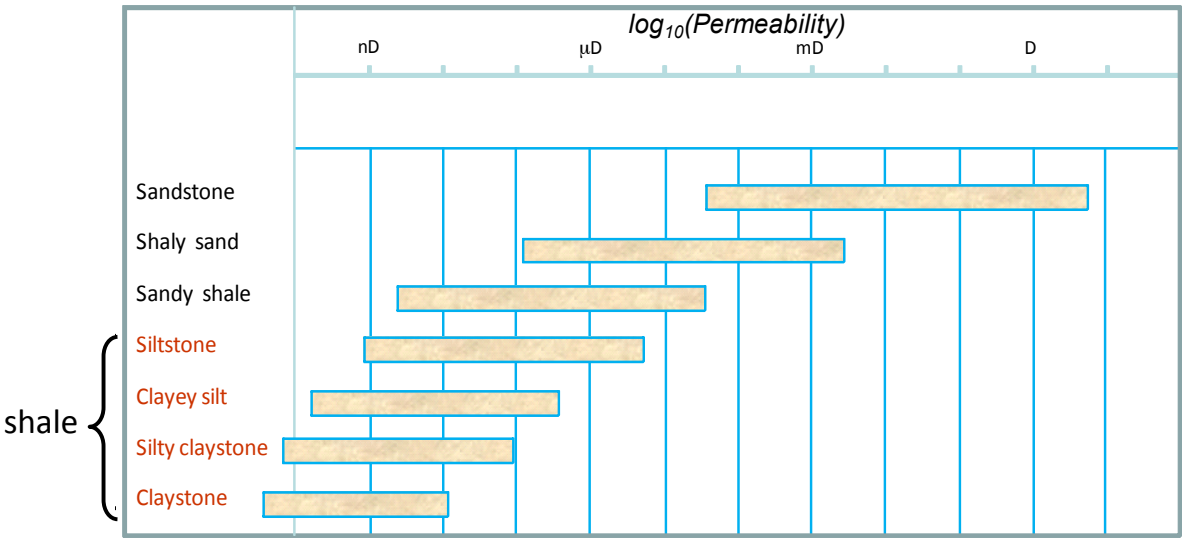

Figure 2.12: General range of permeabilities reported in the literature for shales and associated rocks. Measurements are for reservoir rocks over a range of depths, diverse geographical locations and for both laminated and massive shales. Values are extracted from Howard (1991), Katsube (2000), Best and Katsube (1995) and Schloemer and Krooss (1997). 'Shales' are defined as having more than 50% of terrigeneous clastic components <0.0625 mm and thus bracket a range of possible rocks. A more precise classification of shales is unclear as none have wide acceptance.

2.8 Mechanical properties of shale

Shale mechanical properties are important from a petroleum industry perspective as input for basin models, seal evaluation, pore pressure prediction, seismic interpretation with regard to wellbore stability. In recent years, some data have become available detailing shale geomechanics. Several studies have evaluated the influence of composition, lithology, organic content, and stress history on the mechanical properties of the shales. There are two types of measurement for the mechanical properties. There are the static moduli derived from stress-strain measurements, and then the dynamic moduli obtained from acoustic wave velocities P and S-wave measurements. In most cases shale samples are seldom available for laboratory measurement. Therefore mechanical properties are usually derived from geophysical well logs. Several measurements indicate that the dynamic modulus is higher than the static modulus, roughly up to twice or three times the static modulus (Ramana and Venkatanarayana, 1973, Cheng and Johnston, 1981, Jizba, 1991 and Fjaer, 1999).

2.8.1 Shale strength

Strength is one of the most important parameters in understanding the stress behaviour of the shales. The unconfined compressive strength UCS and angle internal friction of shale are key parameters needed to address a range of geomechanical problems associated with wellbore instabilities during drilling. Furthermore, an extensive geomechanical and rock physics testing on North Sea shale cores aims to derive an empirical correlation to elastic and strength properties. It was noted that such correlations can be strongly affected by the geological history, pore pressure, and shale composition (Dewhurst, Siggins, Kuila, and Clennell, 2008). Horsrud et al., (1998, 2001), have conducted a triaxial test to determine the mechanical properties of North Sea shale. Shale are from four different geological periods: Tertiary, Cretaceous, Triassic, and Jurassic. The depth of the shale samples range from 1370m to 4870m. The results of these triaxial tests are converted into a Mohr-Coulomb failure criterion. The uniaxial compressive strength for the shales varied between 6 and 77.5MPa and the average value is around 14.3MPa. The failure angle varied between 48 and 60. These values are low compared to sand, which is normally in the range of 60 to 70. Muniz and da Fontoura (2005) have performed a similar test on shale from an offshore location in the Norwegian North Sea. These shales are extracted at an average depth of about 2300m. The

uniaxial compressive strength and failure angle derived from this experiment agree with the measurements published by Horsrud et al., (1998, 2001).

In a recent study, Dewhurst et al., (2008) performed consolidated untrained (CU) multi-stage triaxial tests on shale core from North Sea. Choosing the muti-stage triaxial test instead of the single stage test was because of the limited quantity of core plugs and also to avoid the effect of heterogeneity between core plugs. The experiments aim was to determine a failure envelope. The equipment used for shale testing comprises a high stiffness load frame, a triaxial cell and systems for cell and pore pressure. Because of the low permeability of shale, long-term stability of control systems is very carefully handled. The resulting failure envelope is shown in Figure 2.13.

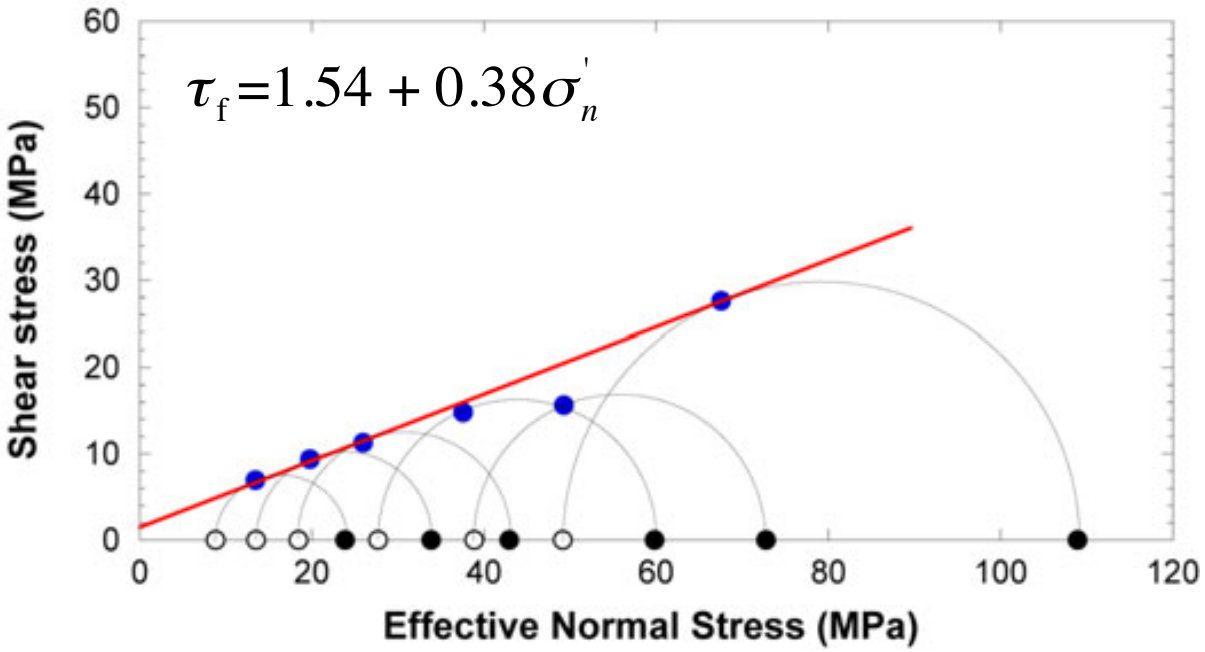

Figure 2.13: Failure envelope measurement using a multi-stage triaxial test on shale core from North Sea

For the plot shown above, two important parameters can be derived; uniaxial compressive strength and failure angle. Such parameters are very critical to understand the geomechanical behavior of the shale. UCS is about 4.2MPa and the failure angle is about 55. Dewhurst et al. (2008) highlighted the fact that due to the wide range of the composition, geological histories and age, shales are expected to have wide range of geomechanical properties.

In a global shale database ranging in time from the Neoproterozoic to Tertiary and space from the North Sea to onshore Australia, predicting shale static mechanical properties from dynamic properties did not yield good correlations (Dewhurst et al., 2010). For the global population, dynamic properties were poor empirical predictors of shale strength. However dynamic properties were better predictors of strength and elastic propeties in a local shale population where the rocks have shared similar compactional and diagenetic histories.

2.8.2 Shale: Young's modulus and Poisson's ratio

Young's Modulus and Poisson's ratio provide measurements of the shale's ductility or brittleness. Rickman et al. (2008) suggested that formations with high Young's modulus and low Poisson's ratio are more brittle, whereas those with low Young's modulus and high Poisson's ratio are more ductile. Chang et al. (2006) presented a static measurment of shale mechanical properties compiled from the litherature (Carmichael, 1982, Lama and Vutukuri, 1978, Jizba, 1991).

Jizba, (1991) presented mechanical propeties of shales with wide range of porosity from different depths in a borehole in Texas, USA. Lama and Vutukuri (1978) and Carmichael (1982) tabbulated extensive lists of various mechanical propeties of shale from different locations around the world (Figure 2.14). The plot shows that the Young's modulus ranges from 0.1GPa to 80GPa. The majority of these shales underwent a higher degree of diagenesis. Lama and Vutukuri (1978), showing that shale with higher Young's modulus generally tends to possess a higher angle of internal friction. A similar correlation has been found by (Lashkaripour and Dusseault, 1993). Horsrud (2001), Bradford et al. (1998), and Muniz and da Fontoura (2005) have published a static measurement of the Young's modulus for North Sea shales. These shale are extracted from an average depth of 2300m. The Young's modulus values range between 0.9 and 12.2GPa. Analysis of the published data indicated an average value of 2.01GPa.

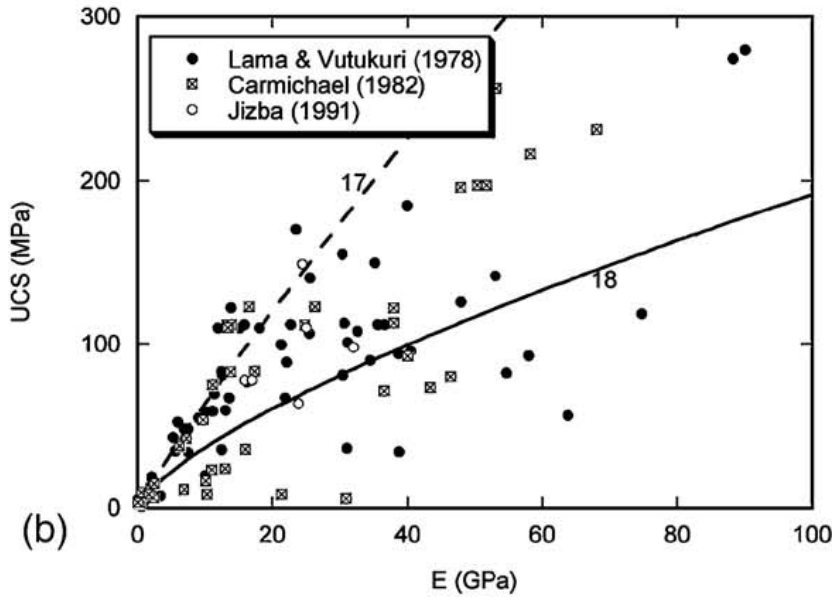

Figure 2.14:Young's modulus measurements for shales from different locations around the world. The data is compiled from the literature (Carmichael, 1982, Lama and Vutukuri, 1978, Jizba, 1991).

Also Dewhurst et al. (2010) has published another measurement of Young's modulus for North Sea Shales, the value ranges between 2GPa and 12.2GPa. The measure of static Young's modulus varies depending on loading/unloading path and the level for confining pressure (Plona and Cook, 1995) and (Dewhurst et al., 2010). These effects could explain the variety of values reported in the litherature. Although the Young's modulus has a wide range in all these experiments, the Poisson's ratio values measured ranges between 0.13 and 0.415, with an average value of 0.32, higher than the value for most sand of 0.2.

2.9 Shale rock physics and implications

Rock physics is used to establish relations between geological rock properties (porosity, mineralogy...) with seismic properties (elastic moduli, P- wave impedance). Most sediments in a basin consist of shales, and therefore the understanding of the seismic response of shale is necessary to improve the interpretation of the seismic data. Modelling shale elastic properties is difficult because of the complex composite nature of shales and the lack of data for elastic properties of individual shale (Pervukhina et al., 2008). The values of elastic parameters of shale reported in the literature vary substantially between different publications see for example, (Katahara, 1996; Vanorio et al., 2003; Bayuk et al., 2007).

The seismic response of shale is a direct result of the original mineral composition, textural configuration at deposition, and the degree of compaction. In a study conducted by Pervukhina, et al., (2008), rock physics measurements on North Sea shale are made during the various deformation stages on horizontal core plugs; thus the maximum principal stress direction is parallel to the shale fabric. The measurements of velocity are measured normal and parallel to shale bedding. V_{pv} increases from about 3300 m/s to 3800 m/s over the mean effective stress range measured of 10 to 70MPa (Figure 2.15). V_{ph} is slightly higher than V_{pv}, indicating slight P-wave anisotropy. The qV_{p45} measurements at 45° to the core axis, are of similar magnitude for V_{ph} and V_{pv}. These results suggest that there is little P-wave anisotropy.

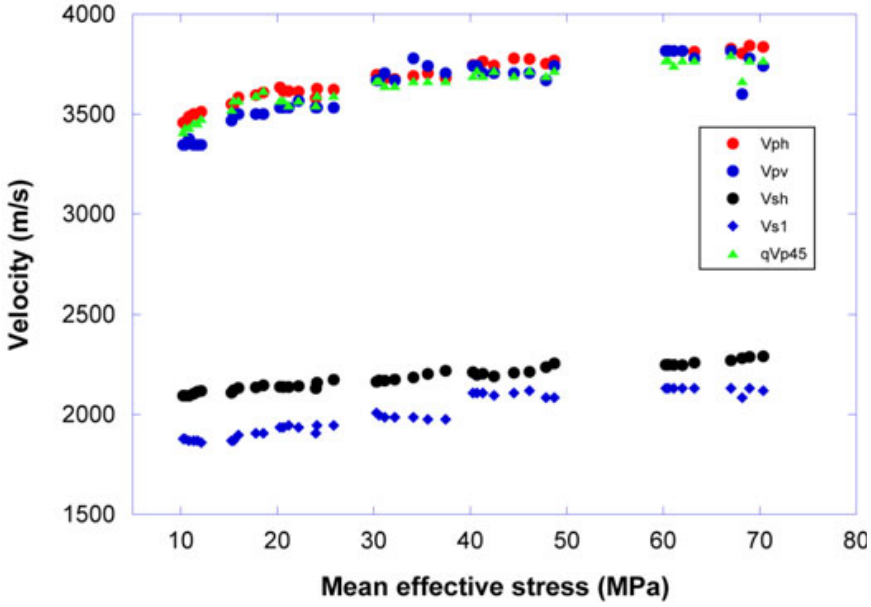

Figure 2.15: Velocity-mean effective stress plot for the North Sea shale.

2.10 Shale anisotropy

For the purpose of this study, shale is assumed to be isotropic, and, shale anisotropy is not the focus of this thesis. This assumption can be valid for some type of shales (Sayers, 2010). A study of the acoustic response of North Sea shales by Holt et al. (1996) showed that shales could in general be considered as transversely isotropic, with P-wave velocity anisotropy in the range of 0 to 25%. This does not exclude the fact that the shale could be anisotropic. There are multiple causes of anisotropy in shales: this includes clay content, organic matter, anisotropic stress, and fractures. Work by (Hornby, 1998) suggested that compaction resulted in increased clay particle alignment that could increase anisotropy. Sayers (1994, 2008) sugested that the deformation and pore structure is a controller on anisotropy. Study by Vernik and Nur (1992), Sondergeld et al., (2000) suggests that anisotropy increased with organic matter content. Prasad et al., (2009) showed that the textural anisotropy tends to decrease with increasing the maturity. Scanning Electron Microscopy studies indicates that micro-structural differences in shale are responsible for pressure dependencies of velocities and anisotropies (Sondergeld and Rai, 2011).

Shale anisotropy could lead to seismic anisotropy, in which seismic wave velocities vary with direction of propagation (Sayers, 2010). Progress in refining our understanding of shales and shale anisotropy requires more and better controlled measurements as well as access to fresh and preserved cores.

2.11 Conclusions

This chapter has provided an overview of various aspects of shale characterization and an understanding of their key properties. In the first section of this chapter, I focused on the shale geology in term of depositional environment and mechanism of deposition. In addition, shale structure was the focus of this study. An extensive literature research was conducted in order to investigate shale geometry for different depositional environments. My approach in evaluating shale geometry is to define a broad quantitative classification of shale thickness and lateral extension against depositional environment. This is based on the principles of sediment deposition guided by knowledge acquired from an understanding of the outcrop geology and sediment architecture. Also I have investigated the shale mineralogy, petrology and maturity. It was found that shales contain a wide range of clay minerals and non clay minerals.

Next, I investigated the key parameters that control the fluid flow transport and the geomechanical behaviour of the shales. Several examples of the laboratory measurement of fluid flow properties are presented. Quantitative studies on shale porosity suggested that shale porosity ranges from 3.6% to 13.7%. Also the presence of silt in the shales served to create a greater pore surfaces and consequently this will enhance the fluid flow in shale. In addition, a quantitative measurement of shale permeability was presented in this chapter. An extensive literature review shows that shale permeability ranges from 1nD up to 1μD. Silt-sized grains and micro-fractures play a very important role in controlling the fluid flow properties of the shale. For Young's modulus of North Sea Shales, the value ranges between 2GPa and 12.2 GPa the Poisson's ratio values measured ranges between 0.13 and 0.41.

An extensive geomechanical and rock physics testing on North Sea shale cores was also presented. It was noted that shale fluid flow and mechanical properties are strongly affected by the geological history, pore pressure, and shale composition.

The purpose of this characterization is to be able to use the fluid flow transport properties in order to investigate the pressure diffusion in the shale in Chapter 3. Then in Chapter 4 use both the mechanical and the fluid flow properties to understand the shale behaviour under the coupled effect of geomechanics and pressure diffusion, and observe the seismic implications.

CHAPTER

THREE

3 Pressure diffusion in the shale

This chapter focuses on calculating the physical effects of pore pressure diffusion both analytically and then numerically for a simplified geological structure based on a real field case. The analytic calculations estimate the time taken for a single shale layer to equilibrate and also for pressure to diffuse from a reservoir into an infinitely thick sideburden or overburden. The estimates provide analytic solutions to these processes, whilst the numerical modelling for a range of scenarios ensures physical correctness and explores a variety of homogeneous and heterogeneous models to further understand what to expect from pore pressure diffusion.*

* The work was done in collaboration with Dr. Ludovic Richard

3.1 Introduction

As previously mentioned, in this study I focus on the shales that are regarded as seals or baffles in the hydrocarbon reservoir, rather than the kerogen rich gas shales that may be regarded as a producing rock (Vernik and Milovac, 2011). In the literature, there is considerably less emphasis on the properties of such shales when compared to sandstones or other lithologies. Thus, from the perspective of fluid flow in the reservoir, shales are almost invariably treated simply as impermeable objects - this being concluded upon consideration of their fluid flow rates and recognised minimal hydrocarbon potential. As fluids usually leak through shales over geological times (unless they are fractured), in the reservoir engineering community, intact shales are recognised as effective reservoir seals or barriers, only affecting production by diverting flow by their geometric distribution (for example, Haldorsen and Lake 1984). Indeed, in numerical simulation studies shales are defined by assigning inactive cells in the model, despite this having the added non-physical drawback of ignoring pressure evolution within these shales. This viewpoint has now propagated into the newly emerging area of reservoir related geomechanics in which assessment of surface subsidence and wellbore stability is obtained by monitoring and modelling of the resultant stress changes. This information is input into the well trajectory plan and casing programme. Thus, in geomechanics, the overburden, sideburden and intra-reservoir shales are typically treated as passive components, which are placed under extension in response to compaction in the reservoir sands (Sayers and Schutjens 2007). However, shales do have a non-negligible permeability and moderate porosity (Neuzil 1994, Best and Katsube 1995, Yang and Aplin 2007). The low permeability values prevent large-scale bulk fluid exchange with the reservoir sandstones due to the large capillary entry pressure of the shale pore network. However, shales do still pressure equilibrate with the adjacent depleting rock mass by the process of pressure diffusion. This phenomenon permits the pressure changes to extend well beyond the sand/shale boundary of the reservoir and into the adjacent shale rock mass. As yet the exact timescale for this mechanism, the size of the equilibration zone and the controlling factors for this process have not been adequately defined. This is the topic of the current chapter. The work is important because if pressure drop in the shale due to the diffusion effect is sizable over production time scales, then it may alter the rock stresses sufficiently to cause critical geomechanical implications such as failure. This phenomenon is recognised in drilling and mining science, but not currently fully recognised in dynamic reservoir characterisation.

These key issues are investigated using a field example as a guide, from which the geological cross-section of Figure 3.1 has been extracted and Table 3.1 supplies some of the reservoir details. I consider a scenario in which the Fulmar sand is depleted, and I seek to understand whether the effects discussed above have an impact on the pressure environment (and hence stability) of future wells such as the drilling of well A into the Fulmar or well B on the opposite side of the fault, isolated from the Fulmar by the Cromer Knoll and Kimmeridge sideburden. Fault properties are not considered in this current study, although these will also be important in controlling the pressure diffusion process. From this model, I examine a range of scenarios for the depleting reservoir, in which the sideburden and overburden is considered to be intact and homogeneous, layered, and heterogeneous.

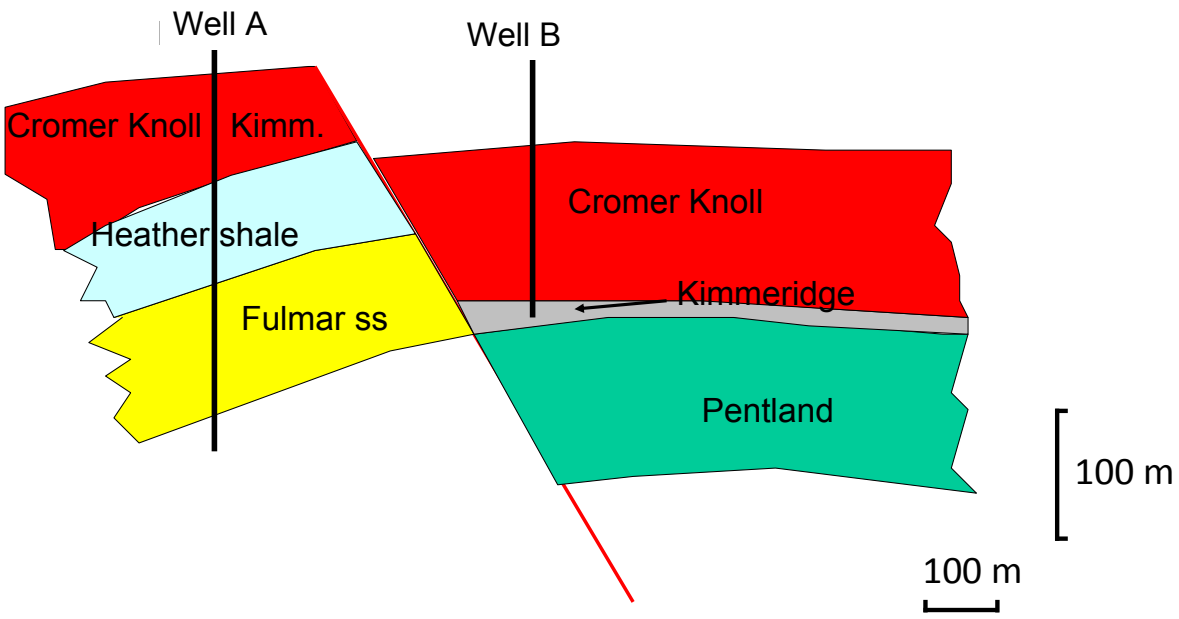

Figure 3.1: Geological section used as a guide in this study on pressure diffusion. Wells A and B are proposed wells drilled into the depleted Fulmar and the Pentland formations respectively. Reservoir details of field X are given in Table 3.1

SHALES

Kimmeridge shale

Laminated mudstone – thin streaks of silt/sand few mm thick
Source rock
Porosity 7 to 14%
Best estimate permeability 1 – 10nD
High estimate permeability 10 – 100 nD

Cromer Knoll (calcareous mudstone, marly)

Porosity 1 to 6%

Fluids

Brine density 1.04 g/cm^3
Viscosity 0.2cP
Brine compressibility 3.0×10^{-6}psi^{-1}

SANDS

Fulmar formation

Porosity 30%
Permeability 1 – 10D
10% organics, 90% water

Pentland

Porosity 17 to 27%
Permeability estimate 1 to 200mD

Fluids

Gas condensate
Viscosity 0.2cP
Condensate gas ratio 0.175 stb/Mscf
Relative permeabilities gas-water rel perm
gas-oil rel perms, no capillary pressure considered
Wet gas above dew point during production
Assume dry gas/water system

Table 3.1: Physical properties and reservoir conditions for the field of interest used as a basis for the analytic calculation and numerical simulation parts of this study.

3.2 Shale fluid flow properties and pressure diffusion

Shale properties have been discussed in more details in Chapter 2. Here I summarize the key properties that might alter the pressure development in the shale. Most shales have low to moderate porosities (2 to 20%) but are known to possess extremely small but widely unpredictable permeabilities. It is well known at the basin evolution scale that shale seal permeability is an important parameter in controlling over-pressure (or under-pressure) build up in sedimentary systems, and the consequent maintenance of present day anomalous pressures (Best and Katsube 1995). Indeed, typical shale permeabilities reported in the literature are in the range 1μD to 1nD, this being many orders of magnitude below that for coarser grained clastics (MacBeth et al. 2011). Such values of shale permeability are thought to arise from the small grain size and hence pore throat size (5nm to 60nm), tortuous pore structure, unimodal pore size distribution and particular mineralogical packing, sorting and rock fabric (see, for example, Neuzil 1994). Figure 2.12 (Chapter 2) gives a general qualitative comparison of the permeability for sands, silts, claystone and their intermediate rocks drawn from a range of available relevant literature. Several orders of magnitude in the range of permeabilities possible for a single porosity value in apparently similar shale samples, as even the exact controlling mechanisms for shale permeability are not yet fully understood (Yang and Aplin, 2007). Such diversity may arise due to permeability anisotropy linked to particle alignment and material heterogeneity, fractures, internal structure and laminations of the sand, silt or clay components and shale maturity. As previously mentioned (see Chapter 2) the shale properties also depend on age, and hence the degree of diagenetic imprint can alter the clay mineralogy.

For the purposes of the current study it is important to point out that although the shale permeability is very low (and hence it possesses high capillary entry pressures which inhibit fluid mobility), it is nevertheless finite and therefore can still cause pore pressure diffusion - a process, which may still be faster than the physical movement of the fluid. Although the low shale permeability inhibits large-scale fluid exchange from shale to reservoir or vice versa on a production time-scale, pore pressure can still diffuse and equilibrate between the reservoir and the shale within this particular time-scale. This effect can, in turn, lead to pore pressure reduction outside the reservoir zone, with implications for production and drilling, as will be shown.

Importantly, shales are rarely homogeneous for a range of depths, and a common situation is where shales are interbedded with fine sand or silt deposits or carbonate streaks – for which a wide range of structures are found (see, for example, Figure 3.2). Laminated shales possess silt present in thick, laterally continuous laminae. These can act as fluid conduits, and can for example enhance gas production or promote illitization (Howard 1991). Massive shales have silt size particles dispersed throughout the lithology. Shales can often be interpreted by the characteristics associated with their interbedded sediments. In flow terms at the larger outcrop to reservoir scale, high permeability interbeds will assist in the pore pressure diffusion mechanism. These interbeds act as high permeability pathways for fluid flow, thus more effectively depleting the bulk rock volume in a similar way to how an open hydraulic fracture would stimulate production. For this reason in my current study I consider a sandstone reservoir, and shale overburden and sideburden units that contain some silts that have a relatively high permeability when compared to the shales. Also, as shales are clearly anisotropic in their flow (and other physical properties) due to the horizontal arrangement of elongate particles at the small-scale or alteration of beds with different composition at the outcrop scale, so anisotropy must also be considered.

To address the above issues, this work calculates the physical effects of pore pressure diffusion both analytically and then numerically for a simplified geological structure based on a real field case. The petrophysical properties of the shale are unknown in the sense that no dedicated laboratory experiments have been done to measure the brine flow or its anisotropy. As this is a feasibility study, I took wireline log data and in-house databases to define ranges of rock properties that capture the shale under investigation. The analytic calculations estimate the time taken for a single shale layer to equilibrate and also for pressure to diffuse from a reservoir into an infinitely thick sideburden or overburden. The estimates provide analytic solutions to these processes, whilst the numerical modelling for a range of scenarios ensures physical correctness and explores a variety of homogeneous and heterogeneous models to further understand what to expect from pore pressure diffusion.

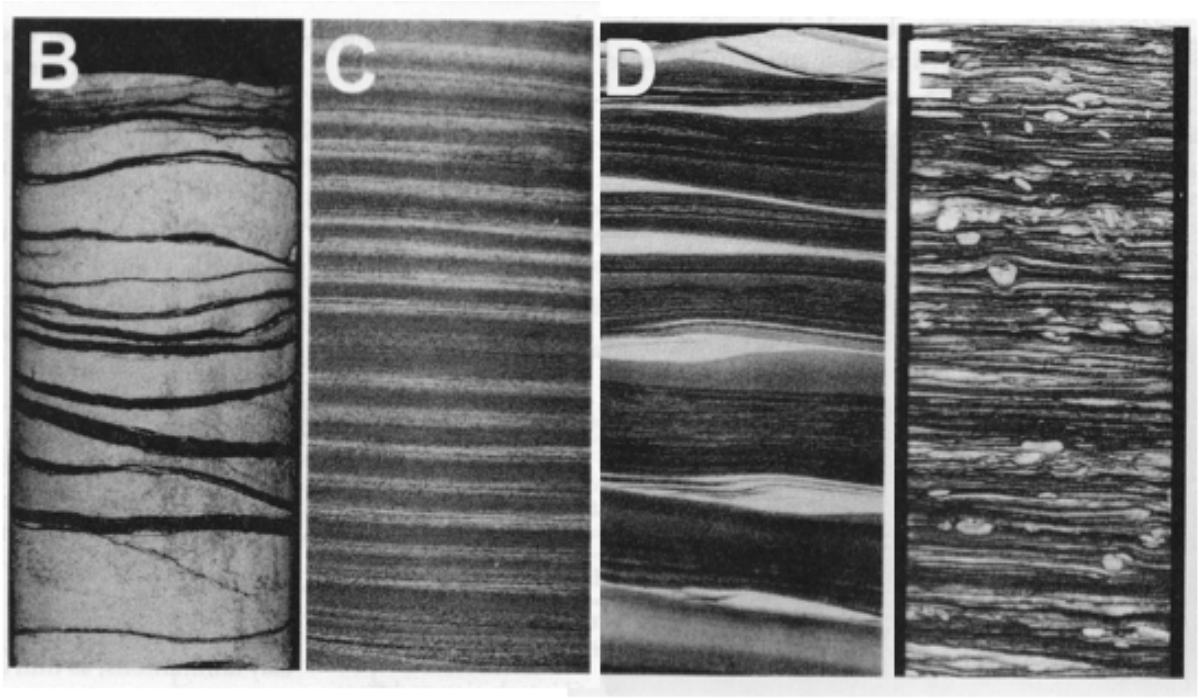

Figure 3.2: X-ray radiographic images of slabbed cores for four shale facies architectures given by Potter et al. (2005), and used as part of my modelling study. B - thin, irregularly inclined mudstone drapes; C - thinly laminated, silt streaked mudstone with some bioturbation; D - even, thinly and rhythmically interstratified and graded mudstone and siltstone; and E - mudstone with isolated cross laminated ripples.

3.3 Analytic modelling of pore pressure diffusion

In this section I am interested to obtain an understanding of the effects of pore pressure diffusion in shales driven by production-induced pore pressure changes in the reservoir. In order to evaluate its likely overall significance, I consider reservoir depletion as inducing the pressure gradient necessary to initiate this phenomenon. Two scenarios are envisaged: in the first, the reservoir sands deplete either a homogeneous (massive) shale in the overburden or sideburden. I will refer to this as the semi-infinite model. In the second, a laminated shale sideburden is considered which provides fast permeability pathways through silt layers and also drives the pressure equilibration vertically across thinner layers of shale which speeds up the rate. The model of vertical diffusion will be referred to as the single layer model. This second scenario might also represent vertical fractures in the overburden, intra-reservoir shale or interbedded shale. In order to obtain ball park values for this process, I will describe results based on analytic solutions to the pressure diffusion equation.

3.3.1 Pore pressure diffusion: the basics

The shale pressure equilibration process, whilst much slower than that in the sands, may still be within the time scale of most production activities. In order to make some predictions about the depth of penetration of a pore pressure drop into the shale and the time scale over which it acts, I firstly consider some analytic solutions to the pressure diffusion equation. Here, approximate solutions for the time taken in the process of shale equilibration are obtained using analytic solutions to the 1D pressure diffusion equation. Assuming application to a homogeneous porous media containing one or more slightly compressible fluid phases, the equation to be solved is (Crank 1975).

$$\frac{\partial P}{\partial t} = D\frac{\partial^2 P}{\partial x^2} \tag{3.1}$$

where P is the desired pressure, t and x the time and spatial coordinate respectively (x may be the horizontal coordinate for the sideburden or the vertical coordinate for diffusion into the overburden). The diffusivity coefficient $D = \lambda / \phi c_t$ accounts for the total (volume-weighted) compressibility of the formation and fluids c_t (sum of rock compressibility c_r and fluid

compressibility c_f), the porosity ϕ, and finally the total fluid mobility λ. This specific form of equation (3.1) considers that the diffusivity coefficient does not vary spatially. The mobility is given by kk_r / μ - where k is the permeability, k_r the relative permeability and μ the fluid viscosity, and the total mobility is the summation of these quantities for all of the fluid phases present in the rock. For the shales in this present work it is assumed that the pore space is 100% saturated with water. The diffusivity coefficient D is thus assumed to be constant with production, as there are no changes in the fluid composition of the shales and negligible changes in the porosity. For the purposes of this work I will consider solutions to Equation 3.1 for several cases of interest.

3.3.2 Instantaneous depletion, semi-infinite medium

Consider a homogeneous sand-filled reservoir terminating abruptly due to structure at a thick shale sideburden (Figure 3.3(a)). Instantaneous depletion is induced at the well due to production and a pressure change ΔP is quickly established in the high permeability sands over only a few seconds (assuming a compartmentalised sand surrounded by shales). A pressure difference is established across the sand-shale boundary, and after some time the part of the shale closest to the boundary starts to deplete due to pressure diffusion. This can be viewed as the semi-infinite medium problem and solved using the 1D pressure diffusivity equation in (3.1) applied along the horizontal x-axis. The solution for the lateral pressure profile $P_{sh}(x,t)$ in the shale is obtained by applying the boundary conditions: $P_{sh}(0,t) = P_{sai}$ for t=0, and $P_{sh}(0,t) = P_{sai} + \Delta P$ for t > 0, where x=0 is the position of the sand-shale boundary, and P_{sai} is the initial pressure in the sand. There is an initial condition in the shale $P_{sh}(x,0) = P_{sai}$ for all x, as the shale and sand are assumed to have already been equilibrated over geological time. The solution to the above can be readily obtained using Laplace transforms (Crank, 1975), and these yield

$$P_{sh}(x,t) - P_{sai} = \Delta P\left[1 - erf\left(\frac{x}{2\sqrt{Dt}}\right)\right] \tag{3.2}$$

where *erf* is the standard error function, which is tabulated (for example, Beyer 1987). The evolution of the solution in time is shown in Figure 3.3(a). Over time, the pressure depletion

ΔP in the sand is transferred to the shale, however the degree of depletion decreases into the shales away from the sand-shale boundary. The lateral distance (diffusion depth) $x=X$ (in metres) into the shale at which the pressure depletion falls by 10% of the pressure change in the sand is given by

$$X = 2.52\sqrt{\frac{kT}{\phi c_t \mu}} \tag{3.3}$$

where t=T is the elapsed time in days, ϕ is the fractional porosity and the diffusivity coefficient D, is replaced by individual rock and fluid properties. X is in metres, when the permeability k is in mD, the viscosity μ in cP, and the total compressibility c_t in MPa. This relation therefore provides a 'penetration distance' which serves as a rough guide of the extent of the depletion effect in the shale. This formula is similar to the cylindrical coordinate solution used by the well test community to determine the radius of investigation of a well (Dake, 2001).

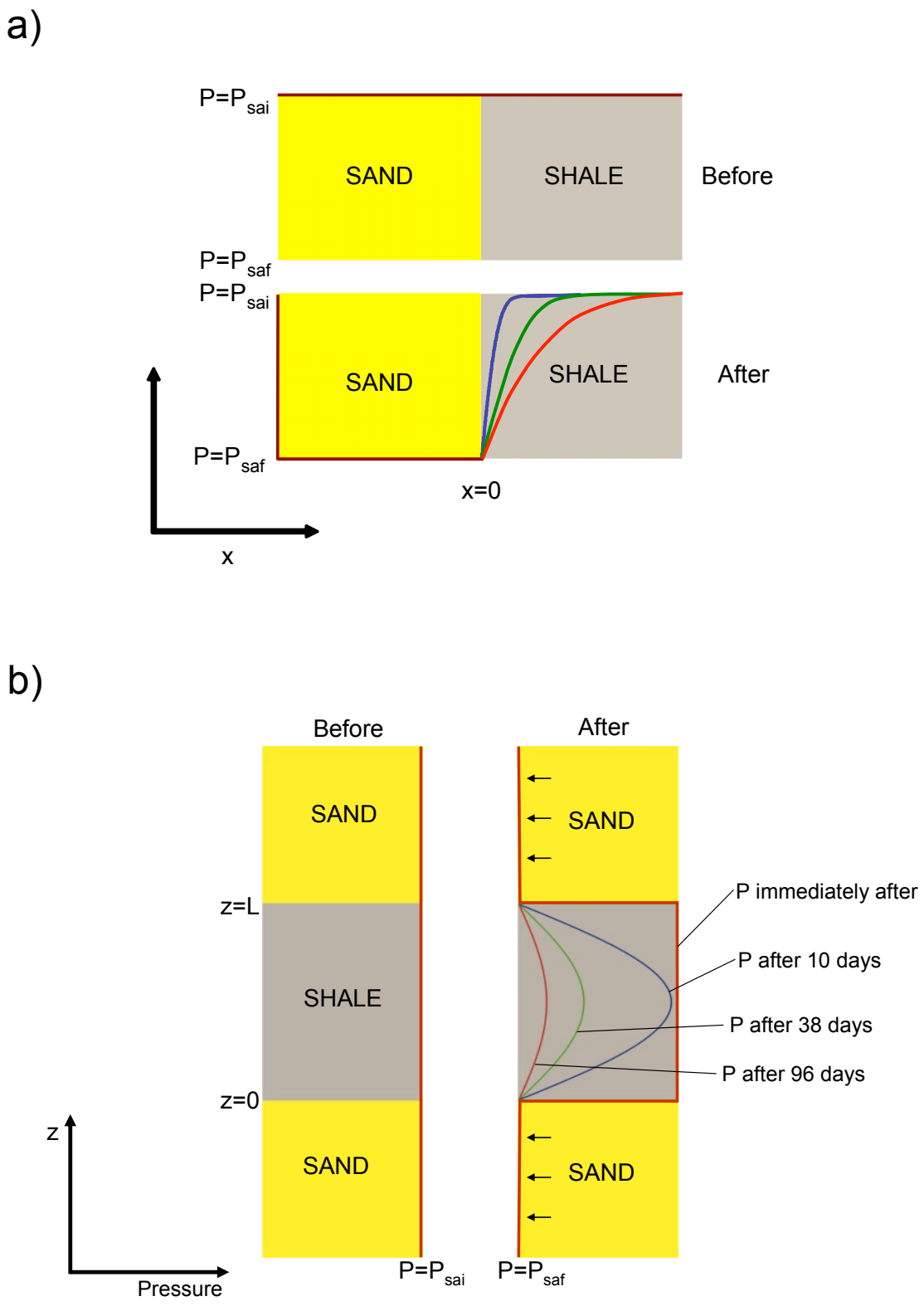

Figure 3.3: Solutions to the problem of pressure diffusion subjected to instantaneous depletion in the sands for the two scenarios of relevance to my current work. (a) The semi-infinite model created at the sand-shale boundary; (b) the single shale layer embedded in the sand.

3.3.3 Linear depletion, semi-infinite model

In the above solution it is assumed that the well activity and its surrounding boundary conditions are such that the reservoir pressure can be depleted over a very short time interval. In the more realistic case of wellbore constraints and production from a finite sized sealed compartment, the decrease in reservoir pore fluid pressure will take years to tens of years, and will vary across the reservoir controlled by the well distribution, reservoir properties and structure. In the model, I use the simplified case of a constant homogeneous depletion rate, so the pore pressure in the reservoir will decrease linearly as a function of time (Dake 2001; Huang et al. 2011). Consider a linear pressure depletion over the time period t=0 to T_P, with the pressure change in the reservoir sands now given by $P_{sa}(t) - P_{sai} = \left(\frac{\Delta P}{T_P}\right)t$, and a constant for $t \geq T_P$. The solution to the semi-infinite problem for $t < T_P$ is (Crank, 1975)

$$P_{sh}(x,t) - P_{sai} = t\left(\frac{\Delta P}{T_p}\right)\left[\left(1+\frac{x^2}{2Dt}\right)\left(1-erf\left(\frac{x}{2\sqrt{Dt}}\right)\right)-\frac{x}{2\sqrt{\pi Dt}}\exp\left(-\frac{x^2}{4Dt}\right)\right] \qquad (3.4)$$

where P_{sai} is the initial pore pressure in the sand, and P_{sh} the pore pressure in the shale. Here, the pressure drop in the shales is defined relative to the final overall pressure drop ΔP in the sands. Clearly, the rate of pressure drop in the shales cannot exceed the rate at which the sands are depleting. Thus, when the diffusion coefficient is large, the pressure in the shales close to the sand-shale boundary will deplete at the same rate as the sands. When the diffusion rate is slow, then the pressure drop in the shales is not unduly influenced by this linear decrease in the sands. Table 3.2 gives the results for the same reservoir as before, with rock and fluid properties as in the previous example. Following the calculation in equation (3.2), when the drop is 10% of the final value in the sand

$$X = 1.2\left(1-\frac{T_p}{T}\right)\sqrt{\frac{kT}{\phi c_t \mu}} \qquad (3.5)$$

For an elapsed time $t = T$, where the units are the same as the previous section.

k (mD)	μ_w (cP)	c_r (1/psi).10^{-6}	c_w (1/psi).10^{-6}	ϕ	D m^2/day	T (days)	X (m)
1	0.38	3.0	3.0	0.1	2612	1	102.23 *5.8*
10^{-3}	0.38	3.0	3.0	0.1	2.61	1	3.23 *0.18*
10^{-6}	0.38	3.0	3.0	0.1	0.0026	1	0.10 *0.0058*
1	0.38	3.0	3.0	0.1	2612	100 (3 months)	1022 *58*
10^{-3}	0.38	3.0	3.0	0.1	2.61	100	32.32 *1.83*
10^{-6}	0.38	3.0	3.0	0.1	0.0026	100	1.022 *0.058*
1	0.38	3.0	3.0	0.1	2612	10000 (30 years)	10223 *580*
10^{-3}	0.38	3.0	3.0	0.1	2.61	10000	323.3 *18.3*
10^{-6}	0.38	3.0	3.0	0.1	0.0026	10000	10.22 *0.58*

Table 3.2: Estimates of the 'penetration distance' X of reservoir depletion effects into a neighbouring shale as a function of elapsed production time T. Estimates are based on the semi-infinite, analytic solutions (3.2) for instantaneous sand depletion (upper set of results) and a linear decrease in pressure over 10 years (lower italicised results) using equation (3.4). Depletion is deemed effective up to distances at which the pressure drop in the shale falls below 10% of that in the reservoir sand. Shale permeability k; viscosity μ_w; rock compressibility c_r; water compressibility c_w; and shale porosity ϕ. The shale is assumed to be 100% saturated with water. D is the diffusivity constant.

3.3.4 Instantaneous depletion, single shale layer

Consider now a homogeneous sand in which is embedded a single thin shale bed (Figure 3.3(b)). Assume that near-instantaneous depletion is induced in the sands due to production. After this, a vertical gradient is then established across the top and base of the shale, which in turn drives the pressure equilibration process that occurs in the shale due to its finite permeability. The pressure diffusivity equation is now applied to the vertical (z) pressure profile $P_{sh}(z,t)$ in the shale, and defined between *z=0* (base of shale) and *z=L* (top of shale), and for all t > 0. The equation is solved subject to a number of boundary conditions. Firstly, the initial pressure inside the shale is uniform and equal to that of the sand: $P_{sh}(z,0) = P_{sai}$ for $0 \le z \le L$. Secondly, compared to the timescale of equilibration in the shale, the pressure in the sand is assumed to instantaneously deplete from P_{sai} to $P_{sai} + \Delta P$ in response to production, this giving a periodic condition at the top and base of the sand: $P_{sh}(0,t) = P_{sai} + \Delta P$ and $P_{sh}(L,t) = P_{sai} + \Delta P$ for all t > 0 and repeated every *L*. Solution using the method of separation of variables leads to a formulation for the pressure in the shale as a series of damped sinusoids (Crank, 1975)

$$P_{sh}(z,t) - P_{sai} = \Delta P\left[1 - \sum_{n=0}^{\infty} b_n \exp\left(-\frac{(2n+1)^2\pi^2 \alpha t}{L^2}\right)\sin\left(\frac{(2n+1)\pi z}{L}\right)\right] \quad (3.6)$$

where $b_n = 4/(2n+1)\pi$. The shale pressure decays exponentially as a function of time and the rate of decay is controlled by the value of the diffusivity coefficient and also the square of shale thickness. At later times the fundamental mode (n=0 term) dominates and the behaviour of this mode may be used to estimate the depletion time (HajNasser and MacBeth 2010, MacBeth et al. 2011). The time at which the amplitude of this mode decays to 10% of the sand depletion is given by

$$T = 2.31\frac{\mu\phi c_t L^2}{\pi^2 k} \quad (3.7)$$

where L is in metres and the other quantities have the same units as in equation (3.3). The time to equilibrate is thus, as expected, quick for thin, high permeable shales or a high permeability (low D). The estimates of T from this formula are given in Table 3.3.

k (mD)	μ_w (cP)	c_r (1/psi).10^{-6}	c_w (1/psi).10^{-6}	ϕ	D m^2/day	L (m)	ΔT (days)
1	0.38	3.0	3.0	0.1	2612	0.1	$8.92.10^{-7}$ *0.000001*
10^{-3}	0.38	3.0	3.0	0.1	2.61	0.1	$8.92.10^{-4}$ *0.001*
10^{-6}	0.38	3.0	3.0	0.1	0.0026	0.1	$8.92.10^{-1}$ *0.96*
1	0.38	3.0	3.0	0.1	2612	1.00	$8.92.10^{-5}$ *0.000001*
10^{-3}	0.38	3.0	3.0	0.1	2.61	1.00	$8.92.10^{-2}$ *0.001*
10^{-6}	0.38	3.0	3.0	0.1	0.0026	1.00	$8.92.10^{+1}$ *0.96*
1	0.38	3.0	3.0	0.1	2612	10.00	$8.92.10^{-3}$ *0.000001*
10^{-3}	0.38	3.0	3.0	0.1	2.61	10.00	8.92 *0.001*
10^{-6}	0.38	3.0	3.0	0.1	0.0026	10.00	$8.92.10^{+3}$ *0.96*

Table 3.3: The effect of pressure diffusion on a shale of thickness L sandwiched between two depleting sandstones. Diffusion times ΔT are estimated using the harmonic analytic solution of (3.4), with the lower italicised results being for a linear decrease in pressure over 10 years in the sands using equation (3.5). Pressure depletion in the shale is considered complete at a time ΔT when its pressure is within 10% of the depletion pressure in the sand. The fluid and rock properties for these calculations are identical to that of Table 3.2. Shale thicknesses are typical of most depositional environments (MacBeth et al. 2010).

3.3.5 Linear depletion, single shale layer

Following the section above, I must also take into account the possibly more realistic case of linear depletion in the sands over a time period t=0 to T_P. Considering the same depletion as in the previous section on the semi-infinite solution, with the pressure change in the reservoir sands given by $P_{sa}(t) - P_{sai} = \left(\frac{\Delta P}{T_P}\right)t$, the solution for the pressure in the shale is now

$$P_{sh}(z,t) - P_{sai} = \frac{\Delta P}{T_P}\left[t + \sum_{n=0}^{\infty} c_n \left(\exp(-\frac{(2n+1)^2\pi^2 z^2 Dt}{L^2}) - 1\right)\sin(\frac{(2n+1)\pi z}{L})\right] \quad (3.8)$$

$c_n = 4L^2/(2n+1)^3\pi^3 D$ and the time taken for the pressure to reach 10% of the final pressure drop in the sands is:

$$T = \frac{2.3L^2}{\pi^3 D}\left(4 + 1.27\pi\right) + 0.1T_p \quad (3.9)$$

where the units are as in (3.7). The diffusion results for this case are also shown in Table 3.3, and the pressure reduction observed in the shale appears to be similar to those results given by equation (3.6). The reason for this is attributed to the fact that the speed of the diffusion process is slower than the production rate.

3.4 Pressure diffusion predictions

Tables 3.2 and 3.3 provide estimates for the speed of the pressure equilibration process between the depleting reservoir sands and the surrounding shales for typical reservoir rock and fluid parameters assigned for the North Sea. The results are given for the wide range of absolute shale permeabilities from 1mD, 1μD to 1nD suggested from laboratory deformation tests on shale core taken at depths of 3 to 5km (Horsrud 2001). My model results show that, after 3 months of production, pressure may penetrate up to 58m into the semi-infinite shale under a favourable permeability of 1mD, whilst for 1nD shales this reduces to only 6cm. The

distance over which the pressure disturbance can be felt scales as the square root of the production time and inverse permeability. Thus, after a production of up to 25 years these figures increase to 580m and only 60cm for 1nD shales. The above results indicate that shale heterogeneity will play a critical role in determining the overall impact of pore pressure diffusion. If the shale contains silt laminations, sand layers or horizontal fractures, these will enhance the horizontal permeability and will significantly increase the penetration distance of the pressure change. (Note here that my results are valid for the problem of a sideburden, and can be considered only as an upper limit for the overburden due to its effective permeability being lower). This is due not only to the enhancement of the effective permeability via the conventional arithmetic average, but also the additional mechanism of vertical equilibration of the shale layers according to the single layer mechanism given by equation (3.6) or (3.8). The equilibration of the thin layers is dramatic and has a larger effect than the semi-infinite solution on the rate of pore pressure equilibration within the shale – for example, a 1m, 1nD layer can equilibrate in 89 days. Thus, composite shale-silt units, one with the silt distributed thinly and one with the same amount of silt but only a few thick layers, will respond quite differently. Ultimate control of this phenomenon is strongly dependent on the petrophysical properties of the shales and their internal sedimentary architecture. As it is unlikely for the large volumes of shale that surround the reservoir to be completely homogeneous, then the upper limit of 1mD on the permeability appears reasonable and thus depletion effects felt metres to tens of metres from the reservoir cannot be ruled out. The results for the linear depletion model indicate that it takes slightly longer for the pressure changes to manifest themselves at a fixed distance when compared to an instantaneous drop. However as mentioned in the section above, this depends on the rate of pressure decrease due to production. The estimates from the instantaneous drop should be seen as overestimates of the actual expected changes in the field.

3.5 Numerical modelling of pore pressure diffusion

The analytic calculations in the previous section have helped to provide a broad and approximate understanding the pressure diffusion into shale, but cannot cover the complexities of the production mechanisms (I assumed only an instantaneous or linear drop) or more realistic lithology (currently assumed homogeneous). Numerical simulation of the fluid flow processes can help in this respect, taking into account the full two phase flow (in this case gas and brine), the realistic history of produced volumes and their associated pressure drop, the full 3D evolution of the pressure field from the cylindrical borehole, in addition to the internal heterogeneity of the shale. To examine these, I use data from field X as a template in the analysis. This field is an HPHT field with 100% gas condensate. The reservoir lies at a depth of 5200m (16000ft) TVDSS, at an initial pore pressure of 15300psi and temperature of 380F^{o} (185C^{o}). A black oil flow simulation model is built for this reservoir which consists of a sand reservoir containing a single producer and a shale sideburden (Figure 3.3(a)). This is a simple replica of the geometry in Figure 3.1. The cells representing the shale are all fully active during the simulation. The model is built in 2D (vertical and horizontal), covering a total size of 900ft (274m) in the horizontal dimension and 430ft (131m) vertically, with a vertical sand-shale boundary in the centre. The grid cell dimensions are 10ftx10ft (3mx3m), and extend into the third (un-simulated) dimension by 150ft (46m). The well volumes are designed to closely follow the production profile measured in field X and are set such that the pore pressure drops by 8600psi (5.9MPa) over 9 years of production. The measured pressure change is modelled by two linear segments (Figure 3.4). This shape is because the reservoir produces gas for three years and then is shut-in. There are two fluid phases in the reservoir: gas and water. Phase change behaviour from gas to a condensate is not modelled as the reservoir pressure is always kept above dew point. The reservoir is assigned a permeability of 1D and porosity of 30% in order to reproduce the observed pressure depletion at the well.

a)

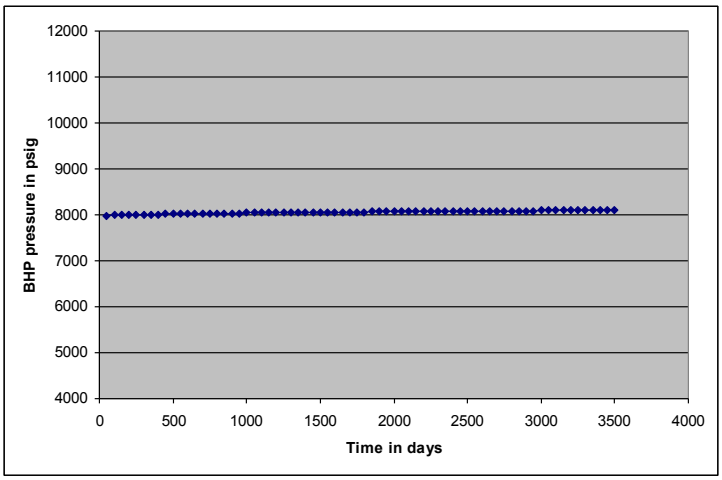

b)

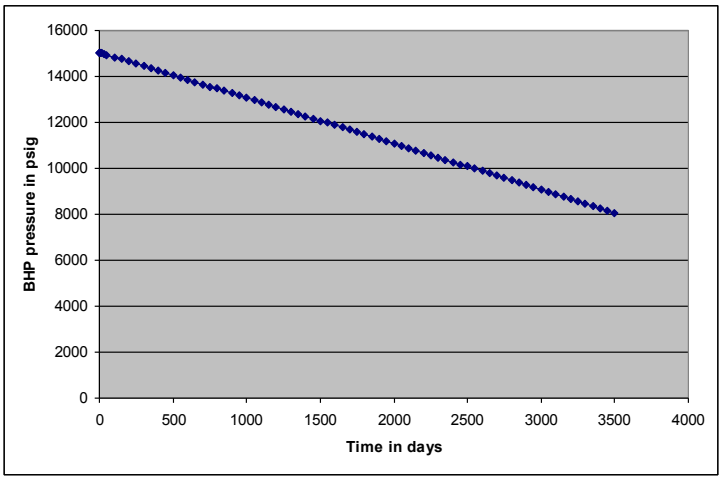

c)

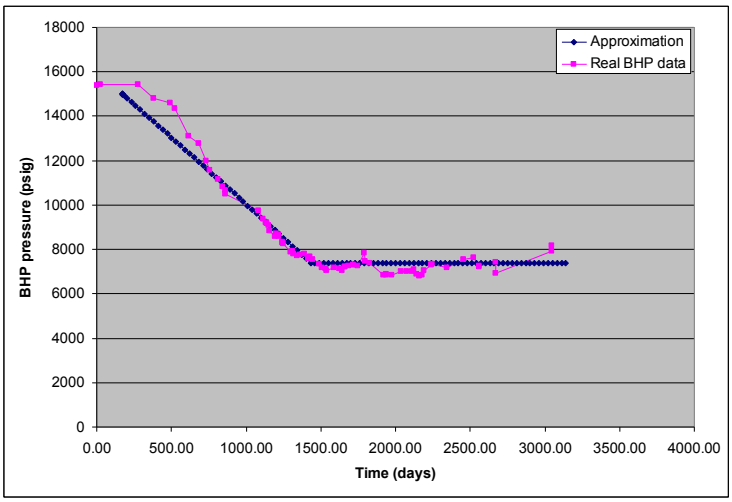

Figure 3.4: Reservoir pressure profiles induced by three different conditions for the numerical simulations (a) near step function; (b) linear decrease; (c) Observed field data approximated by two linearly decreasing segments.

3.5.1 Homogenous model

Simulations are performed firstly for two different production scenarios – near- instantaneous pressure depletion and a linear pressure depletion. This is done as a cross-check against the analytic solutions, and it is found that the resultant pressure profiles agree favourably with those predicted using equations (3.2) and (3.4). thus lending support to the use of the single phase, 1D analytic solutions as a quick-look guide for depletion analysis. Errors between the predictions are less than 5 percent. Next, different combinations of shale permeability (1nD to 100nD) and porosity (10 to 13%) are selected to examine the range of penetration depths for the pressure diffusion effect. The results of this study are shown in Figure 3.5. This exercise indicates that after 10 years of production, most pressure drops can be felt at up to 45m into the shale (occasionally up to 105m), whereas for 2 years of production this figure drops to 20m (occasionally up to 40m). One interesting side effect of the numerical simulation is the prediction that water must flow from the shales over the production time period because of the pressure gradients established – this phenomenon occurs without invoking geomechanics but does not yet fully consider capillary effects.

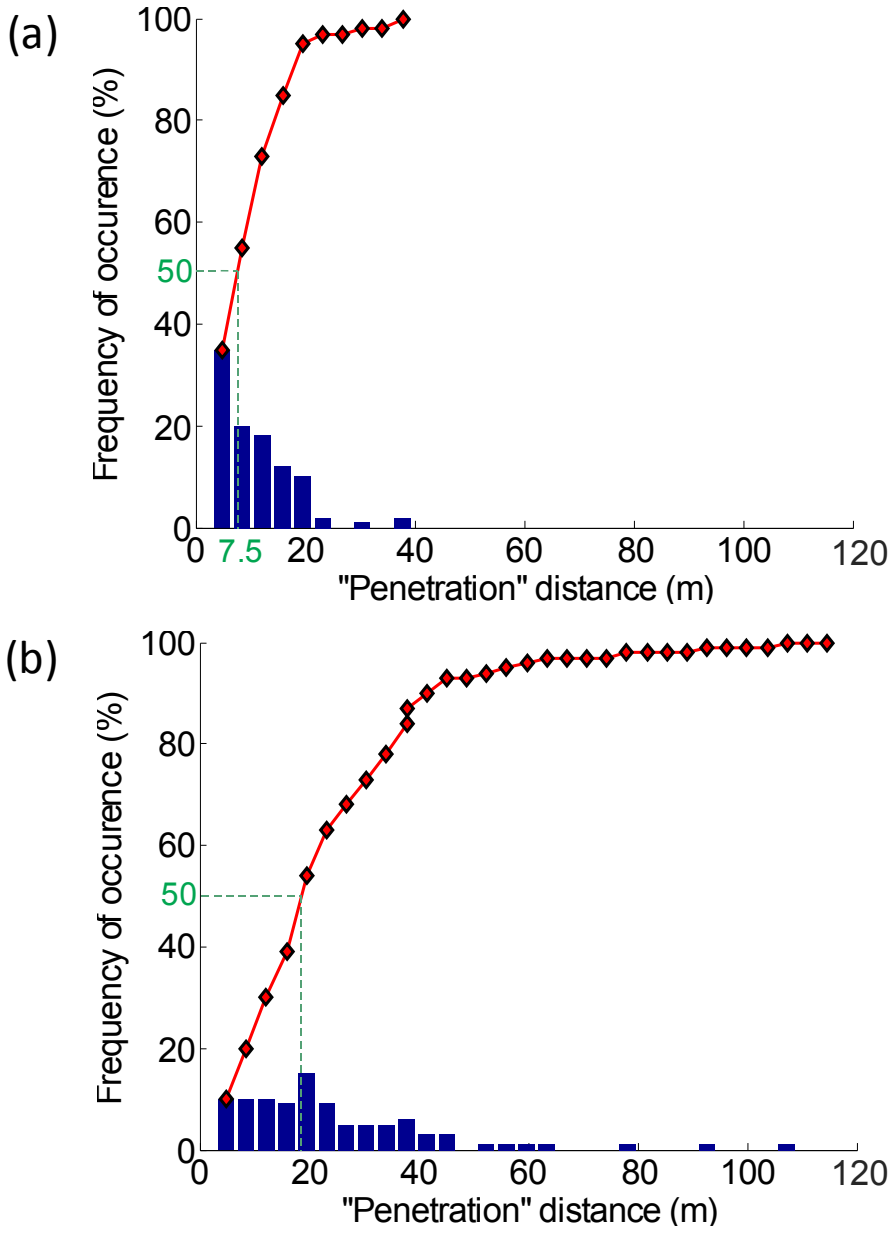

Figure 3.5: Distribution of analytically derived penetration distances for pressure diffusion into a homogeneous shale sideburden for a randomly selected range of background permeability and porosity, after (a) two years; (b) ten years. Penetration distance is defined as the point at which the pressure change reduced to 10% of that in the sand. The red curve corresponds to the cumulative frequency; the penetration depth corresponding to 50% of the cases in the population is marked for reference.

3.5.2 Heterogeneous model

Next I consider the sideburden to be composed of laminated shale and examine the effect of vertical variations in porosity and permeability caused by silt layers (streaks) of different thicknesses and distribution embedded in the shale. These act as high permeability conduits and allow the fast diffusion of pressure horizontally, but also permit equilibration of the shale vertically, albeit at a slower rate. Several model scenarios are considered in which the thickness, number and spacing of the silt layers is varied. Sand thicknesses are varied from 3 to 6m, and shale thicknesses from 4 to 7m, assigned in such a way as to make up a fixed thickness (20m) of the reservoir package (Figure 3.6). Various numbers of silt layers are also embedded in the shale. The models are created so that there are several different layer configurations defined for a common silt proportion. For the purposes of the modelling exercise, the (sandy) silt is assigned a fixed permeability and porosity of 1D and 30% respectively; the shale background is 1nD, 10nD and 100nD, and 10% porosity. The silts and shales are assigned isotropic flow properties. Next, a porosity and isotropic permeability are assigned from the mean values shown in Figure 3.6. To quantitatively examine the impact of the silt or facies distributions on the pressure diffusion mechanism, for each modelling result the mean pressure drop is evaluated across a vertical boundary positioned 50m into the shale after an elapsed time of 5 years. The pressure drop is measured by the PPD metric, defined as

$$PPD = \left| \log_{10} \left(\frac{\Delta P_{res} - \Delta P_{sh}}{\Delta P_{res}} \right) \right| \tag{3.10}$$

where ΔP_{res} is the pressure drop in the (sand) reservoir and ΔP_{sh} the drop in the shale at the reference location. This metric is zero for no pressure drop, and becomes progressively bigger as diffusion becomes more active. The results of the modelling are shown in Figure 3.7. This indicates that an increase in silt from 5% top 20% can increase the drop in pore pressure in the shales by a factor of 5. The range of permeabilities provides a further doubling of the pressure drop. Importantly, pressure drops at 50m become significant (beyond 10%) as the percentage of silt increases, suggesting a strong control from the sedimentary architecture.

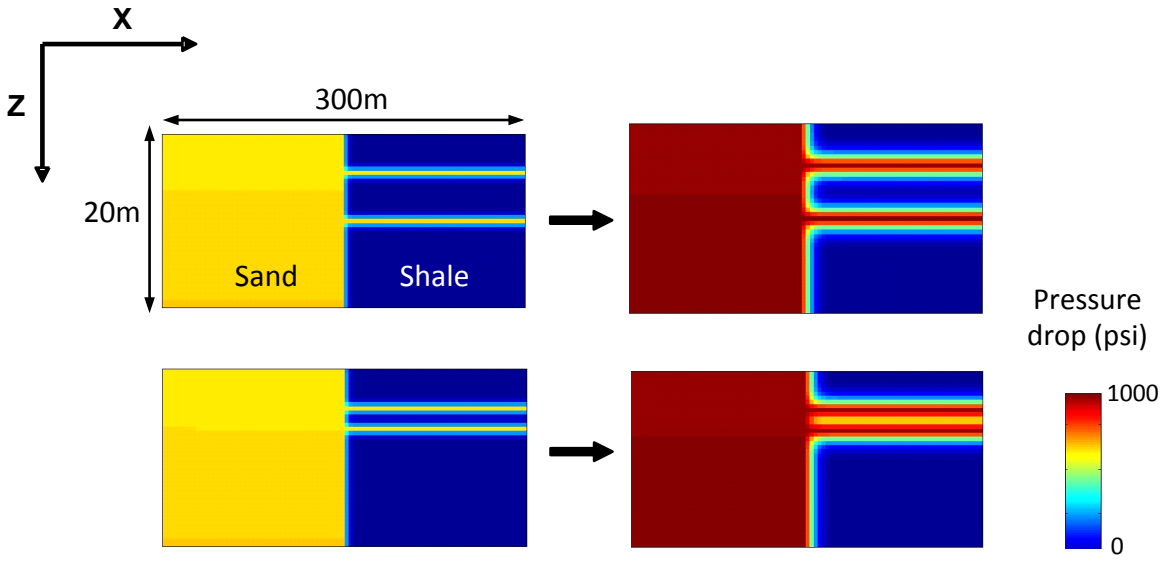

Figure 3.6: Example of the numerical simulation pressure diffusion results for my idealised models. On the left is the model permeability, and on the right are the results of the pressure drop computation. Results here are for 5 years, and show two layers with different spacings to illustrate the influence of the vertical diffusion mechanism.

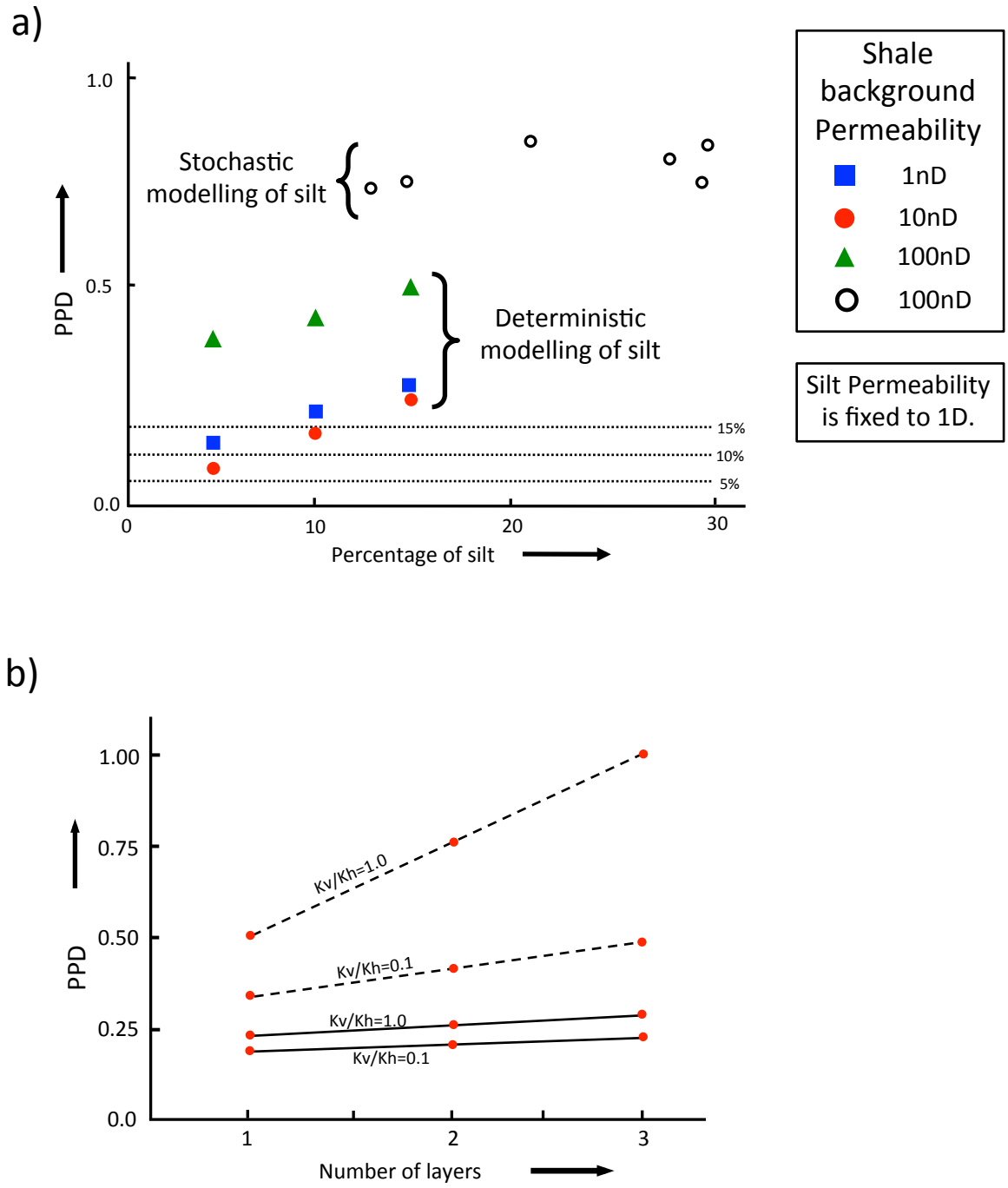

Figure 3.7: Pressure drop in a sideburden of heterogeneous shale due to pore pressure diffusion in heterogeneous shale at a fixed distance of 50m from the sand-shale interface and after a time period of 5 years. The metric for pressure drop is PPD as defined in the text with equation (3.10). (a) plotted as a function of the volumetric percentage of silt in the shale sequence. For the purposes of the modelling exercise, the silt is assigned a fixed permeability and porosity of 1D and 30% respectively; the shale background permeabilities are 1nD, 10nD and 100nD (fixed Kv/Kh=1). Shale porosity is fixed to 10%. Here stochastic and deterministic modelling are used to populate silt. Dashed line correspond to the percentage of pressure drop relative to the reservoir; (b) a fixed 15% of silt is distributed over one, two or three layers, for silts lying in a 100nD (dashed lines) and 1nD (solid line) background of shale.

To further study the impact of heterogeneity on the pore pressure diffusion process, geo-modelling is carried out using the model above, but with shale properties assigned stochastically. The wireline logs in Figure 3.8 show an example of the expected heterogeneity. Here, a vertical well penetrates a 120m thick shale sideburden in the field of interest. Density, neutron, sonic and gamma logs classify the section into several distinct facies: shaley sand, sandy shale, shale and sand layers and suggests that these variations should be taken into account. To capture this facies variability, heterogeneity in the shale, is generated by upscaling the information from the shale core photographs of Figure 3.2, which shows four different shale facies with different degrees of (measurable) silt, sand and shale volume, lateral connectivity and sedimentary expression. For the purposes of this work, a sand porosity of 30% and 1D permeability, silt porosity of 15% and permeability of 5μD, and finally a fixed background shale porosity of 10% and permeability of 10nD are assigned. From these rock properties it is possible to calculate the upscaled porosity, horizontal and vertical permeability using knowledge of the approximate volumetric proportions of the component rocks, and sediments distributed assuming only horizontal laminations are present within each reservoir cell. The results of this calculation are given in Table 3.4 for the six facies, the four defined in Figure 3.2 together with the two end-members of pure sand and shale. In the computation of the mixed facies, the effect of bioturbation is taken into account by assuming the burrow fills are composed of silt (Tonkin et al. 2010). A model is then built which distributes the individual facies elements unconditionally stochastically according to a uniform and then triangular spatial distribution. The facies are inserted into a shale background using object-based modelling as implemented by Petrel (TM Schlumberger). The thickness ranging from 1 to 2.5m, with a mean of 1.5m. The horizontal dimensions range from only 100m to cover the entire model as a single horizontal layer. For each realisation, facies 1,2,4 and 5 are generated in equal proportion, such that the total percentage ranges from 5 to 30% of the total shale volume. A typical set of realisations are shown in Figure 3.9. In the flow modelling all cells were active, and the pressure diffusion in the shales was considered as part of the reservoir (HajNasser and MacBeth 2011).

Figure 3.7(a) shows the result for different percentages of silt. These show that once again the silt proportion increases the pressure drop, and although the drops are generally larger the response to the silt percentage is reduced. The results indicate the expected trend of increasing pressure drop with the proportion of silt, as horizontal diffusion along these layers according to Equation 3.2 is the primary mechanism for diffusion. In the deterministic modelling, the

effect of the internal depositional character on the pressure drop is also considered by separating the volumetric fraction of silt into a number of thinner layers with the same volumetric proportion. As the time constant for the diffusion mechanism is inversely proportional to the square of the thickness, the thinner silts tend to equilibrate much more quickly than the thicker ones, but have less impact on the overall average. Thus, in addition to this mechanism there is also a separate cross-flow mechanism acting vertically across the layers which tends to speed up the diffusion. The higher drops suggest that the interconnectivities between the distribution of silt layers is an important factor in enhancing the overall pressure drop. Again, this emphasises the strong control of the sedimentary architecture. Finally, it is known that cross-flow is affected by the known anisotropic permeability of the shale background. This downweights the vertical diffusion mechanism giving it less weighting. These effects are observed in Figure 3.9(b), which plots PPD for a 100nD and 1nD background shale, with 15% silt volume. As the layering increases, so too does the pressure drop, although the impact is stronger for the higher permeability shales. Kv/Kh is also observed to make a significant difference to this flow.

Facies	Sedimentary structure	Sand:silt:shale (%)	Porosity (%)	Horizontal Permeability Kh (mD)	Kv/Kh
0	Sand	100:0:0	30	1000	1
1	B/Figure 3.7	0:70:30	13.5	3.5×10^{-3}	0.009
2	C/Figure 3.7	0:50:50	12.5	2.5×10^{-3}	0.048*
3	Shale	0:0:100	10	10^{-5}	1
4	D/Figure 3.7	0:42:58	12	2.1×10^{-3}	0.008
5	E/Figure 3.7	0:30:70	11.5	1.5×10^{-3}	0.009

Table 3.4: Definition of the six shale facies considered in this study, and their corresponding porosity, vertical permeability (Kv) and horizontal permeability (Kh) values. *The presence of bioturbation is assumed to increase Kv/Kh (Tonkin et al. 2010).

(a)

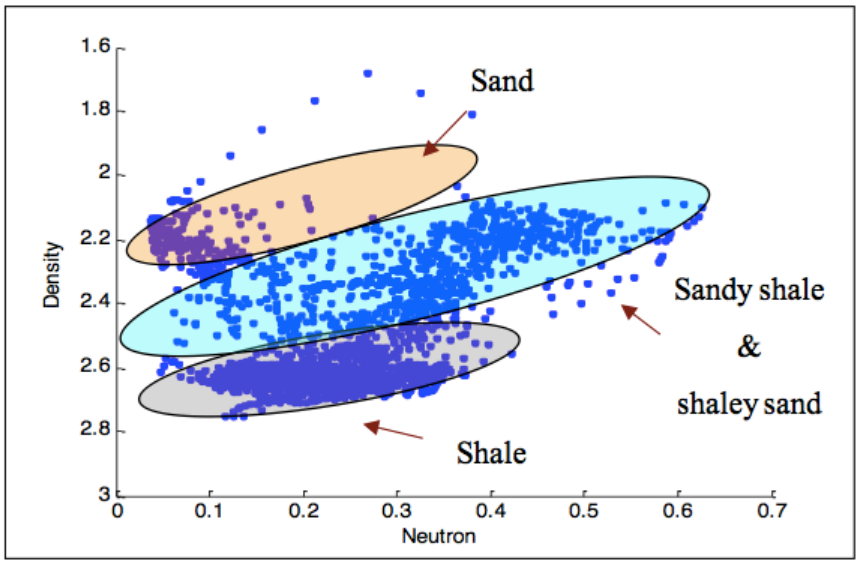

(b)

Thickness (ft)	Facies
126	Shaley sand
5	Sandy shale
28	Shaley sand
63	Sandy shale
7	Shaley sand
80	Sandy shale
4	Shaley sand
26	Sandy shale
22	Shaley sand
Facies 5	Sand
9	Shaley sand
59	Shale

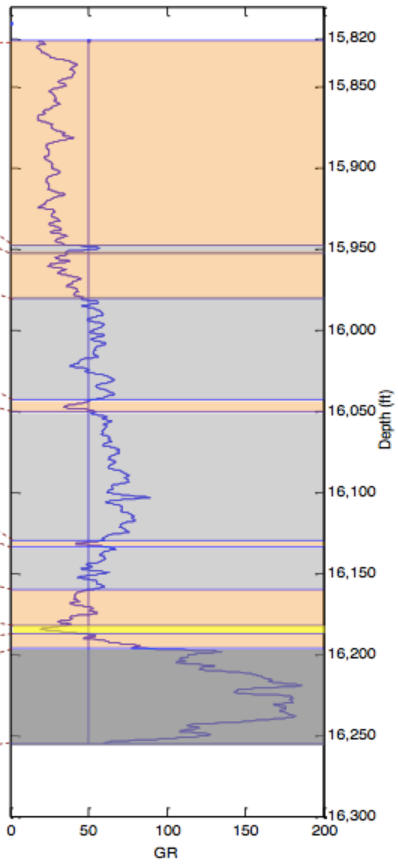

Figure 3.8: (a) One of the cross-plots used to separate sand and shale-related facies from the wireline logs; (b) Resultant facies distribution which is then used for the numerical simulation.

a)

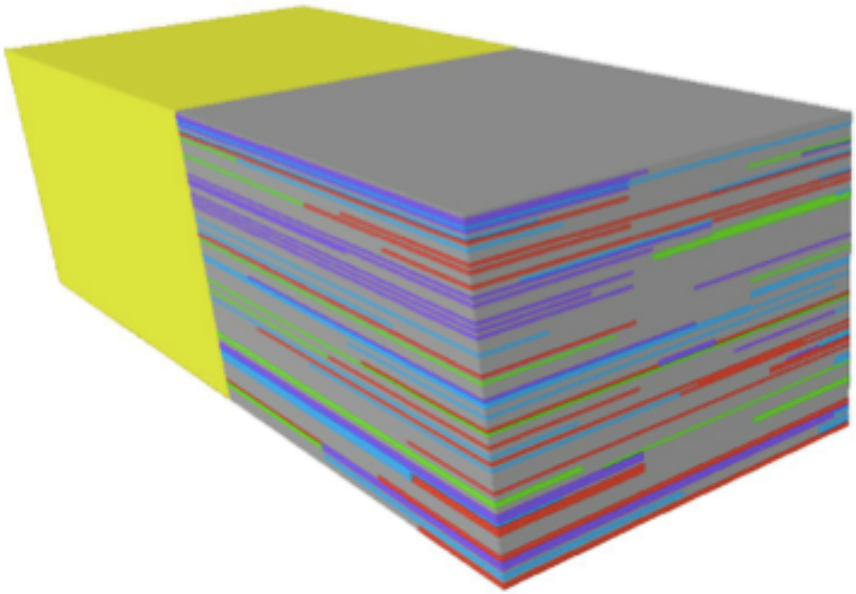

b)

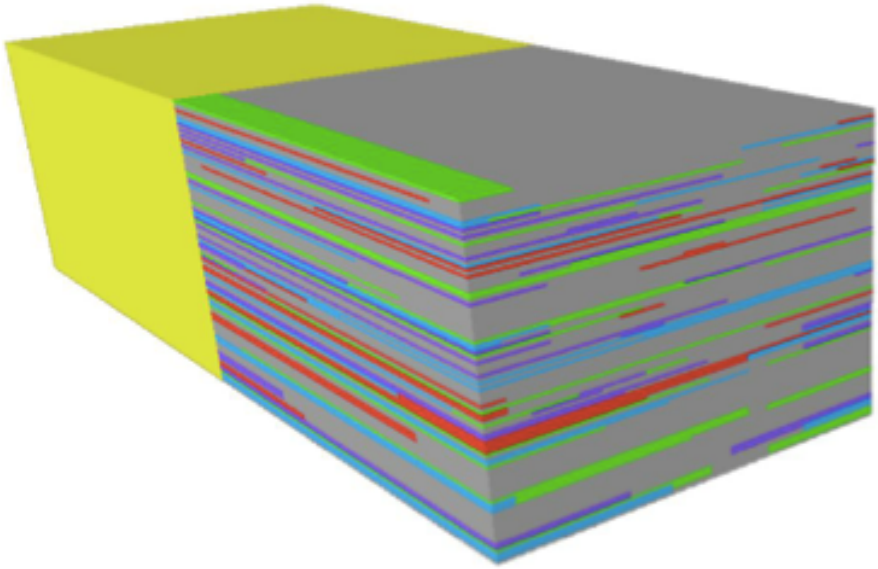

Figure 3.9: (a) and (b) are two stochastic realisations of the facies distribution models used in this study.

3.6 Discussion and conclusions

The results above indicate that pressure diffusion into a shale overburden or sideburden surrounding a depleting hydrocarbon reservoir can prove to be significant over production time scales from several years to several tens of years. Thus, the surrounding shales initially experience a mechanical extension due to the stress created by the compacting sandstones. However as time progresses pressure diffusion reverses this effect near to and around the reservoir, and these shales then experience a compaction (HajNasser and MacBeth 2011, MacBeth et al. 2011). My current analytic and numerical studies suggest that for shale formations with permeabilities in the range 1μD to 1nD, pressure depletes by 10% of that in the reservoir within 10 to 100m of a sand/shale interface, within a period of 5 years. However the impact of the internal sedimentological character of the shale should not be underestimated, and this can give rise to heterogeneities such as silt layers that can considerably enhance the predicted effects which must therefore be considered an underestimate. The results of this study suggest the sideburden may be particularly affected by this effect, and the overburden to a slightly lesser degree.

Historically shale instability and failure is a major concern for the driller. Rock failure, which has been studied extensively within the geosciences and drilling community (Plumb et al. 2000, Schoenberg 2002, Sinha 2005, Pistre et al. 2005, Sayers and Schutjens 2007, and Herwanger et al. 2007), are affected strongly by the effective stress changes associated with pore pressure variations induced by production. Here the idea of pressure diffusion in shale was suggested by Peter Schutjens form the Geomechanical asset team in Shell based on some field obervations. The pressure diffusion simulation showed that shale over time could respond to pressure diffusion (pressure drop) and consequently a reduction in the fracture gradient could occur within the overburden, underburden, and sideburden shales. This stress perturbation can lead to narrow margin between collapse and fracture gradient which in tern could increase the risk of wellbore instability, hole collapse and losses. Subsequently the drilling engineers suggest that an evaluation of shales in the overburden and sideburden in depleting reservoirs needs to be developed.

Pressure diffusion can impact our understanding of the risk involved in drilling a new infill well, particularly as the trajectory approaches near to or into the depleted reservoir. Indeed, in most situations when drilling a new well it is believed that shale formation remains at the

initial pressure while the sands reduce in pressure. The understanding is that the mud-weight should be kept high above the initial collapse limit. However, if the regions of the shale formation deplete significantly within the time scale of production, then in these zones the fracture gradient (defined by the minimum horizontal stress) will have been reduced. Drilling with the initial mud- weight set may therefore lead to mud losses and an increased risk of well failure, particularly in high risk HPHT environments when there is very little margin for error. The effect of pressure diffusion in the context of mechanical interaction is relatively unfamiliar to the current field study, but has been recognised and utilised elsewhere. For example, in the field of drilling and completion, diffusion of a pressure overbalance into surrounding shales is considered to be one of the major failure mechanisms of the wellbore (Bol et al. 1994). Shales give rise to a reduced mudcake, and hence pressure equilibration can occur over time after initially drilling the hole. This overbalance propagates into the formation until the stress path (defined, for example, by the trajectory of the deviatoric to mean effective stress) intersects the Mohr-Coulomb failure envelope and shear failure occurs. To stop this occuring a plugging agent is required to reduce the permeability at the wellbore surface, this reducing the pressure propagation problem and creating more stability at a much lower overbalance. Another example is in mining engineering, where pressure diffusion process is considered a necessity in engineering calculations to ensure stresses are properly taken into account (Wong 1996). In this case diffusion has a pronounced influence as the time scales considered are long.

Unfortunately, in geosciences there is inadequate calibration of the petrophysical, mechanical and transport properties of the shale formation, and its internal architecture. Precise permeability values for reservoir shales are problematic due to the lack of reliable core data and measurement techniques, but also the associated cost in obtaining accurate and representative laboratory measurements. In fact, since several orders of magnitude in range of shale permeability are possible for a single porosity value in apparently similar samples, even the exact controlling mechanisms for shale permeability are not yet fully understood (Yang and Aplin, 2007). Such diversity may arise due to permeability anisotropy linked to particle alignment and material heterogeneity, fractures, internal structure and laminations of the sand, silt or clay components and shale maturity. Hence, for the purposes of this current study a broad spectrum of permeability values has been considered. Also, the internal structure, whilst known to possess many heterogeneities as in the examples of this paper, needs a careful field specific study to pin down the individual properties – this suggests more careful

use of laboratory and outcrop measurements. A careful evaluation of shales in the overburden and sideburden in depleting reservoirs needs to be developed. Sideburden effects may be particularly important in the flanks of reservoirs (for example McInally et al. 2001). What is required is a reservoir-specific collection and evaluation of shales for each producing field. It is possible that methods such as 4D seismic might allow the diffusion effects to be monitored (HajNasser and MacBeth 2011), limits on the shale properties to be determined, and these properties to be factored into planning.

CHAPTER

FOUR

4 The effect of shale beds on the reservoir's stress sensitivity and seismic signature

This chapter focuses on the prediction of the reservoir's in situ elastic wave stress sensitivity and the evolution of the fluid pressure component. First numerical simulation of stress changes is performed for impermeable and mechanically active shales (defined as *Inactive* shale). Next, permeable and mechanically active shales (defined as *Active* shale) are considered. The findings of the geomechanical and the pressure diffusion simulation are used to examine the changes of elastic wave properties for both impermeable and permeable shales. Here the stress changes are assessed using the concept of nucleus of strain. A series of idealized geological models are used for these calculations.

4.1 Introduction

A precise quantitative prediction of the in situ variation in the elastic properties of the reservoir's rock-mass with production-induced changes is an essential element of the petroelastic model that links saturation and pressure changes to the corresponding 4D seismic signatures. Currently, however, the practice of using laboratory measurements to calibrate this variation appears adequate only at a qualitative level and suitable for 4D seismic feasibility studies or crude visual interpretation of the 4D seismic signatures. In particular, the exact magnitude of the in situ stress sensitivity of the reservoir is still largely uncertain and estimates cannot be relied upon for accurate determination of the pressure changes (Eiken and Tondel 2005). This point has been recently highlighted by the results of Floricich et al. (2006) and Stephen and MacBeth (2006), who combined seismic observations with engineering data to conclude that the reservoir's stress sensitivity observed at the seismic scale is smaller than that anticipated from the laboratory. A mismatch between predictions and observations is also reported in other 4D seismic data sets such as those of Fletcher (2004), who revealed an unexplained difference in the sign of the amplitudes and time-shifts associated with depletion in gas condensate reservoirs. A possible explanation for the inability to exactly replicate the 4D seismic observations is offered by a number of well-documented factors that may act to reduce or enhance the stress sensitivity (MacBeth 2004). The (extensive but not exhaustive) list of factors includes: inaccuracies in specifying the 'dry' rock frame properties due to sample conditions and preparation in the laboratory; internal damage due to cutting and stress unloading if controlled stresses and pore pressure are not applied; the statistical bias introduced by the core plug sampling scheme due to core heterogeneity; exact specification of the effective stress coefficient; the true triaxial stress state of the reservoir; creep; and frequency dispersion effects.

An additional item for consideration in the above list is the existence of intra-reservoir scale heterogeneities. In clastic systems an important heterogeneity is the distribution of shale. In particular, this study focuses on discrete intra-reservoir shales that exist as shale beds smaller than the size of a typical sand body (20–30m) and much smaller than the seismic wave- length (50–100m). For the purposes of this paper we refer to such shale beds as 'sub-seismic'. It is known that the seismic response cannot, in general, detect these beds but instead responds as if the reservoir is a single homogeneous unit. The end objective of this work is therefore to

examine the effect of these shales on this overall, composite sand-shale seismic response. As this study focuses on reservoir changes monitored over time periods of several months to tens of years by 4D seismic surveys, the many shale beds of thicknesses less than approximately one meter are not considered – this choice will be observed below to relate to the effect of pressure diffusion. A natural upper limit for investigation is those shales thicker than 10m, which can be detected in the seismic and for which the effective property principle does not apply. In the literature, sub-seismic shales are defined to be 'deterministic' or 'stochastic' (Section 2.4, Figure 2.4). Whilst deterministic shales are continuous and predictable between wells, uncertainty arises for stochastic shales as it is difficult to locate and identify their occurrence and length precisely within the inter-well volume from well data alone. A number of past studies have considered the impact of stochastic shales or shale breaks on the reservoir's fluid flow behavior, well performance and residual oil calculation (for example, Haldorsen and Lake 1984). Sub-seismic shales have also been observed to strongly affect reservoir performance and as a consequence the 4D seismic response (for example, McLellan et al. 2006). In these examples however, shales are treated as inactive and inert barriers perturbing flow in the reservoir and their influence on pressure is largely neglected. Treating shales as barriers is a convenient simplification from the fluid flow perspective but may not necessarily be a valid model of reality. In geomechanical studies, sub-seismic shales have also been studied for their impact on well failure (Schutjens et al. 2005), although they are considered to be non-compacting mainly because their properties cannot be adequately calibrated. Building on this previous work, my current study focuses on the prediction of the reservoir's in situ elastic wave stress sensitivity and the evolution of the fluid pressure component. For this purpose, it is necessary to consider the shales as fully active geomechanical, dynamic and elastically stress sensitive elements of the reservoir. I concentrate only on the effects of pressure depletion as a consequence of an imbalance in pressure support, using a series of idealized geological models.

4.2 Computation of the stress arching ratios γ_{sh} and γ_{sa}

To understand how the sub-seismic shales affect the reservoir stress sensitivity and hence the 4D seismic response, the mechanical and dynamic behaviour of the shales are considered separately at first and then combined. First, stress computation is presented; this calculation is based on the nucleus of strain method of Geertsma (1973). The seismic implications of geomechanics and pressure diffusion of sub-seismic shales are presented. Prior to production, the reservoir and its surrounding rock are in mechanical equilibrium, with the total externally applied stresses matching the internal reservoir stresses. After extraction of a fluid volume during production, the fluid pressure in the reservoir changes by ΔP and this induces a total internal stress change (both vertical and horizontal) of $\Delta\sigma^{tot}\left(\text{int}\right)=\alpha_{sa}\Delta P$ (where α_{sa} is the effective stress coefficient) which consequently creates a mechanical imbalance. The reservoir and surrounding rocks react to this imbalance by straining, the mechanics of which are governed by the total external and internal stresses and the boundary conditions - for laterally extensive reservoirs this strain is mostly directed in the vertical direction. This change of reservoir geometry redistributes the total external confining stress. The degree of redistribution depends on the magnitude of the causative internal stress change, which depends in turn on the change of reservoir pressure and the volume extracted. Following Hettema et al. (2000), the change in the total confining vertical stress $\Delta\sigma_v^{tot}$ induced by this pressure change can be written as $\Delta\sigma_v^{tot}\left(ext\right)=\gamma_v\Delta P$, where γ_v is a positive coefficient. Thus, the resultant change in the effective stress loading the rock frame of the reservoir is $\Delta\sigma_v^{eff}=\left(\gamma_v-\alpha_{sa}\right)\Delta P$. It is this effective stress that is important when determining the material properties of the rock in this calculation. A similar change and definition exists in the horizontal direction, for which γ_h is defined. For the models considered in this current work it is found that $\gamma_h>\gamma_v$ Both γ_v and γ_h are non-negligible in this particular case study due to the geometry of the reservoir, and thus unequal velocity changes due to the vertical and horizontal total stress changes are expected. However, as my work focuses only on the impact of vertical velocities and these velocities are affected only by the vertical stress changes (assuming material isotropy and homogeneity), variations in γ_h are ignored. Thus, in the subsequent analysis γ_v will be referred to as either γ_{sh} for shale and γ_{sa} for sand.

The work below considers the influence of intra-reservoir shales on the stress arching ratios for both the sands γ_{sa} and shales γ_{sh}. I consider the geomechanical behaviour due to a single sand body containing layers of sand and shale beds responding to production-induced depletion. Depletion is only in the sands as the intra-reservoir shales cannot be produced due to their very low permeability, however they do interact mechanically due to the stress imbalance created by the surrounding sands. The γ_{sh} values depend primarily on the thickness and distribution of the beds in the channel, and the channel geometry and dimensions. To determine γ_{sh} for the purpose of the current study, 3D numerical modelling of the mechanics of depletion is carried out for a range of channel models containing a distribution of thin shale beds. Each channel cross-section is assumed to be semi-elliptical and is extended in the transverse direction (Figure 4.1). The channels consist of alternating layers of thicker sandstone beds separated by shale eroded by various degrees. The sand quality is assumed to be highest at the base and the center of the channel, and to decline upwards and outwards (Stephen, Clark and Gardiner 2001). For the purpose of this modelling, the channel body is discretised into a number of orthogonal cells with dimensions 0.5mx0.5mx0.5m (Figure 4.1).

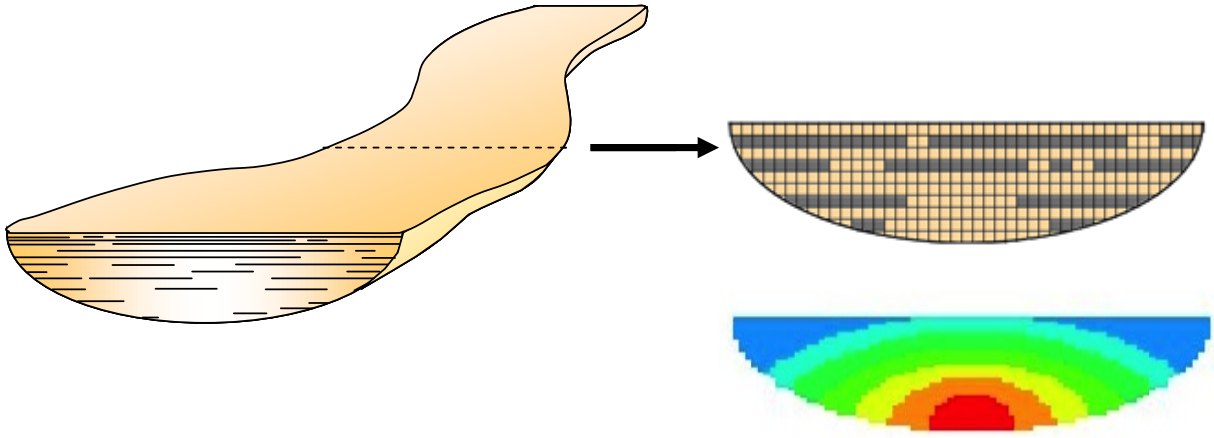

Figure 4.1: The channel sand model is discretised into cubes of 0.5m in dimension. Calculations based on the equations of Geertsma (1973) and described in the next section are performed for a central vertical slice through this model. Intra-channel shales are distributed according to the erosional model of Stephen et al. (2001). The lower right figure is the contoured net-to-gross in the channel, where red is low and blue is high.

The reservoir deformation resulting from withdrawal of fluid from each individual sand cell is calculated, the result summed for all sand cells in the reservoir, and then the theory of linear poroelasticity used to calculate the impact on the effective stress and total stress. The reservoir deformation calculation is performed using the method of infinitesimal inclusions (the nucleus of strain method of Geertsma (1973)) as implemented by Hu (1989). This gives the displacement, U_i, at a specific point due to an infinitesimal inclusion subject to depletion-induced strain (in this case an individual sand cell) embedded in an isotropic homogeneous half-space. An assumption implicit in the use of this approach, is that the elastic constants for the sand and shale must be identical. The vertical and horizontal displacements at the cell-cell interfaces due to pressure change in the whole reservoir can thus be readily obtained as the superposition of the displacements due to each depleting sand cell in the reservoir. Having obtained the displacements at each interface between the sand-sand cells or sand-shale cells, the cumulative strain $\varepsilon_{ij} = \frac{1}{2}\left(\frac{\partial U_j}{\partial x_i} + \frac{\partial U_i}{\partial x_j}\right)$ on each shale bed or particular portion of sand can be determined. The strain field in turn can be converted into the total stress perturbation $\Delta\sigma_{ij}^{tot}$ by applying the theory of poroelasticity

$$\Delta\sigma_{ij}^{tot} = \mu\left(\frac{\partial U_i}{\partial x_j} + \frac{\partial U_j}{\partial x_i}\right) + \frac{2\mu\nu}{1-2\nu}\left(\frac{\partial U_i}{\partial x_j} + \frac{\partial U_j}{\partial x_i}\right)\delta_{ij} - \alpha\Delta P\delta_{ij} \qquad (4.1)$$

where μ is the shear modulus, ν the Poisson's ratio and δ_{ij} Kronecker's delta (in this case μ =25GPa and ν is fixed at 0.25). After the stress change is known, the γ values can be determined by dividing by the pressure drop ΔP. In the case of the sand, the effective stress coefficient, $\alpha = \alpha_{sa}$ is set to unity, whilst for the shale it is zero for the impermeable case and 0.7 for the permeable case (once pressure diffusion has begun, see Chapter 3). The choice of these values is explained in the next sections. The above calculation is carried out for four different sizes of channel with thickness: width ratios: 10x50m, 10x100m, 15x250m, and 20x500m, and five different thicknesses of shale bed (0.5, 1, 2, and 10m). It is performed in 3D, but the results for only a vertical section in the center of an 800m long sand body are used – i.e. in the calculation I choose to ignore the calculations at the channel edge.

4.3 The prediction for impermeable but mechanically active shales

Here, it is assumed that the shale beds are completely impermeable and therefore act as non-conducting barriers to fluid flow in the reservoir. This assumption is commonly made (and justified) for most reservoir simulation studies. Consider the effect of instantaneous pressure depletion in a sand body consisting of several sand and shale beds sandwiched between a shale overburden and underburden as in Figure 4.2(a). All of the sands are assumed to be connected to the well and hence are fully produced. Good horizontal and reasonable vertical connectivity within the sands ensures that the resulting pressure drop spreads quickly and the pressure reaches a stable state within a few seconds. Although in favourable circumstances the majority of the fluid volume removed is replaced by the aquifer or injectors, I consider there to be an imbalance and hence a net pressure drop. The individual sand beds are expected to compact in response to this depletion because the effective stress acting on their rock frame has increased. Intra- reservoir shales, however, cannot respond to the depletion in the same way as the sands, as fluid is not extracted from them (at least not over the time scale of production). They do nevertheless interact indirectly and because the shales stay coupled to the sands there will be deformations and total stress changes in the shales also. Thus, in a similar way to the more widely recognized shale overburden deformation in response to reservoir compaction (for example, Hodgson et al. 2007), intra-reservoir or inter-reservoir shales may mechanically extend in response to pressure depletion in the sand. Figure 4.2(b) from the published numerical modelling example of Sayers and Schutjens (2007) illustrates this effect. Further details on the stress calculation are described in the following section.

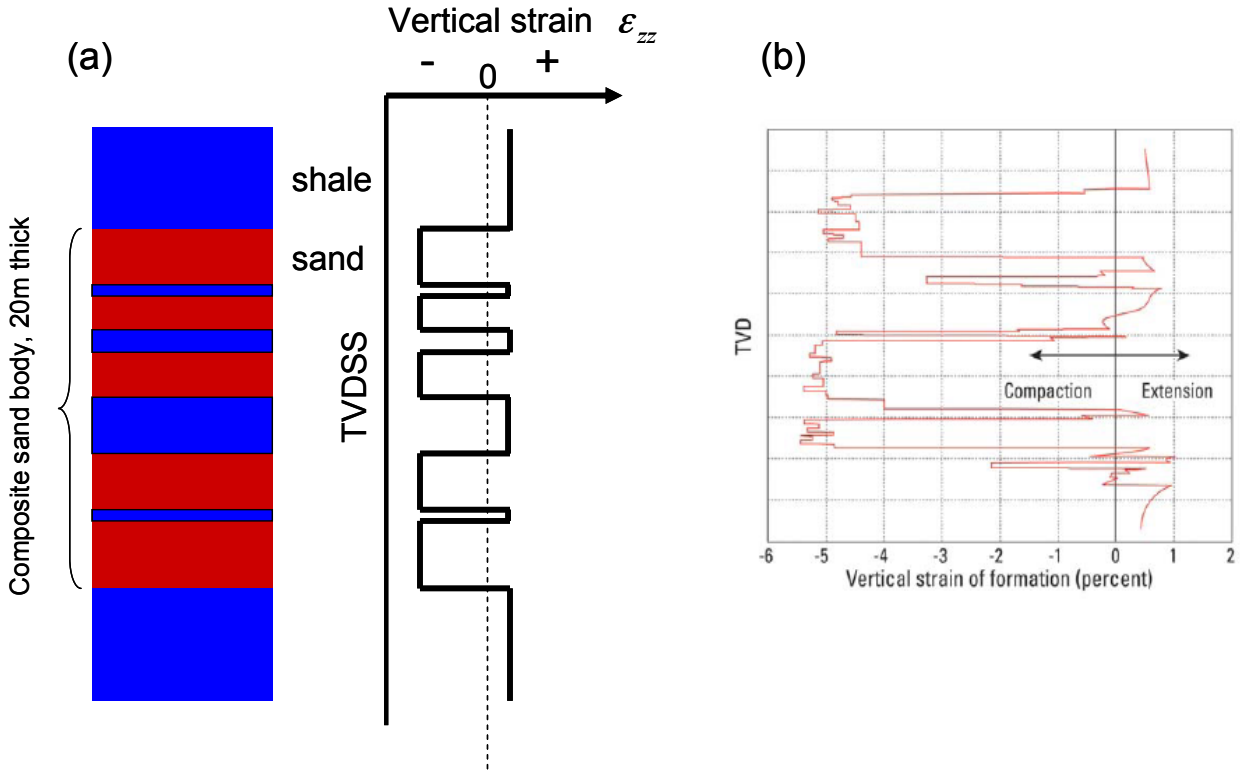

Figure 4.2: (a) Schematic illustrating the impact of production on a sequence of sands separated by shales. (b) Modelled vertical strain alternation at the location of a well in a deepwater Gulf of Mexico turbidite as a function of true vertical depth (TVD) (Sayers and Schutjens 2007).

4.3.1 Geomechanical predictions: Stress changes

In this section, I carry out the geomechanical calculation using the model described earlier in Section 4.2. Here the shale is assumed impermeable therefore the calculation is performed to predict the stress changes induced by the pressure depletion in the sand. To treat the mechanical effect on the shale beds, consider the influence of a pressure depletion of ΔP on the elastic wave properties of the reservoir (ΔP is defined as negative for a drop in pressure). For each sand bed, the reduction in reservoir fluid pressure leads instantaneously to an overall stress change of $\alpha_{sa}\Delta P$ relative to the pre-production state (where α_{sa} is the effective stress coefficient describing the contribution of the fluid pressure to the overall stress it is defined as a positive number). Upon sand compaction in response to this stress change, the total vertical stress state inside the reservoir is changed by $\gamma_{sa}\Delta P$ (where γ_{sa} is the stress arching ratio, γ values are defined as positive numbers). This changes the effective stress acting on the sandstone rock frame by an amount $(\gamma_{sa}-\alpha_{sa})\Delta P$, where $\gamma_{sa}<\alpha_{sa}$. Impermeable shales, on the other hand, are not subjected to pressure change due to fluid production, and hence their stress state changes by virtue of the pull exerted by the neighbouring compacting sand layers - this leading to a change in total stress acting internally on the shale. The total stress change in the shale due to this mechanism (also equal to its change in effective stress) is given by $\gamma_{sh}\Delta P$ where γ_{sh} is the stress arching ratio for the shales.

In addition to the above, a secondary effect occurs in the shales - as they extend, the pore volume expands and the pore pressure decreases by an amount determined by their Skempton B_{sh} coefficient (Detournay and Cheng, 1993). The change in effective stress on the shale rock frame is given by $(\gamma_{sh}-\alpha_{sa}B_{sh}/3)\Delta P$, however as B coefficients are typically similar in magnitude to the effective stress coefficients; the combination $\alpha_{sa}B_{sh}/3$ is chosen to be neglected in the discussion here and in the next sections as it is small compared to γ_{sh}. For the calculation of the stress arching ratios γ_{sh} and γ_{sa}, I use the model of semi-elliptical channel described in the Section 4.2. This calculation is performed in 3D using the concept of nucleus of strain. Further details about the nucleus of strain concept (Geertsma, 1973) are shown in Appendix A.

As anticipated, for each channel I find that the deformation of the top and bottom of the channels are in opposite direction, i.e. the roof subsides and floor rises. Inside the reservoir, the displacements at the sand/shale boundaries are also not identical, and they all indicate shale dilation, but by differing amounts. For each of the chosen models, the number of shales and hence the net-to-gross, is varied. Net-to-gross is also varied laterally across each sand channel in agreement with the conclusions of Stephen et al. (2001). The results show that for the range of models considered γ_{sa} is approximately equal to γ_{sh}. Also, as net-to-gross increases, so too does γ_{sh}, (Figure 4.3(a)). Thus, for example, γ_{sh}, varies from 0.2 to 0.5 for a shale thickness of 1m. In addition, γ_{sh}, is greater for shales at the top of the channel than for shales near the base of the reservoir (where there is more depleting sand and thus more shale extension) (Figure 4.3(b)). γ_{sh}, also varies with the shale thickness, and for the 1m thick shales it lies between 0.1 and 0.4, whilst for 2m thick shales the range reduces to between 0.1 and 0.2. For the 10m thick case net-to-gross is very low in some of the channels, γ_{sh} is small, less than 0.1 (but still positive). My four cases and their channel thickness to width ratio R give: 10x50m (R=0.2, $\gamma_v = 0.25$), 10x100m (R=0.1, $\gamma_v = 0.15$), 15x250m (R=0.06, $\gamma_v = 0.04$), and 20x500m (R=0.04, $\gamma_v = 0.02$). The values are similar to those reported in the literature for a disc-shaped or ellipsoidal reservoir as most of the changes are found to be governed by the thickness to width ratio (Hu 1989). The results described above are used as input to the rock and fluid physics calculations in the following section.

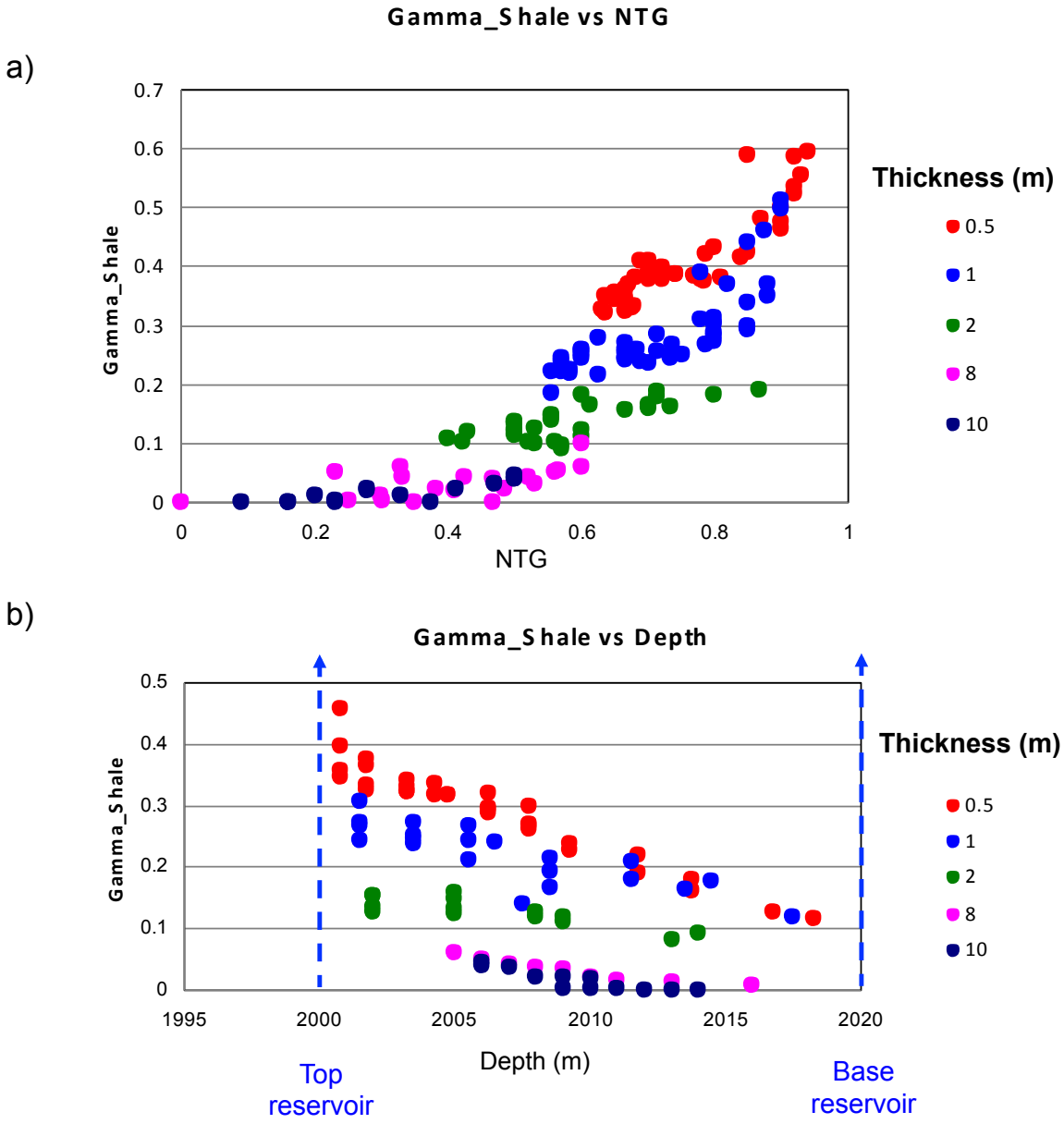

Figure 4.3: Gamma values for shale γ_{sh}, for a range of thicknesses, and channel dimensions. (a) as a function of net-to-gross in the channel and (b) depth location in the channel. Channel depths have maximum limits from 1995m (top reservoir) to 2020m (base reservoir).

4.3.2 Seismic implications

The seismic-scale consequence of an extension-induced stress change in the shales is illustrated in the schematic of Figure 4.4. The stress sensitivities of the sand and shale rock frame may be defined by the characteristic non-linear function observed and measured in the laboratory for single core plugs (MacBeth 2004). The sands and shales are assumed to have a similar stress sensitivity behaviour (although a different magnitude) when compacting but different elastic moduli (red curve segment). The shale has an enhanced stress sensitivity upon extension (blue curve segment) as the magnitude upon elongation is known to exceed that of compaction (Sayers, 2007). Upon depletion, the sands follow the red curve and increase their impedance, whilst the shales follow the solid blue curve and decrease their impedance. Due to the non-linear shape of the stress sensitivity curves (which in practice requires adequate calibration), for any given pressure drop the shales may reduce their impedance by an amount greater than the increase of impedance in the sands due to compaction. Thus the impact of the shale stress sensitivity could be a strong component of the reservoir's overall stress sensitivity.

To quantify the impact of the above phenomena on the overall seismic response of the reservoir, the change in the elastic wave properties of the sandbody are calculated for vertical P-wave propagation through the central portion of the body containing a stack of sand and shale beds. For this, Backus averaging (1962) and a mass balance calculation are used to determine the pre-production composite P-wave elastic modulus M_{av} and density ρ_{av} from the individual moduli M_{sa} *and* M_{sh}, and densities ρ_{sa} and ρ_{sh} for the sands and shales initially when reservoir pressure is P_0

$$\frac{1}{M_{av}(before)} = \frac{NTG}{M_{av}(P_0)} + \frac{1-NTG}{M_{sh}(P_0)} \tag{4.2}$$

and

$$\rho_{av}(before) = NTG\rho_{av}(P_0) + (1-NTG)\rho_{sh}(P_0) \tag{4.3}$$

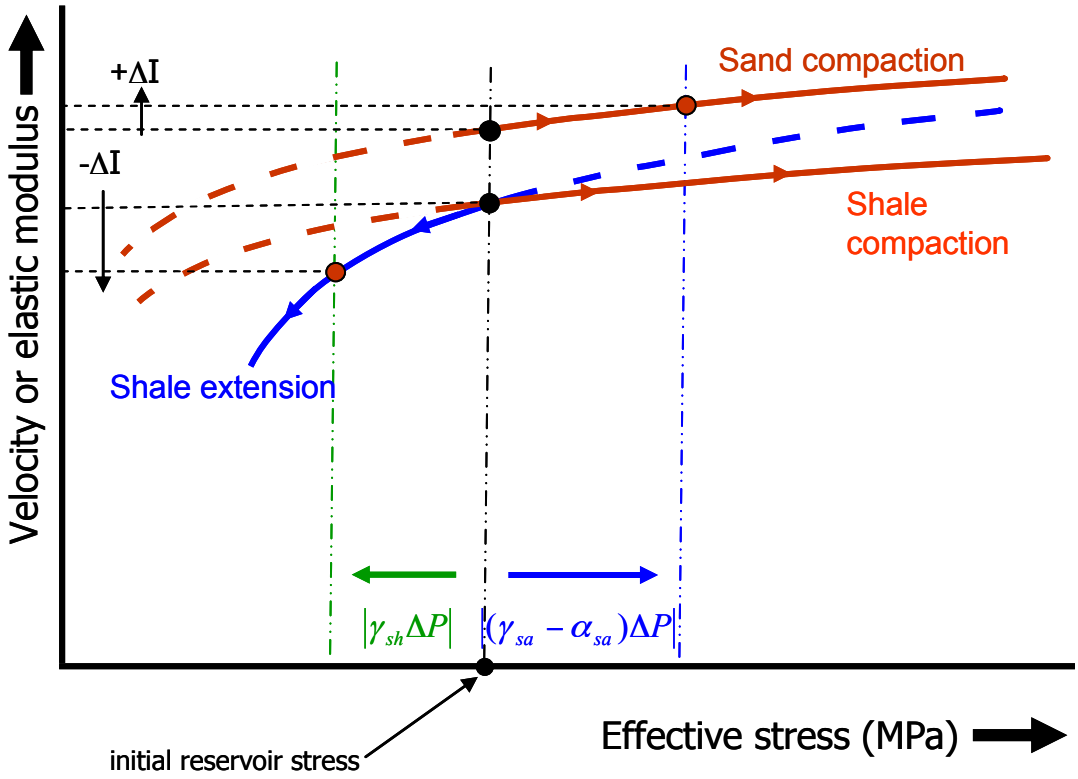

Figure 4.4: Schematic stress sensitivity curves for reservoir sand and shale, illustrating the effect of pressure depletion and compaction versus dilation or extension on the elastic properties. Dashed segments indicate portions of the curves not thought to be accessed by the rocks in-situ and are the stress arching factors and is the effective stress coefficient for the sand. Here the compaction path of the shale is different form the compaction path of the sand (red curves)

and also the modulus and density for the post-production state

$$\frac{1}{M_{av}(after)} = \frac{NTG}{M_{av}(P_0 + |(\gamma_{sa} - \alpha_{sa})\Delta P|)} + \frac{1 - NTG}{M_{sh}(P_0 - |\gamma_{sh}\Delta P|)} \tag{4.4}$$

and

$$\rho_{av}(after) = NTG\rho_{av}(P_0 + |(\gamma_{sa} - \alpha_{sa})\Delta P|) + (1 - NTG)\rho_{sh}(P_0 - |\gamma_{sh}\Delta P|) \tag{4.5}$$

Here, *NTG* refers to the net-to-gross (ratio of cumulative sand thickness divided by the total thickness of the sandbody) for the sandbody at a particular horizontal location, and the γ_{sa} and γ_{sh} are the depth averaged quantities at that location. As only vertical velocity for P-waves is considered, these results are sensitive only to changes in the vertical effective stress. P-wave impedance is calculated from (4.2), (4.3), (4.4) and (4.5) for a typical, good quality (25 percent porosity) sand from a normally pressured reservoir in the North Sea with top reservoir lying at 7000ft (similar to that of the Nelson and Schiehallion fields in the UKCS). An instantaneous pressure depletion of $\Delta P = -10MPa$ is chosen, this representing a reasonable upper limit on the pressure fluctuation in an oil-water reservoir due to production with partial support. Note that in practice larger local variations are still be possible depending on the degree of compartmentalization, type of reservoir, and rates of production. Sand stress sensitivity parameters and elastic properties published for the Schiehallion field by MacBeth (2004) are used. As measurements of shale stress sensitivity are not available for this area, this property is selected arbitrarily by manual adjustment of the shale parameters to be firstly greater than that of the sand, then identical to that of the sand, and finally to be stress insensitive (see Table 4.1 for details). Note that from published literature it appears that the shale stress sensitivity upon compression and extension may be smaller than that of sands (for example, Jones and Wang, 1981, Sarout and Guegen 2008), if this is the case then my results for only the latter two conditions may bracket reality. Density variation is included for completeness, despite the magnitude being no more than 0.1 to 0.2%. The final numerical results are shown in Figure 4.5 for the three shale stress sensitivity scenarios and as a function

of the vertically defined net-to-gross. To select values for γ_{sa} and γ_{sh} in this specific case, extensive geomechanical modelling is carried out for a range of sand channel model dimensions, geometries, mechanical properties, and shale bed distributions – as described in the section on stress arching calculation (Section 4.2). These results indicate that $\gamma_{sh} \approx \gamma_{sa}$, and also that the γ's lie mainly between 0.05 (shale thickness of 10m) and 0.5 (shale thickness of 1m) for this particular model selection. For this reason, results for the lower and upper extremes of the γ's are used as input into the depth averaged quantities used to generate Figure 4.5. Whilst it is understood that the effective stress coefficient α_{sa} is likely to be stress dependent and less than unity for most consolidated sands (for example, Christensen and Wang 1985), to avoid specifying a particular rock in my current work it is assumed to be 1.0.

	κ_∞ (GPa)	P_κ (MPa)	E_κ No units	μ_∞ (GPa)	P_μ (MPa)	E_μ No units	ρ_0 (g/cm^3)	P_ρ (MPa)	$\Delta\rho$ (g/cm^3)	Comments
Sand	9.94	6.32	1.00	7.75	7.23	1.22	1.91	8.40	-0.15	
Shale 1	8.94	10.32	1.00	6.25	10.23	1.22	2.10	8.40	-0.15	Identical stress sensitivity as sands
Shale 2	9.94	6.32	1.00	7.75	7.23	1.22	1.91	8.40	-0.15	Less stress sensitivity than the sand
Shale 3	9.94	-	0.00	7.75	-	0.00	1.91	-	0.00	More stress sensitivity than the sands

Table 4.1: Elastic wave stress-sensitivity parameters for the sands and shales used in this work, defined according to the parameters of MacBeth (2004) κ_∞ and μ_∞ are high pressure asymptotes of the behaviour, E_κ and E_μ control the magnitude of the effect, and P_κ and P_μ control the onset of the low pressure non-linear behaviour. The pressure relationship is given by $\rho(P) = \rho_0 + \Delta\rho e^{-P/P_\rho}$

The results shown in Figure 4.5 indicate that there may only be a complete guarantee of an increase in the reservoir impedance with pressure depletion when the shales are stress insensitive. Indeed, when the shales have identical stress sensitivity to the sands, or are more stress sensitive, the intuitive interpretation of reservoir 'hardening' (i.e. increase in the overall P-wave impedance) is valid only above a certain threshold net-to-gross value (in this case it is 0.8 for 1m thick shales and 0.20 for 10m thick shales). The greater the amount of shale in the composite reservoir package, the greater this 'softening' (i.e. decrease in overall P-wave impedance) effect with pressure depletion. Clearly, however, a limit will be reached where the geomechanical effects of the sands on the inter-bedded shales is insufficient to cause the necessary extension to induce this effect. Softening results in a dimming of the top reservoir response instead of a brightening (or vice-versa), a result contrary to our prior conceptual understanding. Further, for any given net-to-gross, the shale extension effect reduces the stress sensitivity of the reservoir below that anticipated for a homogeneous and connected sand body. Note that a similar result is possible if only a small proportion of the sand beds are hydraulically connected or they become more shaley or possess a high clay content. When there are only a very few thin sands in the reservoir it is unlikely that their combined strain would be sufficient to produce the desired change in the shales (for a fixed pressure drop in the sands). The current theory does not anticipate this lower net-to-gross limit. Thus it is anticipated that for very small values of net-to-gross the above calculation might be unrepresentative of the true physics of deformation.

In summary, considering the geomechanical effects alone and the assumptions of linearity, elasticity, isotropy and homogeneity inherent in this analysis, it appears that whether the reservoir hardens or softens with depletion depends on the net-to-gross, together with the exact stress sensitivity, mechanical properties, stress arching ratios γ_{sa} and γ_{sh}, and the effective stress coefficient α_{sa}.

a)

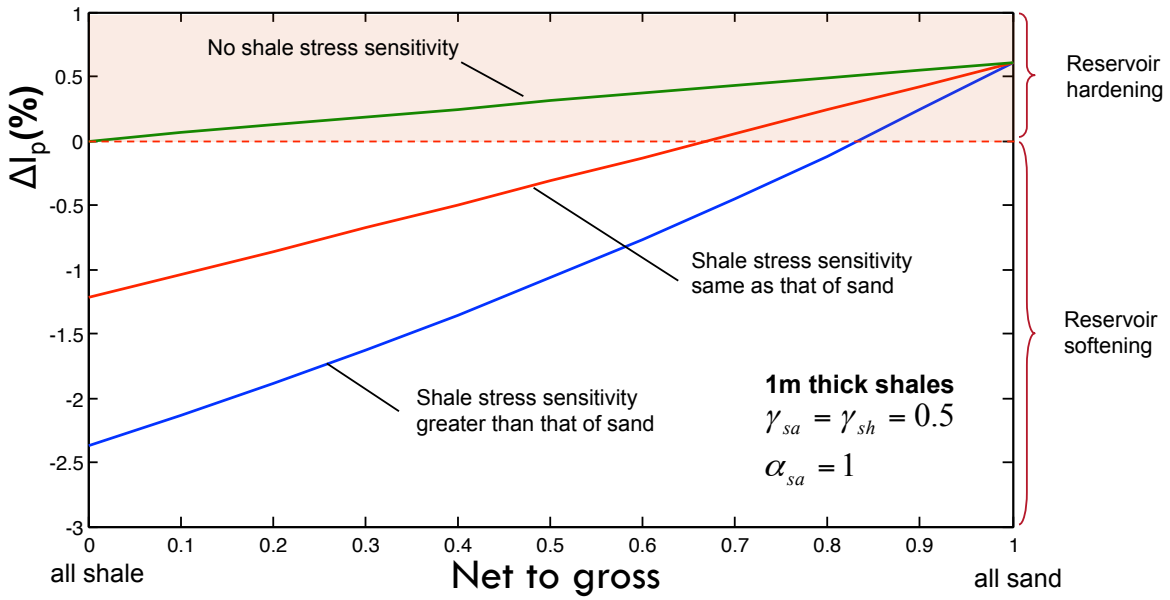

b)

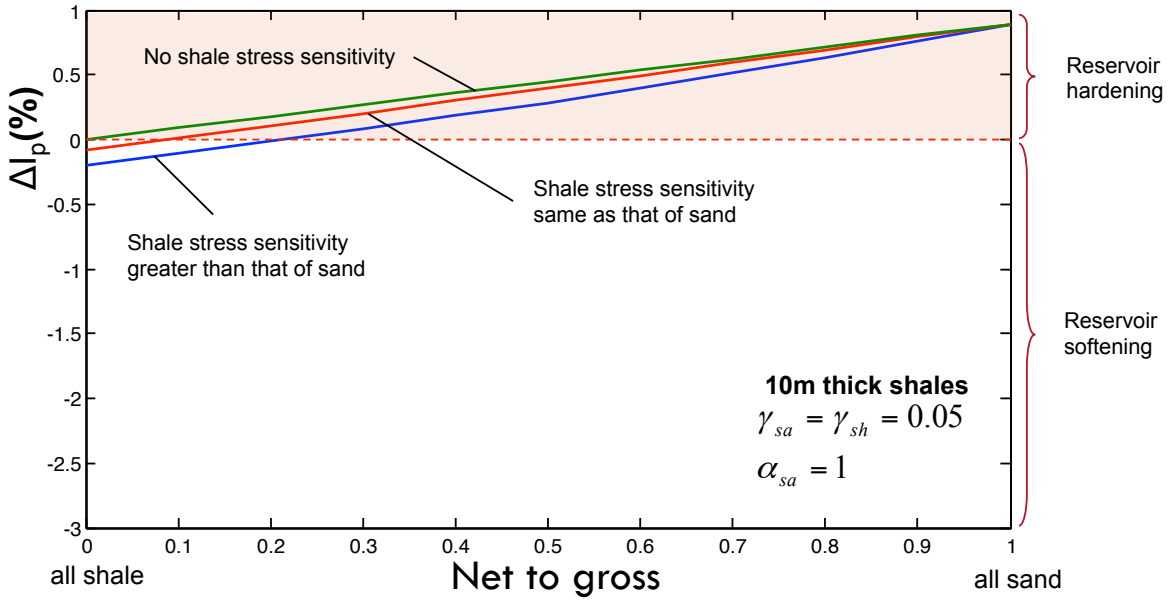

Figure 4.5: Calculated percentage changes in P-wave impedance (DI) for a reservoir comprising of a mixture of sand and impermeable shale layers undergoing mechanical changes due to a pressure depletion of 10MPa. For the generation of these figures γ_{sa} and γ_{sh} are equal, and are fixed at two values: 0.05 (corresponding to a shale thickness of 10m) and 0.5 (shale thickness of 1m). The effective stress coefficient α_{sa} is set to unity in both cases. These results correspond to a reservoir pressure for a normally pressured reservoir at 7000ft.

4.4 The prediction for permeable but mechanically inactive shales

In fluid flow simulations, the assumption of impermeable shales is usually based on consideration of the fluid flow rates. As fluids usually leak through shales over only thousand to millions of years i.e. geological time-scales (unless fractured), intact shales are effectively recognised as reservoir seals and barriers for production time-scales (years to tens of years). Shales do have fairly moderate porosities (5 to 20%) but they are known to possess very small permeabilities and thus high capillary entry pressures, which inhibit fluid mobility. Typical permeabilities reported in the literature are in the range 1μD to 1nD, this being many orders of magnitude below that for the coarser grained clastics that make up the hydrocarbon reservoir. These values are thought to arise from the small grain size and hence pore throat size (5 to 60nm), tortuous pore structure, unimodal pore size distribution and particular mineralogical packing/sorting/fabric of the shales (see, for example, Neuzil 1994). Figure 2.12 presented in Chapter 2, Section 2.7.2, gives a general qualitative measure of permeability for sands, silts, claystone and their intermediate rocks drawn from a range of relevant available literature. Unfortunately, permeability values for reservoir shales are problematic due to the lack of reliable core data and measurement techniques, but also the associated cost in obtaining accurate and representative laboratory measurements. In fact, since several orders of magnitude in range are possible for a single porosity value in apparently similar samples, even the exact controlling mechanisms for shale permeability are not yet fully understood (Yang and Aplin, 2007). Such diversity may arise due to permeability anisotropy linked to particle alignment and material heterogeneity, fractures, internal structure and laminations of the sand, silt or clay components and shale maturity. Hence, for the purposes of this current study the broadest spectrum of permeability values, 1μD to 1nD, must be considered and the implications in terms of the stress sensitivity of the shale properties addressed accordingly.

The shale permeability is low but finite, and thus can affect the pressure evolution but not necessarily large-scale fluid movement. To investigate this more fully, consider a homogeneous sand-filled reservoir in which is embedded a single thin shale bed. Instantaneous depletion is induced in the sands due to production and the pressure change is quickly established in the (high permeability) sands over only a few seconds. After this, a vertical gradient is then set up across the top and base of the shale, which in turn drives the pressure equilibration process that occurs in the shale due to its finite permeability (Figure 4.6). Although, being relatively impermeable compared to the surrounding sand, the shale is

still potentially capable of reaching pressure equilibrium with the reservoir sands. A key question is the exact time scale for this process, which depends on both the thickness of the shale and its absolute permeability. Calculations based on the 1D pressure diffusivity equation are given in Chapter 3, Section 3.3 for a reservoir consisting of a single shale layer embedded between two sands, these yielding the results of Figure 4.7. These show that a 1m thick 1nD shale takes months to equilibrate, whereas a 10m thick 1nD shale can take over 10's of years. These times scale inversely with permeability, and thus will be 1000 times smaller for 1μD shales. Thus, in a reservoir it appears that 1nD permeability shales thinner than a meter will be fully equilibrated in the time between the baseline and monitor survey for most 4D projects (5 to 10 years repeat time). If, however, the shales are closer to 10m thick then there may be partial equilibration and the results of the previous section on impermeable shales become relevant.

The above results (which do not yet include the effects of geomechanical extension of the shales) indicate that shales will deplete partially or totally according to a pressure diffusion phenomenon. The prediction in this case is therefore that all shales will ultimately compact with depletion in the sands and hence the whole reservoir interval will eventually harden – the degree and speed at which this occurs depends on the shale thickness and diffusivity properties.

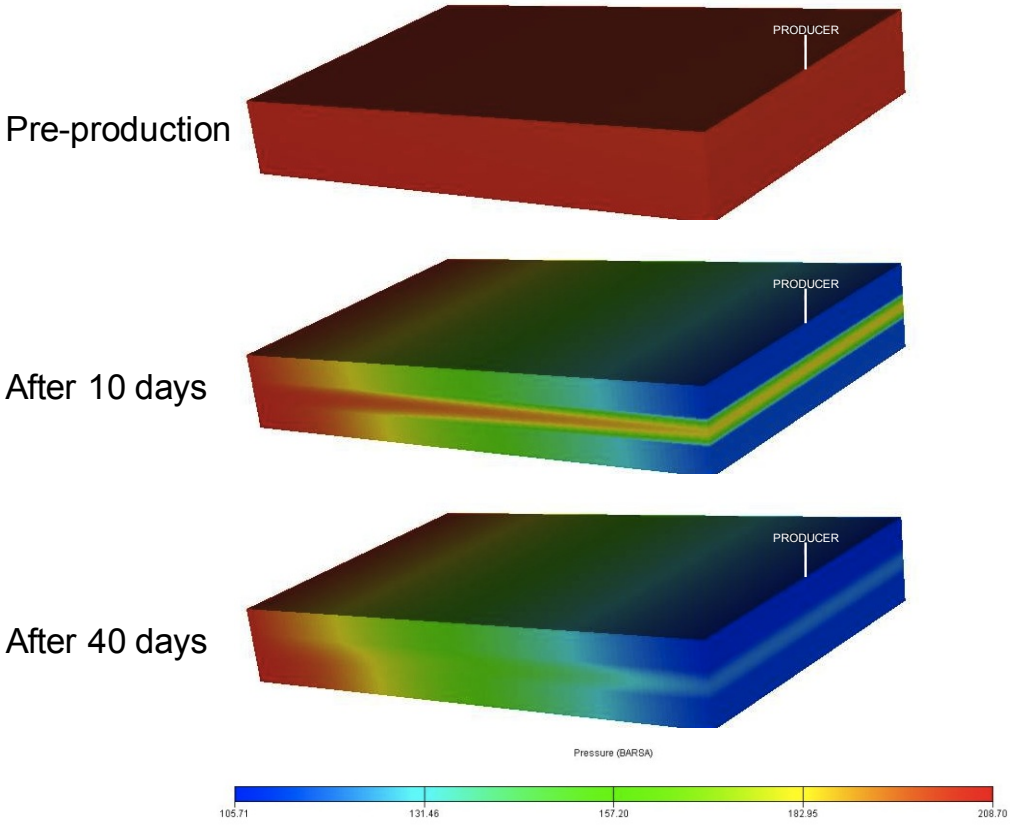

Figure 4.6: 3D numerical simulation of pressure evolution in a two-phase (oil and water) 2D reservoir model defined by a homogeneous sand with an embedded central shale layer. The sand has a permeability of 500mD and the shale is 1μD. Porosity is 20% throughout. There is a single production well of variable rate regulated to give 5–10MPa depletion and there is some aquifer support from below the model.

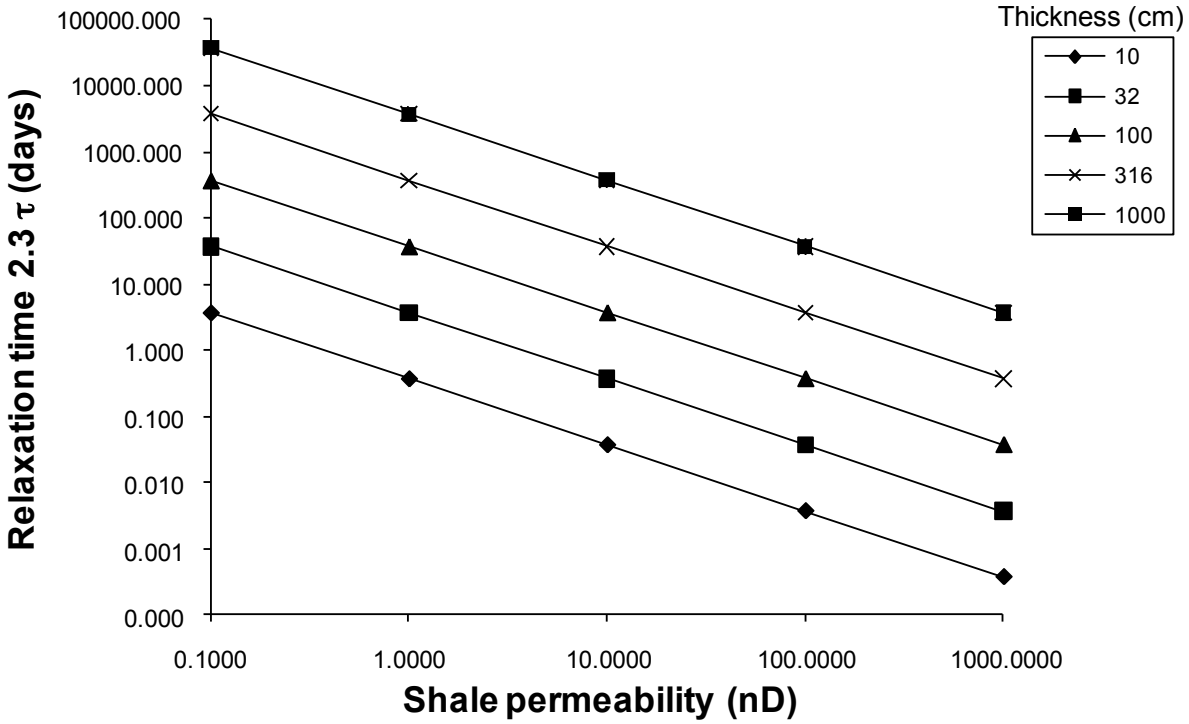

Figure 4.7: Relaxation time for a thin shale sandwiched between two instantaneously depleted sands. Numbers in the box refer to the shale thickness in centimeters. The relaxation time is defined as the point at which the pressure perturbation induced in the shale by the process of diffusion is $9/10^{th}$ of the perturbed value in the sand ($t = 2.3\tau$ –Equation 3.7). This is derived from the solution of the 1D pressure diffusivity equation (see Chapter 3, Section 3.3.4)

4.5 The prediction for permeable AND geomechanically active shales

It has been concluded from the previous section that intra-reservoir, sub-seismic shales with a small but finite permeability can partially deplete over time scales typical of most repeated seismic surveys. The anticipated degree of shale depletion however depends on the shale thickness and properties and the specific time scale involved. Depending on the conditions, shales may become completely depleted, partially depleted or remain close to their initial pressure. Depletion offsets the geomechanical extension effects driven by the pressure (and hence stress) difference across the sand-shale boundary. Total stress change in response to sand depletion is (almost) instantaneous, whereas the pressure diffusion acts over a much longer time period. It is anticipated that the shales will firstly experience an extension in response to the depleted sands, and this will be followed by a slow re-compaction with a time constant of months to tens of years. If the shales can tolerate this mechanical behaviour without failure, then the net consequence of the process depends, once again, on the time scale involved and the shale thickness. Thinner shales equilibrate quickly, but also experience a greater geomechanical response initially. Thicker shales equilibrate at a slower rate but experience a smaller initial mechanical impulse. The extent of interaction between the geomechanical and pressure diffusion phenomena is quantified below. A small, secondary effect may be noted again for completeness as arising from the Skempton coefficient described above. Mechanical extension of the shales causes a small reduction in the pore pressure, which in turn reduces the rate of equilibration. This is not considered as a first order effect in the current analysis.

4.5.1 Geomechanics and pressure diffusion predictions

To analyse the combined effects of geomechanics and pressure diffusion, numerical calculation of the deformation of sand bodies with different geometries and aspect ratios is performed for a variety of intra-reservoir shale thicknesses and distributions. This deformation analysis is performed independently of the pressure diffusion calculation. A separate calculation is performed for each shale pressure equilibration state, ranging from $\Delta P_{sh} = 0$ (no shale depletion) to $\Delta P_{sh} = \Delta P$ (shales fully depleted with pressure drop being that in the sand). Note that when the pressure in the shales starts to equilibrate ($\Delta P_{sh} \neq 0$), it

becomes necessary to also specify the effective stress coefficient, α_{sh}, for the shale – thus the change of effective stress for the shale is now $\left(\gamma_{sh}\Delta P - \alpha_{sh}\Delta P_{sh}\right)$ rather than $\gamma_{sh}\Delta P$ in the shales. The geomechanical scheme used is that of Geertsma (1973) implemented according to Hu (1989) and is identical to the nucleus of strain summation for a half-space described in Appendix A. The stress arching ratios for the sand γ_{sa} and shales γ_{sh} are evaluated for each depletion state during the continuous diffusion process and thus can also be mapped as curves defined as a function of time. The results (see Figure 4.8(a) and (b)) indicate that the stress arching ratios for the shales vary with time (and hence depletion) and the net-to-gross and those for the sand follow a roughly similar trend (although the variation with the net-to-gross is slight and thus not shown). The non-linear nature of the decrease in γ_{sa} and γ_{sh} is due to the particular shale distribution and thicknesses in the sand body. The numerical calculations show that as pressure equilibrates the γ_{sh} values eventually decrease below $\alpha_{sh}\frac{\Delta P_{sh}}{\Delta P}$. The point at which this occurs once again depends on the shale thickness and can vary between three months for the 1m thick shale to 20 years for a 10m thick shale. There is a smaller, secondary variation of this point with net-to-gross. The cross-over point varies with the particular values assigned for the stress arching ratios and effective stress coefficients. In these particular calculations α_{sh} is set at 0.7 – the effective stress coefficient of shale is poorly documented and this is obtained from the low porosity shale results of Hornby (1996).

a)

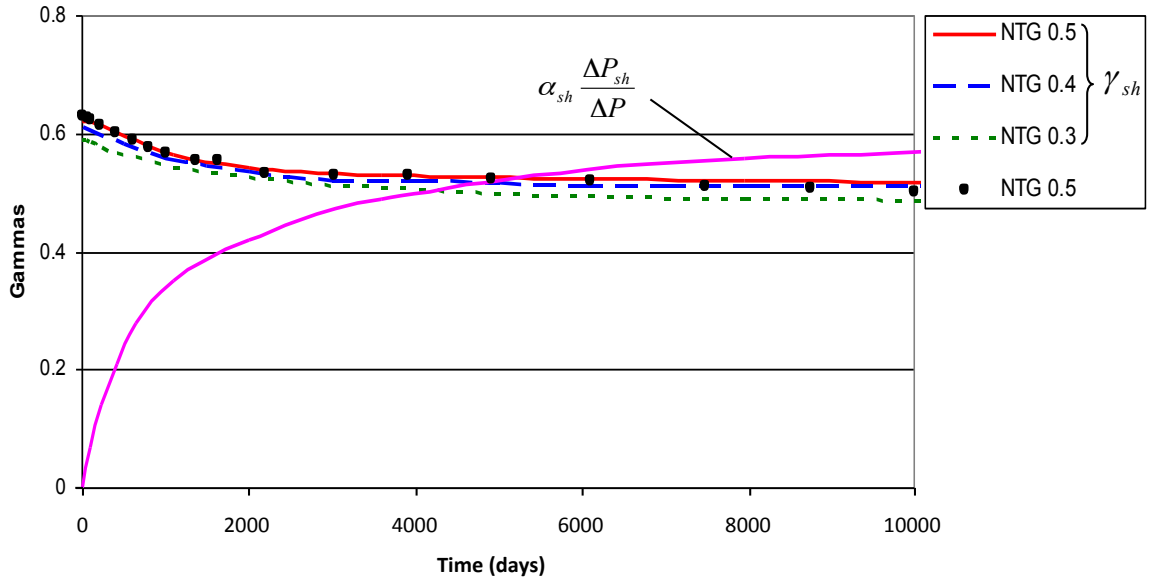

b)

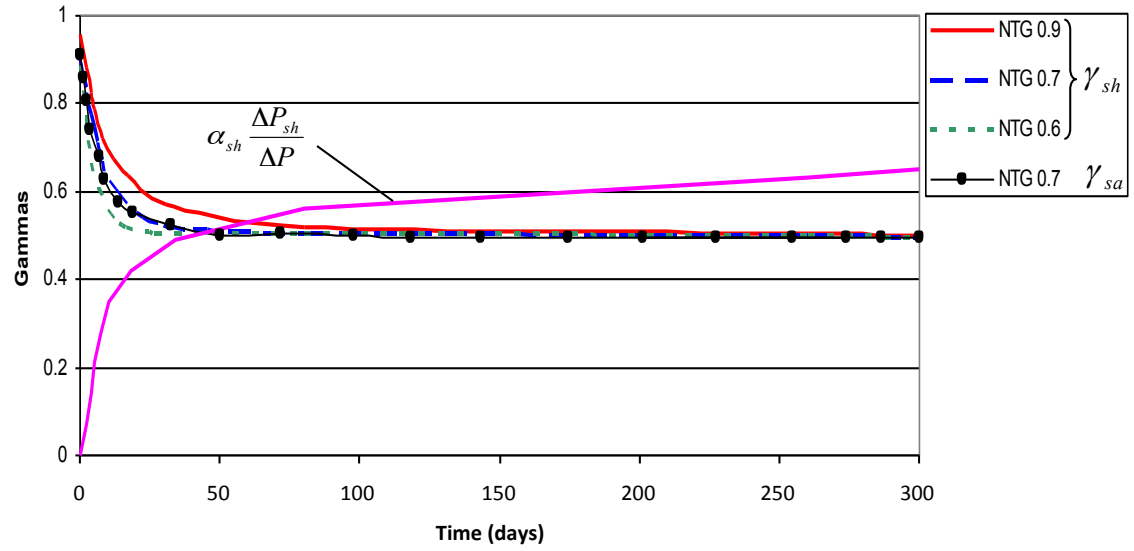

Figure 4.8: Variation of the stress arching ratios γ_{sh} and γ_{sa} with time for: (a) a shale thickness of 1m and permeability of 1nD; (b) a shale thickness of 10m and permeability of 1nD. Note that the time to reach any given depletion state varies depending on the shale thickness and permeability. The effective stress coefficient α_{sh} for the shale is selected as 0.7 whilst for the sand α_{sa} is 1.0. The calculations used to generate these curves are made continuously for every pressure change. For visual clarity only, γ_{sa} points for a fixed net-to-gross of 0.7 are drawn instead of curves.

4.5.2 Seismic implications

Figure 4.9 shows the implications of variable γ_{sh} (and γ_{sa}) on the overall elastic properties of the reservoir. Whilst the sands continue to compact, as before, the shales will experience extension at first and the composite elastic response will be in accordance with Figure 4.4. However as time progresses γ_{sh} reduces below $\alpha_{sh}\frac{\Delta P_{sh}}{\Delta P}$ and the shales reverse their geomechanical behaviour and start to compact as the effective stress applied to the shales increases. In practice this process is a continuous accommodation of the geomechanical effects by the progression of pressure diffusion as described in Figure 4.10, such that the strain field in the shale slowly reverses its behaviour and evolves towards its final state. It is a fully coupled process and needs a fully coupled geomechanical and flow simulator to verify these findings, which is beyond the scope of the current work. Once again, the exact pathway of this progression depends on the shale properties – thickness and permeability.

To understand what final impedance may be found by combining geomechanical and diffusion effects, a calculation is performed again using the Backus averaging equations (4.2)–(4.5) for one of my idealized geological models. Stress arching ratios are computed numerically using the same scheme as that described in Section 4.2 for a sand channel of dimensions 25 m × 250 m. Shales with a thickness 1m and permeability of 1nD are embedded in the sand channel and their number varied to simulate a range of net-to-gross. After depletion in the sands, the time taken for these particular shale layers to equilibrate to within 10 per cent of the final sand pressure is 82 days. The results of impedance calculation for two different states of pressure equilibration and elapsed time are shown in Figures 4.11(a) and 4.11(b). The two pressure states considered are: $\Delta P_{sh} = 0.1\Delta P_{sa}$ and $\Delta P_{sh} = 0.3\Delta P_{sa}$, these occurring after two days and seven days respectively and the $\gamma_{sh} \le \alpha_{sh}\frac{\Delta P_{sh}}{\Delta P}$ condition is achieved by the time 47–53 days have elapsed (when $\Delta P_{sh} = 0.7\Delta P_{sa}$). Thus, beyond approximately 50 days the reservoir zone is expected only to harden. By contrast, 10m thick shales take 250 days to equilibrate to $\Delta P_{sh} = 0.1\Delta P_{sa}$, 520 days to reach $\Delta P_{sh} = 0.3\Delta P_{sa}$ and approximately 4500 days to reach the $\Delta P_{sh} = 0.7\Delta P_{sa}$ point. It can be concluded that, for a time period of months or greater a reservoir with 1m thick shales will not exhibit an anomalous softening response, whilst for the 10m thick shales there is a possibility of overall reservoir softening. However, the likelihood of observing this softening effect diminishes over time.

For example, five years after the depletion change it is predicted to be visible only for the 10m thick shales and in regions with net-to-gross values of 0.2. As a general principle, unless the shales in the reservoir are fully equilibrated then it is expected that the effects described above will lead to a reduction in the overall stress sensitivity from that expected for a fully connected, homogeneous body.

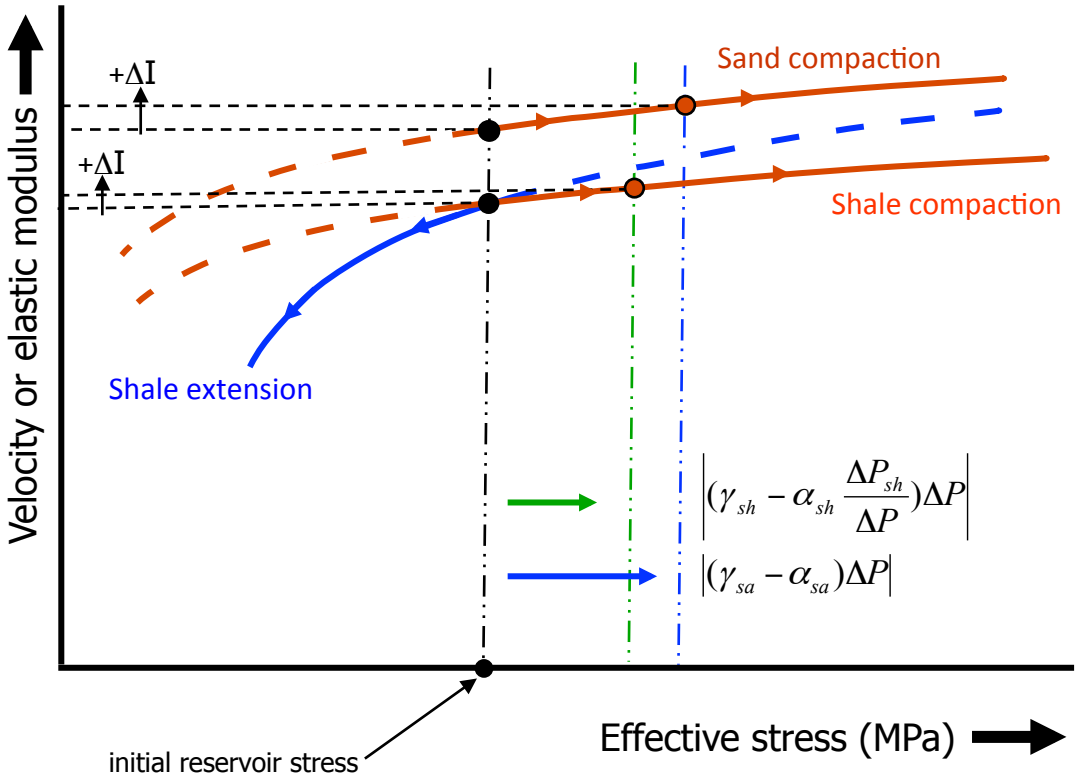

Figure 4.9: Stress sensitivity curves for reservoir sand and shale as in Figure 4.4 but at a later time after pressure equilibration has occurred and γ_{sh} is now less than $\alpha_{sh}\frac{\Delta P_{sh}}{\Delta P}$. Here the compaction path of the shale is different from the compaction path of the sand (red curve).

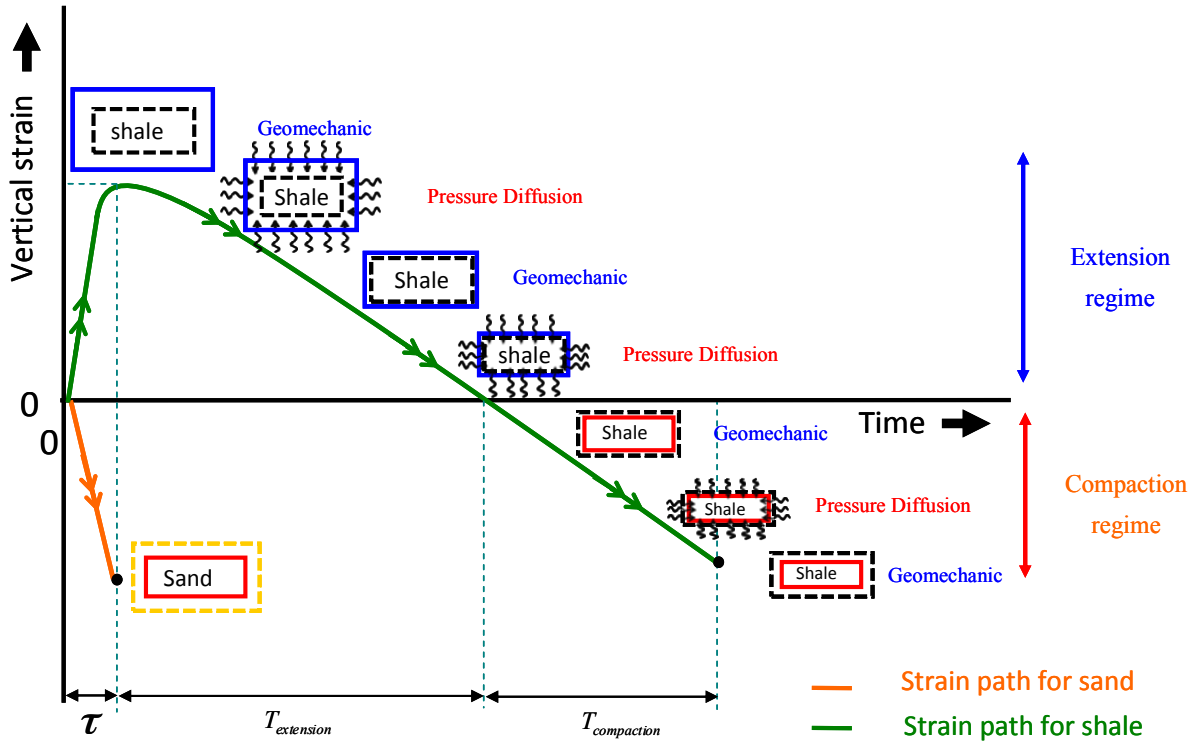

Figure 4.10: Strain paths for the shales and sand in an instantaneously depleted sand body. The shales slowly evolve to a strain condition similar to the compaction in the sands, crossing over between an extensional and compactional regime.

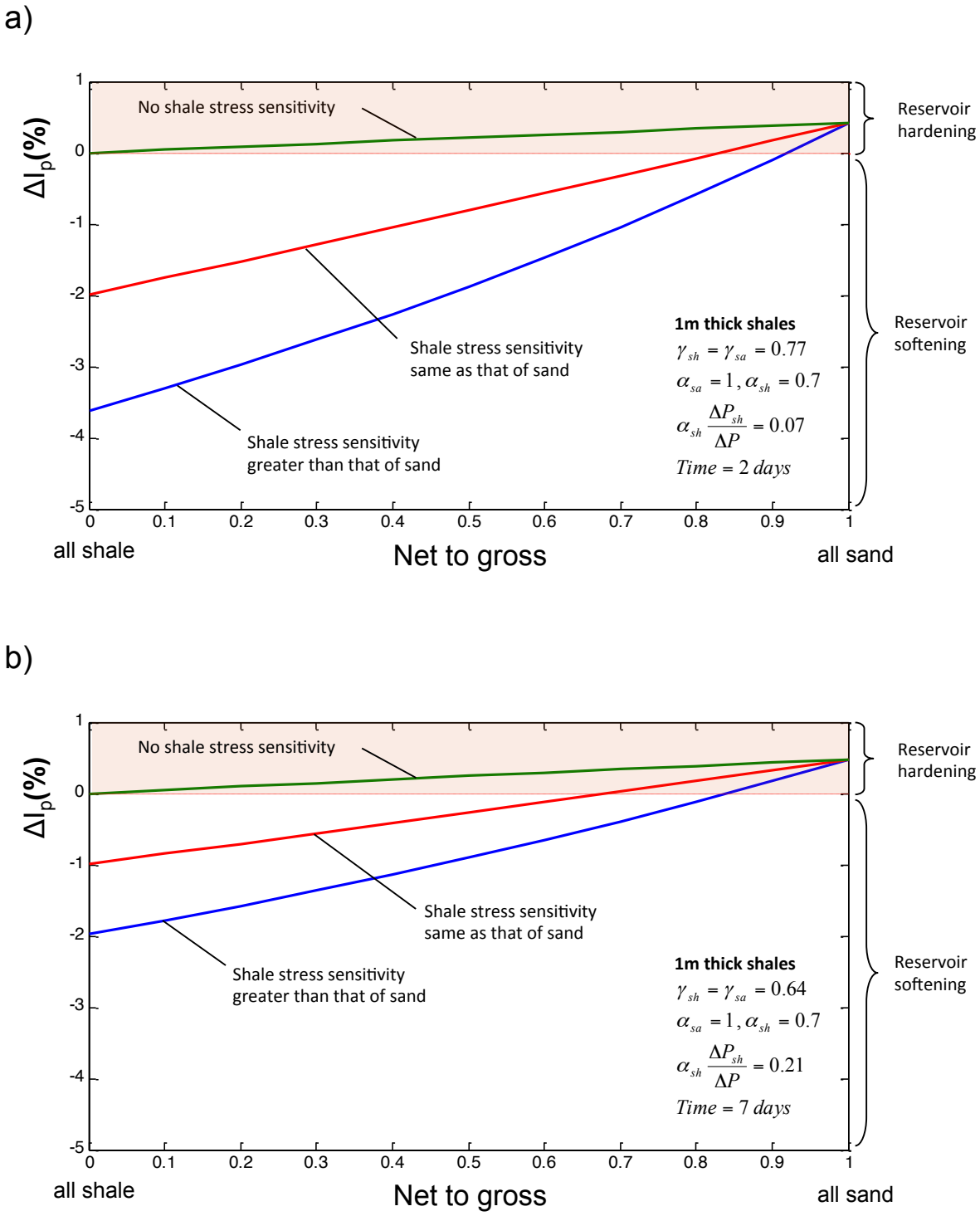

Figure 4.11: Time-lapsed change in impedance for a reservoir composed of sands and shales distributed with a varying net-to-gross. As in Figure 4.5, the stress sensitivity of the shale properties is chosen to be twice as great as the sand, the same and then stress insensitive. Results are for shales of thickness 1m and permeability 1nD. Results are after an elapsed time of: a) two days and 10% depletion and b) seven days and 30% depletion.

4.6 Conclusions

Sub-seismic, intra-reservoir shales of 1 to 10m thick strongly affect the time-lapse seismic response of a reservoir. Coupled pressure diffusion and geomechanical effects acting on these shales have an influence on the apparent in situ stress sensitivity of the reservoir, and act to reduce the sensitivity from that expected by applying laboratory measurements carried out on predominantly sandstone core plugs. This effect adds to the list of factors contributing to a modification of the stress sensitivity when applied to the in situ reservoir state. Under certain conditions (low net-to-gross, frequently repeated seismic, thick shales and low shale permeability) the reduction in stress sensitivity anticipated from my modelling may in fact reverse the polarity of the usually expected response, causing an apparent softening instead of hardening of the reservoir impedance with depletion. It is shown, for example, that seismic surveys repeated over 5 to 10 years are likely to be influenced by 5 to 10m thick shales such as those found in low energy depositional systems, whilst thinner shales will not present a problem for these surveys as they will pressure equilibrate over that time period. However frequent seismic monitoring on a 3 monthly basis will be strongly influenced by sub-seismic shales over the entire thickness range of 1 to 10m, and this is likely to be apparent for a wide range of depositional environments.

The results of this work are strongly controlled by the mechanical, transport and elastic properties of the shales. Such properties are notoriously difficult to assign due to a generally insufficient knowledge and sampling of these rocks. Additionally, such sub-seismic intra-reservoir shales may be difficult to precisely identify within the inter-well volume, particularly if they are truly ‘stochastic’ in nature. Thus the results must currently carry an uncertainty which cannot be adequately calibrated in practice – this is why I have considered in this paper simplified geology models, but with realistic rock properties and the correct physical mechanisms. By contrast, the contribution from shales with more correlation and continuity between wells is easier to analyse. Some control over the expected reduction in stress sensitivity can be obtained from geological interpretation of outcrops, log and core data together with geomechanical and elastic wave stress sensitivity property measurements. Detailed facies analysis from 3D geological models could also help to calibrate the predictions made in this study, by constraining the shale size distributions and helping modelling studies to estimate the arching factors and pressure equilibration effects. The

results of this work strongly indicate that meso-scale geology is essential to adequately assign elastic wave stress sensitivity to the reservoir.

Industry is currently doing very little about shales. Treated as barriers to flow, they are generally assumed to have zero permeability for the purpose of predicting flow rate at wells and fluid flow in the reservoir. However, is it adequate to represent shales simply as barriers in fluid flow calculations or should they be assigned their own distinct permeability, capillary pressure and mechanical properties? Shale mechanical properties are particularly important for drilling, but their ability to alter the seismic scale response also needs to be addressed and may in turn feed back into monitoring the drilling programme. This work suggests that this should be recognised as more common practice. For this to occur, an accurate assignment of reservoir shale properties is a topic that requires much more future attention.

CHAPTER

FIVE

5 Validation of predictions using coupled geomechanics and pressure diffusion simulation

In this chapter a fully coupled geomechanics and fluid flow simulation is performed in order to validate the predictions presented in the previous chapters. First, a theoretical background of the coupled fluid flow and geomechanical simulation is illustrated. Next the workflow that integrates these coupled mechanisms into the forward modelling of time lapse seismic is presented. Finally the integrated workflow of seismic forward modelling is applied to a synthetic case and then to the full field simulation model from the Schiehallion field in the North Sea.

5.1 Introduction

Time-lapse changes in seismic data are commonly evaluated in term of changes of pressure saturation inside the reservoir. However, several studies by Hatchell (2005), Tura et al. (2005), and Sayers (2010) showed that the pressure changes induced by production can trigger significant stress changes within the reservoir and the surrounding rocks. In order to interpret time lapse seismic more accurately, a quantitative understanding of the variation in the elastic properties of the reservoir and the non-reservoir surrounding rock is necessary. Fluid pressure changes induced by the production of hydrocarbons can lead to changes in the effective stresses inside and around a reservoir. At present the exact magnitude of the in-situ stress sensitivity is still largely uncertain, and cannot be relied upon (Eiken and Tøndel 2005). Ambiguity is also reported in some seismic datasets such as those of Fletcher (2004), who revealed an unexpected difference in the sign of time shifts associated with depletion. A potential reason for such seismic observations is offered by a number of well-documented factors that may act to reduce or enhance the stress sensitivity (Nunez and MacBeth 2006). It has been shown by HajNasser and MacBeth (2010) that the existence of sub-seismic intra-reservoir shales could have a significant impact on the overall reservoir stress sensitivity, and therefore could well be a major factor contributing to uncertainty in the pressure related component of the 4D seismic response.

Often in geomechanics the overburden, sideburden and intra-reservoir shales are typically treated as passive components, which are placed under extension in response to compaction in the reservoir sands (Sayers and Schutjens 2007). However shales have a non-negligible permeability and moderate porosity (Neuzil 1994, Yang and Aplin 2007), and whilst the low permeability values prevent large-scale bulk fluid exchange with the reservoir sandstones, shales do still pressure equilibrate with the adjacent depleting rock mass by the process of pressure diffusion. Here I extend and refine the prediction of my previous work by considering the seismic response associated with the combined effects of geomechanics and pressure diffusion on the intra-reservoir and the non-reservoir shales. In order to account for changes occurring within and around the reservoir, an integrated workflow that combines the results of reservoir simulation and geomechanical modelling is used to update the elastic properties. The fluid flow simulation is performed using a three-phase black oil simulator, and the contribution of rock deformation to fluid flow is calculated using a coupled flow and geomechanical simulator. The resulting stress fluid flow changes are then converted into the

corresponding seismic response. In this chapter, first the theoretical background of the coupled fluid flow and geomechanical simulation is presented. Next the implementation of these coupled mechanisms to forward modelling of time lapse seismic is considered for a synthetic case and then a full field simulation model of the Schiehallion field from the North Sea.

5.2 Theory of coupled geomechanics and pressure diffusion simulation

Recently, considerable interest has been generated in the area of the coupled fluid flow and geomechanical simulation. This growing interest has initiated several studies on mathematical theory and the numerical methods used to predict the coupled effects. In this section the governing equations of fluid flow for a black-oil reservoir model is presented. The simulation of reservoir behaviour is based on mass conservation of fluids and material. Based on the conservation of mass for the fluid water, oil, and gas phases and Darcy's law, the following equations describe the equations of the fluid flow simulation (Thomas et al., 2003).

$$\nabla\left[\lambda_w\left(\nabla p_w - \gamma_w \nabla z\right)\right] = \frac{\partial}{\partial t}\frac{\phi S_w}{B_w} + q_w \tag{5.1}$$

$$\nabla\left[\lambda_o\left(\nabla p_o - \gamma_o \nabla z\right) + r_s\lambda_g\left(\nabla p_g - \gamma_g \nabla z\right)\right] = \frac{\partial}{\partial t}\left[\frac{\phi S_o}{B_o} + \frac{r_s S_g}{B_g}\right] + q_o + q_g r_s \tag{5.2}$$

$$\nabla\left[\lambda_g\left(\nabla p_g - \gamma_g \nabla z\right) + R_s\lambda_o\left(\nabla p_o - \gamma_o \nabla z\right)\right] = \frac{\partial}{\partial t}\left[\phi\left(\frac{S_g}{B_g}\right) + \frac{R_s S_o}{B_o}\right] + q_g + q_o R_s \tag{5.3}$$

Additional equations include the constraining equations for the sum of saturation and capillary functions:

$$S_w + S_o + S_g = 1 \tag{5.4}$$

$$P_{cwo} = f\left(S_w\right) \tag{5.5}$$

$$P_{cgo} = f\left(S_g\right) \tag{5.6}$$

The differential equations above are normally discretised using the finite difference methods. The governing equations for the geomechanical model are derived from the balance of linear momentum and the effective stress law (Terzaghi, 1943). The equations are stated as follow:

$$\nabla\left(\sigma^{eff} - \delta p\right) + f = 0 \tag{5.7}$$

where f is the body force per unit volume.

$$\sigma^{eff} = g(\varepsilon, K) \tag{5.8}$$

ε is the strain; K denotes a set of history-dependent tensorial quantities. Also

$$\varepsilon_{kk} = \nabla u_{kk} \tag{5.9}$$

where ∇u_{kk} is the symmetric part of the displacement gradient, u , is the displacement vector.

The 3D finite-element-based geomechanics simulator contains numerous stress models (for example elastic, plastic, elasto-visco-plastic) used to simultaneously solve Equations 5.7, 5.8, and 5.9, along with the appropriate boundary conditions. The displacement vector u at the corner points of each element is calculated for each iteration of the coupled analysis as well as the effective stress tensor σ^{eff} and the strain tensor ε of each element (gridblock). The volumetric strain ε_v is calculated from the normal components of the strain tensor of each element:

$$\varepsilon_v = \varepsilon_{xx} + \varepsilon_{yy} + \varepsilon_{zz} \tag{5.10}$$

The approach used for solving two sets of equations; mechanical equilibrium and the fluid flow problem, is based on using two conventional reservoir and geomechanical simulators, each simulator solves its own system. Information is passed in both directions between the simulators (Settari and Mourits, 1998; Settari and Walters, 1999). In this method fluid flow and formation deformation (geomechanics) are coupled in a sequential manner, that is, the two calculations are done alternately, while passing information back and forth. Within a given time step and for each coupled iteration, pressure and water saturation values obtained from the reservoir simulation – (via Eclipse 100 (TM Schlumberger)) - are directly passed to the geomechanical simulation – (via Visage (TM Schlumberger)) - The geomechanics simulation updates the formation deformation in response to the new pressure changes. To

complete the loop, the geomechanics module sends the new deformation information back to the fluid flow calculation to be used in the next time-step. Depending upon the total strain tensor calculated, the porosity of each element can increase, remain unchanged, or decrease. The geomechanical deformation response is expressed in the fluid flow calculation by changing the porosity according the volumetric strain changes. Based on the mass conservation for the rock, the updated porosity after the geomechanical deformation is given by the following equation:

$$\phi = 1 - \left(1 - \phi_0\right) e^{-\varepsilon_v} \tag{5.11}$$

where ϕ_0 is the initial porosity.

Here the porosity of each element (gridblock) is calculated at the end of each iteration and passed back to the reservoir simulation. For the purpose of this thesis, the reservoir and non-reservoir (overburden, underburden, and sideburden) shales are made active for the fluid flow simulation and the mechanical deformation. Therefore the fluid flow property update will take into account the reservoir shale as well as the surrounding shales.

5.3 Implementation of coupled geomechanics and fluid flow simulation into the seismic forward modelling

As previously mentioned, the objective of implementing the coupled geomechanics and fluid flow simulation, is to be able to include the pressure, saturation and effective stress changes of the reservoir and the surrounding rock into the seismic modelling. In this workflow, the reservoir and non-reservoir shales are active and their dynamic behaviour in terms of pressure and stress is examined. The seismic modelling fundamentally relies on being able to incorporate reservoir fluid flow and stress changes into elastic wave propagation. Here, the stress sensitivities of the elastic moduli of the sands and shales are defined by the non-linear functions given by Macbeth (2004). The model is implemented to compute the effective bulk, shear moduli, and density for dry rock as function of effective stress. For a given time step the elastic modulus for dry rock is calculated using the effective stress resulting from the simulation. The equations used to calculate the elastic moduli for dry rock are:

$$\kappa_{dry}\left(\sigma^{eff}\right) = \frac{\kappa_{\infty}}{1 + E_{\kappa} e^{-\sigma^{eff}/P_{\kappa}}} \tag{5.12}$$

$$\mu_{dry}\left(\sigma^{eff}\right) = \frac{\mu_{\infty}}{1 + E_{\mu} e^{-\sigma^{eff}/P_{\mu}}} \tag{5.13}$$

$$\rho_{dry}\left(\sigma^{eff}\right) = \rho_{\infty} + \left(\rho_0 - \rho_{\infty}\right) e^{-\sigma^{eff}/P_{\rho}} \tag{5.14}$$

where $\sigma^{eff} = \frac{\sigma_{xx}^{eff} + \sigma_{yy}^{eff} + \sigma_{zz}^{eff}}{3}$ is the mean effective stress.

κ_{∞}, μ_{∞}, ρ_{∞}, E_{κ}, E_{μ}, p_{κ}, p_{μ}, and p_{ρ} are determined from laboratory measurements for core plugs (MacBeth 2004) or by history matching (Stephen and MacBeth 2006b) and represent the dry bulk modulus at standard temperature and pressure, the excess compliance present in the rock as a result of geological or mechanical processes, and stress sensitivity. κ_{∞}, μ_{∞}, and ρ_{∞} are high pressure asymptotes of the behaviour, E_{κ} and E_{μ} control the magnitude of the effect, and P_{κ} and P_{μ} control the onset of the low pressure non-linear behavior.

However, to account for the fluid effect, Gassmann's (1951) fluid substitution equations are used. These equations provide a way to compute the effective bulk and shear moduli, (κ and μ respectively) of reservoir rock saturated with a given composition of pore fluids. These equations are

$$\mu_{sat} = \mu_{dry} \tag{5.15}$$

$$\frac{\kappa_{sat}}{\kappa_{solid} - \kappa_{sat}} = \frac{\kappa_{dry}}{\kappa_{solid} - \kappa_{dry}} + \frac{\kappa_{fluid}}{\phi\left(\kappa_{solid} - \kappa_{fluid}\right)} \tag{5.16}$$

Gassmann's equations require knowledge of the effective bulk modulus of the pore fluid κ_{fluid} the porosity ϕ, the bulk and shear moduli of the dry rock κ_{dry} and μ_{dry} and the bulk modulus of the mineral material making up the rock κ_{solid}. In a three phase system (oil, water, and gas) the total fluid bulk modulus in calculated as:

$$\frac{1}{\kappa_{fluid}} = \frac{S_w}{\kappa_w} + \frac{S_o}{\kappa_o} + \frac{S_g}{\kappa_g} \tag{5.17}$$

to calculate the total fluid density, the saturation-weighted average of the three phase densities as follows:

$$\rho_{fluid} = S_w\rho_w + S_o\rho_o + S_g\rho_g \tag{.5.18}$$

From the Gassmann's equations and relationships between elastic parameters, I can determine the density ρ, compressional wave velocity V_p, and the shear wave velocity V_s at the given fluid saturation, pressure, effective stress and porosity:

$$\rho_{sat} = (1-\phi)\rho_{solid} + \phi\rho_{fluid} \tag{5.19}$$

$$V_{p_{sat}} = \sqrt{\frac{\kappa_{sat} + \frac{4}{3}\mu_{sat}}{\rho_{sat}}} \tag{5.20}$$

$$V_{s_{sat}} = \sqrt{\frac{\mu_{sat}}{\rho_{sat}}} \tag{5.21}$$

In this workflow there are a number of places where output from coupled flow and geomechanics are used as input for Gassmann's equations will influence the results. As mentioned in the previous section, when pore pressures are used as input loads for the geomechanics calculation, new values of porosity of the reservoir and the surrounding rock resulting from stress changes in turn affect the future pressure and saturation calculations.

To evaluate the implication of the coupled mechanics of fluid flow simulation and mechanical deformation into the seismic modelling, at first, the workflow described above is applied into the forward modelling of time lapse seismic of a synthetic case and then of the full field simulation model for the Schiehallion field from the North Sea.

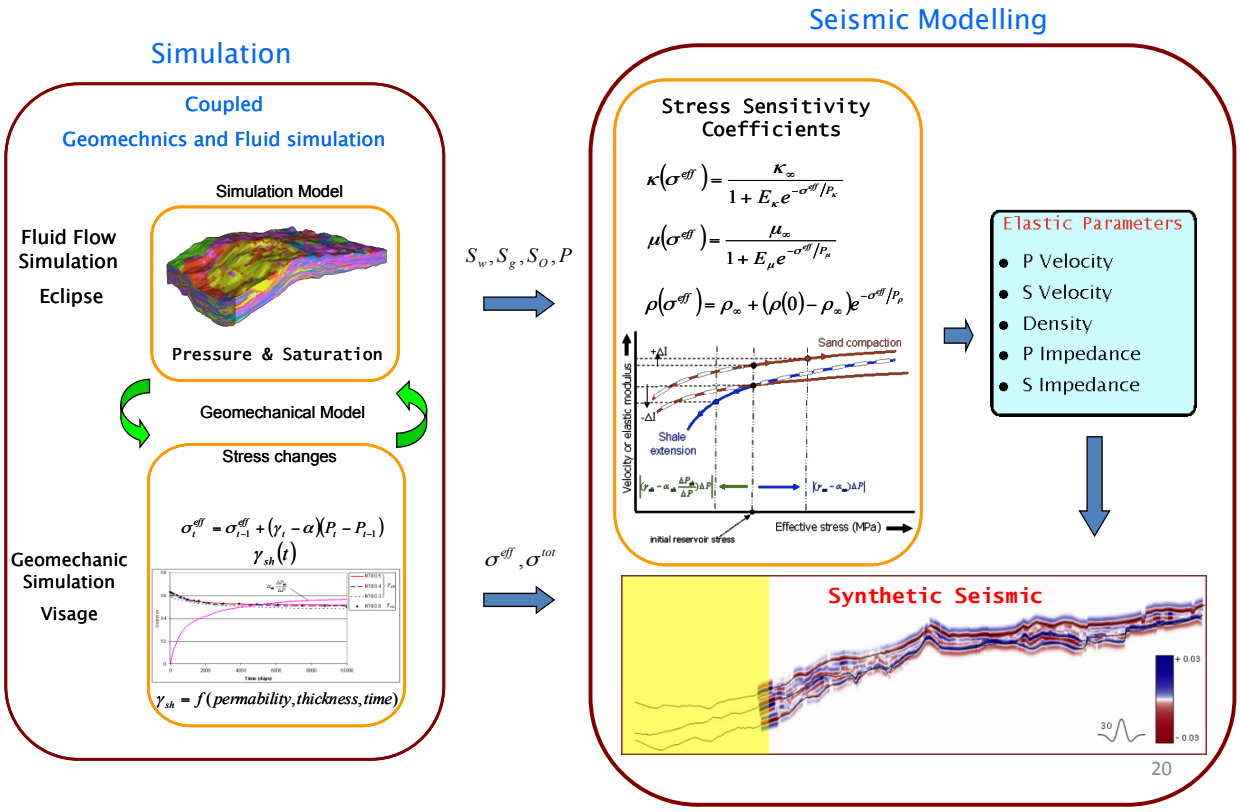

Figure 5.1: Integrated workflow of forward seismic modelling. The seismic modelling is based on the output of coupled fluid flow and geomechanical simulation. The computation of the elastic wave stress sensitivity coefficients is governed by the non-linear model derived by MacBeth (2004).

5.4 Application to a synthetic case

The aim of performing this synthetic case study is to validate the previous shale prediction using coupled geomechanics and fluid flow simulation. The first part of this case study will focus on the combined effect of geomechanics and pressure diffusion response of intra-reservoir shales and their impact on the seismic response. Furthermore, the second section of this synthetic case investigates the implications of the geomechanics and pressure diffusion response into the overburden and underburden shale for the seismic and 4D signature. To be able to account for the dynamic behavior of reservoir (intra-reservoir) and non-reservoir (overburden and underburden) shales, the shales are assumed to be active and part of the fluid flow simulation as well as the geomechanical simulation.

5.4.1 Predictions for intra-reservoir shales

Here the simulation model is populated with sand bodies of different geometries and aspect ratios, chosen for a variety of intra-reservoir shale thicknesses and distributions. In order to perform a study, object-based stochastic modelling was performed in order to populate a geological model for a fluvial depositional environment. An important part of any object-based modelling is the geometric form and parameters used to represent each facies unit (Deutsch and Wang, 1996). The ranges of parameters used in the stochastic modelling are from the work published by Deutsch (2002). Two wells data of the Wytch Farm field in the North Sea are used here to condition the modelling.

For this case study the fluid flow and mechanical properties of intra-reservoir shales are populated based on the extensive literature reviews presented in Chapter 2. The permeability and the porosity assigned to the intra-reservoir shales are in the range of 100μD to 1nD and 3.6% to 13.7% respectively. In term of geomechanical properties, values in range of 2 to 10 GPa are assigned to the Young's modulus of the reservoir shales. In addition, the Poison's ratio assigned to the intra-reservoir shales varies between 0.2 and 0.4. These properties are then stochastically assigned to the intra-reservoir shales. Here the intra-reservoir shales are assumed to be permeable and mechanically active. The well conditions are set such that a 10MPa depletion is obtained over a period of 10 years. The resulting strain from the simulation for the case of *active* and *inactive* intra-reservoir shales is shown in Figure 5.2.

This figure shows strain logs across a sequence of sands and shales after 6 years and 10 years of production and a pressure depletion of 10MPa.

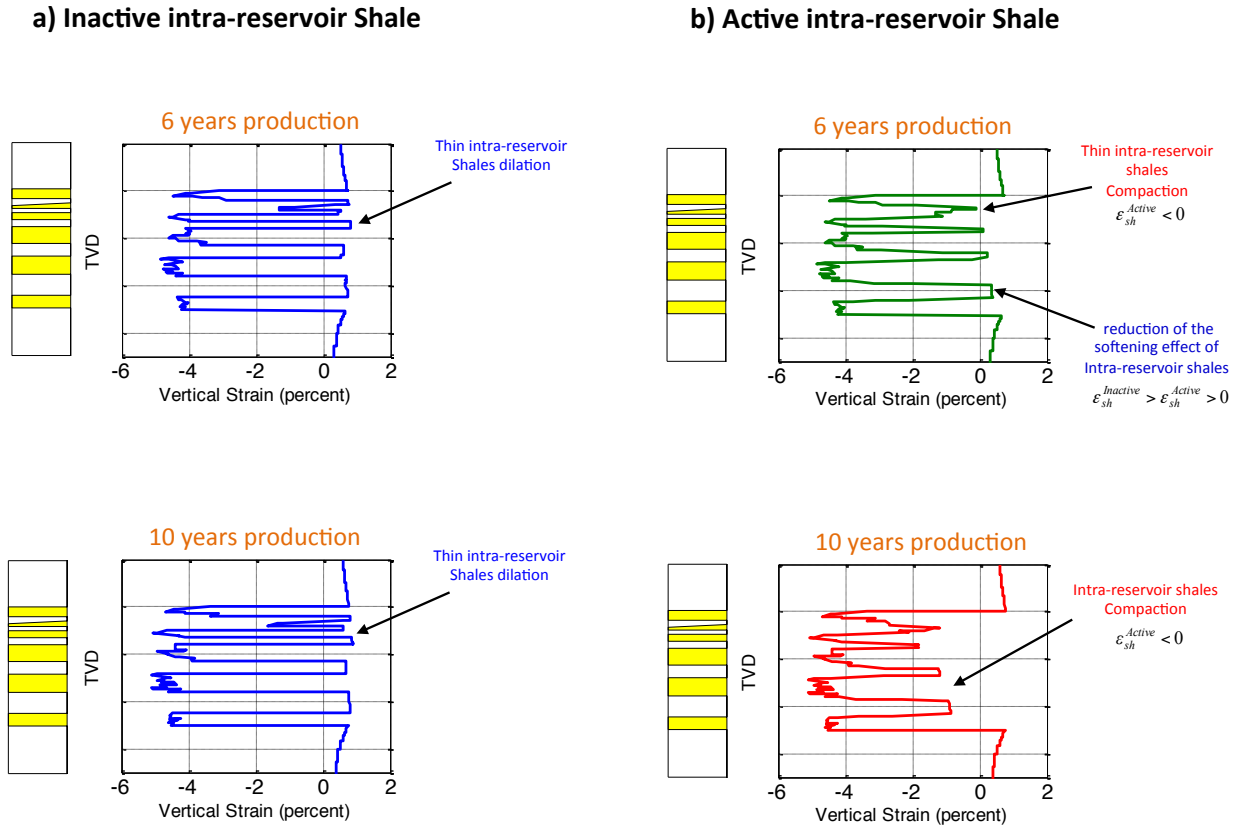

Figure 5.2: Vertical strain across a sequence of sand (yellow) and shale (white) at one of the wells as function of depth using coupled numerical calculation of pressure diffusion and geomechanics response. Comparison of vertical strain between (a) inactive intra-reservoir shales and (b) active intra-reservoir shales. Active (permeable) intra-reservoir shales show compressive strains (negative strain) in response to the pressure diffusion.

Following Hettema et al. (2000) and Sayers (2010), reduction in fluid pressure leads to a total stress change of $\gamma_{sa}\Delta P$. In turn, this increases the effective stress acting on the sandstone rock frame by an amount $(\gamma_{sa} - \alpha_{sa})\Delta P$, where $\gamma_{sa} < \alpha_{sa}$, and hence the sand will compact due to pressure depletion. As a reference case, the shale is assumed to be impermeable (inactive). Under these assumptions it cannot respond to the pressure depletion. Thus, in similar way to the more widely recognized shale overburden deformation in response to reservoir compaction (Hodgson et al. 2007), intra-reservoir shale undergoes mechanical extension Figure 5.2(a). These results are in agreement with those published by Sayers and Schutjens 2007. When the shale is assumed to be active in term of pressure diffusion, they undergo an increase of effective stress and hence experience compaction Figure 5.2(b). These results are in agreement with those from HajNasser and MacBeth (2011). The modelling study concludes that the combined effect of pressure diffusion and geomechanics is to equilibrate pressure between the sands and the shales. Whilst the sand continues to compact, the shales experience extension at first, but as time progresses they reverse their geomechanical behaviour and start to compact in response to the increasing effective stress. In practice, this process is a continuous accommodation of the geomechanical effects by the progression of pressure diffusion such that the strain field in the shale is reversed towards compaction. In Figure 5.2(b) intra-reservoir shales mainly show compaction (negative vertical strain).

To evaluate the seismic scale consequence of the above phenomena on the overall seismic response of the reservoir, the changes in P-wave impedance $(\Delta \mathrm{I}_p)$ for the mixture of sand and permeable shale undergoing stress changes are calculated. For this, the workflow of the seismic modelling presented in Section 5.3, is implemented to calculate the P-wave impedance changes for each grid block of the reservoir. As only the vertical P-wave velocity is considered, a thickness weighted harmonic averaging is used to calculate the overall vertical impedance changes for the reservoir interval. For this particular calculation the stress sensitivity of the shale is assumed to be higher than that in the sand. The results of P-wave impedance changes for three time steps; 30, 360, and 2000 days are shown in Figure 5.3. The general conclusions of the coupled modelling are roughly identical to those from HajNasser and MacBeth (2011). For a monitor time period of few months, a reservoir with shales of a few metres thick might exhibit an anomalous softening response, but this may only be possible for a monitor period of 10 years if thicker 5 to 10m shales (or low NTG ratio) are present. Here only the intra-reservoir shales are used, however the overburden and

underburden shale effect are excluded. The next section will focus on non-reservoir shales (overburden and under burden shales) and their impact on the 4D seismic signature.

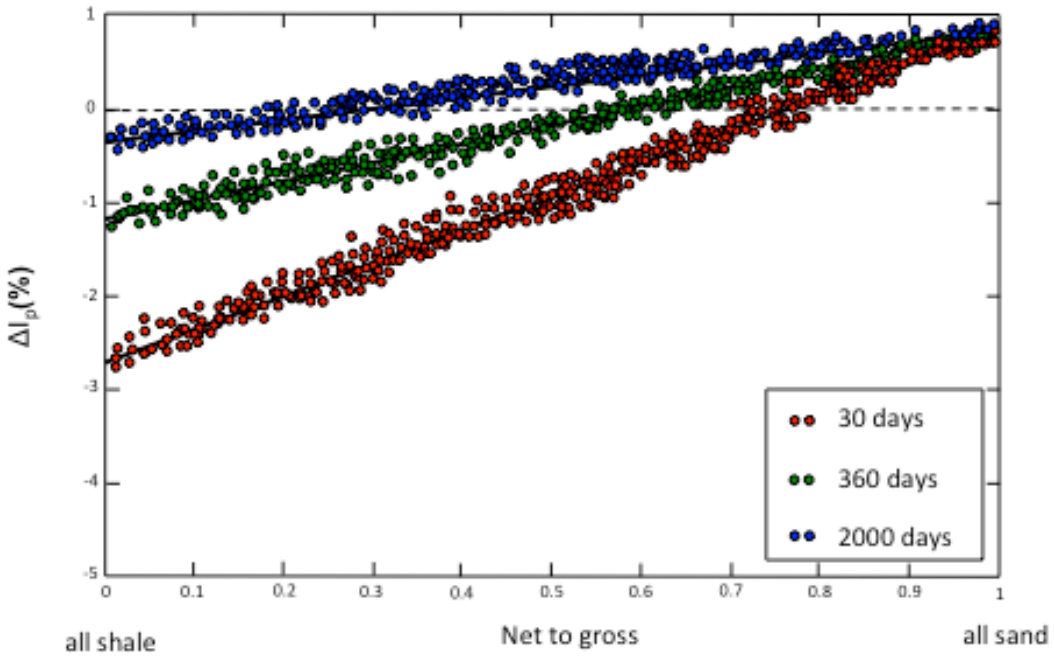

Figure 5.3: Calculated percentage changes in P-wave impedance $\left(\Delta \mathrm{I}_p\right)$ for a reservoir comprising of a mixture of sand and active (permeable) intra-reservoir shales undergoing the combined effects of geomechanics and pressure diffusion. These results correspond to three time steps; 30, 360, and 2000 days.

5.4.2 Predictions for overburden/underburden shales

Whilst it is well known that the effects of reservoir depletion and subsequent compaction lead to a strain in the overburden and underburden (for example, Hodgson et al. 2007), pressure diffusion into this region is less well documented in the geophysical literature (see for example Barkved and Kristiansen 2005). The diffusion rate is controlled by identical factors to the intra-reservoir shale problem, and although the governing equations are different, the time scales for this process are similar (Crank 1975). The combined effect of geomechanics and diffusion is investigated by performing a coupled simulation with active non-reservoir shales and a high permeability (350mD) homogeneous reservoir. The well conditions are set such that a 10MPa depletion is obtained over a period of 10 years. The workflow of Section 5.3 is used to calculate the time lapse seismic response associated with non-reservoir shales.
For this study, non-reservoir shale are considered permeable and mechanically active. The permeabilities of 1nD, 100nD, 1μD, and 100μD are simulated. The resultant effective stress profiles are shown in Figure 5.4(a) and the corresponding P-wave vertical velocity changes profiles after 10 years of production in Figure 5.4(b). As one might expect, shales with a higher permeability give a larger surrounding volume experiencing positive effective stress changes (and hence compaction). The shale diffusion process appears to smooth out the sharp geomechanical effects over a significant zone around the reservoir.

Furthermore, the effective stress output from the coupled simulation is converted firstly to strain, then time strain by assuming an R factor (Hatchell and Bourne 2005) of 1.2 for the reservoir compaction and 6 for the shale extension. By integration, this provides a time shift distribution (and hence velocity change) both inside and around the reservoir. Although the strain in the overburden is small, it occurs over a large volume of the overburden and the cumulative effects lead to detectable time shifts. Figure 5.5 shows that this translates to a modification of the classic time-delay profile for shale extension alone, and this could be perceived as an effective thickening of the reservoir. Furthermore, there is a significant reversal of the measured time-shift from a slow down above the reservoir to a speed up beneath the reservoir. If no diffusion occurs, then the speed up below is reversed to a slow down. For example, for this particular model and a shale permeability of 1μD, the cumulative time shift below base-reservoir can be as much as 2ms compared to +1ms for the case of impermeable shale with less than 1nD permeability.. This suggests careful quantitative evaluation of the pressure equilibration of non-reservoir shales is required.

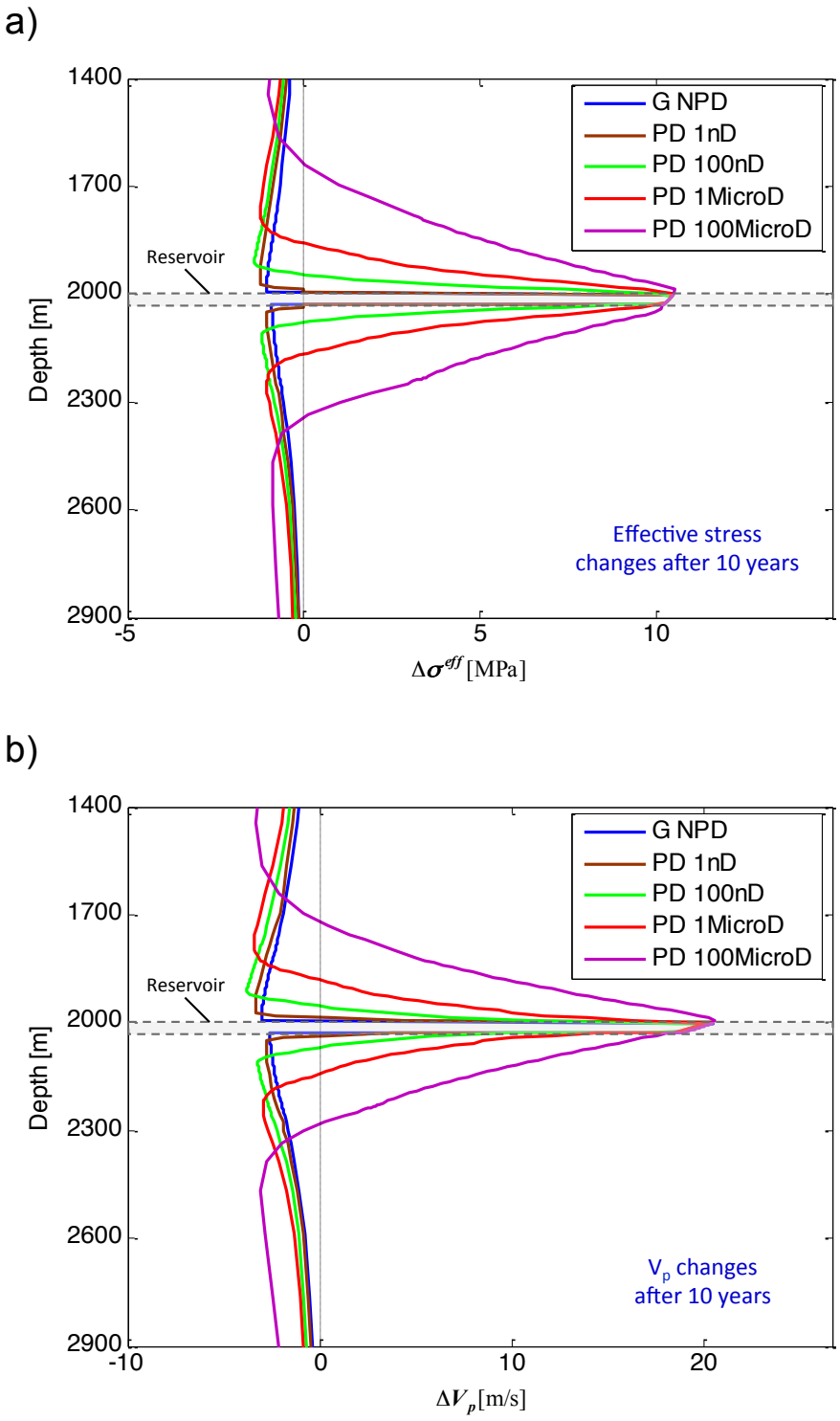

Figure 5.4: Variation of the vertical (a) effective stress (b) P-wave velocity within the reservoir and the surrounding shales after ten years of production. Cases are for: impermeable shales (blue curve), shale permeabilities of 100nD (green curve), 1mD (red curve), and 100 mD (magenta curve).

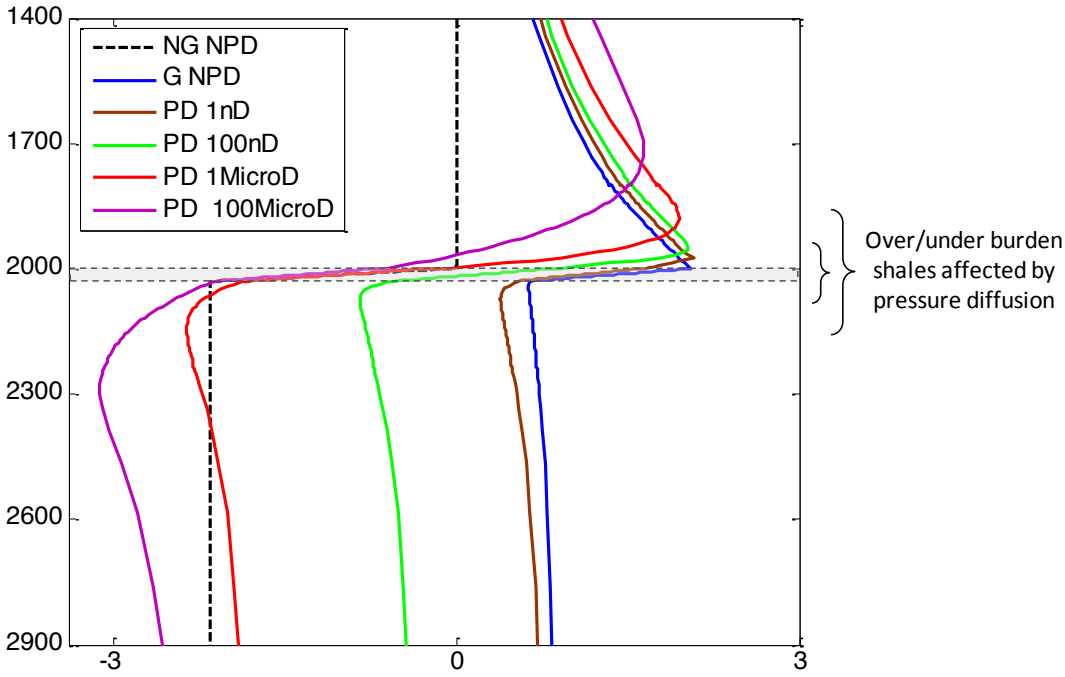

Figure 5.5: Computed time shift profiles after ten years production for: impermeable and mechanically inactive non-reservoir shales (dashed line); impermeable and mechanically active non-reservoir shales (blue curve); non-reservoir shale permeability of 100nD (green curve); 1mD (red curve), 100mD (magenta curve)(HajNasser et al. 2011).

5.5 Field case application: Schiehallion field

To evaluate these effects more fully in relation to the seismic response, fully coupled fluid flow and geomechanical simulation is performed again. Here, a sector of the Schiehallion field is considered.

5.5.1 Reservoir geological background

The Schiehallion field is situated on the Atlantic margin of the UK Continental Shelf (UKCS), about 200 km to the west of Shetland, and holds most of the hydrocarbon reserves in the area. The Schiehallion reservoir sands lie at a depth of 1800–2064m (~1800–2000ms TWT). Based on the seismic interpretation and attribute mapping, the Schiehallion field is deposited in deep-water fan complex composed of highly channelized and amalgamated units (see Figure 5.7(a)). Reservoir quality varies in character from thinly interbedded sand and shale to massive sand (Lancaster and Whitcombe, 2000). Figure 5.7(b) shows Gamma-ray (GR) log response and facies interpretation at one of the wells in the Schiehallion field (Amini, 2011). The sequence of interbedded sands and shales observed in the well logs have made the Shiehallion field to be a favourable geological setting to investigate the 4D implication of the shales.

5.5.2 Seismic data and area of interest

Several seismic surveys have been acquired over Schiehallion. Two pre-production seismic surveys were acquired in 1993 and in 1996. The 1996 pre-production survey is used as base line for the 4D surveys (Altan et al. 2001). Following feasibility studies of time lapse seismic, the 4D surveys were shot at time intervals of 1 to 2 years. For this particular field, the acquisition parameters of 1996 baseline survey are repeated in 2002, 2004 surveys. In this work, in order to maintain a good repetability and a low NRMS of 4D seismic data, the baseline 1996 seismic survey and the monitor 2002 seismic survey are used for the 4D seismic analysis. The Schiehallion field is a large hydrocarbon accumulation (approximately 10 ×12km) and structurally divided into several isolated segments by major faults. In terms of 4D, there are many remarkable 4D anomalies on the difference maps of the seismic attributes. In order to carry out detailed studies, this chapter focused on segment 1 and segment 4. These

two segments are believed to be isolated (Floricich, 2006). Figure 5.8 shows the areas of interest for this study. Because of the good quality of the simulation model in segment 1, the main 4D seismic modelling and analysis in this work will focus on segement 1.

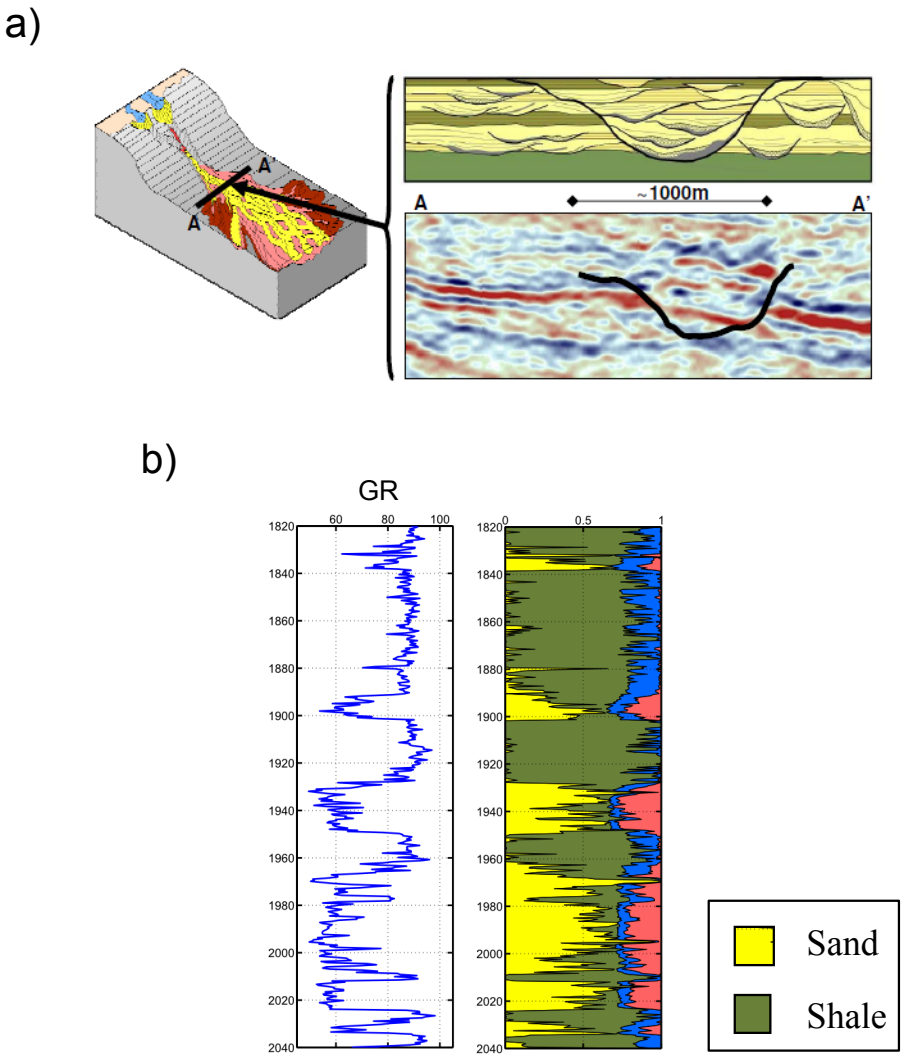

Figure 5.6: The geological background of the Schiehallion, (a) Geological model of the Schiehallion field: the cross-section *A-A'* shows the amalgamated sands of the deep water channelized complex, (Karen Martin and Chris Macdonald, 2010) (b) well log at one of the wells showing the interbedded sand and shales with the reservoir interval (Amini 2011).

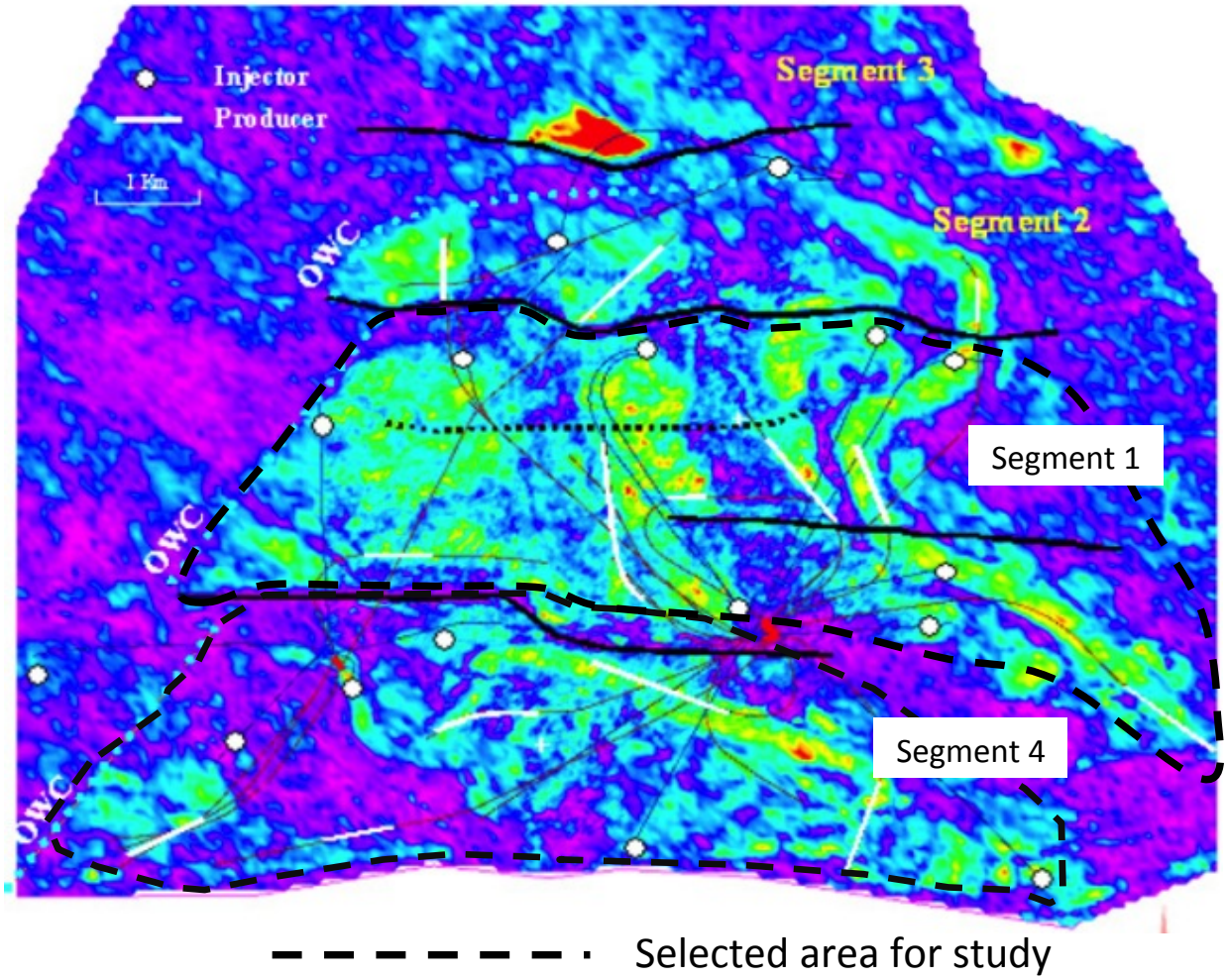

Figure 5.7: RMS average amplitudes generated from the 1996 baseline survey. The selected areas of study are outlined by black dashed line. The highlighted segments 1 and 4 are believed to be completely or nearly closed (Floricich, 2006).

5.5.3 Shale activation

In order to be able to investigate the dynamic behavior of shales in term of pressure and stress changes, all the intra-reservoir shales as well as the non-reservoir shales have to be permeable and mechanically active. This procedure will allow both the intra-reservoir and non-reservoir shales to be part of the coupled fluid flow and geomechanical simulation. In this simulation model, all inactive shale cells are converted to being active and assigned a permeability of 1nD. In addition, non-reservoir (shale) cells of 1nD are included in the overburden, underburden and sideburden of the model for simulation purposes. These will accommodate the mechanical and diffusion effects. The chose of shale permeability was based on a personal communication with John Fletcher and Prof Patrick Corbett. This modifies the numbers of cells to be simulated from 26,612 to 109,208 in the particular model used. Well production and recovery activity induces a combination of pressure increase but also decrease. In term of geomechanical properties, values of 5 and 10GPa are assigned to the Young's modulus of the non-reservoir and reservoir shales respectively. In addition, the Poison's ratio assigned to the shales is 0.3. These geomechanical properties are taken from the database presented in Chapter 2.

5.5.4 Pressure and gas saturation changes

Using the existing well controls, the coupled fluid flow and geomechanical simulation is performed. The resulting pressure development across the field during 1996, 2000, and 2002 for both cases; active and inactive shales is shown in Figure 5.9. The coupled simulation indicates that in the early stage; from 1996 to 2000 the pressure development across the field is similar for the both cases; inactive and active shale. During this time scale, because the low permeability of the shales only the pressure changes with the highly permeable sand is observed. However as time elapses, after 4 years of production pressure diffusion becomes important in the case of active shales and consequently a different pressure profile will be observed (see Figure 5.9, and the pressure map for 2002). The time scale of these observations is in agreement with those calculated in Chapters 3 and 4. Figure 5.10 shows the pressure difference between 1996 and 2002 for the case of active and inactive shale. In the area around the water injectors I17 and I13 different polarity in response to pressure changes are observed. Here, in the case of inactive shales, the shale is acting as barriers for diffusion of the pressure build up coming for the injectors and therefore pressure depletion is recorded.

However for the case of active shale, the pressure diffusion in the shale shows pressure build up around the same area. Due to different pressure development across the field for the case of active and inactive shale, the simulated gas saturation is also different. Figure 5.11 shows the gas saturation changes for the case of active and inactive shale.

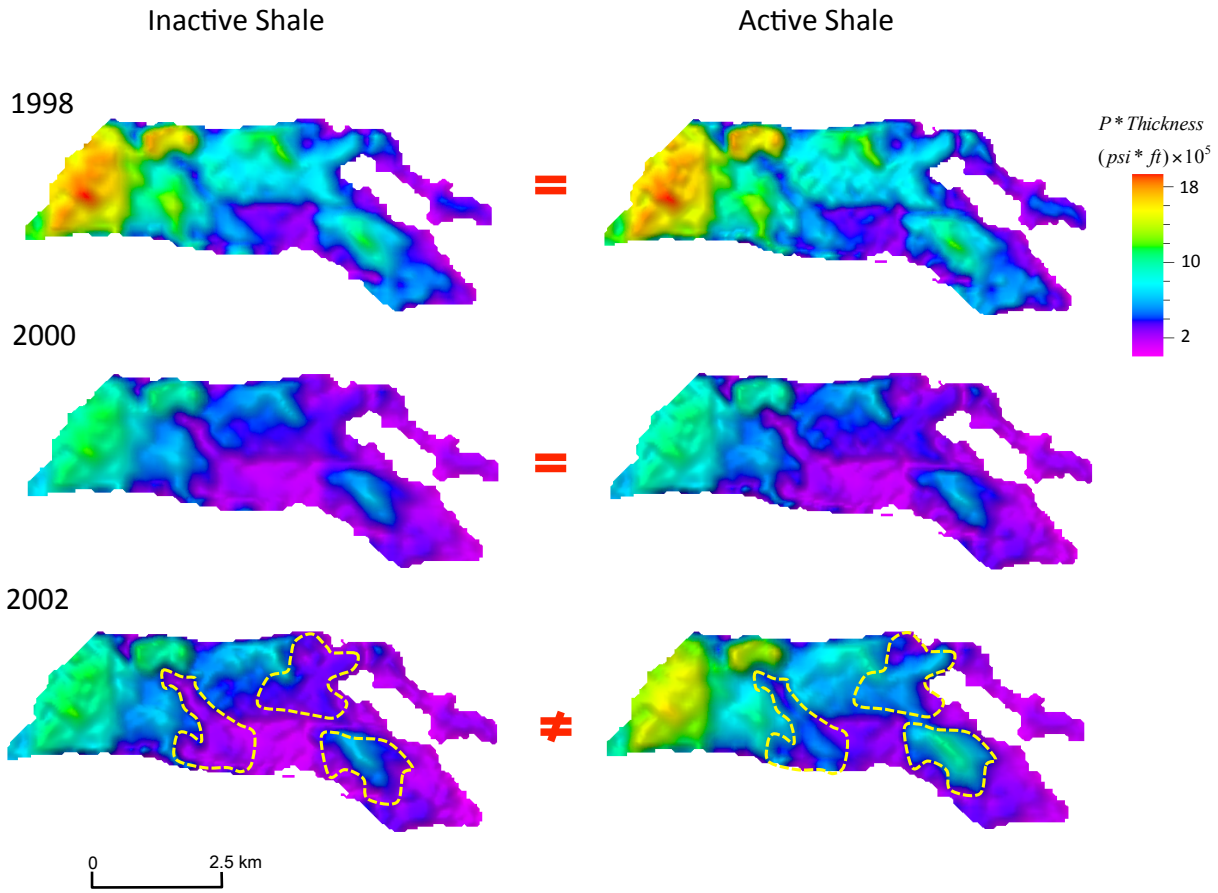

Figure 5.8: Thickness weighted pressure map across the field during 1996, 2000, and 2002 for both cases; inactive and active shale. At early stage; 1996 and 2000 the pressure profile is similar for the case of inactive and active shales. However as time elapses the pressure diffusion becomes important in the shales (active shale case) and consequently a different pressure profile will be observed. The dashed yellow lines highlight the area with a different pressure response.

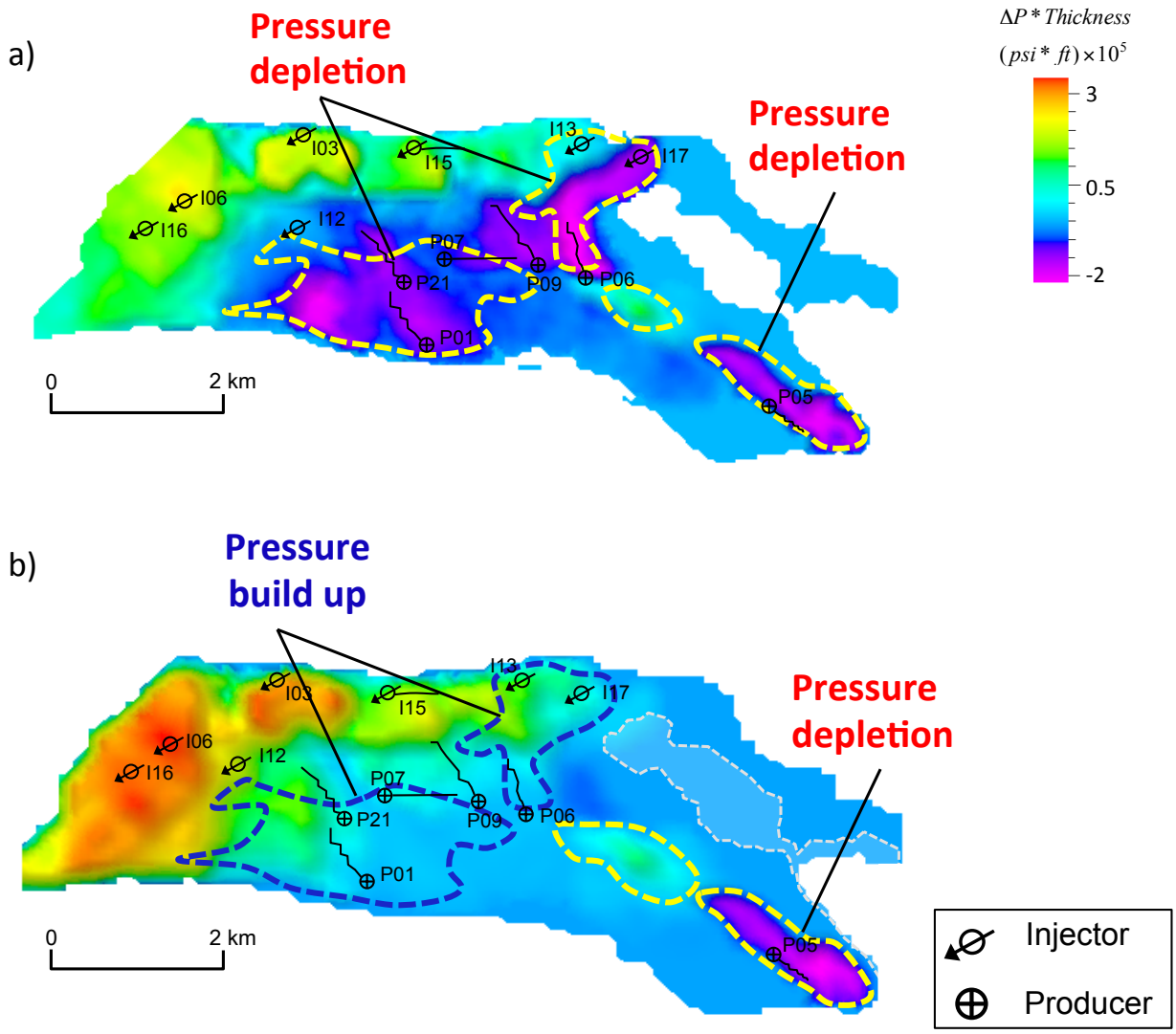

Figure 5.9: Thickness weighted pressure difference map between 1996 and 2002 for (a) inactive shale, and (b) active shales. Different polarity of pressure changes is observed in the northern area (around injectors I17 and I13) and the southwest area of the field.

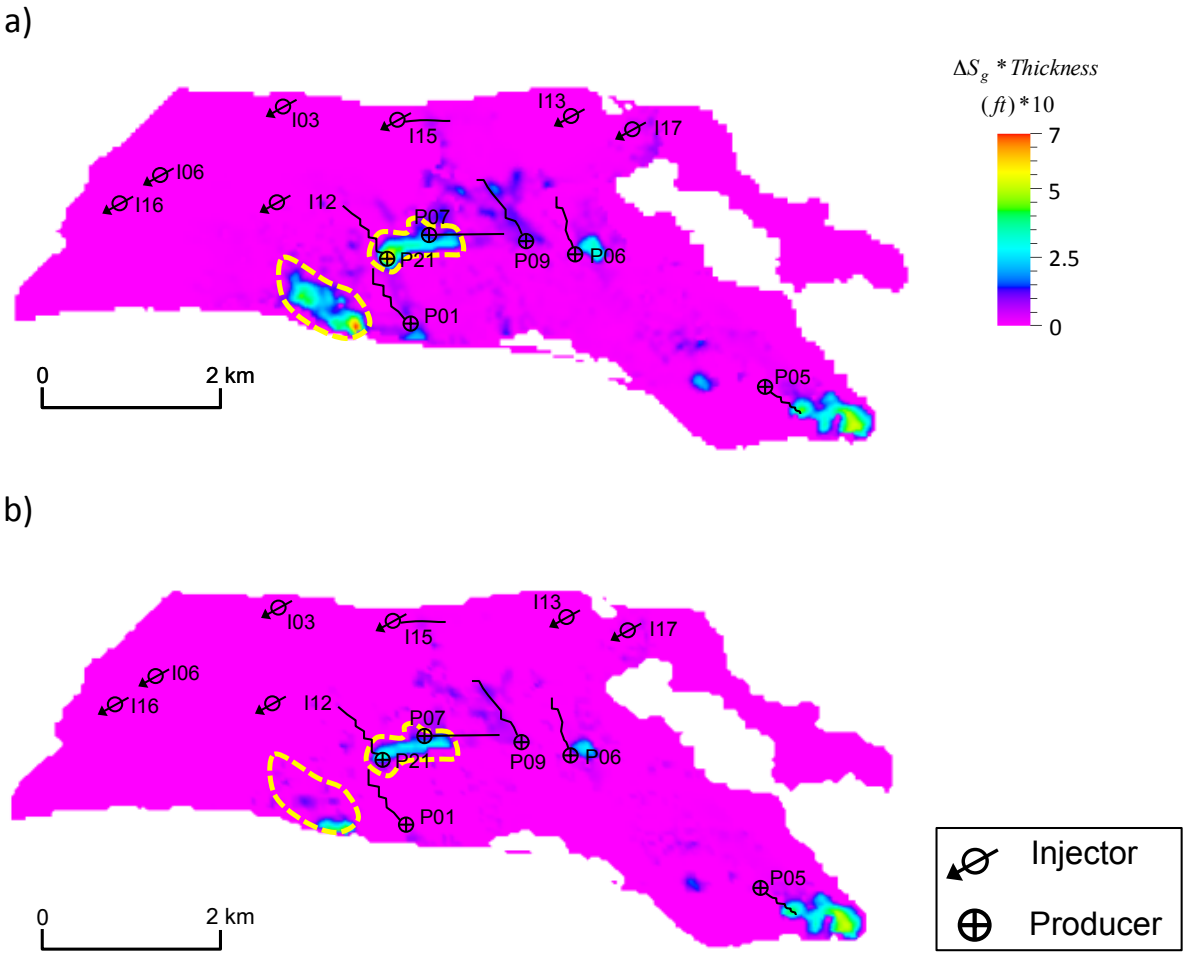

Figure 5.10: Thickness weighted gas saturated change maps between 1996 and 2002 for (a) inactive shale, and (b) active shales. Less free gas is observed for the case of active shales. Yellow dashed lines highlight the area of different gas saturation changes.

5.5.5 Seismic modelling

After simulation, the changes in effective stress and saturation are converted into V_p, V_s, and ρ changes and the corresponding time-lapse seismic is modeled using the workflow shown in Section 5.3. To be able to investigate the effect of shale, the seismic modelling for active and inactive shales are performed. Here the output of the coupled simulations is integrated into the seismic modelling in order to understand the implications of the active shale concept on the 3D seismic response. Figure 5.12 shows a vertical cross section of the synthetic seismic with and without the combined effects of pressure diffusion and geomechanics. When the shales are inactive, the modelled seismic shows abrupt discontinuous values and high intensity reflectivity along events – related to the positions of the shales. These features change as the shales become active, and it is also possible to see some evidence of a polarity shift in the seismic at specific locations. These observations suggest that active shales with finite permeability do need to be assigned to simulation models. Hence this will give more representative synthetic seismic modelling.

5.5.6 Time lapse seismic modelling

In this section, the integrated workflow of the forward seismic modelling is used to generate synthetic seismic before and after production for the case of active and inactive shale, then the resulting synthetic time lapse seismic is compared to the observed seismic. Here, the observed seismic surveys with similar acquisition parameters and good repeatability are selected. For this purpose the baseline seismic survey 1996 and the monitor survey 2002 are chosen.

Figure 5.13 shows the resulting changes in P-wave velocity for the case of inactive (Figure 5.13(a)) and active shale (Figure 5.13(b)), and the corresponding impedance changes are shown in Figure 5.14. It is clear in Figure 5.14, that the polarity of the velocity changes for the case of active shale is different from the one for the case of inactive shale. Similar observation is observed in the Acoustic impedance changes (Figure 5.14). In model with inactive shale, the synthetic seismic modelling shows a velocity increase between 2002 and 1996 in the north and southeast area. These areas are highlighted with dashed red lines in Figure 5.13(a). However, by making the shale permeable and mechanically active, a decrease of velocity is observed.

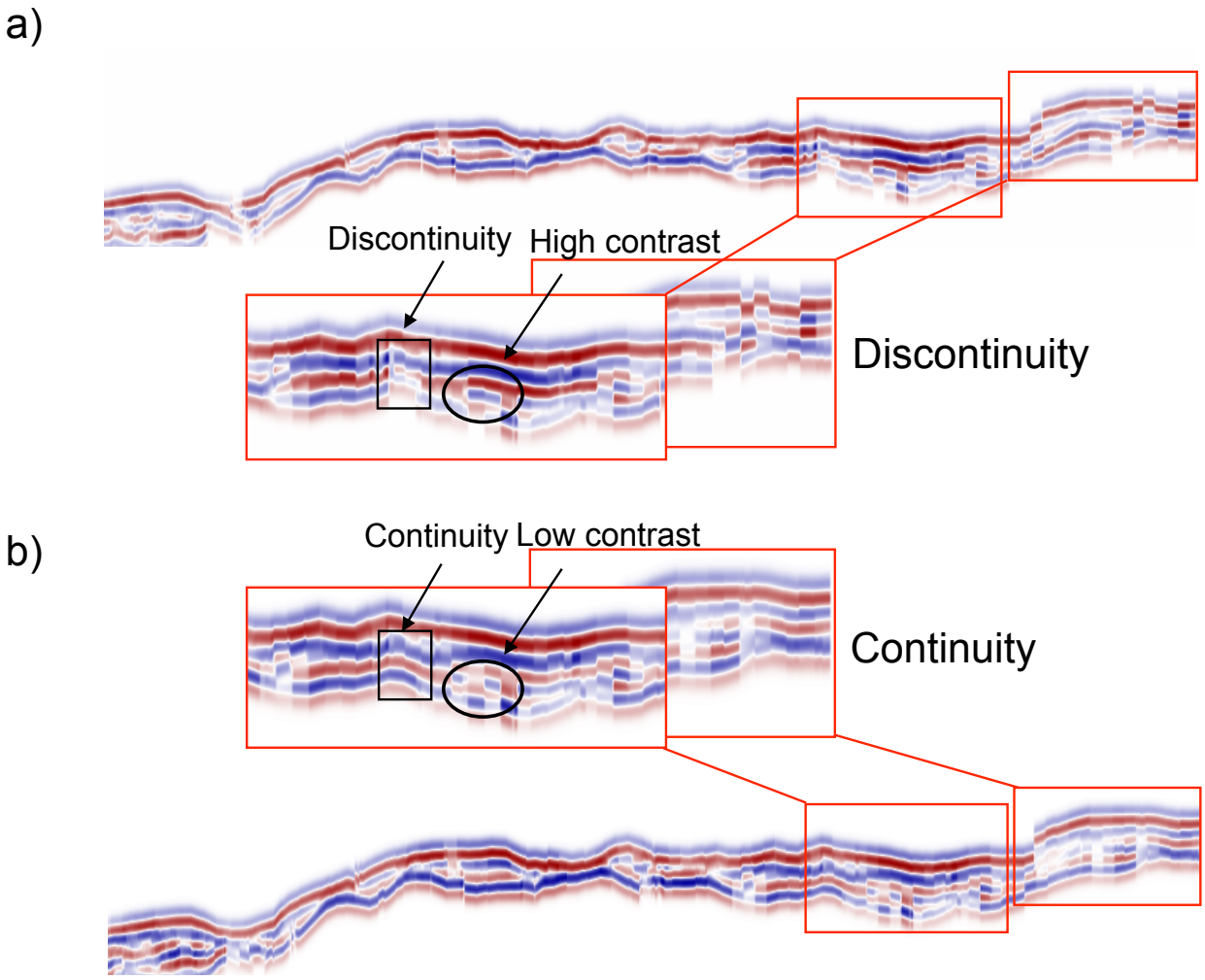

Figure 5.11: Vertical cross section of modelled seismic for: a) impermeable and mechanically inactive shales; b) mechanically active shales with a permeability of 1nD.

In this particular case, the softening response observed in the north area is reflecting the pressure diffusion in the shale and the pressure build up from the injectors I17 and I13 (see Figure 5.13(b). However in the southeast area, although there is pressure depletion with no free gas, an acoustic impedance decrease is observed. In this particular area, the known thick shales (4 to 5m) are not responding to the pressure diffusion and are only experiencing dilation. Hence, despite the pressure depletion in the sand, the shale dilation is softening the overall impedance. To validate these observations, the resulting synthetic amplitude changes for both cases; active and inactive shale is generated, and then compared to the observed data. Figure 5.15 shows amplitude changes within the reservoir interval between 2002 and 1996 for the inactive (Figure 5.15(a)) and active (Figure 5.15(b)) shale cases. Here the attribute of Sum of Negative Amplitude (SNA) is used to calculate the amplitude changes between top and base reservoir. The amplitude changes are calculated as follow:

$$\Delta A = SNA_{Base}^{Top}(02) - SNA_{Base}^{Top}(96) \tag{5.22}$$

where SNA is the sum of negative amplitude between the top and base of the reservoir. According to this calculation and the trend of the impedance inside and outside the reservoir, a negative change of amplitude ($\Delta A < 0$) corresponds to softening (blue colour) and the hardening effect (red colour) corresponds to a positive change of amplitude ($\Delta A > 0$). Clearly in Figure 5.15, a different polarity of the amplitude changes is observed around the north and the southeast area of the reservoir for the case of active and inactive shale. This is in agreement with the synthetic impedance and velocity changes. Figure 5.16 shows the observed data in terms of amplitude changes between 2002 and 1996 within the reservoir. From the observed seismic data, the amplitude changes around the north and the southeast areas (the areas highlighted with blue dashed line in Figure 5.16) are indicating a softening effect of the overall impedance. Interestingly the same magnitude and polarity of amplitude changes are only observed in synthetic time lapse seismic from the model with active permeable and mechanically active shale. These observations suggest that the combined effects of geomechanics and pressure diffusion can affect the effective seismic response. Furthermore the active shale concept could be another additional parameter to be considered in order to achieve a better prediction and more reliable seismic synthetic seismic. In addition, this seismic modelling workflow can offer the opportunity to have a better calibration of the dynamic and the static properties of the shales.

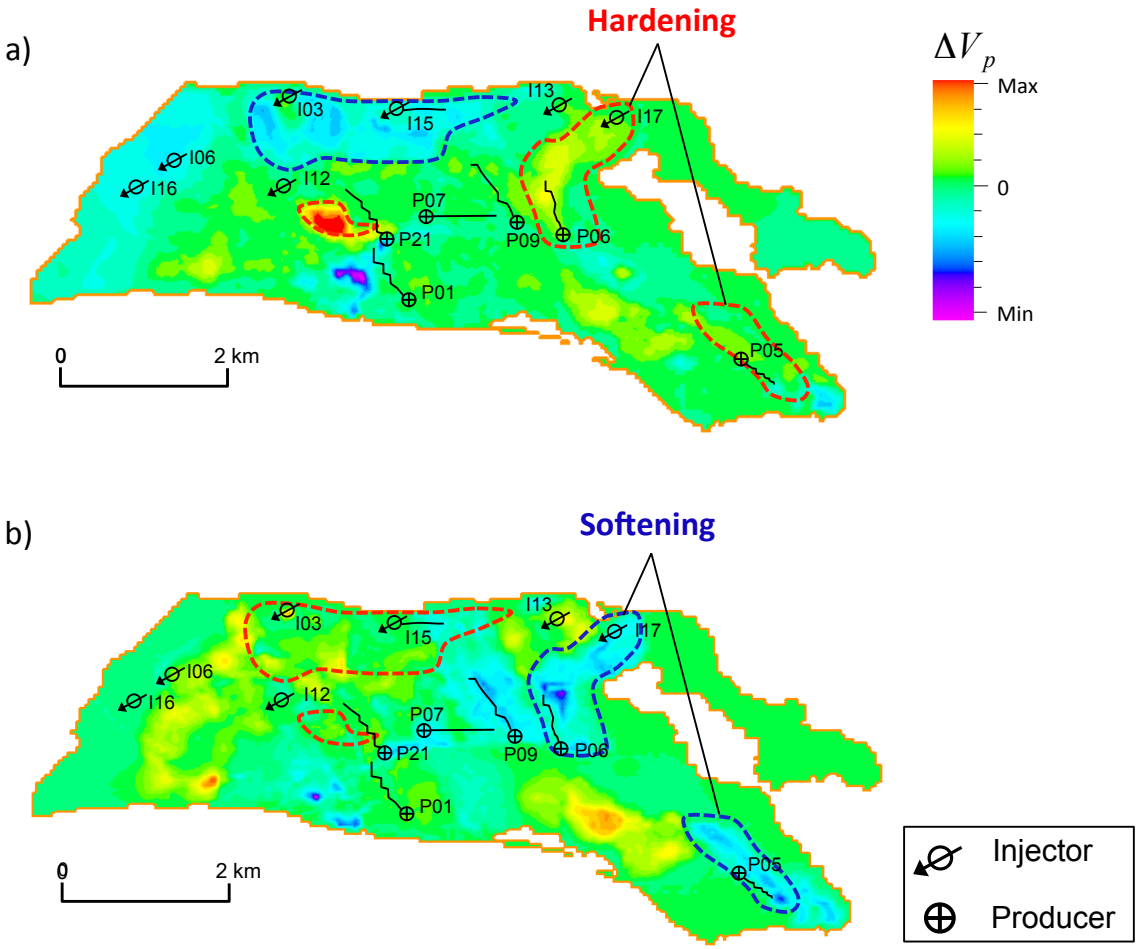

Figure 5.12: Maps of synthetic P-wave velocity changes within the reservoir between 2002 and 1996 for (a) inactive shale and (b) active shale. Different polarity of velocity changes is observed in the north and the southeast area of the reservoir.

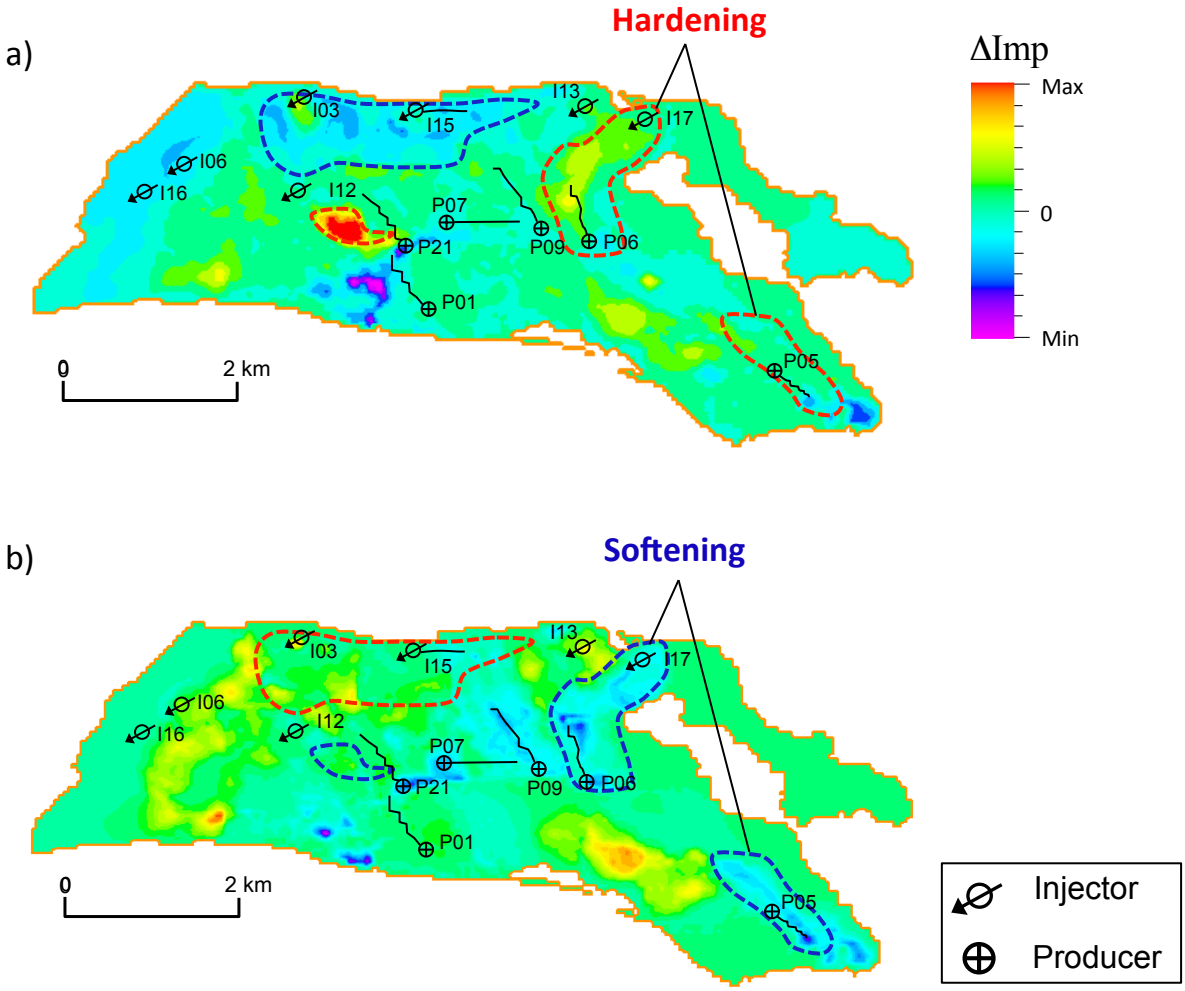

Figure 5.13: Maps of synthetic P-wave impedance changes within the reservoir between 2002 and 1996 for (a) inactive shale and (b) active shale. Different polarity of velocity changes is observed in the north and the southeast area of the reservoir.

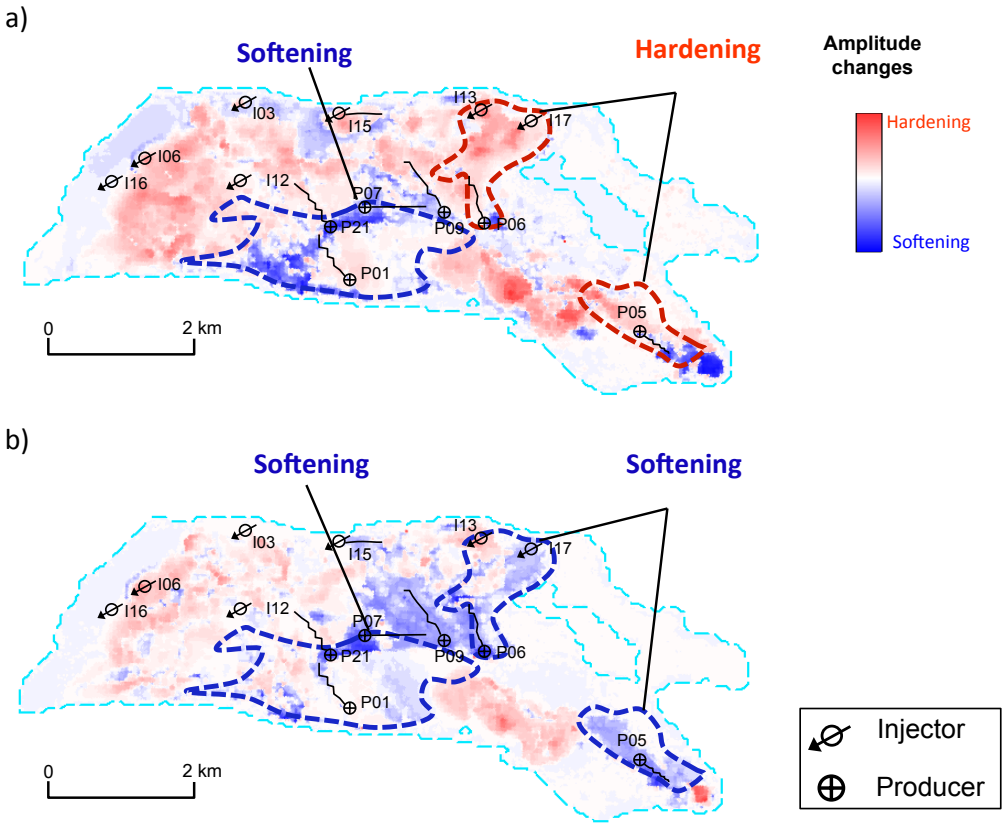

Figure 5.14: Maps of sum of negative amplitude (SNA) changes within the reservoir between 2002 and 1996 for the synthetic seismic of (a) inactive shale, (b) active shale. Different polarity of amplitude changes recorded in the north and the southeast areas.

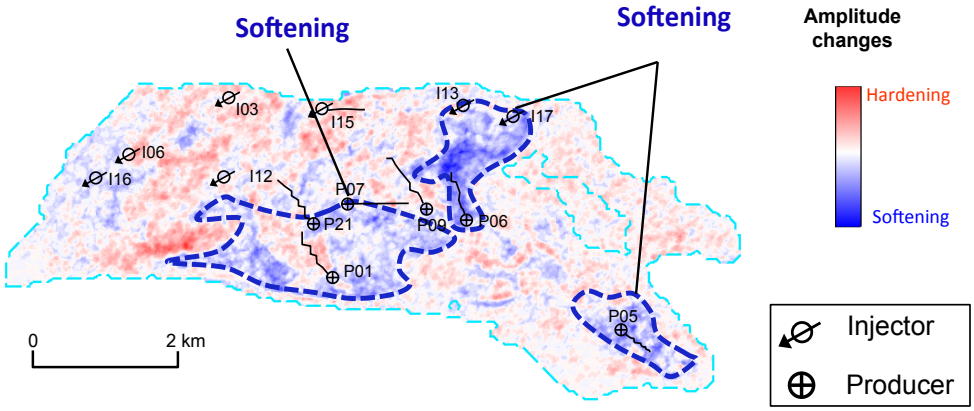

Figure 5.15: Maps of the observed sum of negative amplitude (SNA) changes within the reservoir between 2002 and 1996. The observed time-lapse amplitude changes show softening effect around the north and southeast area (highlighted with blue dashed line). These observations are in agreement with those shown in the case of active shale (Figure 5.15(b)).

5.6 Discussion and conclusions

The integration of the combined effects of geomechanics and pressure diffusion into shales can affect the effective seismic response. Coupled pressure diffusion and geomechanical effects acting on these shales have an influence on the apparent in situ stress sensitivity of the reservoir and act to reduce the sensitivity from that expected by applying laboratory measurements carried out on predominantly core plugs. Under certain conditions, the reduction in stress sensitivity anticipated from the modelling may in fact reverse the polarity of the expected response, showing less contrast between sand and shale and more continuity of the seismic horizons. Fully coupled numerical computation indicates that for a monitor time period of a few months, a reservoir with shales of a few metres thick might exhibit an anomalous softening response, whilst this may only be possible for a monitor period of 10 years if thicker 5 to 10m shales are present. Pressure diffusion into a shale overburden or under/side burden can prove to be significant over the production (and recovery) time scale from several years to tens of years. In 5 years, pressure can diffuse by as much as 50m into a 1nD shale. The surrounding shales initially experience a mechanical extension due to the stress created by compacting sandstones. However as time progresses pressure diffusion reverses this effect near to and around the reservoir, and these shales then experience a compaction. However the impact of the sedimentology of the shale should not be underestimated and this can give rise to heterogeneities such as silt layers or tensile fractures that can considerably enhance the predicted effects. Pressure diffusion can modify the time-shift profile beyond that expected of a conventional reservoir compaction-overburden extension scenario.

In this chapter, segments of the Schiehallion field were studied. For this, the active shale concept is used, where the reservoir and non-reservoir shale are permeable and mechanically active. When the shales are inactive, the modelled seismic shows abrupt discontinuous values and high intensity reflectivity along events – related to the positions of the shales. These features change as the shales become active, and it is also possible to see some evidence of a polarity shift in the seismic at the location of high concentration of shale. At some locations where NTG is low, the polarity of the synthetic impedance changes and the corresponding synthetic 4D amplitude in the case of active shale are different from those where shale is inactive. Interestingly the synthetic 4D seismic amplitude generated with that active shale is in agreement with the observed 4D amplitude. These results suggest that the integration of the

combined effects of geomechanics and pressure diffusion of the intra-reservoir and the surrounding shales into the seismic forward modelling can affect the seismic response.
The time shifts at the Schiehallion field, between 1996 and 2002 are very small (less than 1ms) for this, the analysis of the time shifts were excluded from the study. Further research is recommended to investigate the time shifts.

The results of a synthetic case study for the Schiehallion field suggest that the integration of the above effects can affect the seismic response. For the Schiehallion field, the polarity of the P-wave impedance changes and the corresponding synthetic 4D amplitude changes obtained from the coupled mechanisms are different from those modelled using geomechanics alone. Remarkably the synthetic 4D seismic amplitude generated using the coupled mechanisms is in agreement with the observed 4D amplitude. Based on these results the active shale concept could be another additional parameter to be considered in order to achieve a better prediction and more reliable synthetic seismic modelling. In addition, this workflow of seismic modelling can offer the opportunity to provide a better calibration of the dynamic and the static properties of the shales. This practice is high recommended in the case of dense presence of intra-reservoir shales. To name some, this could be applied to turbidite, fluvial, and delta system where shale is an abundant facie.

It is known that the results of this work are strongly controlled by the coupled mechanical, transport and elastic properties of the shales. However, the exact time scales involved in these predictions are dependent on the static and dynamic properties of the shales. As indicated previously, these properties are currently hard to calibrate precisely due to an insufficient knowledge of these rocks for the specific depositional environments of relevance.

CHAPTER

SIX

6 Application of active shale concept to the Erskine field

This chapter presents the application of the active shale concept to the HPHT Erskine Field. For this, first the field geological background and seismic anomalies are presented. Next a 3D finite element based geomechanical and fluid flow simulation is performed where the reservoir and non-reservoir shales are active. The geomechanical modelling and conversion of model results to synthetic seismic time shifts will be used to perform a quantitative comparison of model-based results with the observed 4D seismic time shifts. This study aims to calibrate the shale properties and to identify geohazards and the formations of high risk for the future development of the field.

6.1 Introduction

The findings of the previous chapter are assessed by the integration of coupled mechanisms into forward modelling of time lapse seismic for the Schiehallion field. The setting was a channelized turbidite system, where shale is an abundant facies in the reservoir and the surrounding rocks. In this chapter, the active shale concept is used to perform a quantitative interpretation of the time lapse seismic for the high-pressure high temperature Erskine field.
A study published by Fletcher (2004), first reported an expected 4D seismic anomaly at the Erskine field. Despite a pressure depletion of 6000psi, a positive time shift is observed across the field. The following investigates the possible reasons for the unexpected seismic response. For this, the field geological background and seismic anomalies are initially presented. Next, a 3D finite element based geomechanical and fluid flow simulation is performed, in which the reservoir and non-reservoir shales are active. The geomechanical modelling and conversion of the model results to synthetic seismic time shifts will be used to perform a quantitative comparison of the models with the observed 4D seismic time shifts. This study aims to identify geohazards in the formation with high risk for future development of the Erskine field.

6.2 Field background

The history of Erskine is well documented in the literature. A detailed description of the structure and sedimentology is published by Coward (2003). The field is a high temperature (340° F), high pressure (14000psi), gas condensate rich field, located on the western margin of the East Central Graben, at the southern toe of the Forties-Montrose High in Block (see Figure 6.1). Hydrocarbons are produced from three separate reservoirs of Jurassic age. These are the Erskine sandstone reservoir, the Pentland Formation reservoir, and the Heather Turbidite reservoir. Neighbouring high temperature, high pressure (HTHP) fields are the Elgin and Franklin Fields and the Shearwater Field. The field was evaluated based on seven appraisal wells, drilled between 1981 and 1993. The extended appraisal period reflects the technical and commercial risk associated with the extreme reservoir conditions.

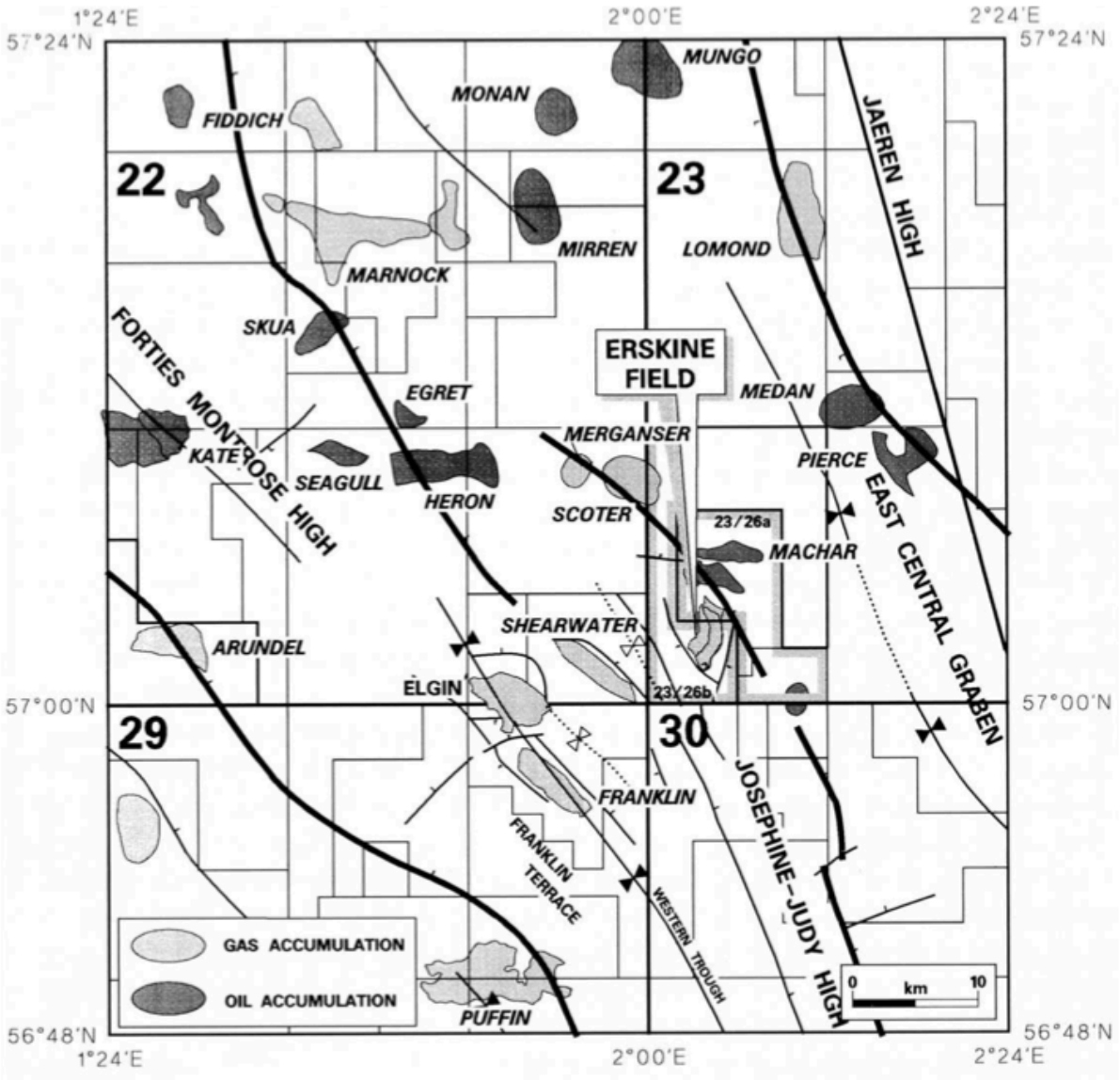

Figure 6.1: Location map of the Erskine field in the North Sea

6.2.1 Field structure

The field seismic database comprises of a 3D seismic dataset shot in 1989, with a field bin spacing of 12.5 metres. The following seismic events have been mapped: Top Balder, Top and Base Chalk, Base Black Limestone Marker, Base Cretaceous, Top Erskine, and Top Pentland. Figure 6.2 show an In-line cross section across the field from the baseline seismic shot in 1989. Here the main reservoir horizons and the major boundary faults are observed. All mapped events are generally good quality; however over the crest of the structure, the top Erskine event deteriorates as it approaches the base cretaceous unconformity.

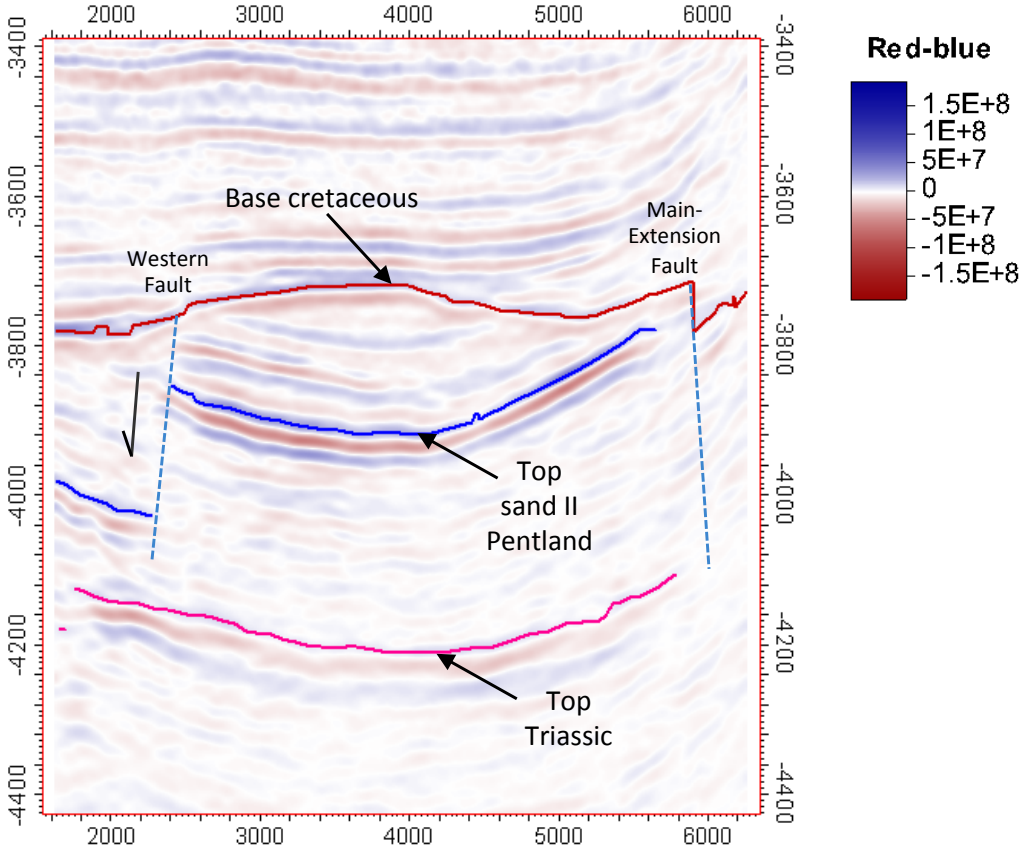

Figure 6.2: In-line seismic cross section across the field from the baseline seismic survey of 1989. The base cretaceous shows top reservoir reflector and the Top Triassic reflector is the reservoir base. The major boundary faults as well as top Pentland are generally of good quality.

Figure 6.3 shows the time structure map for the top of the Pentland Reservoir. Three structural blocks are recognized within the field: the Main Block, the Beta Terrace, and the

Alpha Terrace. All three are components of large-scale block rotation associated with Late Cimmerian extensional tectonism. Lines of geoseismic dip and strike cross section are shown in Figure 6.4.

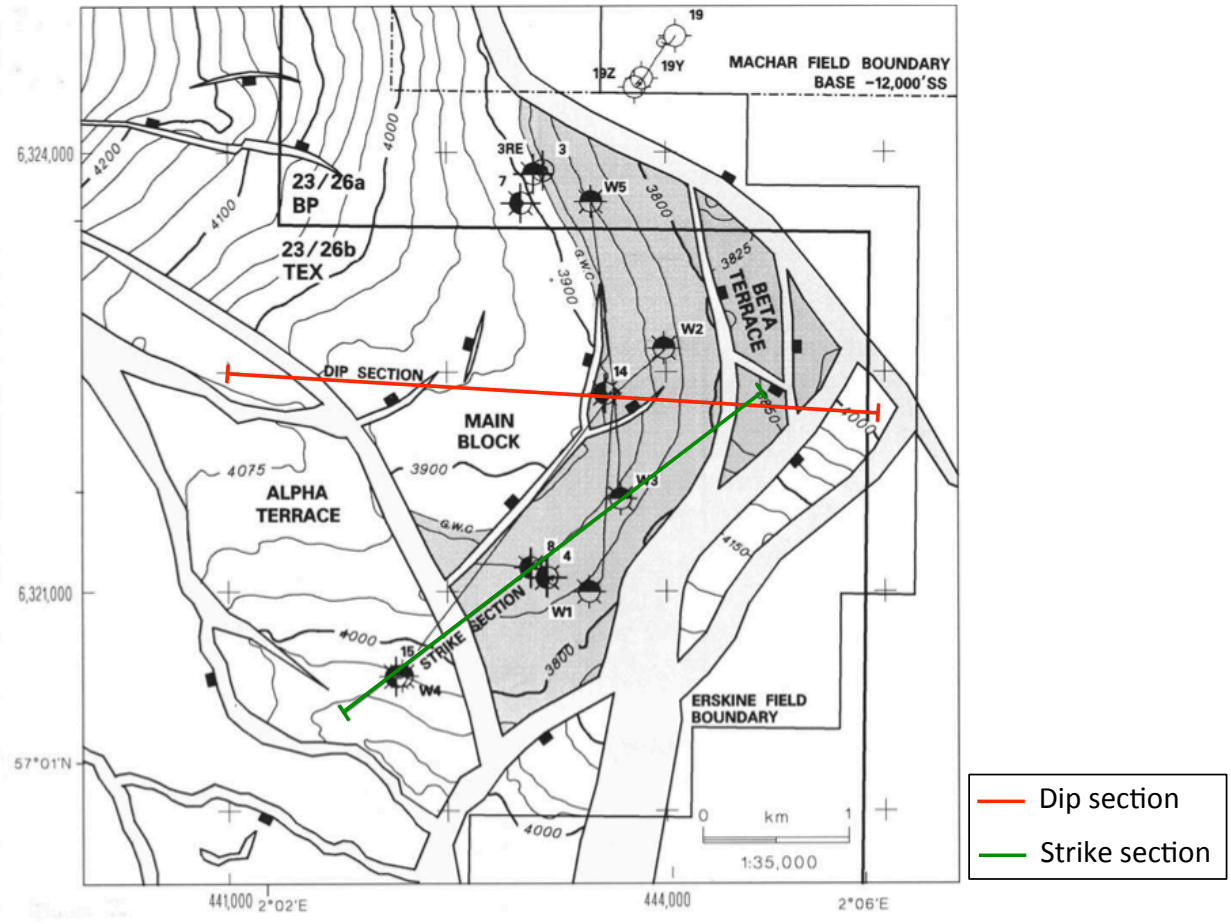

Figure 6.3: Time structure map for the top of the Pentland Reservoir. Three structural blocks are recognized within the field: the Main Block, the Beta Terrace, and the Alpha Terrace. The orientation of the dip and strike section is shown in red and green respectively (after Coward, 2003)

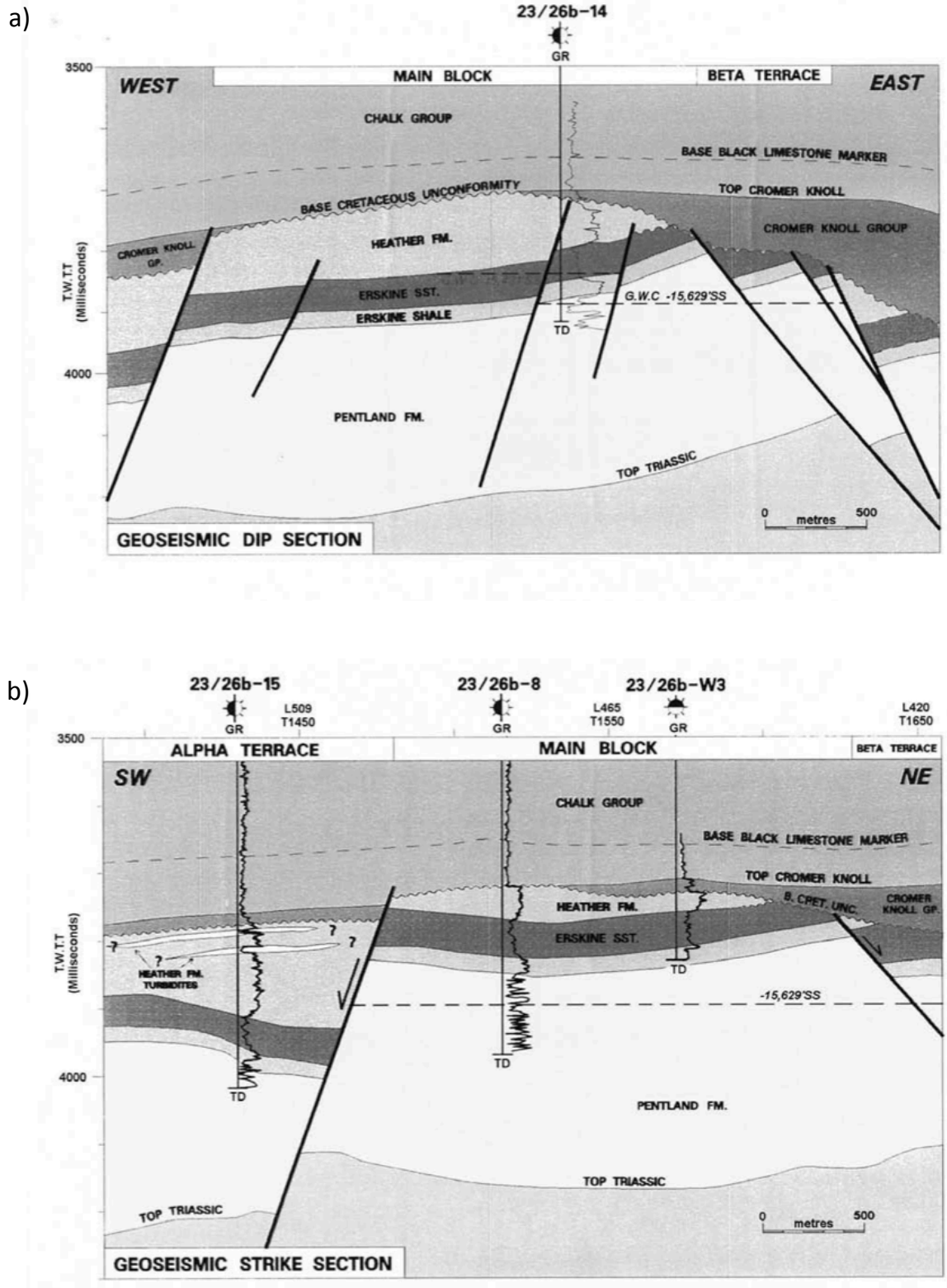

Figure 6.4: Schematic interpretation of the vertical cross section of the Erskine field. (a) dip and (b) strike cross-section (Coward, 2003)

Coward (2003) described the structure as: *"a westerly dipping, scallop-shaped, tilted faults block. The up-dip (eastern) edge of the main block has undergone progressive erosion by the base cretaceous unconformity that resulted in complete removal of the Erskine Sandstone. The block is heavily faulted with at least three compartments recognized from the seismic data (Figure 6.4). The focus of the structural analysis conducted by David (2001) is to identify the main formations present in the basin of the Erskine field. Here the oldest formation is the Triassic formation. it consists of interbedded sequence of sandstones, siltstones and shale. This sequence constitutes the underburden of the reservoir. The middle Jurassic deposit of the Pentland Formation is overlying the Triassic unit. The Pentland formation comprises of sandstones siltstone and shale deposited in the fluvial to lacustrine environment. The sequence is approximately 1800ft thick over the field. The lower part of the Pentland sequence is Bathonian or older however the upper part is found to be early Oxfordian and probably deposited in marginal marine setting (Geostrat 1997). The overlying is the Erskine shale. It has been found that the Erskine Shales were deposited in an open marine environment and are Early-late Oxfordian in age. The Erskine shale has uniform thickness across the field of approximately 100ft. The overlying formation is known as Erskine Sand, and it is between 200 and 300ft thick. The unit is thought to be deposited in offshore transition zone setting. The Heather formation above the Erskine sand is a shale-dominated sequence. Its thickness is controlled by the degree of erosion by the base Cretaceous unconformity. The overlying formation is the Cromer knoll group and the Chalk group. These units constitute the overburden of the Erskine Field."*

The structural analysis described above, is very helpful to spot the formations of interest for the purpose of this thesis. For this particular case study, the Erskine shale and the shale-dominated Heather formations are the focus of the active shale study. Here, based on stratigraphical analysis, the Erskine shale is considered to be a representative example of intra-reservoir shale. On the other hand, the shale-dominated Heather formation is considered to be the immediate overburden shale. The thickness and the quality of the Erskine shale and the Heather formation suggest that their corresponding response to the mechanical deformations and pressure diffusion process will be pronounced and detected in the time lapse seismic. To understand more about the reservoir and the behaviour of the field, the reservoir quality is presented in the following section.

6.2.2 Reservoir quality

As mentioned earlier, the hydrocarbons are produced from three separated reservoirs. In order of decreasing importance, these are: Erskine Sand, Pentland Sand, and the Heather formation. Here Figure 6.5 shows the correlation between the wells and the reservoir zonation (Coward, 2003). The Erskine reservoir is the principal reservoir in term of reserves; it is between 200 and 300ft thick. The majority of the Erskine sandstone has porosities in the range of 20-25%. Permeability is typically low, ranging from 0.1 to 100mD. Some units such as E70 and E30 (see Figure 6.5) have an average porosity of 30% and permeability up to 100mD. Also rock mechanics tests on cores from these formations indicated that the weaker nature of these rocks may lead to sand grain production following a reduction in pore pressure. The Pentland Reservoir is a regionally extensive sequence of interbedded sandstone, shales and siltstone deposited in a fluvial-lacustrine environment. Permeability in the Pentland is in general higher than the values observed in the Erskine sandstone. It is approximately between 0.1mD and 1D, and porosity ranges between 15 and 25%. Within the Pentland there are laterally continuous lacustrine shales P30 and P50, which are correlated across the field. The Heather Turbidite Reservoir is the third reservoir in the Erskine Field, and occurs within turbidite sandstone beds in the Heather Shale formation. Two sand beds were identified from the well log data. The average permeability of these is about 80mD and porosities are around 20%. These beds are drained by a single development well. Based on the reservoir zonation, a simulation model was built to simulate the production scenario.

6.2.3 Reservoir simulation

The simulation model used for the study was obtained from the Erskine Team in Chevron, Aberdeen. The Erskine full field simulation model was built for the Eclipse-300 (E300) (TM Schlumberger) compositional simulator. E300 has been selected as the preferred solution that can address complex PVT and fluid flow behaviour near the wellbore.

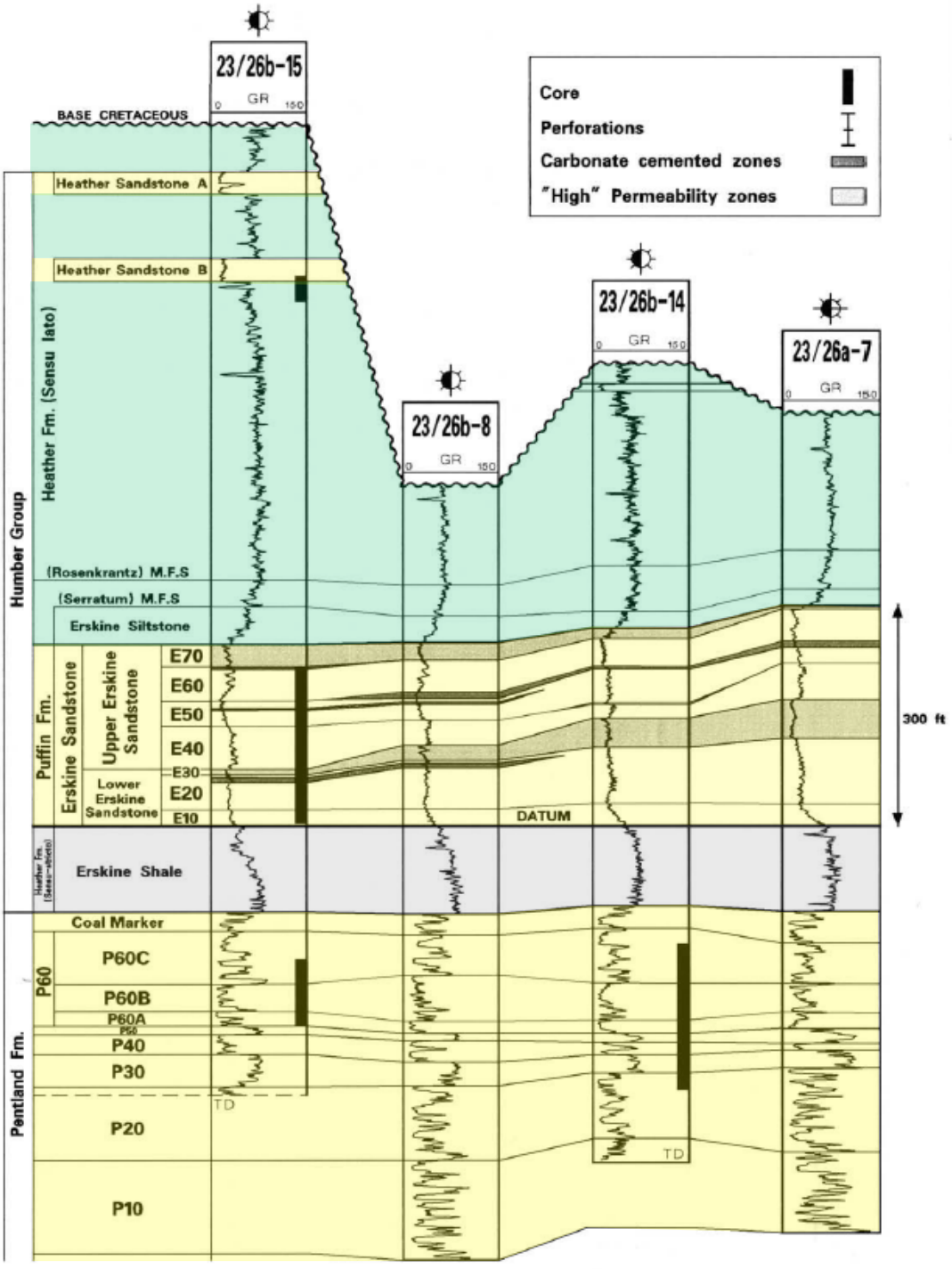

Figure 6.5: Well correlation, reservoir zonation of the Erskine Field (Coward, 2003)

The Erskine earth model has been built to capture fine scale flow characteristics in the Erskine reservoir with a total of 54 layers. The vertical resolution was based on assessment of heterogeneity that can be observed from the logs and the PLT data. The Erskine reservoir model size is 92×125× 58 cells. Chevron's recommended workflow was followed for history matching of the Erskine field. This workflow takes into account four controlling parameters to perform history matching. It is based on matching pressure, saturation, total voidage, and gas rate. In addition, a model properties calibration is performed before running the simulation for prediction

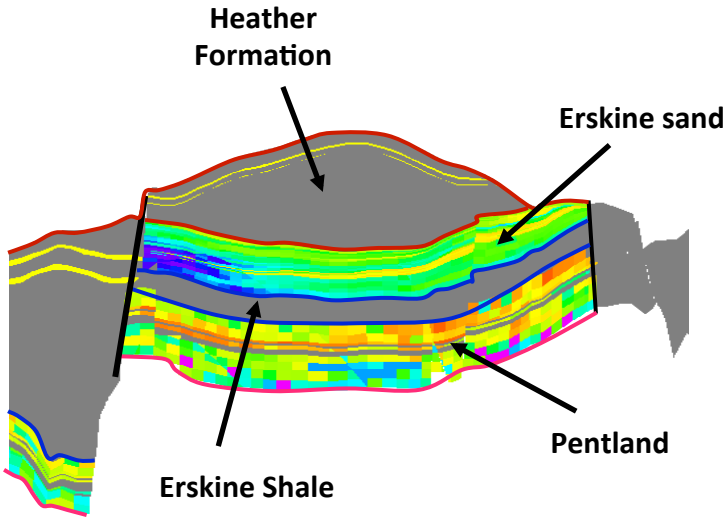

Figure 6.6: Vertical cross section though the simulation model for the Erskine field. The main formations modelled are: Heather formation, Erskine sand, Erskine shale, and Pentland.

Given the high-pressure environment of the field, the production mechanism in the Erskine reservoirs (Pentland formation, Erskine sands and the Heather turbidite sand) is mainly driven by pressure depletion. Also at the Pentland level, aquifer support is also considered as another drive mechanism. The production scenario is based on the production from five wells; PW1, EW2, PW2, EW3, KW4, and EW5. PW1 and PW2 targetted the Pentland formation, EW2, EW3 and EW5 targetted the Erskine sand, and KW4 targetted the sand units in the Heather formation. The production scenario is only based on draining the three reservoirs with six producers. More details on the layers in the simulation model are presented in Appendix B.1.

6.2.4 Reservoir management and time lapse seismic

The philosophy of the reservoir management and development is to continue the production scenario, which is based on draining three reservoirs with six producers. In addition to other geoscience technology, time lapse seismic monitoring is considered as option for the field management. For this purpose a monitor seismic surveys was shot in 2001. To insure a good seismic quality and high repeatability, the acquisition parameters used for the baseline seismic survey shot in 1989 are again used for the monitor survey. The following sections of this chapter will focus on the interpretation of the time-lapse seismic data and the integration of these findings into the field management and future development.

6.3 Time lapse seismic signature at the Erskine field

Here, the 1989 pre-production survey and the the 2001 monitor seismic survey are used to conduct the time lapse seismic analysis. In this study, I firstly examine the time lapse amplitude changes. Next the time lapse time shift induced by production is assessed using the active shale concept.

6.3.1 Amplitude anomalies at the Erskine field

At the Erskine field, hydrocarbon production has caused significant decrease in pore pressure and an increase in effective stress. This has led to velocity changes within the reservoir interval and detectable variations in the seismic-reflection amplitude. Figure 6.7 shows an in-line and cross-line vertical cross sections of the amplitude changes across the field. These amplitude changes are calculated after aligning the monitor seismic survey to the baseline survey. This operation aims to avoid the effect of the time shift on the amplitude changes. Clearly, from Figure 6.7, the amplitude changes are mainly concentrated around the Pentland formation. In addition amplitude changes around the Heather and Erskine formation are detected. To further assess these 4D amplitudes, a map of the changes between 2001 and 1989 is generated within the reservoir interval. The amplitude changes are measured by a calculating the difference of the RMS amplitudes between monitor 2001 and baseline 1989 (Figure 6.8). Changes are mainly concentrated around the location of the producers; EW3, EW2 PW2, and PW1.

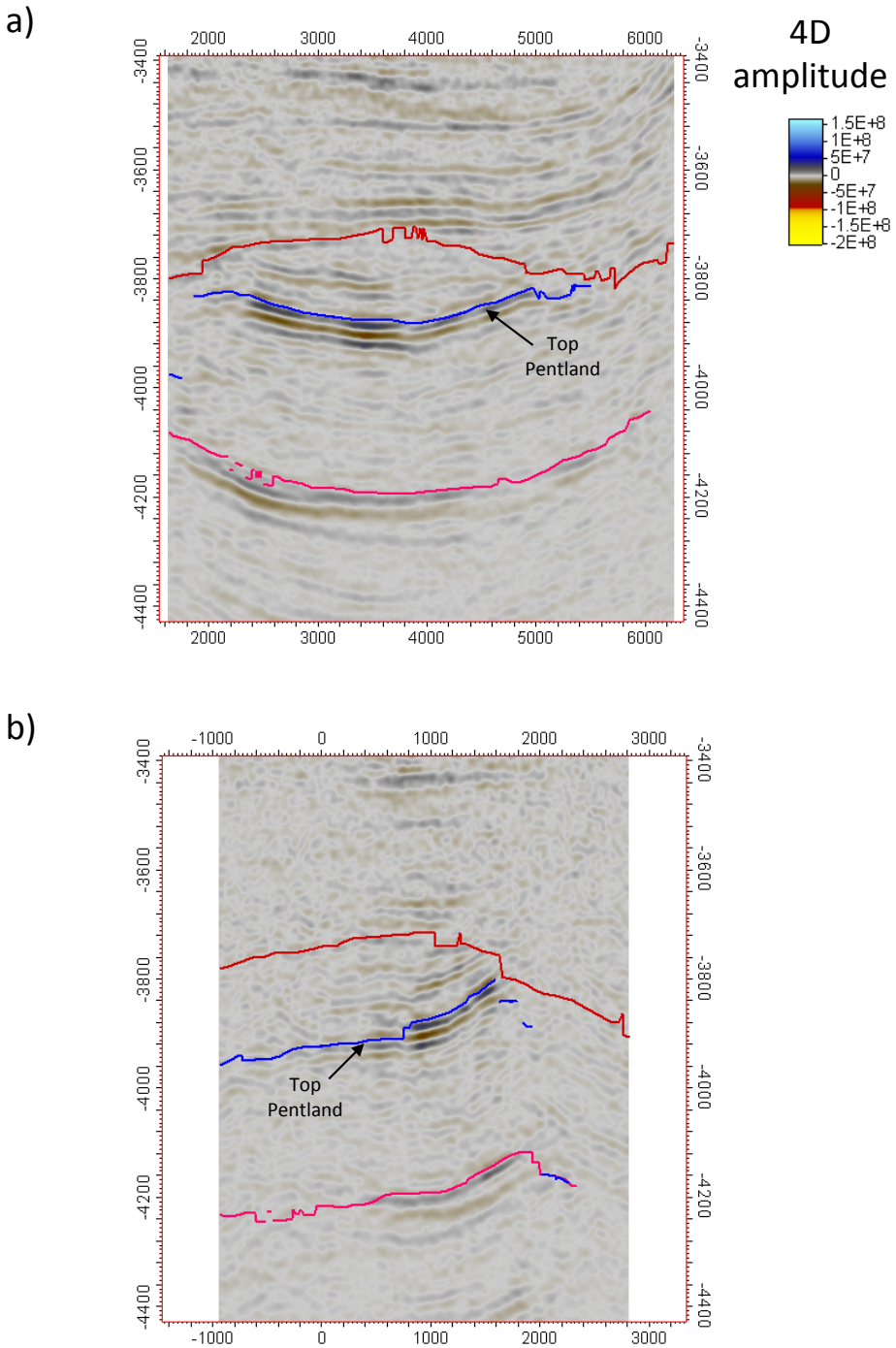

Figure 6.7: Time-lapse amplitude changes between 2001 and 1989; (a) in-line, and (b) cross-line section through the reservoir. The 4D anomalies are concentrated above the Top Pentland and within the Pentland formation.

The time lapse amplitude changes are calculated as follow:

$$\Delta A = RMS_{base}^{top}\left(Monitor\_2001\right) - RMS_{base}^{top}\left(Baseline\_1989\right) \tag{6.1}$$

where RMS is defined as the Root Mean Square. For this calculation, the RMS attribute measures the average of the amplitude between the top and base reservoir of the reservoir.

$$RMS = \sqrt{\frac{\sum_{base}^{top} a_t^2}{N}} \tag{6.2}$$

where a is the amplitude, and N is the number of samples between top and base of the reservoir. For this calculation the Base Cretaceous horizon is the top reservoir, and the top Triassic is the horizon associated with the base reservoir.

It is clear in Figure 6.8 that the negative amplitude changes are concentrated around the producers. Here, given the way the amplitude change is calculated and the fact the seismic wavelet crosses from a high impedance in the overburden to a low impedance in the reservoir interval, the negative changes of amplitude around the depleted area is an expected result (see Figure 6.8). After pressure depletion, the P-wave velocity and density in the reservoir increase, giving a hardening effect, thus increasing the impedance in the reservoir. Consequently this will reduce the contrast of the impedance between the overburden and the reservoir interval, and hence the seismic trough recorded at the top reservoir will decrease. Accordingly, the amplitude in the 2001 monitor survey is weaker than in the 1989 baseline seismic survey. Examination of the 4D amplitude shows that the amplitude response is reflecting the pore pressure behaviour within the reservoir interval. To further investigate the 4D seismic response, the analysis of the time shift attribute will be the focus of the following section. This objective of the time shift analysis is to be able to have a better understanding of the behaviour of the reservoir and non-reservoir shales.

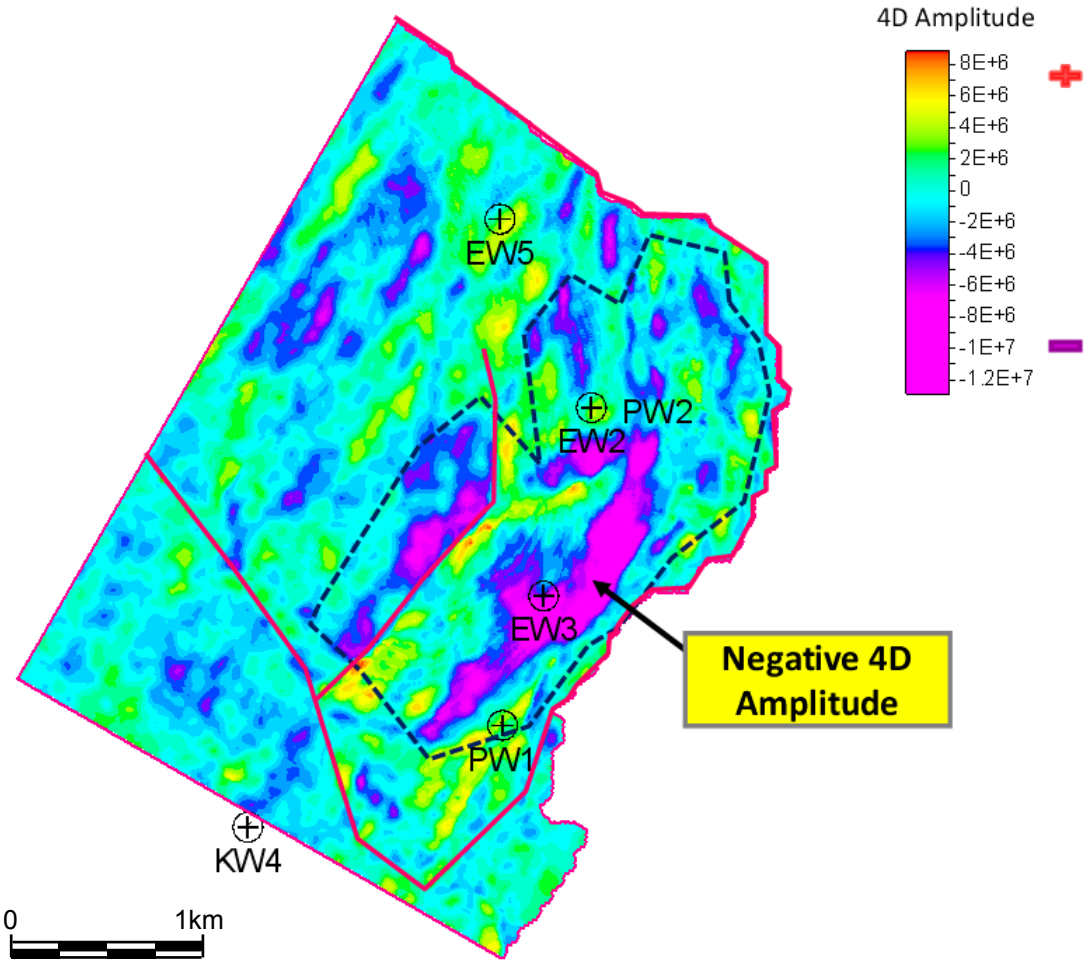

Figure 6.8: Map of 4D amplitude changes across the reservoir. Negative amplitude changes concentrated around the producers. The area of strong amplitude changes is highlighted with the black dashed line.

6.3.2 Time lapse time shift at the Erskine field

Production of hydrocarbons changes reservoir pore pressure and alters the stress acting on the reservoir and on the surrounding rocks (Addis, 1997; Hettema et al., 2000; Hatchell et al., 2003; Sayers, 2005b). Strong evidence for altered stress in and around the reservoirs undergoing pressure depletion is provided by observed time-lapse time shift (Segall, 1989; Hatchell et al., 2003; Tura, 2005). In this study, I analyse the time shift between the pre-production seismic survey and the monitor seismic survey. Here I must highlight that the ability to use these time shifts qualitatively for reservoir management relies on our ability to confidently and accurately measure them. Here, a local cross-correlation approach is used to estimate time shift (Hall et al. 2002). This technique is also known as the warping method, as it finds the maximum cross-correlation in a 3D sense to estimate a 3D shift that aligns the data. This method of fast cross-correlation proposed by Hale (2007) uses Gaussian tapers so that 3D 'blobs' of data are cross-correlated. For this study, the open source algorithm of Hale (2007) is used to calculate the time shifts.

Hodgson et al. (2009) studied the accuracy of the time shift estimation using the warping method. He concluded that the warping technique is sensitive to the vertical size of the 3D window used for the local cross-correlation. The use of a large window tends to give a very smooth time shift with poor resolution. However a short window tends to give a very noisy time shift. In order to optimize the vertical size of the window used for the time shift calculation, first I estimated the time shifts using various sizes of window. The size used for the time shift calculation varies from 8 to 44ms (Figure 6.9). Next I calculated the time shift using the traditional technique, where I compare the event locations picked manually between the baseline and the monitor surveys at the well location. This manually calculated time shift is also shown in Figure 6.9. It is found that the magnitude of the time shift calculated using the widow size of 44ms is in agreement with the one measured manually. Thus, time shift calculated using a widow size of 44ms is used for the rest of the analysis. Time shifts accumulate through the overburden, reaching a maximum at the Base Cretaceous. A reduction in travel time can clearly be seen throughout the shale-dominated Heather formation and the Erskine sand. Based on the understanding I have built throughout previous work, the time shift decrease at the level of the shale-dominated Heather formation can be explained by the compressional strain caused by pressure diffusion. This will be examined in more detail in the geomechanical modelling section. At the level of the Erskine shale, the time shifts start to

accumulate again and reach a maximum of +4ms at the top Pentland. However, throughout the Pentland formation the time shifts start decreasing again.

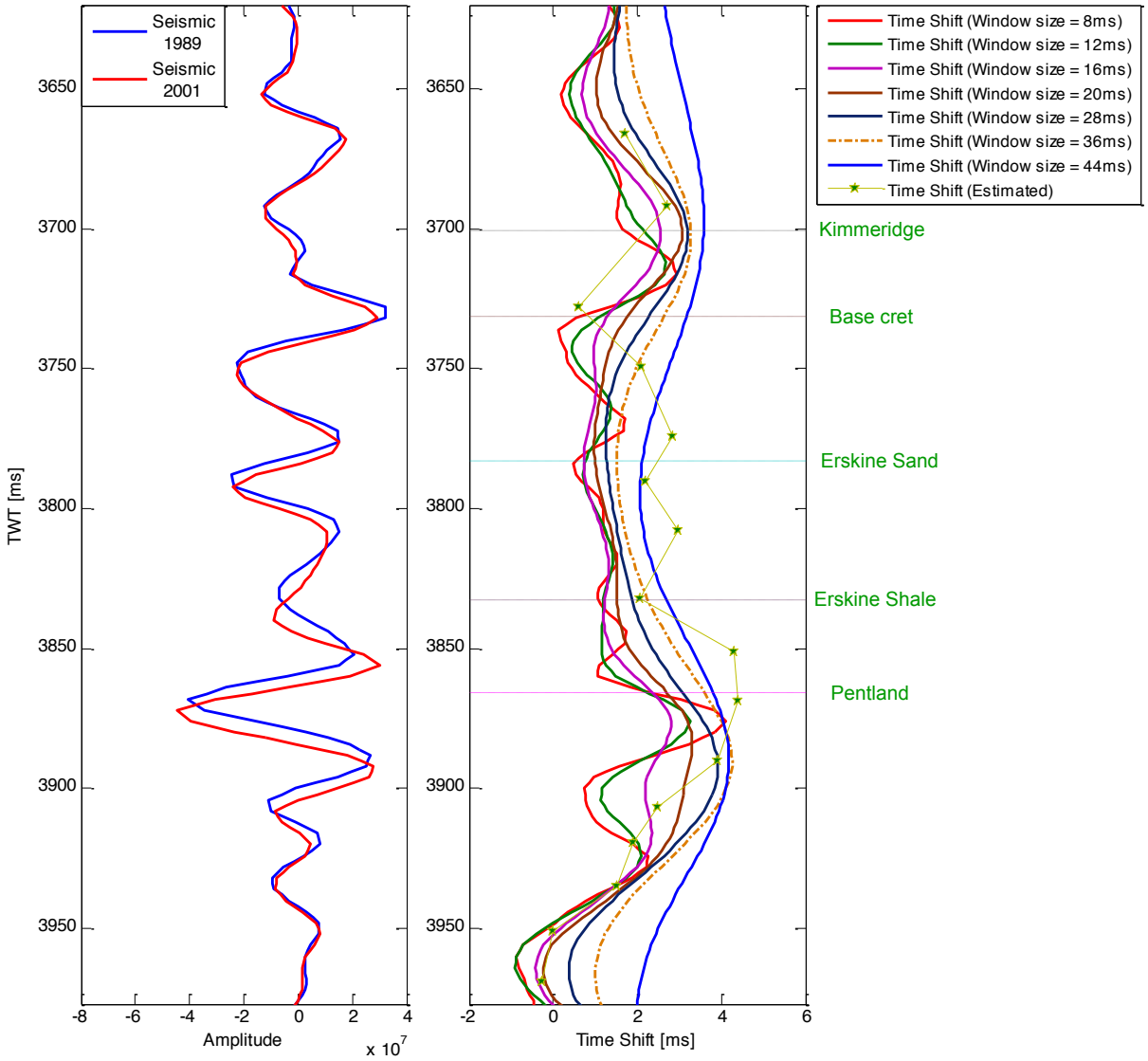

Figure 6.9: Time shifts between two time-lapse traces measured at the well location. The window sizes used for time shift calculation are 8, 12, 16, 20, 28, 36, and 44ms. The curve with the asterisk is showing the manually calculated time shift. The main horizons are shown.

Figure 6.10 shows a map view of the average time shift between top and base of the reservoir. Around the depleted area the average time shift reaches a maximum of +5.4 ms. These results are in very good agreement with those published by Fletcher (2004).

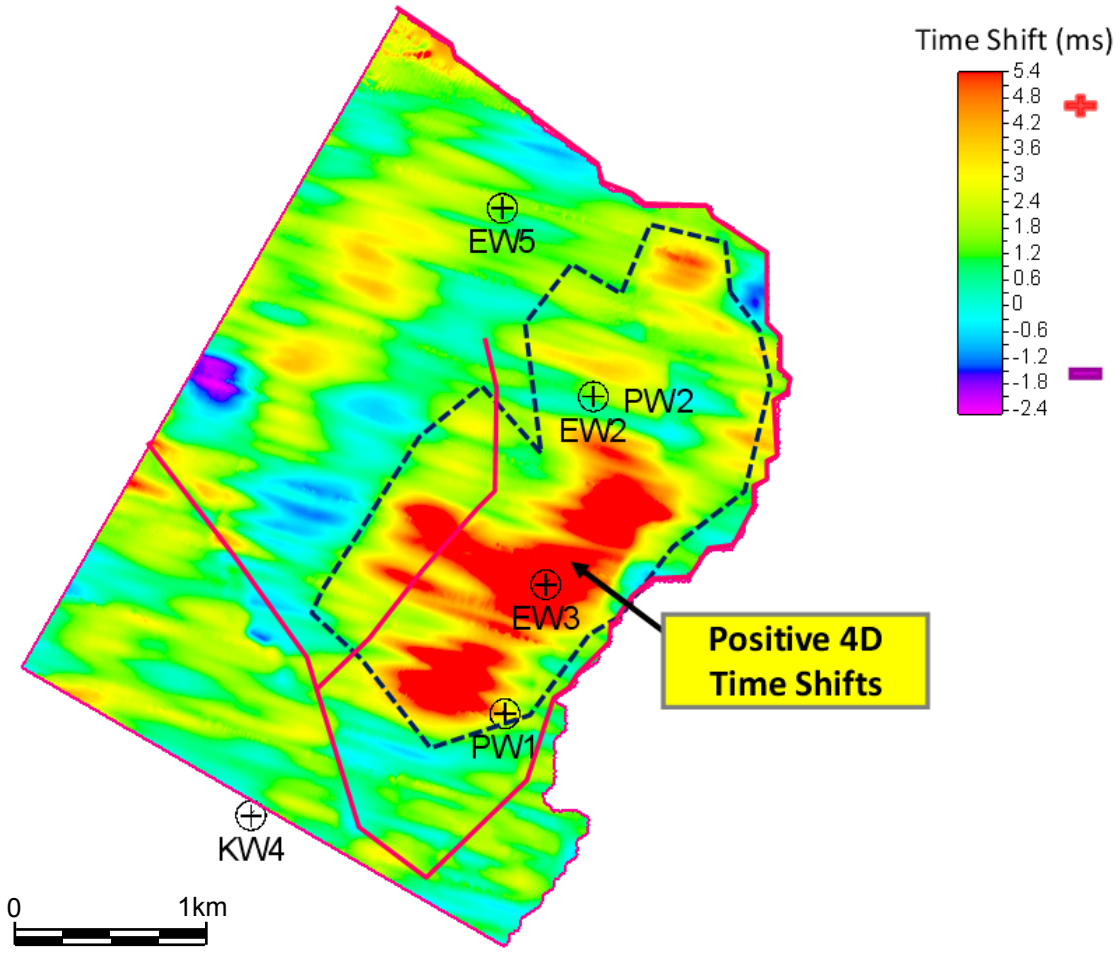

Figure 6.10: Map of the average observed time shift calculated between top and base reservoir. Around the depleted area the average time shift reaches a maximum of +5.4 ms.

Remarkably, in Figure 6.10, positive time shifts are observed which were not the expected response to the pressure depletion of 6000psi recorded at the Erskine field. In order to understand this 4D anomaly I have looked at the possible scenarios that could lead to such an observation. Positive time shift is a result of velocity decrease, which could be related to pressure increase or an increase in gas saturation. Here for the Erskine field, the drive

mechanism of production is based on pressure depletion. Figure 6.11(a) shows a map of pressure depletion across the field between 2001 and 1989. Based on this observation, the pressure behaviour is not causing the unexpected positive time shift. Also, I thought about the consequences of the pressure depletion on the composition of the hydrocarbon. For this, the examination of pressure measurement at the reservoir level (Appendix B.2) shows that the pressure did not reach the dew point, and hence there are no changes of fluid composition. Figure 6.11(b) describes the distribution of gas saturation changes across the field. A decrease is mainly recorded; therefore the gas behaviour is not triggering the unanticipated softening. Clearly, the fluid flow simulation model is not enough to understand the time-lapse signature at the Erskine field. For this, a combined fluid flow and geomechanical simulation study is needed to comprehend the time shift response. The following section will focus on the use of the active shale concept and the integration of the production-induced stress changes in the 4D seismic interpretation.

6.4 Active shale concept and 4D seismic interpretation

As it was previously mentioned in Chapter 5, by implementing the active shale concept, where shale is permeable and mechanically active, the combined effect of pressure diffusion and geomechanics could lead to detectable time shift response. Here, this concept is implemented in order to understand the 4D signature. For this, a geomechanical model is built for the Erskine field. Next, seismic modelling is performed for the case of inactive shale where only the mechanical deformation is considered. Nest, finite-element modelling of pressure diffusion and geomechanics is used to compute the corresponding time shift. For this case, the synthetic time shift helps to calibrate the shale properties and understand the pressure behaviour within the reservoir and non reservoir shales.

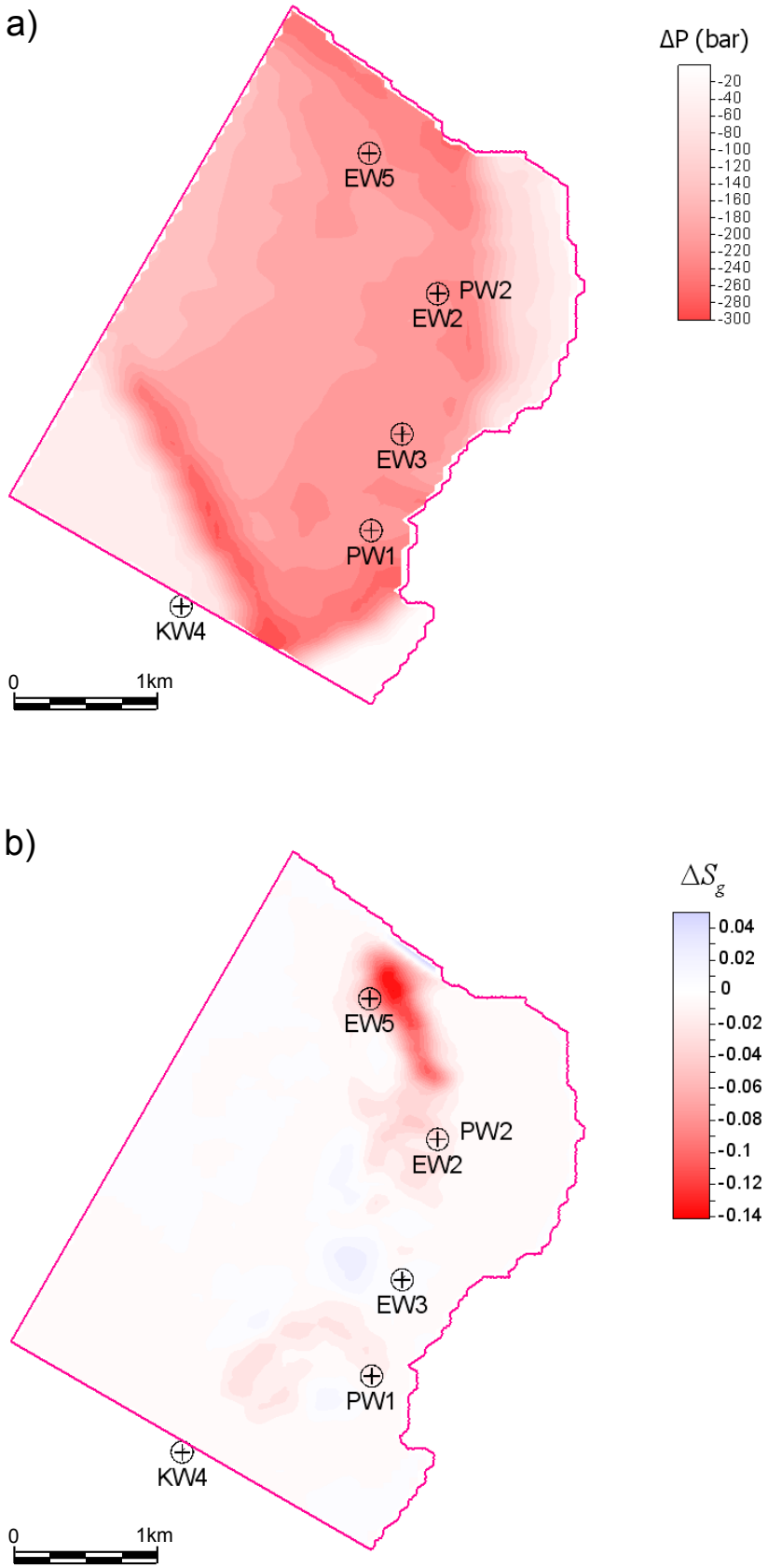

Figure 6.11: (a) Map of pressure changes across the field between the surveys dates 2001 and 1989, in which only pressure depletion is observed. (b) Map of gas saturation changes across the field for the same period.

6.4.1 Building the geomechanical mode

In this section the process used to build the geomechanical model is presented. To construct the geomechanical model the software 'Visage modeller' (TM Schlumberger) is used. This process includes constructing and adding overburden, underburden and sideburden layers to the existing simulation model grid. Figure 6.12 shows the size of the geomechanical model, containing 112x145x111 grid cells. In this model, fine grid blocks are used near the reservoir boundary in order to minimize the effect of the numerical dispersion associated with the numerical simulation. Furthermore appropriate boundary condition and the geomechanical properties are populated throughout the reservoir and the surrounding rocks. The mechanical properties are widely varying, with properties initially determined from laboratory core measurements. Here, the static mechanical properties are derived form the dynamic properties (V_p, V_s). The Young's modulus in the shallow overburden is in the range of 2 to 5GPa. However, in the substantial Cretaceous chalk unit above the reservoir, the Young's modulus varies between 10 and 20GPa. The Cromer Knoll formation has Young's modulus between 6 and 8GPa. The measurement of Young's modulus at the shale-dominated Heather formation shows low values that range between 3 to 4GPa. The Erskine sand units have Young's modulus that ranges between 5 and 15GPa. The Erskine shale unit has a Young's modulus that ranges from 5 to 10GPa. The Pentland unit, which consists of a series of sand and shale, has a Young's modulus that ranges between 15 and 22GPa. The underburden Triassic shale has a Young's modulus that varies between 15 and 25GPa. The above mechanical properties are provided by Chevron. Laboratory measurements at the Erskine field indicated that magnitude of the Poisson's ratio is depending on whether the formation has a drained or undrained behaviour (Chevron report, 2009). For this study, the Poisson's ratios used are in the range 0.15 and 0.25 for sands and 0.25 to 0.35 for shales. After building the geomechanical model, a coupled geomechanical and fluid flow simulation is performed for the case of inactive shale and then the active shale. Then, Hatchell's approach (2005) of time shift calculation is used to convert the results of the simulation to a synthetic time shift. Finally this allows a quantitative comparison of the models with the observed time lapse time shift.

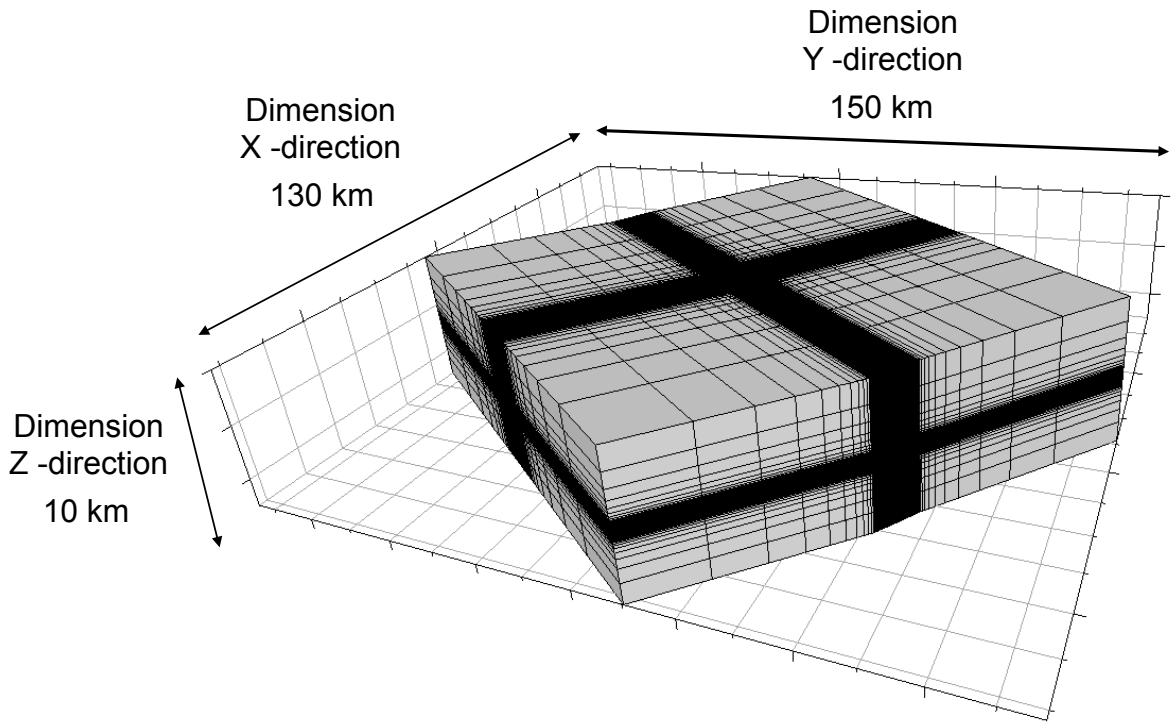

Figure 6.12: The geomechanical model built for the Erskine field. The model has 112x145x111 grid cells. The fine grid blocks around the reservoir boundary serve to minimise the numerical dispersion associated with the numerical simulation.

6.4.2 Inactive shale modelling

In this section, I examine the case of inactive shale. Here, the interbedded Erskine shale, as well as the overburden Heather shale and the underburden Triassic shales are assumed impermeable and only mechanically active. This modelling permits calculation of the stress changes on the reservoir and the surrounding rocks, without considering the pressure diffusion mechanism. In this modelling, the reservoir pore pressure changes derived from fluid flow simulations are used as a mechanical load for the geomechanical simulation. Figure 6.13 shows the simulated changes in pore pressure, effective stress, and strains that resulted from five years of production. For the fluid flow simulation, the reservoir quality such as permeability and connectivity are the main driving mechanism for the pore pressure changes. From Figure 6.13(a), at the level of the Erskine sand the pore pressure decrease is about 100 bars. However at the Pentland formation, heterogeneity plays an important role in the pressure development. The clean sand in the upper Pentland undergoes a pressure drop of 300bars, however the lower Pentland shows only a pressure depletion of 200bars. In my modelling example, because the reservoir and non-reservoir shales are assumed impermeable, neither the overburden Heather shale nor the Erskine shale shows a pressure change (Figure 6.13(a)). As pore pressure decreases in the Erskine sand and the Pentland formation, the vertical effective stress increases inside the reservoir and decreases in the Erskine shale, the overburden Heather shale and the underburden Jurassic shale. The compressive effective stress is defined as positive in Figure 6.13(b). Figure 6.13(c) shows the corresponding strain changes in and around the reservoir. Due to this increase of effective stress, the Erskine sand and the Pentland formation undergo a compressional strain (negative strain). However, the Erskine shale, the overburden Heather shale, and the underburden Jurassic shale undergo extensional strains (negative strain).

6.4.3 Comparison of modelling and time shift data

In this section I convert the results of the geomechanical modelling to synthetic time shift. This process is applied at the well location. The time shift modelling is based on the model proposed by Hatchell and Bourne (2005b).

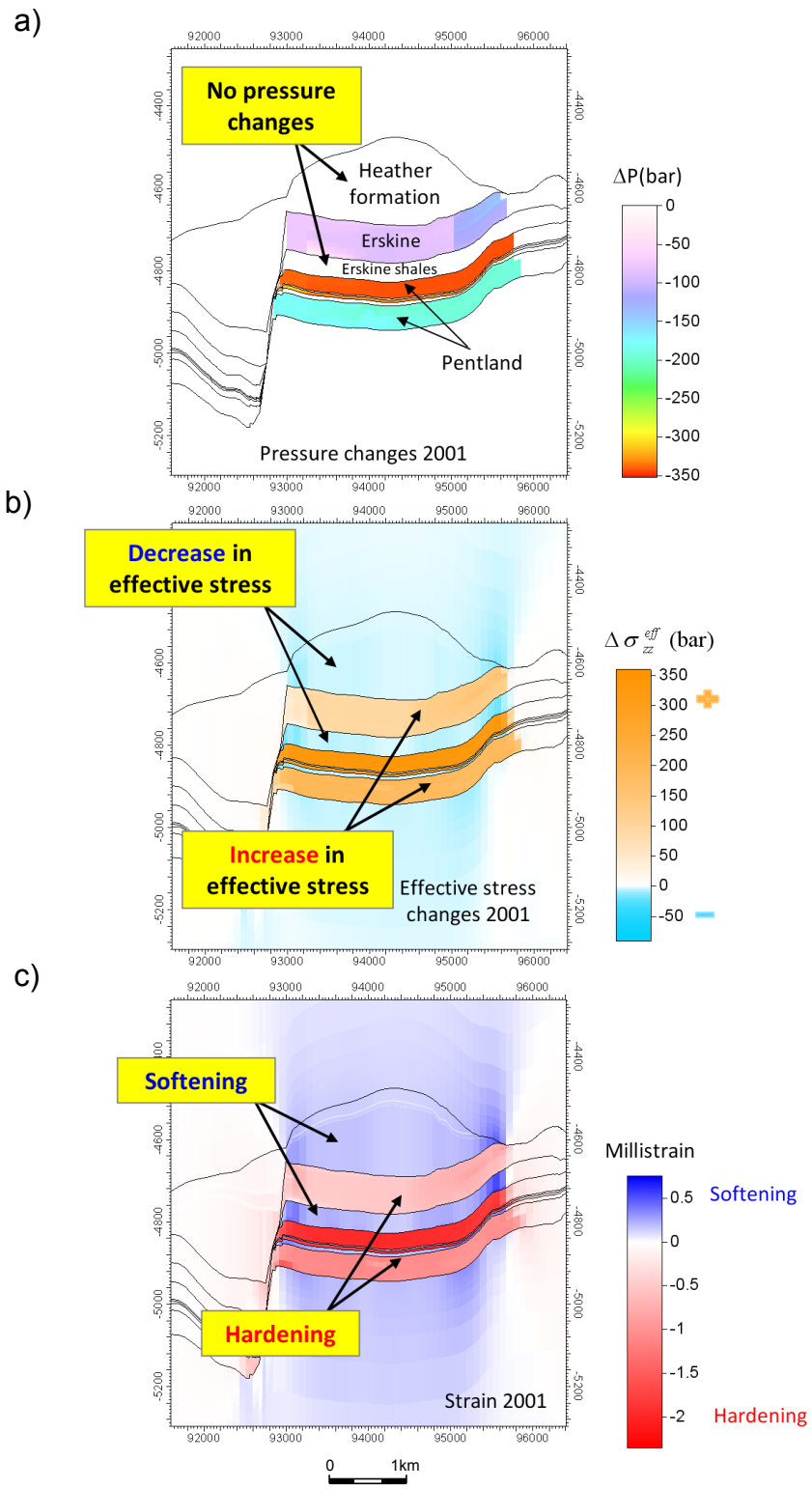

Figure 6.13: Simulated changes in (a) pore pressure, (b) effective stress, and (c) strain that resulted from five years of production for the case of inactive shale. The vertical effective stress increases inside the reservoir and decreases in the Erskine shale, the overburden Heather shale and the underburden Jurassic shale. The reservoir flow units undergo compressional strain (negative strain). However, the reservoir and no-reservoir shales undergo extensional strains (negative strain).

In this model, fractional changes in the velocity are assumed to be proportional to the fractional changes in path length so that for a vertically propagating P-wave

$$\frac{\Delta V_p}{V_p} = -R\varepsilon_{zz} \tag{6.3}$$

where ε_{zz} is the vertical strain and R is the constant of proportionality for the model. Landro and Stammeijer (2004) noted that for small changes in acoustic velocity V_p, the change in transit time across an interval of time thickness, t, and actual thickness, z, can be given by

$$\frac{\Delta t}{t} = \frac{\Delta z}{z} - \frac{\Delta V_p}{V_p} \tag{6.4}$$

Given that ε_{zz} is defined as $\frac{\Delta z}{z}$, the use of equation 6.3 and 6.4 gives

$$\frac{\Delta t}{t} = (1+R)\varepsilon_{zz} \tag{6.5}$$

Here $\frac{\Delta t}{t}$ is defined as the time stain and it is described as the vertical derivative of the time shift. Over a series of layers the time shift is computed as fellows:

$$\Delta t(Z) = \int_0^Z (1+R)\frac{\varepsilon_{zz}}{V} dz \tag{6.6}$$

From equation 6.5, it is clear that the R factor and the vertical strain govern the time stain and hence the time shift. On the basis of analysis of time-lapse seismic data sets from several locations worldwide, Hatchell and Bourne (2005b) find that the magnitude of the R factor depends on the type of rock and the strain applied. For reservoir rock undergoing compaction or compressional strains, the R factor lies in the range of 0 and 2. However for reservoir rocks undergoing extension or extensional stain, the R factor varies between 4 and 8. Nevertheless, because of the small magnitude of the extensional strain in the overburden and underburden shales, the R factor used to model the overburden time shift is higher than the one used inside the reservoir. I use the R-factor relationship to compute the synthetic time shift at the well location. The effective stress resulting from the geomechanical simulation is converted firstly to strain, then time strain by assuming an R factor. The R factor used for the Erskine sand and Pentland formation lies in the range of 0 and 2. However for the interbedded Erskine shale I use a factor of 6. In the overburden Heather shale and the underburden Jurassic shale I use an

R that ranges between 9 and 15. By integration, this provides a time shift distribution both inside and around the reservoir along the well. Figure 6.14 shows logs of pressure changes, strain, and the time shift at the well location. It is clear in Figure 6.14(c) that there is a mismatch between the predicted and the observed time shift.

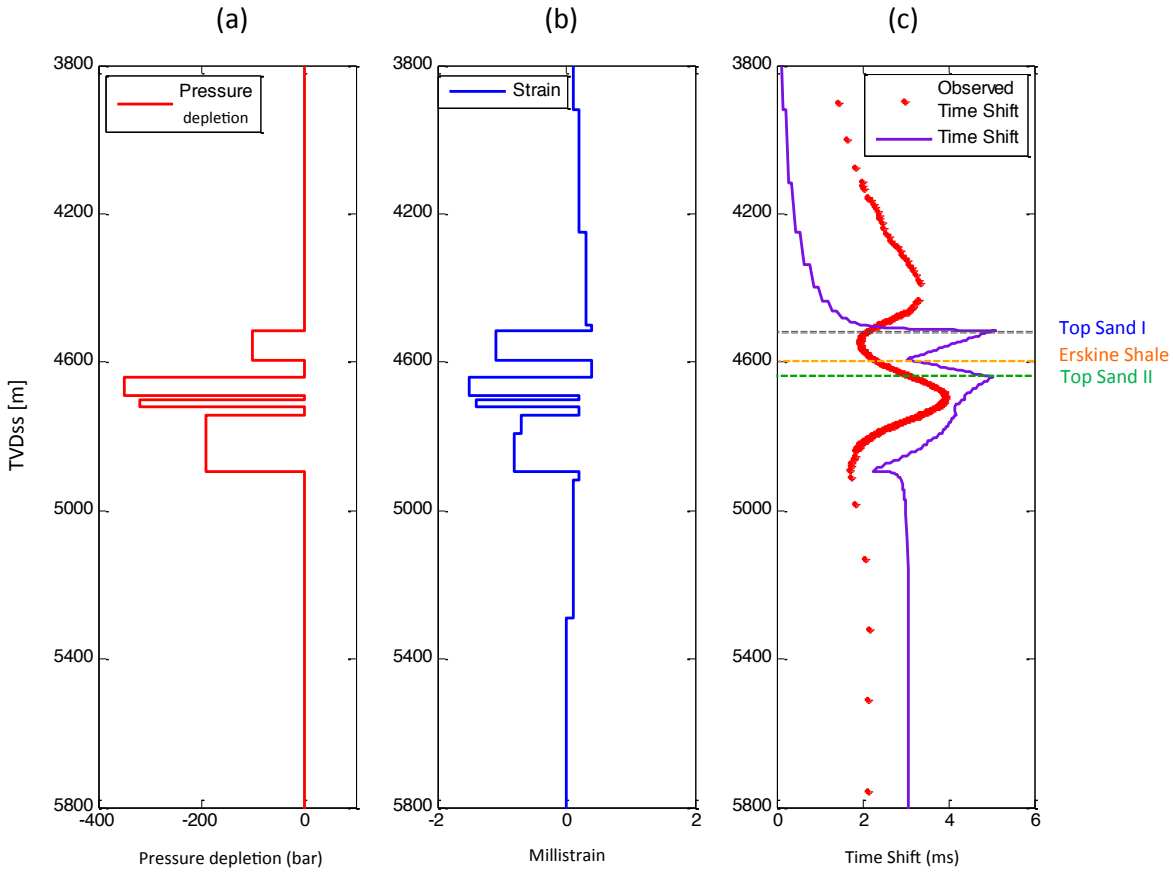

Figure 6.14: Logs of (a) pressure changes, (b) strain, and the (c) time shift at the well location after 5 years of production. Top Erskine Sand (sand I), Top Erskine shale, and Top Pentland (Sand II) are shown. The synthetic time shift is shown in purple and the observed time shift is shown with red asterisks symbols. Clearly there is a mismatch between the predicted and the observed time shift.

Time shifts accumulate through the overburden, reaching a maximum above the top of the reservoir. There is a reduction in travel time throughout the overburden Heather shale and Erskine sand. Based on the understanding built in this thesis, this time shift decrease at the level of the shale-dominated Heather formation can be explained by compressional strain caused by pressure diffusion. To investigate this further, the active shale concept is applied in the next section.

6.4.4 Active shale modelling

In this section, I examine the case of active shale and the corresponding time shift modelling. The objective of this study is to calibrate the shale properties in order to achieve a better match between the synthetic and the observed time shift. For the overburden Heather shale is now made permeable and mechanically active, however the Erskine shale is assumed to be only mechanically active. Here, I used the coupled fluid flow and geomechanical simulation to assess the combined effect of pressure diffusion and mechanical deformation in and around the reservoir. Multiple models with different properties for the reservoir and non-reservoir shales are used for the simulation and subsequent seismic modelling. For each model, the results are converted to synthetic seismic time shifts and then compared to the real 4D time shifts. This process is repeated until a match between the observed and the predicted time shift is achieved. This quantitative comparison of the synthetic and observed time shift helps to calibrate the shale properties. This calibration could give rise to a model which more reliably predicts the pore pressure and stress tensor. After running several scenarios, the model with a permeable Heather shale and impermeable Erskine shale leads to the best match between the observed and the predicted time shift. In this particular model, the permeability of the Heather shale is in the range of 10μD to 100μD. However the Erskine shale is assumed to almost impermeable, with a permeability less than 0.001nD. For this, the output of the simulation is converted to synthetic shifts using the R-factor relationship described in the previous section. First the effective stress is converted to strain and then to time strain by the R-factor relation of 6.5. As in the previous case, the R factors used for the Erskine sand and Pentland formation range between 0 and 2. In the Erskine shale, because of the extensional strain, I use an R factor of 6. However, because of the compressional strain induced by the pressure diffusion in the overburden shale, the R factor I use in the Heather formation is

between 0 and 3. For the formations above the Heather shale and the underburden Jurassic shale I use an R factor that ranges between 9 and 15. Integration of the time strain over depth provides the time shift distribution thought out the reservoir and surrounding rocks. Figure 6.15 shows the logs of pressure changes, strain and time shift at the well location. It is clear from Figure 6.15(c) that the predicted time shift is in good agreement with the observed.

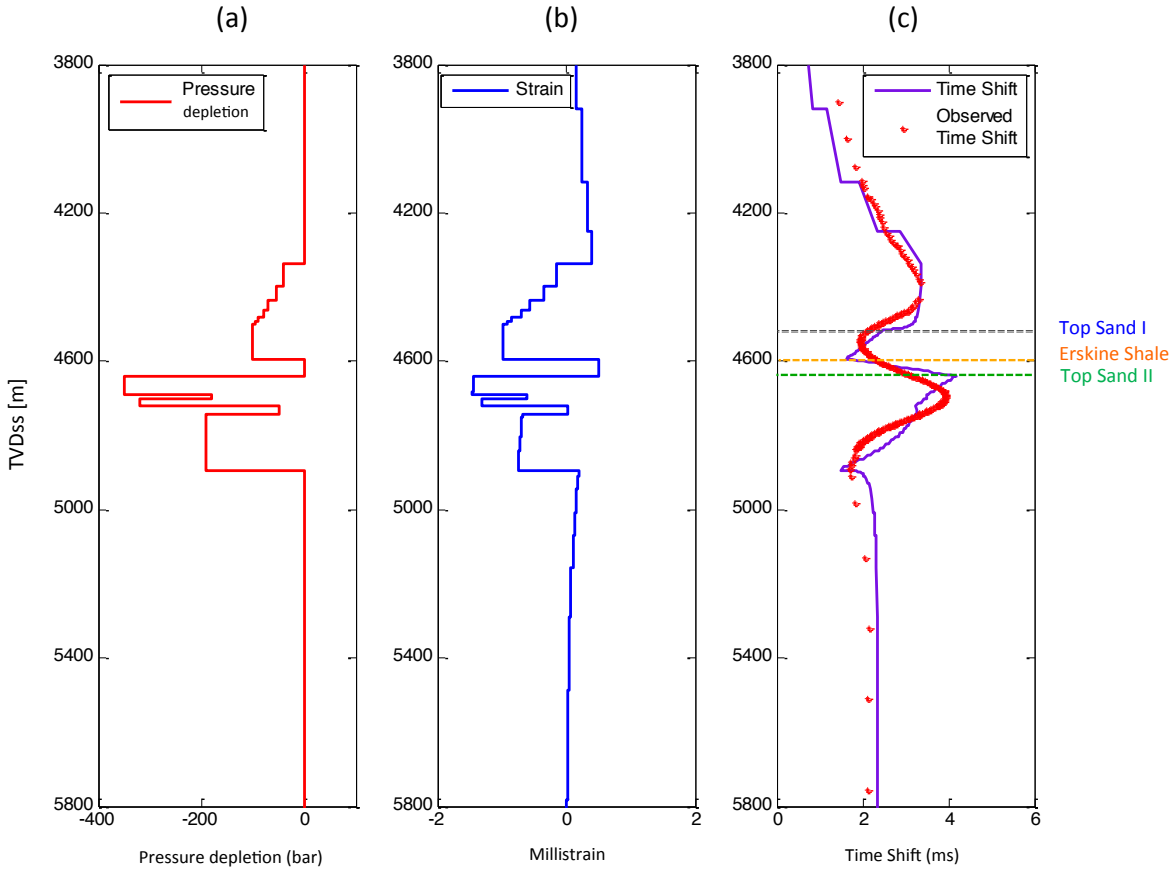

Figure 6.15: Logs of (a) pressure changes, (b) strain, and the (c) time shift at the well location after 5 years of production for the case of active shale. The permeability of the Heather shale is in the range of 10μD and 100μD however the Erskine shale is assumed to almost impermeable. Under these assumptions, the predicted time shift is in good agreement with the observed. The synthetic time shift is shown in purple and the observed time shift is shown with red asterisks symbols.

Quantitative comparison of the model results with the observed 4D seismic time shifts has provided a method to calibrate the properties of the shale-dominated Heather formation and the Erskine shale. The best match model is now used to predict the pore pressure and stress changes across the entire field. Figure 6.16 shows the pore pressure, effective stress, and strain changes that resulted from the coupled simulation after five years of production. In this model, the Heather shale formation is permeable and mechanically active (the permeability ranges between 10μD and 100μD). Consequently, due to the pressure diffusion process, coupled simulation shows a pore pressure decrease at the level of the Heather shale formation. This decrease of pore pressure triggers an increase of effective stress and vertical compressional strain in the Heather shale formation (Figure 6.16(b) and 6.16(c)). Also in the best match model, the Erskine shale is assumed to be impermeable and not responding to the pressure diffusion. However as the pore pressure decreases in the Erskine sand and the Pentland formation, the effective stress and the vertical strain in the Erskine shale decreases (Figure 6.16(b) and 6.16(c)).

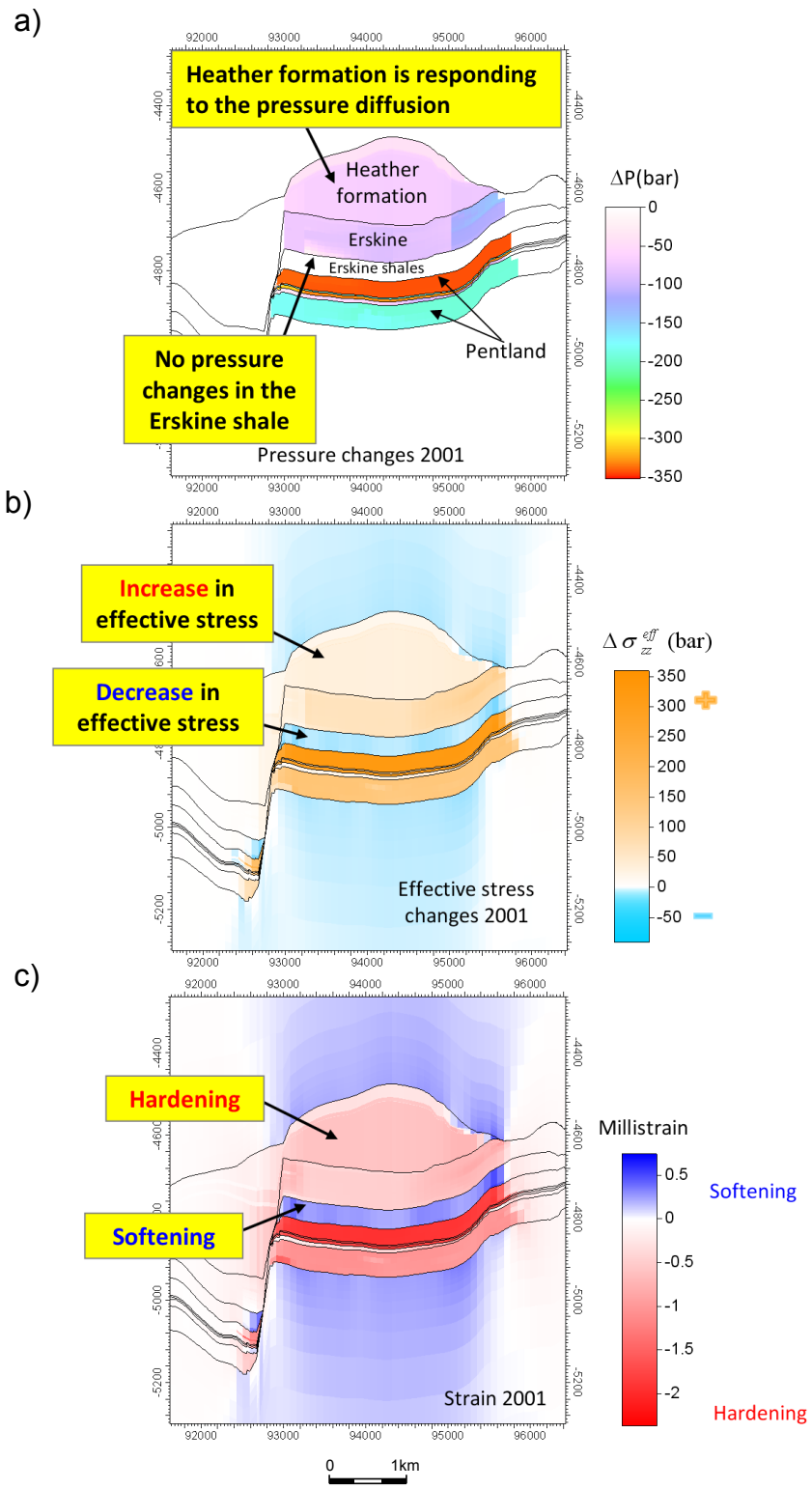

Figure 6.16: Simulated changes in (a) pore pressure, (b) effective stress, and (c) strain that resulted from five years of production for the case of active shale. The Heather shale is assumed permeable and mechanically active. Due to the pressure diffusion process, the decrease of pore pressure in the Heather formation triggers an increase of effective stress and vertical compressional strain. The Erskine shale is assumed to be impermeable and therefore it is not responding to the pressure diffusion. As the pore pressure decreases in the Erskine sand and the Pentland formation, the effective stress and the vertical strain in the Erskine shale decreases.

To further investigate the effect of pressure diffusion in the Heather, Erskine and the Pentland on the observed 4D seismic response, time shift maps inside these formations are generated. Map of Time shift across the Heather and Erskine sand is shown in Figure 6.17(a). To eliminate the time shifts accumulated above the Heather formation, the time shifts map is the result of the difference between the time shifts at the base of the Erskine sand and the time shift at the top heather (Base cretaceous). Around the depleted area (highlighted with dashed line) negative time shifts in the range of -2.5ms are observed. This reflects the speed up inside the heather and Erskine sand due to the pressure depletion and the associated compensational strain. In a similar way, the difference between time shifts at the base Pentland and time shifts at the Top Pentland shows a speed up (negative time shifts) across the Pentland formation (Figure 6.17(b)). Here, both observations are in agreement with those obtained from the amplitude changes across the field. Here the time shifts are calculated using method of fast cross-correlation proposed by Hale (2007) that uses Gaussian tapers so that 3D 'blobs' of data are cross-correlated. The block size of the cross correlation is set to 10m x 10m x 44ms.

The results of the simulation are converted into synthetic time shifts using R-factor relationship described in the Section 6.4.3. For this, the physical strain is converted to time strain, and then by integration the synthetic time shift across field is computed. Figure 6.18 compares the time-lapse time shifts observed from the stacked data (Figure 6.18(a)) with those calculated from coupled geomechanics and pressure diffusion simulation (Figure 6.18(b)). A similar distribution and magnitude of time-lapse time shift is observed in both the synthetic and the observed data. Based on these results, the match between synthetic and observed time shifts is only achieved when the model with the active shale concept incorporated is used in the simulation. For this model the Heather shale is assumed to be permeable and is responding to pressure diffusion. However the Erskine shale is considered to be an effective pressure barrier and is undergoing extensional strain.

The comparison between the observed (Figure 6.18(a)) and the modeled time shifts (Figure 6.18(b)) is not only showing similarity but also some differences. The observed time shifts show a clear anomaly that is crossing the main fault, however the modeled time shifts are contained by the main fault. Here the simulation model used for the time shifts calculation is assuming the main fault to be sealing. The analysis of the observed 4D seismic data stresses the possibility of a leakage within the main fault. Interestingly the observed amplitude across the field (Figure 6.8) is showing a compartmentalized 4D amplitude anomaly at the edges of

the main fault. Based on these observations, clearly the assumption of sealing fault can directly affect the seismic modeling. The fault transmissibility is not the scope of this thesis and therefore further detailed understanding of fault transmissibility and its effect on time lapse seismic amplitude and time shifts is recommended.

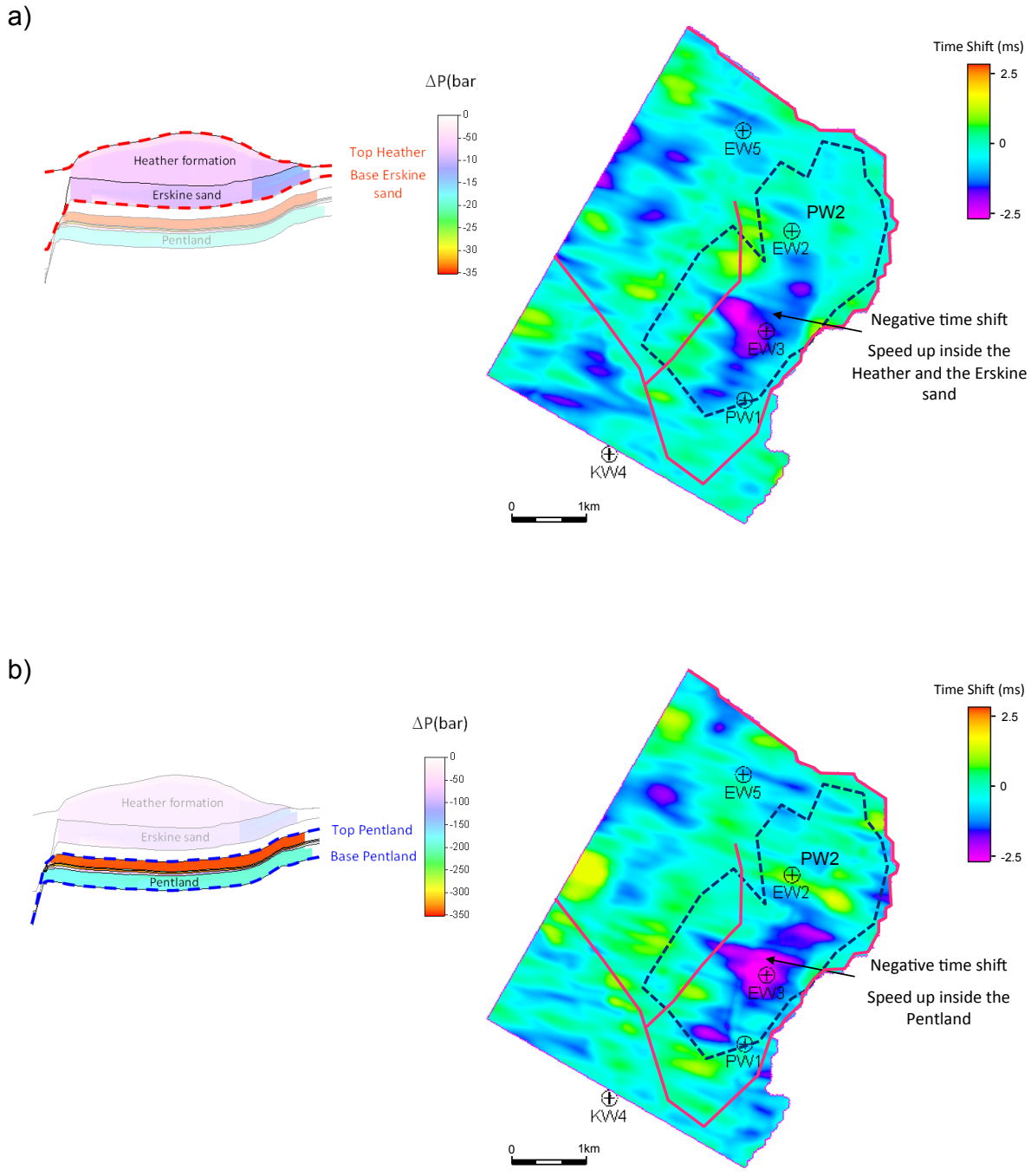

Figure 6.17: (a) Time shifts map across the Heather and Erskine formation (b) time shifts map across the Pentland formation. Negative time shifts (-2.5ms) reflect the speed up in time travel induced by the pressure depletion inside the Heather, Erskine and the Pentland. Formation.

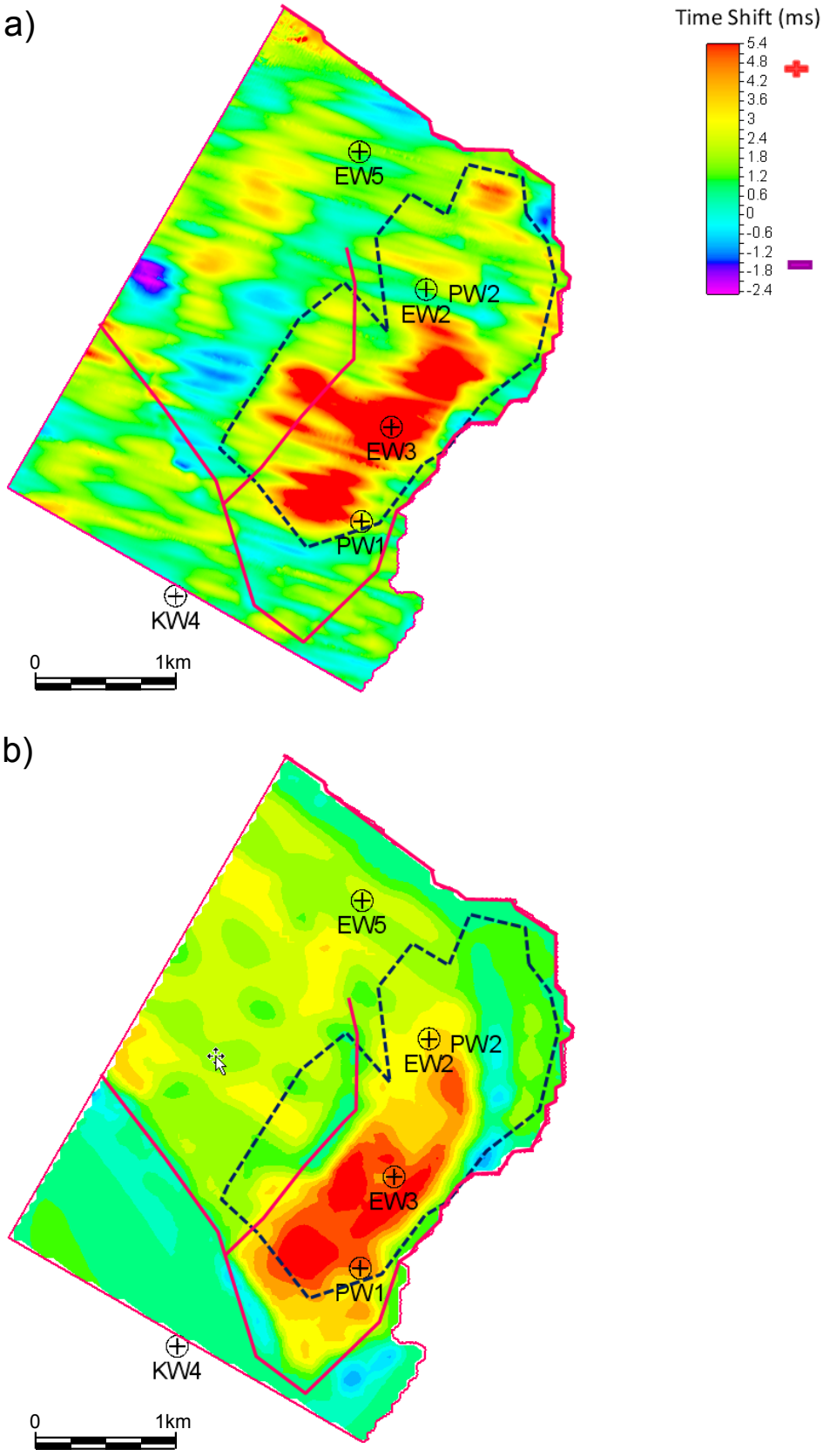

Figure 6.18: Maps of average (a) time-lapse time shifts observed from the stacked data and (b) time shifts calculated from the coupled geomechanics and pressure diffusion simulation using the active shale concept.

6.5 Reservoir geohazards

In this section I used the calibrated model incorporating active shales concept to examine the redistribution of stress in the vicinity of the wellbore at the level of the shale-dominated Heather formation and the Erskine shale. Here the deformation and risks that might occur in response to the redistribution in stress is discussed. In this work, the principal minimum and maximum horizontal stress σ_h and σ_H that resulted from the coupled simulation is used to investigate the variation of stress in the vicinity of simplified model of a circulate hole in an elastic medium under the assumption of plane strain (Kirsch, 1898; Jaeger and Cook, 1979). The mathematical model of stress redistribution near the borehole is described in Appendix C. Figure 6.19 shows an example of the effective hoop stress $\sigma_{\theta\theta}^{eff}$ that can occur around the borehole at Heather shale formation (Figure 6.19(a)) and the Erskine shale levels (Figure 6.19(b)). The pore pressure, maximum, and minimum horizontal stresses used in this calculation are taken from the coupled geomechanics and fluid flow simulation. At the level of the Heather formation shale, due to the pressure diffusion and pore pressure decrease, the effective hoop stress increases and become strongly compressive at an azimuth of $\theta = 90^{\circ}$. This increase of effective hoop stress will escalate the shear stress and hence can trigger shear failure on the plane of the shear stress. However at the level of the Erskine shale, the effective hoop stress $\sigma_{\theta\theta}^{eff}$ at the borehole decreases and become negative at an azimuth of $\theta = 0^{\circ}$ (Figure 6.19(b)). The negative effective hoop stress leads to a tensile stress, which might results in a tensile failure along the plane perpendicular to the tensile stress. These results suggest that monitoring the stress changes at the wellbore in the Erskine shale and the Heather formation is very useful to prevent well deformation and failure. Furthermore, based on the coupled fluid flow and geomechanical simulation, the Erskine shale is acting as an effective pressure barrier, and hence it is overpressured relative to the surrounding formations and could be a high-risk formation for future drilling programs. Figure 6.20 shows a schematic illustration of the lithostatic, fracture, pore and hydrostatic pressures versus depth. The drilling tolerance window between the pore pressure and the fracture pressure is very narrow at the Erskine shale. These findings suggest that the calibration of the drilling mud pressure at the Erskine shale is very useful for safe well paths.

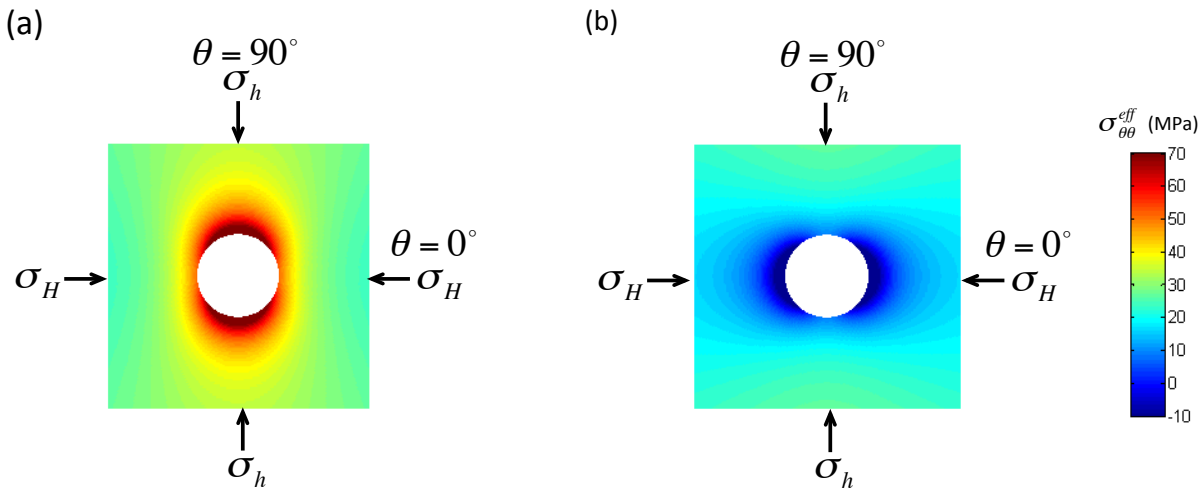

Figure 6.19: Variation of effective hoop stress in the vicinity of a borehole at the (a) Heather shale formation and (b) Erskine shale. (a) At the Heather formation shale the effective hoop stress increases and become strongly compressive at azimuth $\theta = 90^\circ$. (b) In the Erskine shale the effective hoop stress $\sigma_{\theta\theta}^{eff}$ at the borehole decreases and becomes negative at an azimuth $\theta = 0^\circ$.

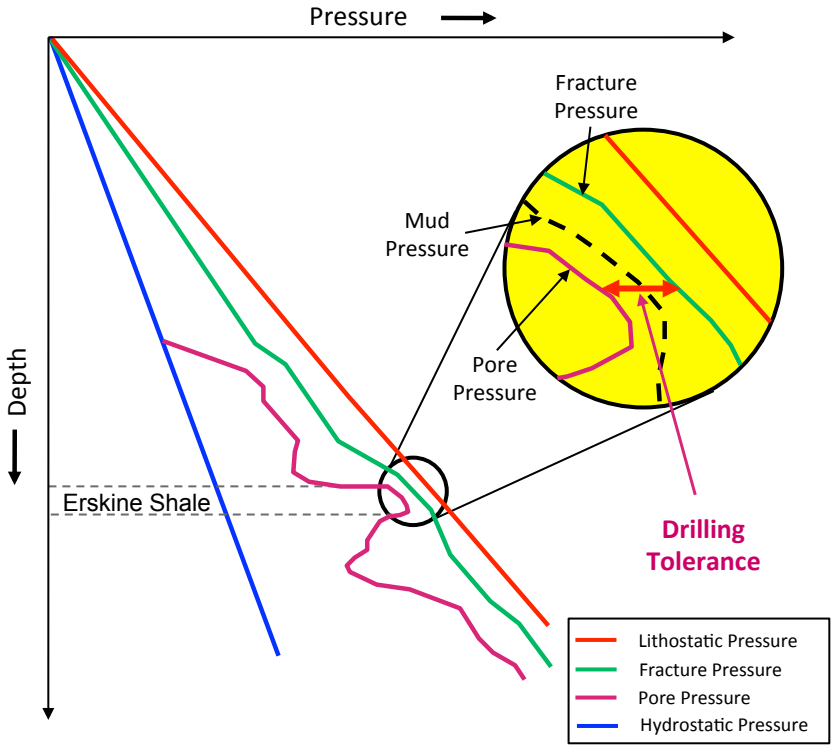

Figure 6.20: Schematic illustration showing the drilling window at the Erskine shale. The drilling tolerance between the pore pressure and the fracture pressure is very narrow.

6.6 Conclusions

Shales are often regarded as inactive barriers in the reservoir simulation model and the surrounding rocks. Whilst this appears the correct approach for fluid flow modelling purposes, it is inaccurate for the pressure component of this process. In this chapter, 4D seismic data have been used to investigate the combined effects of geomechanics and pressure diffusion on the intra-reservoir and non reservoir shales in the high pressure high temperature (HPHT) Erskine field in UK central North Sea. Geomechanical modelling and conversion of model results to synthetic seismic time shifts allows a quantitative comparison of models with the observed 4D seismic time shifts. This comparison helps to calibrate the range of permeability for the Heather formation and the Erskine shale units. This calibration could give rise to a model which more reliably predicts the pore pressure and stress tensor, allowing more confidence in selecting safe well paths, mud weights, and casing schemes. The observed time shifts from this case study are consistent with the combined effects of geomechanics and pressure diffusion, and are preferable to taking into account only the geomechanical effects. The results suggest that the Heather formation, which is silty marine shale, has permeability values above 10μD and below 100nD. However the clay rich Erskine shale has a very low permeability. The results also demonstrate that the Heather formation undergoes pressure diffusion and consequently the trapping mechanism at the Heather shale is highly uncertain. The Erskine shale, however acts as an effective pressure barrier, and hence it is overpressured relative to the surrounding formations and could be a high-risk formation for future drilling programs. Also the analysis of the stress distribution at the wellbore for the Heather formation shale and Erskine shale suggest that a careful calibration of drilling mud weight and stress monitoring at the well casing could be very useful to prevent the risk of well deformation and failure.

CHAPTER

SEVEN

7 Conclusions and recommendations

Conclusions and recommendations
for future research

7.1 Summary and conclusions

This thesis has presented a study of the implications of the reservoir and non-reservoir shales for time lapse seismic interpretation. This analysis is based on the use of the active shale concept, in which the reservoir and non-reservoir shales are made permeable and mechanically active. Implementation of these phenomena allows the assessment of the pressure development and the mechanical deformation across the interbedded reservoir shales as well as the surroundings: overburden, underburden and sideburden shales.

In Chapter 2, I presented a geological characterization of the shale. Here, shale structure and geometry, such as thickness and lateral extension, is examined against the depositional environment. Furthermore, shale fluid flow transport and mechanical properties are presented and discussed. Based on this literature study, I concluded that shales have a fairly moderate porosity (5 to 20%) and a finite permeability (1nD to 1μD) that can affect the pressure evolution. This literature review was essential to understand the key properties that might affect the dynamic behaviour of the shale.

In Chapter 3, the findings from Chapter 2 are used to calculate the physical effects of pore pressure diffusion both analytically and then numerically for a simplified geological structure based on a real field case. The results indicate that pressure diffusion could have significant penetration depth in the reservoir and the non-reservoir shale over production time scales. These findings helped to further understand what to expect from pore pressure diffusion in the shales.

In Chapter 4, I studied the combined effect of geomechanics and pressure diffusion of intra-reservoir shales on the 4D seismic response. Here, the computation is based on the nucleus of strain method of Geertsma (1973). The numerical calculations indicate that intra-reservoir shale initially experiences a mechanical extension due to the stress created by the compacting sandstones. However as time progresses pressure diffusion reverses this effect near to and around the reservoir, and these shales then experience a compaction (HajNasser and MacBeth 2010, MacBeth et al. 2011). This effect adds to the list of factors contributing to a modification of the stress sensitivity when applied to the in situ reservoir state. Under certain conditions (low net-to-gross, frequently repeated seismic, thick shales and low shale permeability) the reduction in stress sensitivity anticipated from my modelling may in fact

reverse the polarity of the usually expected response, causing an apparent softening instead of hardening of the reservoir impedance with depletion.

In Chapter 5, a fully coupled geomechanical and fluid flow simulation is presented to validate the findings in Chapter 4. The results of the coupled simulation were similar to those generated using the nucleus of strain. Also, I presented the possible 4D seismic responses associated with the combined geomechanics and pressure diffusion into the reservoir and non-reservoir shales. For this, I presented a workflow on the integration of the coupled simulation and the forward seismic modelling. I tested this workflow on synthetic data. The numerical computation gives similar results to those presented in Chapter 4. I concluded that thinner shales equilibrate quickly but also experience a greater geomechanical response initially. Thicker shales equilibrate at a slower rate but experience a smaller initial mechanical impulse. Consequently, for a monitor time period of a few months, a reservoir with shales of a few metres thick might exhibit an anomalous softening response, whilst this may only be possible for a monitor period of 10 years if thicker 5 to 10m shales are present.

Finally, in this thesis I presented two case studies where shale is an abundant lithology, which might have an impact on the 4D seismic response. The case studies for Schiehallion and the Erskine field are presented in Chapters 5 and 6 respectively.

7.1.1 Schiehallion field

In Chapter 5, a segment of the Schiehallion field was studied. For this, the reservoir and non-reservoir shales are made permeable and mechanically active. Next, a coupled fluid flow and geomechanical simulation is run based on a built geomechanical model. Finally, the pore pressure, saturation, and stress changes are used to generate the synthetic seismic. Here, the forward seismic modelling workflow takes into account the updated porosity that resulted from the coupling between geomechanics and fluid flow. When the shales are inactive, the modelled seismic shows abrupt discontinuous values and high intensity reflectivity along events – related to the positions of the shales. These features change as the shales become active, and it is also possible to see some evidence of a polarity shift in the seismic at the location of high-density shale. At some locations where NTG is low, the polarity of the

synthetic impedance changes and the corresponding synthetic 4D amplitude in the case of active shale are different from those where shale is inactive. Interestingly the synthetic 4D seismic amplitude generated with that active shale is in agreement with the observed 4D amplitude. These results suggest that the integration of the combined effects of geomechanics and pressure diffusion of the intra-reservoir and the surrounding shales into the seismic forward modelling can affect the effective seismic response. The active shale concept could be another additional parameter to be considered in order to achieve a better prediction and more reliable synthetic seismic modelling. In addition, this workflow of seismic modelling can offer the opportunity to have a better calibration of the dynamic and the static properties of the shales.

7.1.2 Erskine field

Chapter 6 presents the application of the active shale concept for the HPHT Erskine Field. For this, I presented the geological background and the seismic anomalies. For this case study I performed a 3D finite element based on geomechanical and fluid flow simulation where the reservoir and non-reservoir shales are active. In this work, I converted the results of the coupled geomechanical and fluid flow simulation to synthetic seismic time shifts. This has allowed me to perform a quantitative comparison of models with the observed 4D seismic time shifts. This comparison helps to calibrate the range of permeability for the Heather formation and the Erskine shale units. This calibration could give rise to a model which more reliably predicts the pore pressure and stress tensor, allowing more confidence in selecting safe well paths, mud weights, and casing schemes. The observed time shifts from this case study are consistent with the combined effects of geomechanics and pressure diffusion, and are preferable to taking into account only the geomechanical effects. The results suggest that the Heather Formation, which is silty marine shale, has permeability values above 100nD and below 10μD. However the clay rich Erskine shale has a very low permeability values below 0.001nD. The results also demonstrate that the Heather formation undergoes pressure diffusion and consequently the trapping mechanism at the Heather shale is highly uncertain. The Erskine shale, however acts as an effective pressure barrier, and hence it is overpressured relative to the surrounding formations and could be a high-risk formation for future drilling programs.

7.2 Future work recommendation

The methodology presented in this thesis is a proposal that the dynamic behaviour of the shale should be taken into account when assessing the 4D seismic data. The integration of the active shale concept into the 4D seismic interpretation has been well established after three years of research and tests on synthetic and real field data. However, further research is suggested in order to refine and make this approach more robust and applicable. This further research could be addressed under the following categories:

7.2.1 Use of Active shale concept to calibrate the 4D seismic analysis

As discussed throughout this thesis, coupled fluid flow and geomechanical modelling in which the reservoir and non-reservoir shales are considered *active* is proven to be a very valuable element to have a better understanding of 4D seismic signature. Therefore, the practice of *active* shale concept should be always used in performing fluid flow and geomechanical simulation. With the growing focus on seismic history matching nowadays, the findings of the this thesis suggest that the *active* shale concept can be incorporated into the close-the-loop workflow with the objective of updating the static and dynamic reservoir model to match production data, time lapse amplitudes, and time-lapse time shifts (Figure 7.1). The coupled fluid flow and geomechanical simulation is part of the workflow, the resulting fluid saturation, stress, and strain changes are in tern used to compute the corresponding amplitude and time shifts response and then compared to the field data. In order to achieve a better match between the synthetic and field 4D seismic data, an optimization algorithm is used to update and improve the reservoir model. Updating the fluid flow and mechanical properties as well as implementing the *active* shale concept will allow to fit production, time lapse amplitude and time shift data more accurately. This integrated workflow of coupled geomechanics and fluid flow simulation and seismic modelling is considered as key component for building accurate reservoir model. Reliable reservoir models are used to predict future reservoir behaviour and used to design optimal wells paths, and extend the production lifetime of the wells (Tura et al., 2005)

The 4D seismic data has proven to be a useful tool for reservoir surveillance and management. To maximize the value of 4D seismic data, planning for 4D is a critical part of an overall field lifecycle strategy. Within this cycle, the seismic data plays an explicit role

between survey design and reservoir characterization. Early in development planning, 4D seismic models based on reliable reservoir model are used to estimate the magnitude and interpretation of the 4D response, evaluate optimal survey repeat times, and potential business impact. To achieve this, a multidisciplinary approach in which collaboration among asset team geoscientist, engineers, and geophysicists is require.

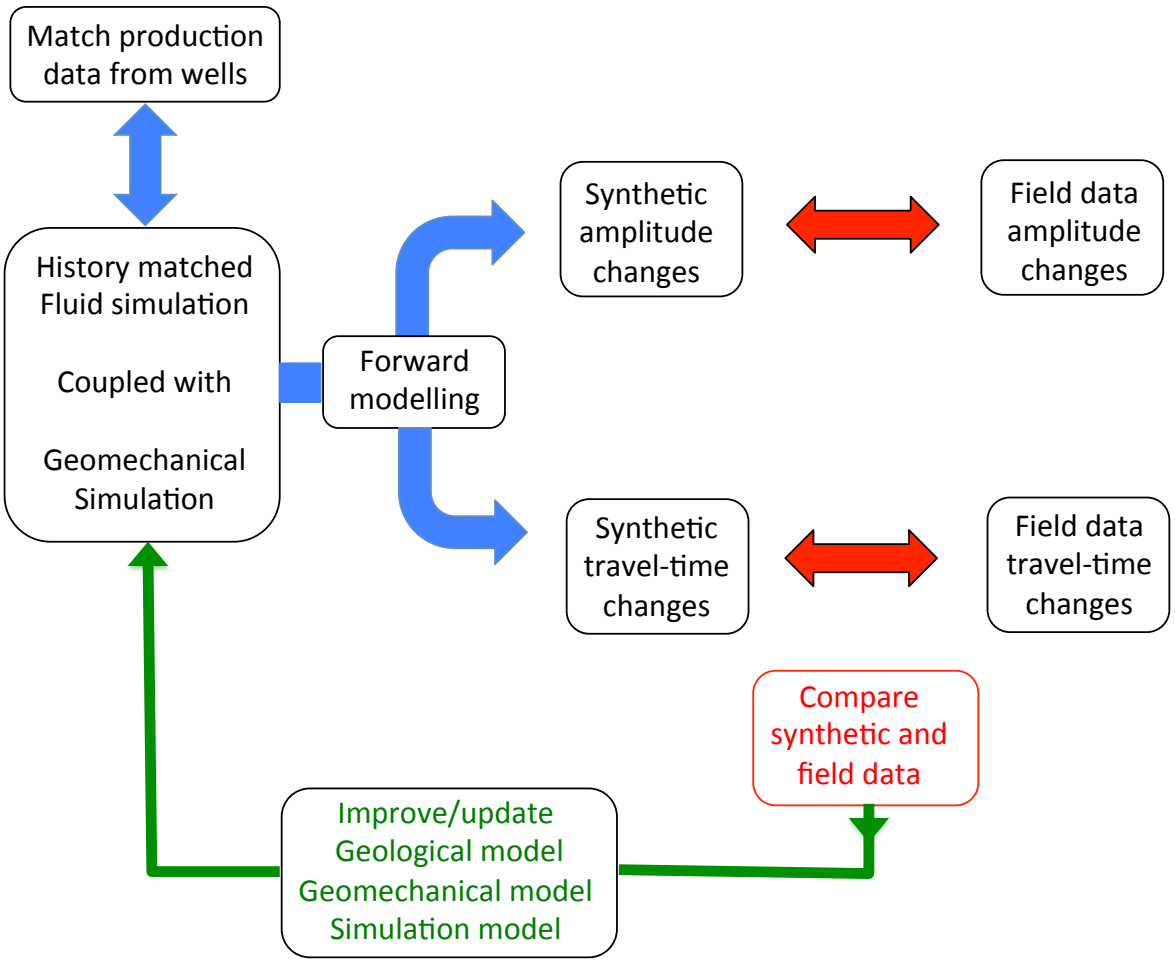

Figure 7.1: "Closing the loop" workflow to update the static and dynamic reservoir model to match production data, time-lapse amplitudes, and time-lapse time shifts via a coupled fluid flow and geomechanical simulation (adopted from Tura et al., 2005)

7.2.2 Shale anisotropy

The work presented in this thesis is based on the assumption that shale is isotropic. Many shales encountered in the subsurface can be described to a good approximation as being transversely isotropic (Sayers, 2010). Nevertheless, the shale anisotropy microstructure could play a decisive role in the fluid flow and seismic wave propagation. A study by Banik (1984) on 21 seismic data sets from the North Sea found an excellent correlation between the occurrences of depth errors obtained from surface seismic data and the presence of shales in the subsurface. Failure to account for shale anisotropy in seismic processing can lead to errors in normal-movement (NMO) correction; dip movement-out (DMO) correction, and analysis of amplitude variation with offset. Shale anisotropy also affects variation in stresses in sedimentary basins, along with containment of hydraulic fractures (Higgins et al., 2008). This results in significant differences in mechanical properties parallel to and perpendicular to laminations (bedding planes). Failure to consider the effect of this anisotropic behaviour can result in underestimated stresses that in turn lead to incorrect conclusions about safe trajectories and mud weights. (Khan et al., 2011). Introducing shale anisotropy to the active shale concept will be very beneficial to obtain a more reliable information on reservoir in-situ stresses, pore pressure prediction, lithology deformation from seismic data. For this it is highly recommended to properly characterize shale anisotropy. Some of these issues are currently being addressed by another PhD project within the ETLP (Edinburgh Time-Lapse Project) group.

7.2.3 Mechanical deformation and shale failure

In this thesis I assumed that shales can tolerate the mechanical behavior without failure. Nevertheless, shale failure and fracture reactivation can be associated with stress and pore pressure changes. Injection and production cause changes in pore pressure and effective stress. The response of fracture to an applied stress is important to shale characterization. This phenomenon is mainly driven by the shale strength and also whether the shale is brittle or ductile. Shale can develop fractures as results of brittle failure caused by stress changes. These fractures could have an important effect on fluid flow transport and mechanical

properties, and hence the seismic elastic properties. The fractures in the shales can increase the porosity and permeability. Because fractures have preferred orientations, they can lead to significant permeability anisotropy, and hence to unexpected pressure development across the field.

As future work, modelling the orientation and density of fractures associated with stress changes in the reservoir and non-reservoir shales is necessary to optimize the sealing capacity of the shales. Also, the integration of fracture modelling into the coupled geomechanical and fluid flow simulation and into the forward seismic modelling will allow the seismic characterization of the fractures. This could be the topic of another research project.

7.2.4 Shale geomechanics and visco-plasticity

In this study I only considered the linear elastic behavior of stress deformation. Characterization of the mechanical properties of reservoir and non-reservoir shales often focuses on its elastic properties through sonic log data and laboratory tests on core samples; however, it is also important to understand the time-dependent mechanical properties of these rocks in order to predict the long-term behavior over production time scales. Recent laboratory studies by (Sone and Zoback, 2011) suggest that deformation of some shale rocks occur through elastic-visco-plastic constitutive behavior, where a significant portion of the deformation takes place by a non-linear response not predicted by linear elasticity. Failing to address the time-dependent response of these reservoir rocks would, for instance, lead to a significant under-estimation of stress and shale properties changes. As future work, it is recommended to address the visco-plastic deformation when assessing the stress and strain changes. Also introducing this concept into the coupled simulation and the seismic forward modelling allow examination of the corresponding time lapse seismic response. Understanding controls on the visco-plastic deformation of these samples helps understand the potential well instability. In addition, this is important for designing hydraulic fracturing operations in shale gas reservoirs.

7.2.5 Unconventional shale gas

In this thesis, I focused on the brine-saturated shales with no hydrocarbon potential. However with the growing interest in shale gas. The active shale concept could be very useful concept to assess the geomechanical and the fluid flow behaviour of the shale. Geologists, geophysicists and engineers are coming to learn that shale can be remarkably different, and that those differences have a substantial impact on how hydrocarbons are generated, and what the best technologies are for extracting gases and fluids from these ultralow-permeability rocks (Hart et al., 2011). In similar way to the work done here for the brine-saturated shales with no hydrocarbon potential, a dynamic seismic characterization of the gas shale will help to understand the pressure development across the shale and the associated stress changes. This will allow a better management of the hydraulic fracturing.

As future work, integrating sedimentological, stratigraphic, petrophysical, and mechanical analysis will help to illustrate depositional controls on geomechanical and seismic properties of the gas shale. In turn, this will permit a more calibrated analysis to be used to better plan hydraulic fracturing. The seismic data available in Haynesville, Bekken (US and Canada), Monteney, Marcellus, Eaglebine, Utica, and the Tuscaloosa Marine shale has provided a valuable subsurface information that allow a more reliable dynamic characterization of the shale gas. In addition, a limited 4D seismic studies have shown the importance of a prestack seismic data analysis in identifying rock strength and stress field orientation which are very valuable in optimizing the drilling and the hydraulic fracturing activities.

Appendix A

A. The concept of nucleus of strain

A.1. Introduction

Expressions for the internal displacement due to a nucleus of strain in a poroelastic half-space with a traction-free surface are provided by Geertsma (1966). In this document, equations to calculate the full strain tensor due to a nucleus of strain are given by taking the appropriate derivatives of the x, y and z components of displacement.

A.2. Displacements

The coordinate system used by Geertsma is shown in Figure B.1. Note that the z-axis is taken as positive in the downward direction. The expression for displacement due to a unit pressure change outside a nucleus at depth z = c and a radial distance $r^2 = (x-a)^2 + (y-b)^2$ from the nucleus located at (a, b, c) as:

$$\overrightarrow{u_i^*} = \frac{C_m}{4\pi}\left[\frac{\overrightarrow{R_1}}{R_1^3} + \frac{(3-4\nu)\overrightarrow{R_2}}{R_2^3} - \frac{6z(z+c)\overrightarrow{R_2}}{R_2^5} - \frac{2\vec{k}}{R_2^3}\{(3-4\nu)(z+c)-z\}\right] \quad \text{(A.1)}$$

where

$$R_1^2 = (x-a)^2 + (y-b)^2 + (z-c)^2 \quad \text{(A.2)}$$

$$R_2^2 = (x-a)^2 + (y-b)^2 + (z+c)^2 \quad \text{(A.3)}$$

$$\overrightarrow{R_1} = (x-a)\vec{i} + (y-b)\vec{j} + (z-c)\vec{k} \quad \text{(A.4)}$$

$$\overrightarrow{R_2} = (x-a)\vec{i} + (y-b)\vec{j} + (z+c)\vec{k} \quad \text{(A.5)}$$

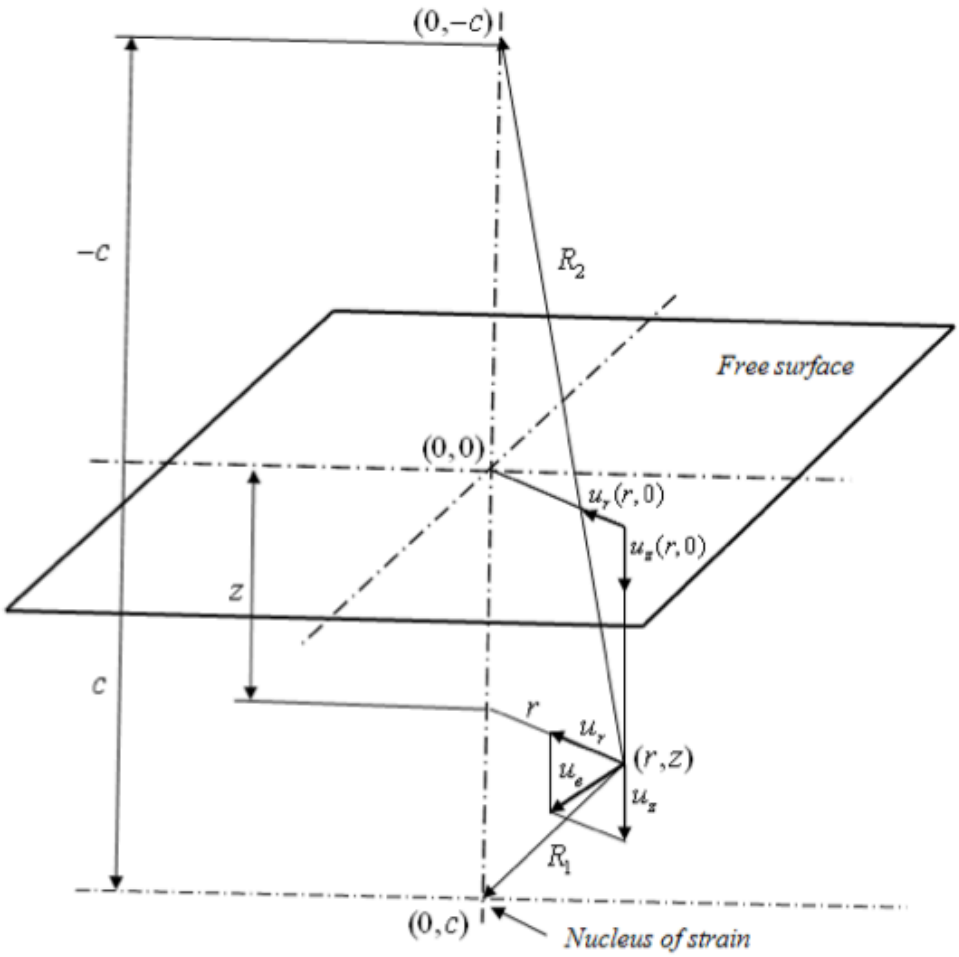

Figure A.1: Figure taken from Geertsma (1966), defining the geometry used in the subsequent equations.

and $\vec{i}$, $\vec{j}$, and $\vec{k}$ are the unit vectors in the x, y, and z directions respectively. The constant C_m is the uniaxial compressibility coefficient which is given by:

$$C_m = \frac{(1-\beta)(1-2\upsilon)}{2G(1-\upsilon)} \tag{A.6}$$

where β is given by the ratio rock bulk compressibility to rock matrix compressibility C_b/C_r . Redefining $x' = (x-a)$ and $y' = (y-a)$ for ease of notification, the individual components of the displacement are:

$$u_x = \frac{C_m}{4\pi}\left[\frac{x'}{R_1^3} + \frac{(3-4\upsilon)x'}{R_2^3} - \frac{6z(z+c)x'}{R_2^5}\right] \tag{A.7}$$

$$u_y = \frac{C_m}{4\pi}\left[\frac{y'}{R_1^3} + \frac{(3-4\upsilon)y'}{R_2^3} - \frac{6z(z+c)y'}{R_2^5}\right] \tag{A.8}$$

$$\text{and } u_z = \frac{C_m}{4\pi}\left[\frac{z-c}{R_1^3} + \frac{4\upsilon(z+c)-(z+3c)}{R_2^3} - \frac{6z(z+c)^2}{R_2^5}\right] \tag{A.9}$$

A.3.Strain tensor

The tensor is defined as

$$\varepsilon = \begin{bmatrix} \varepsilon_{xx} & \varepsilon_{xy} & \varepsilon_{xz} \\ \varepsilon_{yx} & \varepsilon_{yy} & \varepsilon_{yz} \\ \varepsilon_{zx} & \varepsilon_{zy} & \varepsilon_{zz} \end{bmatrix} \tag{A.10}$$

The individual components of the strain tensor are given by:

$$\varepsilon_{ij} = \frac{1}{2}\left(\frac{\partial u_i}{\partial x_j} + \frac{\partial u_j}{\partial x_j}\right) \tag{A.11}$$

where the subscripts *i* and *j* can be the numbers 1,2,3 representing the x-, y-, and z-axis respectively.

To populate the strain tensor, nine derivatives are required (the derivatives with respect to x, y and z of all three components of displacement).

A.4.Stress tensor in 3D

In three dimensions, the stress is completely described by the stress tensor which we have all together nine stress components related to one point in three dimensions as following:

$$\sigma = \begin{bmatrix} \sigma_{xx} & \sigma_{xy} & \sigma_{xz} \\ \sigma_{yx} & \sigma_{yy} & \sigma_{yz} \\ \sigma_{zx} & \sigma_{zy} & \sigma_{zz} \end{bmatrix} \tag{A.12}$$

x, y, and z can be written 1,2, and 3

$$\sigma = \begin{bmatrix} \sigma_{11} & \sigma_{12} & \sigma_{13} \\ \sigma_{21} & \sigma_{22} & \sigma_{23} \\ \sigma_{31} & \sigma_{32} & \sigma_{33} \end{bmatrix} \tag{A.13}$$

A.5.Principal stresses

At any point in a homogeneous stress field we can find three planes upon which shear stresses are zero. These planes are called principal planes of stress. Stresses normal to these planes are principal stresses: σ_1, σ_2 and σ_3. In this case, the stress tensor can be presented as:

$$\sigma = \begin{bmatrix} \sigma_1 & 0 & 0 \\ 0 & \sigma_2 & 0 \\ 0 & 0 & \sigma_3 \end{bmatrix} \tag{A.14}$$

So, the state of stress can be characterized into: six independent stress components or magnitude and direction of σ_1, σ_2 and σ_3. This study mainly deals with stress of reservoir and stress within the earth's crust in which vertical stress due to overburden rock can be considered as a principal stress. Hence, the two remaining stresses are principal horizontal stresses. With such assumptions, the stress tensor can be written as

$$\sigma = \begin{bmatrix} \sigma_H & 0 & 0 \\ 0 & \sigma_h & 0 \\ 0 & 0 & \sigma_v \end{bmatrix} \tag{A.15}$$

where σ_v is the vertical principal stress, σ_h is the minimum horizontal principal stress and σ_H is the maximum horizontal principal stress.

Appendix B

B. Additional data for the Erskine field

B.1. Reservoir simulation model

The Erskine full-field simulation model was built using Eclipse-300 (TM Schlumberger) compositional simulator. Various simulation options have been studied in the past and historically E300 has been selected as the preferred solution that can address complex PVT and near-wellbore issues e.g. enhanced well deliverability associated with high velocities near the wellbore known as 'velocity stripping' can be accurately modelled only in Eclipse-300 (TM Schlumberger) (not in E100). The table below shows the simulation model layers used in Chapter 6, Section 6.2.3.

Model Layer	Description	
1	Heather Shale	Heather Formation
2	Heather Sand	
3	Heather Shale	
4	Heather Sand	
5	Heather Shale	
6 to 10	Erskine Sand E70	Erskine
11 to 13	Erskine Sand E60	
14 to 17	Erskine Sand E50	
18 to 20	Erskine Sand E40	
21 to 38	Erskine Sand E30	
39 to 41	Erskine Sand E20	
42	Erskine Sand E10	
43	Erskine Shale	
44	Coal Unit	
45	Upper Pentland Sand P60	Upper Pentland
46 to 48	Upper Pentland Sand P55	
49 to 51	Upper Pentland Sand P53	
52	Upper Pentland Shale P50	
53	Upper Pentland Sand P40	
54	Upper Pentland Shale P30	
55	Lower Pentland Sand P20	Lower Pentland
56	Lower Pentland Sand P20	
57	Lower Pentland Sand P10	
58	Lower Pentland Sand P10	

Table B.1: The layers used in the simulation model for the Erskine field.

B.2.Pressure measurements at the well locations

As mentioned in Chapter 6, Section 6.3.2, at the time of the monitor survey (2001) the pressure at the well location is still above the dew point pressure (400bars). This confirms that there are no changes in the fluid composition. Figure B.1, B.2, and B.3 show respectively the pressure measurement of all the wells at in Erskine Sand, Pentland Formation, and the Kimmeridge.

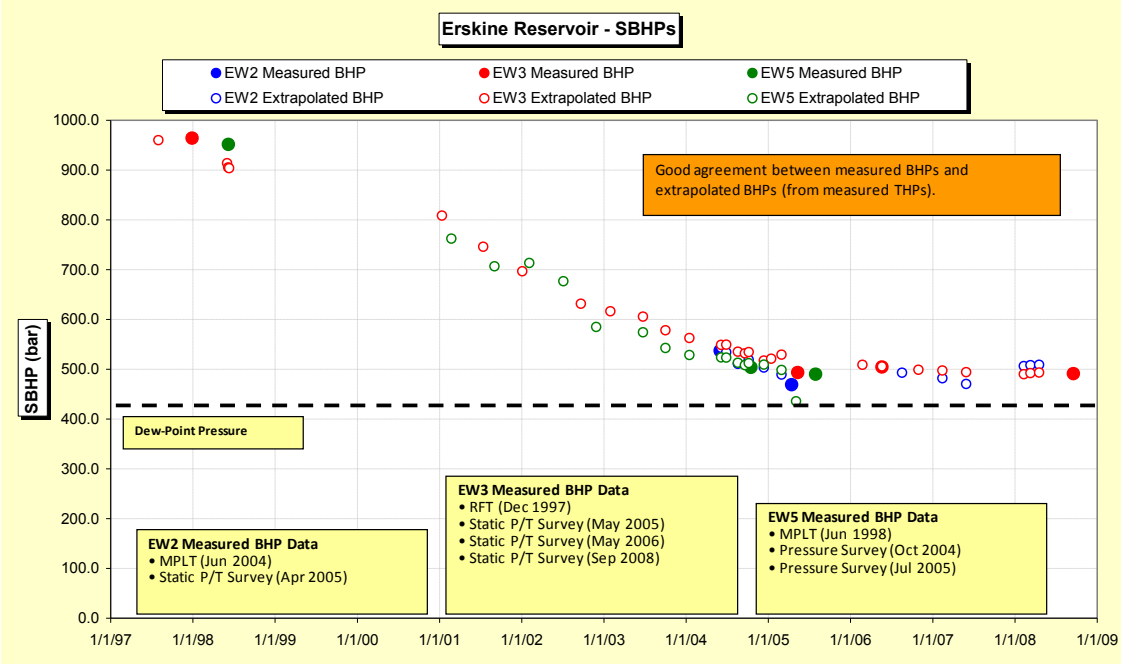

Figure B.1: Bottom hole pressure measurement in the Erskine sand between 1997 and 2009.

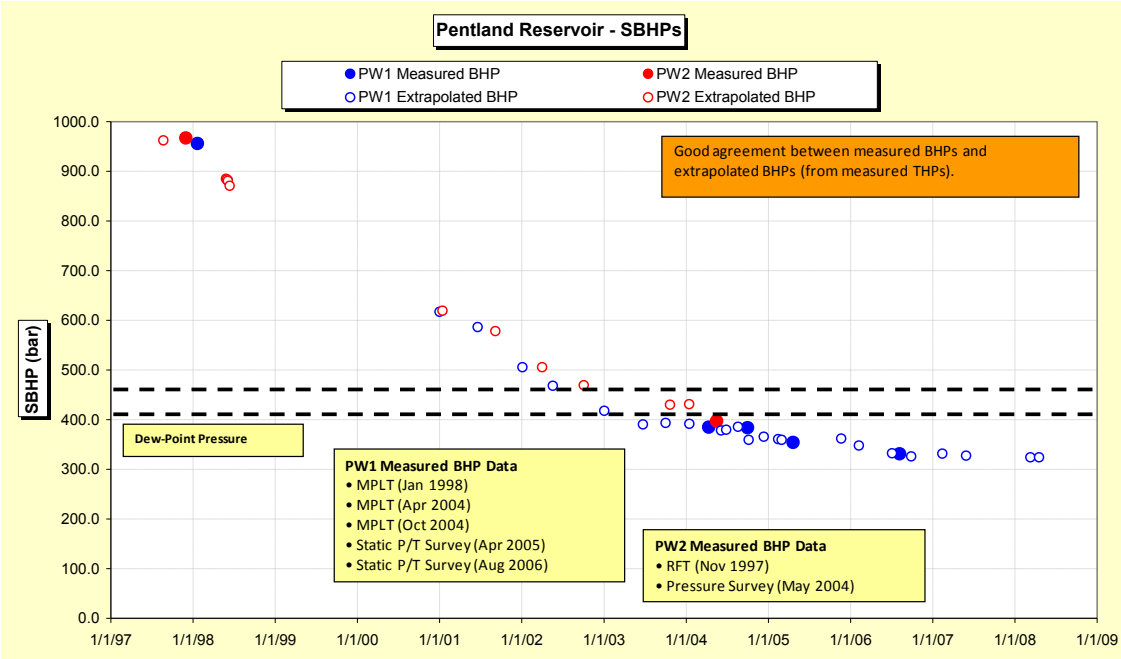

Figure B.2: Bottom hole pressure measurement in the Pentland between 1997 and 2009.

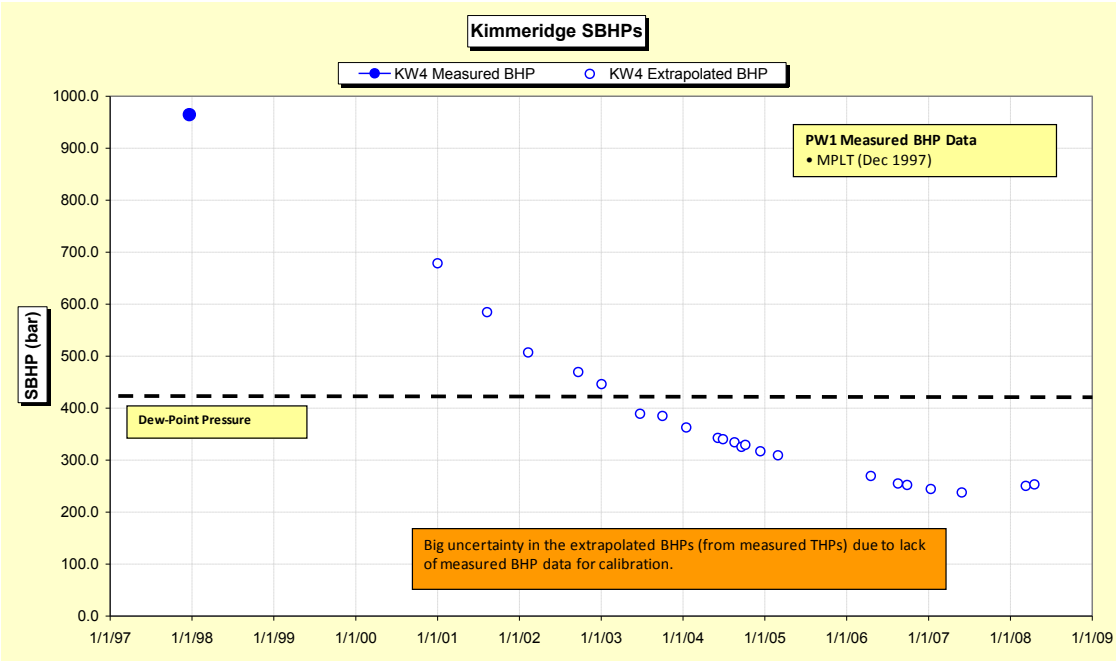

Figure B.3: Bottom hole pressure measurement in the Kimmeridge 1997 and 2009.

B.3.Geophysical data from the Erskine field

Here a geophysical data related to the case study of Chapter 6 is presented. Figure B.4 is showing Gamma Ray (GR), volume of shale V_{sh}, observed time shift and the observed time stain log at the well location. The Gamma Ray (GR) log shows high values at the level of the Heather shale and the Erskine shale. A positive time shift is observed along the well log. At the level of the Heather shale a negative time strain is observed. This could reflect the compressional strain induced by the pressure diffusion. At the Erskine shale, a positive time stain is observed. This reflects the extensional strain in the Erskine shale.

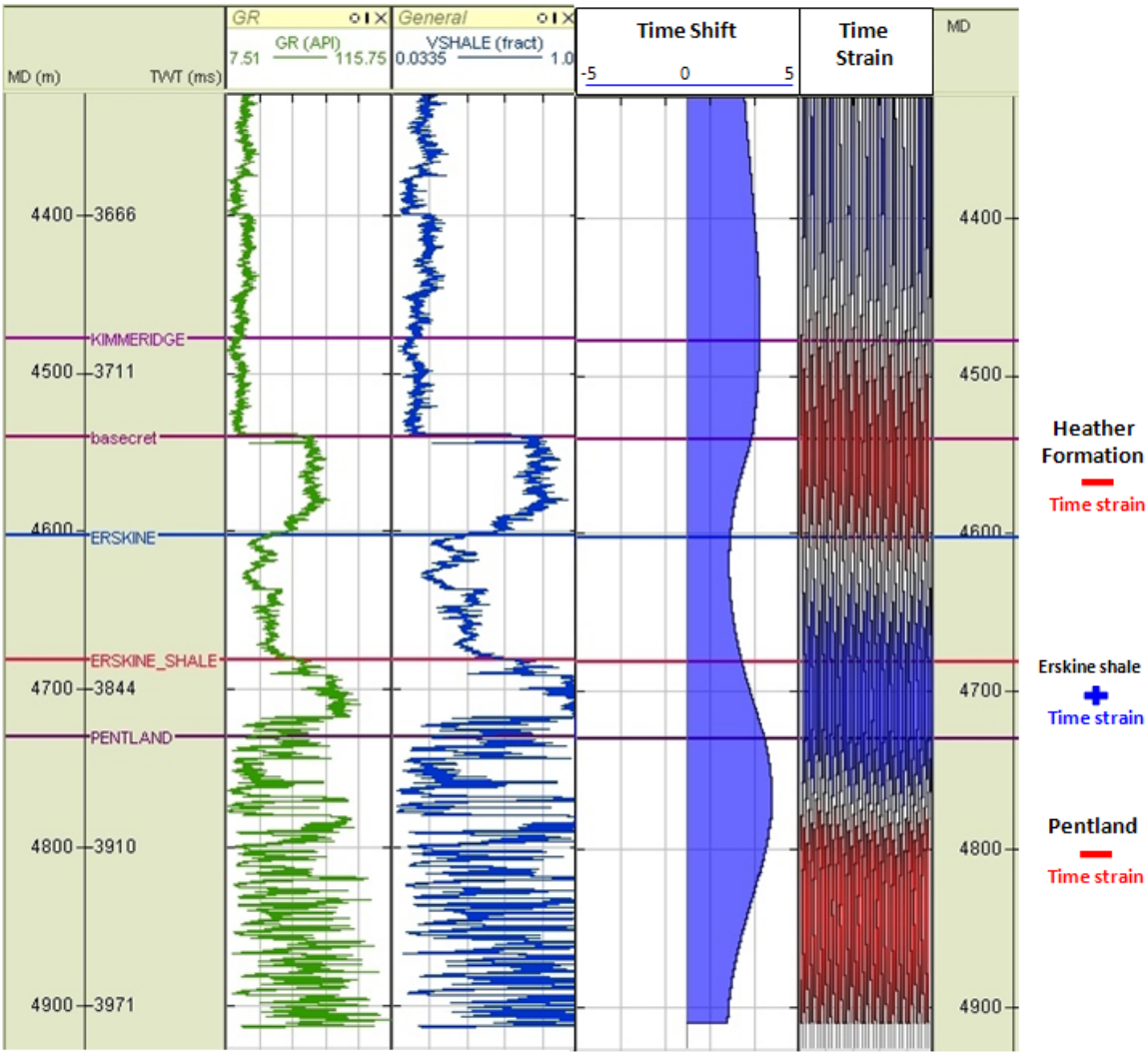

Figure B.4: Gamma Ray, volume of shale, Time shift and Time strain log at the well location.

Appendix C

C. Stress redistribution near a borehole

This section illustrates the mathematical equations that govern the stress redistribution near a borehole (Chapter 6, Section 6.5). Considering an elastic medium that is subjected to principal stresses σ_H, σ_h, and σ_v and that contains a borehole drilled parallel to the vertical axis. Assuming a plane strain, the radial σ_{rr}, hoop $\sigma_{\theta\theta}$, vertical σ_{zz}, and the shear $\sigma_{r\theta}$ components of the stress tensor, in cylindrical polar coordinates with radius r and azimuth θ, are given by the Krisch equations (Kirsch, 1898; Jaeger and Cook, 1979):

$$\sigma_{rr} = \frac{1}{2}(\sigma_H + \sigma_h)\left(1 - \frac{a^2}{r^2}\right) + \frac{1}{2}(\sigma_H - \sigma_h)\left(1 - \frac{4a^3}{r^2} + \frac{3a^4}{r^4}\right)\cos 2\theta + \frac{a^2}{r^2} p_b \tag{C.1}$$

$$\sigma_{\theta\theta} = \frac{1}{2}(\sigma_H + \sigma_h)\left(1 + \frac{a^2}{r^2}\right) - \frac{1}{2}(\sigma_H - \sigma_h)\left(1 + \frac{3a^4}{r^4}\right)\cos 2\theta - \frac{a^2}{r^2} p_b \tag{C.2}$$

$$\sigma_{zz} = \sigma_v - 2\nu(\sigma_H - \sigma_h)\frac{a^2}{r^2}\cos 2\theta \tag{C.3}$$

and

$$\sigma_{r\theta} = \frac{1}{2}(\sigma_H - \sigma_h)\left(1 + \frac{2a^2}{r^2} - \frac{3a^4}{r^4}\right)\sin 2\theta \tag{C.4}$$

where a is the radius of the borehole and p_b is the pressure exerted on the borehole wall by the fluid in the borehole.

Bibliography

Addis M. 1997. The stress depletion response of reservoirs. 72nd SPE Annual Technical Conference, San Antonio, Texas, USA. SPE 38720

Al-Rawahy S. Y. and Goulty N. R. 1995. Effect of mining subsidence on seismic velocity monitored by repeated refletion profile. *Geophysical Prospecting* **43**, 191-201.

Alsos T. 2009. The many Faces of Pressure Changes in 4D seismic at the Svale Field and Its Implication on reservoir Management. 71st EAGE meeting, Amsterdam, the Netherlands, Expanded Abstracts.

Amini H. and MacBeth C. 2011. Calibration of simulator to seismic modelling for quantitative 4D seismic interpretation. 73rd EAGE meeting, Barcelona, Spain, Expanded Abstracts.

Arts R., Elsayed R., Meer L. van der, Eiken O., Ostmo S., Chadwick A., Kirby G., Zinszner B. 2002. Estimation of the mass of injected CO_2 at Sleipner using time-lapse seismic data.. 64th EAGE meeting, Florence, Italy, Expanded Abstracts.

Barkved O.I. and Kristiansen T. 2005. Seismic time-lapse effects and stress changes: Examples from a compacting reservoir. *The Leading Edge* **24**, 1244.

Barton N. 2006. Rock quality, seismic velocity, attenuation and anisotropy. Taylor & Francis, UK.

Backus G.E. 1962. Long-wave elastic anisotropy produced by horizontal layering. *Journal of Geophysical Research* **67**, 4427-4440.

Best M.E. and Katsube T.J. 1995. Shale permeability and its significance in hydrocarbon exploration. *The Leading Edge* **14**, 165-170.

Beyer W.H. 1987. CRC Standard Mathematical Tables. 28th Edition, CRC Press Inc. Boca Raton, Florida.

Bol G.M., Wong S-W., Davidson C.J., and Woodland D.C. 1994. Borehole stability in shales. *SPE Drilling and Completion* **9**, 87-94.

Borst R. 1982. Some effects of compaction and geological time on the pore parameters of argillaceous rocks. *Sedimentology* **29**, 291-298.

Boyd-Gorst J., Fail P., and Pointing L. 2001. 4D time lapse reservoir monitoring of the Nelson Field, Central North Sea: Successful use of an integrated rock physics model to predict and track reservoir production. *The Leading Edge* **20**, 1336-1350.

Calvert R. 2005. Insights and methods for 4D reservoir monitoring and characterization. 2005 SEG/EAGE Distinguished Instructor Short Course.

Charlez P. and Heugas O. 1994. Evaluation of optimal mud weight in soft shale levels. 32nd U.S. Rock Mech. Symposium, Norman, Oklahoma, USA.

Cheng C. H. and Johnston D. H. 1981. Dynamic and static moduli. *Geophysical Research Letters* **8**, 39-42.

Chopra S. and Marfurt K. 2007. Seismic attributes for prospect identification and reservoir characterization. SEG, Tusla, Oklahoma, USA.

Christensen N.I. and Wang H.F. 1985. The influence of pore pressure and confining pressure on dynamic properties of Berea sandstone, *Geophysics* **50**, 207-213.

Crank J. 1975. The mathematics of diffusion. 2nd Edition, Clarendon Press, Oxford.

Corbett P. 2009. Petroleum geoengineering: Integration of Static and Dynamic Models. 2009 SEG/EAGE Distinguished Instractor Short Course.

Coward R. N. 2003. The Erskine Field, Block 23/26, UK North Sea. *Geological Society, London, Memoirs* **20**, 523-536.

Da Fontoura S. A., Rabe C., and Lomba R. F. 2002. Characterization of shales for drilling purposes. SPE/ISRM Rock Mechanics Conference, Irving, Texas, SPE 78218.

Dake L.P. 2001. The Practice of reservoir engineering. Elsevier.

Daniel R. B. 2001. Pressure prediction for a Central Graben wildcat well, UK North Sea. *Marine and Petroleum Geology* **18**, 235-250.

Dewhurst D. N., Siggins A. F., Kuila U., and Clennell M. B. 2008. Elastic, Geomechanical and petrophysical properties of shales. 42nd US Rock Mechanics Symposium and 2nd US-Canada Rock Mechanics Symposium, San Francisco, California, USA.

Detournay E. and Cheng A.D.H. 1993. Fundamentals of poroelasticity. In: *Comprehensive Rock Engineering: Principles, Practices & Projects.* Volume II: *Analysis and Design Method* (ed. C. Fairhurst), pp. 113–171. Pergamon.

Edris N.R. 2009. Identification of an appropriate data assimilation approach in seismic history matching and its effect on prediction uncertainty. PhD thesis, Heriot-Watt University.

Eiken O. and Tondel R. 2005. Sensitivity of time-lapse seismic data to pore pressure changes. Is quantification possible?. *The Leading Edge* **24**, 1250-1254.

Fletcher J. 2004. Rock and fluid physics understanding the impact of pressure changes: What do petroleum engineers expect from time lapse seismic, and do geophysicists answer the right questions? Copenhagen, 23-25 March, Copenhagen, Denmark.

Floricich M. 2006. An engineering-consistent approach for pressure and saturation estimation from time-lapse seismic data. PhD dissertation, Heriot-Watt University.

Floricich M., MacBeth C., Stammeijer J., Staples R., Evans A., and Dijksman C. 2006. A new technique for pressure-saturation separation from time-lapse seismic: Schiehallion case study, 68th EAGE meeting, Vienna, Austria, Expanded Abstracts.

Fjaer E. 1999. Static and dynamic moduli of weak sandstones. 37th US symposium on Rock Mechanics for Industry, Vall, Colorado, USA.

Furre A., Bakken E., Kløv T., and Nordby L.H. 2006. Heidrun 2001-2004 time-lapse seismic project: integrating geophysics and reservoir engineering. *First Break* **24**, 33-39.

Geertsma J. 1973. Land subsidence above compacting oil and gas reservoirs. *Journal of Pteroleum Technology* **25**, 734-744

Gladwin M. T. 1977. Simultaneous monitoring of stress and strain in massive rock. *Journal of Pure and Applied Geophysics* **115**, 267-274.

Grasso J.-R. 1992. Mechanics of Seismic Instabilities Induced by the Recovery of Hydrocarbons. *Journal of Pure and Applied Geophysics* **139**, 507-534.

Greaves R.-J. and Flup T.J. 1987. Three-dimentional seismic monitoring of an enhanced oil recovery process. *Geophysics* **52**, 1175-1187.

Guilbot J. and Smith B. 2002. 4D constrained depth conversion for reservoir compaction estimation: Application to Ekofisk field. *The Leading Edge* **21**, 302-308.

HajNasser Y. and MacBeth C. 2011. The effect of intra-reservoir and non-reservoir shales on 4D seismic signatures. 81st SEG meeting, San Antonio, Texas, Expanded Abstracts.

HajNasser Y. 2011. Application of the "Active Shale" concept to the Erskine field. Presented at Chevron Upstream Europe Reservoir Management Forum 'The Resource Factory – Enhancing Value', Aberdeen, UK

HajNasser Y. and MacBeth C. 2010. The effect of intra-reservoir shales on effective stress sensitivity. 72nd EAGE meeting, Barcelona, Spain, Expanded Abstracts.

HajNasser Y. 2010. Effect of discontinuous intra-reservoir shales on CO_2 storage. MSc dissertation, Heriot-Watt University.

Hale D. 2007. A method for estimating apparent displacement vectors from time lapse seismic images. 77th SEG meeting, San Antonio, Texas, USA, Expanded Abstracts, 2939-2943.

Haldorsen H. and Lake L. 1984. A new approach to shale management in field scale simulation models. *SPE Journal* **24**, 447-457.

Harris P. E. and Henry B. 1998. Time Lapse processing: A North Sea case study. 68th SEG meeting, New Orleans, USA, Expanded Abstracts.

Hatchell P. and Bourne S. 2005. Rocks under strain: Strain induced time-lpase time shift are observed for depleting reservoirs. *The Leading Edge* **24**, 1222-1225.

Hatchell P., Van Den Beukel A., Molenaar M., Maron K., Kenter C., Stammeijer J., et al. 2003. Whole earth 4D: monitoring geomechanics. 73rd SEG meeting, New Orleans, Louisiana, USA, Expanded Abstracts, 1330-1333.

Hawkins K. 2007. Production-induced stresses from time-lapse time shifts: A geomechanics case study from Franklin and Elgin fields. *The Leading Edge* **26**, 655-662.

Herwanger J. V. and Horne S. A. 2009. Linking reservoir geomechanics and time-lapse seismics: Predicting anisotropic velocity changes and seismic attributes. *Geophysics* **74**, 13-33.

Herwanger J. and Horne S.A. 2005a. Linking geomechanics and seismics: Stress effects on time-lapse multi-component seismic data. 67th EAGE meeting, Madrid, Spain, Expanded Abstracts.

Herwanger J., Palmer E., and Schiott C.R. 2007. Anisotropy velocity changes in seismic time-lapse data. 77th SEG meeting, Expended Abstracts, San Antonio, Texas, USA, 2883-2886.

Hettema M., Schutjens P., Verboom B., and Gussinklo H. 2000. Production-induced compaction of sandstone reservoirs: the strong influence of field stress. *SPE Reservoir Evaluation & Engineering* **3**, 342-347.

Hodgson N., MacBeth C., Duranti L., Rickett J., and Nihei K. 2007. Inverting for reservoir pressure change using time-lapse time strain: Application to Genesis field, Gulf of Mexico. *The Leading Edge* **26**, 649-652.

Hornby B.E. 1998. Experimental laboratory determination of the dynamic elastic propeties of wet, drained shales. *Journal of Geophysical Research* **103**, 29945-29964.

Howard J.J. 1991. Porosimetry measurement of shale fabric and its relationship to illite/smectite diagenesis. *Clays and Clay minerals* **39**, 355-361.

Hu S.M. 1989. Stress from a parallelepipedic thermal inclusion in a semi space. *Journal of Applied Physics* **66**, 2741-2743.

Jackson M. and Muggeridge A. 2000. Effect of discontinuous shales on reservoir performance during horizontal waterflooding. *SPE Journal* **5**, 446-455.

Jizba D. 1991. Mechanical and acoustical properties of sandstones and shales. PhD thesis, Stanford University.

Katahara K. 2008. What is shale to a petrophysicist?. *The Leading Edge* **27**,738-741.

Katsube T.J. 2000. Shale permeability and pore-structure evolution characteristics. Geological Survey of Canada Report 2000-E15.

Klemme H.D. and Ulmishek G. 1991. Effective petroleum source rocks of the world: stratigraphic distribution and controlling depositional factors. *AAPG Bulletin* **75**, 1809-1851.

Kloosterman H.J., Kelly R.S., Stammeijer J., Hartung M., Van Waarde J., and Chajecki C. 2003. Successfull application of time-lapse seismic data in Shell Expro's Gannet fields, Central North Sea, UKCS. *Petroleum Geoscience* **9**, 25-34.

Kunka J., Williams G., Cullen B., Boyd-Gorst J., Dyer G.R., Garnham J.A., et al. 2003. The Nelson field, blocks 22/11, 22/61, 22/7, 22/12a, UK North Sea. *Geological Society, London, Memoirs* **20**, 617-646.

Lafet Y. 2008. Global 4D seismic inversion and fluid prediction. 70th EAGE meeting, Rome, Italy, Expanded Abastracts.

Landrø M. 2001. Discrimination between pressure and fluid saturation changes from time-lapse seismic data. *Geophysics* **66**, 836-844.

Lashkaripour G.R. and Dusseault M.B. 1993. A statistical study on shale properties: Relationships among principal shale properties. Conference on Probablistic Methods in Geotechnical Engineering, Camberra, Australia.

Leach H., Herbert N., Los A., and Smith R. 1999. The Schiehallion development. Geological Society, 5th Conference Petroleum Geology of Northwest Europe, London, UK.

MacBeth C. 2004. A classification for the pressure-sensitivity properties of a sandstone rock frame. *Geophysics* **69**, 497-510.

MacBeth C., Stephen K.D., and McInally A. 2005. The 4D signature of oil-water contact movement due to natural production in a stacked turbidite reservoir. *Geophysical Prospecting* **53**, 183-203.

MacBeth C., Stammeijer J., and Omerod M. 2006. Seismic monitoring of pressure depletion evaluated for a United Kingdom continental-shelf gas reservoir. *Geophysical Prospecting* **54**, 29-47.

MacBeth C. HajNasser Y., Stephen K., and Gardiner A. 2011. Exploring the effect of meso-scale shale beds on a reservoir's overall stress sensitivity to seismic waves. *Geophysical Prospecting* **59**, 90–110.

MacLellan A., Rowbotham P., Rogers R., Busink P., and Millington J. 2006. Integrated 3D/4D structural and stratigraphic interpretation on Nelson accounts for variable fluid contact levels. 68th EAGE meeting, Vienna, Austria, Expanded Abstracts.

Makhous M., and Galushkin Y. 2005. Basin analysis and modelling of the burial, thermal and maturation histories in sedimentary basins. Editions Technip, New York.

Marsh J. 2004. 4D in Reservoir Management - Successes and Challenges. IOR Views e-newsletter, 8.

Martin J. and Cooper J. 1984. An Integrated approach to the modelling of permeability barrier distribution in a sedimentologically complex reservoir. 59th SPE Annual Technical Conference, Houston, Texas, USA, SPE 13051.

Mutti E. and Normark W. 1987. Comparing examples of modern and ancient turbidite systems: Problems and concepts. In *Marine clastic sedimentology*, concepts and case studies, (Leggett, J. K. and Zuffa, G.G. Eds.), Graham and Trotman, London, UK, 1-37.

Navarre J.Cl., Claude D., Liberelle E., Safa Ph., Vallon G., and Keskes N. 2002. Deepwater turbidite system analysis, West Africa: sedimentary model and implications for reservoir model construction. *The Leading Edge* **21**, 1132 - 1139.

Neuzil C.E. 1994. How permeable are clays and shales?. *Water Resources Research* **30**, 145-150.

Nunez J. and MacBeth C. 2006. Evaluation of the mismatch between observed and predicted 4D effects on the Genesis Field: GOM. 13th Venezuelan Geophysical Congress.

Ouair Y.E. 2005. Integrated reservoir management approach: from time-lapse aquisition to reservoir model update at the Norne Field. The International Petroleum Technology Conference, Doha, Qatar.

Peters K.E., Walters C.C., and Moldowan J.M. 2004. The Biomarker guide: biomarkers and isotopes in the environment and human history. 2nd Edition, Cambridge University Press, England.

Pistre V., Kinoshita T., Endo T., Schilling K., Pabon J., Sinha B., Plona T., Ikegami T., and Johnson D. 2005. A modular wireline sonic tool for measurement of 3D (azimuthal,

radial, and axial) formation acoustic properties: Proceedings of the 46th Annual Logging Symposium, SPWLA, 1-13.

Plona T.J. and Cook J.M. 1995. Effects of stress cycles on static and dynamic Young's moduli in Castlegate sandstone. 35th US Rock Mechanics Symposium, Reno, Nevada, USA.

Plumb R.A., Edwards S., Pidcock G. and Lee D. 2000. The mechanical earth model concept and its application to high-risk well construction projects. IADC/SPE 59128.

Potter P., Maynard J., and Pryor W. 1980. Sedimentology of shale. Springer-Verlag, New York.

Pryor W. and Fulton K. 1978. Geometry of reservoir-type sandbodies in the Holocene Rio Grande delta and comparison with ancient reservoir analogs. 5th SPE/DOE Enhanced Oil-Recovery Symposium, Tusla, USA.

Questiaux M. 2010. Geomodelling course notes. Heriot Watt University.

Ramana Y.V. and Venkatanarayana B. 1973. Laboratory studies on Kolar rocks. *International Journal of Rock Mechanics and Mining Sciences & Geomechanics Abstracts* **10**, 465-489.

Reynolds B.E. 1970. Predicting overpressured zones with seismic data. *World Oil* **171**, 78-82.

Ricard L., MacBeth C., HajNasser Y., and Schutjens P. 2012. An evaluation of pore pressure diffusion into a shale overburden and sideburden induced by production-related changes in reservoir fluid pressure. *Journal of Geophysics and Engineering* **9**, 345-358.

Rider M. 1996. The Geological interpretation of well logs. Whittles Publishing, London.

Sarkar D. 2003. Anisotropic inversion of seismic data for stress media: Theory and physical-modelling study on Berea sandstone. *Geophysics* **68**, 690-704.

Sayers C. 2010. Geophysics Under Stress: Geomechanical applications of seismic and borehole acoustic wave. 2010 SEG Distinguished Instractor Short Course.

Sayers C. 2009. Introduction to this special section shale geophysics. *The Leading Edge* **27**, 736-737.

Sayers C. 2004. Monitoring production-induced stress changes using seismic waves. 74th SEG meeting, Denver, Colorado, USA, Expanded Abstracts.

Sayers C. 2005b. Sensitivity of elastic-wave velocities to stress changes in sandstones. *The Leading Edge* **24**, 1262-1266.

Sayers C. 2006a. An intorduction to velocity-based pore pressure estimation. *The Leading Edge* **25**, 1496-1500.

Sayers C. 2006b. Sensitivity of time lapse seismic to reservoir stress path. *Geophysical Prospecting* **54**, 369-380.

Sayers C. and Schutjens P.M.T.M. 2007. An introduction to reservoir geomechanics. *The Leading Edge* **26**, 597-601.

Schutjens P., Hindriks K., An Der Horst J., Hatchell P., Van Den Beukel A., Barker T., Wills P., and Davis J. 2005. Reservoir monitoring with seismic timeshifts: Geomechanical modelling for its application in stacked pay. 1st Paper IPTC meeting, Doha, Qatar, Expanded Abstracts, 10511.

Schieber J., Zimmerle W., and Sethi P.S. 1998. Shales and mudstones. E.Schweizerbart'sche Verlagsbuchhandlung, Stuttgart.

Schloemer S., and Krooss B.M. 1997. Experimental characterisation of the hydrocarbon sealing efficiency of cap rocks. *Marine and Petroleum Geology* **14**, 565–580.

Schoenberg M. 2002. Time-dependent anisotropic induced by pore pressure variation in fractured rock. *Journal of Seismic Exploration* **11**, 83-105.

Segall P. 1989. Earthquakes triggered by fluid extraction. *Geology* **17**, 942-946.

Segall P. 1992. induced stresses due to fluid extraction from axisymmetric reservoirs. *Journal of Pure Applied Physics* **139**, 536-560.

Sinha B.K., Vissapragada B., Kisra S., Sunaga S., Yamamoto H., Endo T., Valero H.P., Renlie L., and Bang J. 2005. Optimal well completions using radial profiling of formation shear slownesses. SPE 95837.

Skaug M. and Gundesco R. 1986. Geological modelling of the Frigg field with special emphasis on shale mapping, SPE European Petroleum Conference, 20-22 October, London, UK, SPE 15859.

Slatt R. 2009. Studies shedding shales secrets, AAPG Explorer, March 2009.

Sone H. and Zoback M. 2011. Visco-plastic Properties of Shale Gas Reservoir Rocks. 45th U.S. Rock Mechanics / Geomechanics Symposium. San Francisco, California, USA.

Staples R. 2006. Integration of 4D seismic data and the dynamic reservoir model reveal new targets in Gannet C. *The Leading Edge* **25**,1126-1133.

Staples R. 2007a. Monitoring pressure depletion and improving geomechanical models of the shearwater field using 4D seismic. *The Leading Edge* **26**, 636-642.

Staples R. 2007b. Using 4D seismic data and geomechanical modelling to understand pressure depletion in HPHT fields of the Central North Sea. 69th EAGE meeting, London, UK, Expanded Abstracts.

Stephen K.D., Clark J.D., and Gardiner A.R. 2001. Outcrop-based stochastic modelling of turbidite amalgamation and its effects on hydrocarbon recovery. *Petroleum Geoscience* **7**, 163-172.

Stephen K.D. and MacBeth C. 2006. Seismic history matching in the UKCS Schiehallion field. *First Break* **24**, 43-49.

Talukdar S. 2008. Reservoir management of the Gullfaks main field. 70th EAGE meeting, Rome, Italy, Expanded Abstracts.

Thomas J. 1990. The movement of oil initially bypassed behind stochastic shale barriers: North Sea oil and gas reservoirs. SPE Reservoir Simulation Symposium, San Antonio, Texas, USA, SPE 16012.

Tjolsen C. 1996. Seismic data can improve stochastic facies modelling. *SPE Formation Evaluation* **11**, 141-146.

Tonkin N.S., Mcllroy D., Meyer R., and Moore-Turpin A. 2010. Bioturbation influence on reservoir quality: A case study from the Cretaceous Ben Nevis formation, Jeanne d'Arc Basin, offshore Newfoundland-Canada. *AAPG Bulletin* **94**, 1059-1078.

Tura A., Barker T., Cattermole P., Collins C., Davis J., Hatchell P., et al. 2005. Monitoring primary depletion reservoirs using amplitudes and time shifts from high-repeat seismic surveys. *The Leading Edge* **24**, 1214-1221.

Tura A. and Lumley E.D. 1999. Estimating pressure and saturation changes from time-lapse AVO data. 69th SEG meeting, Houston, Texas, Expanded Abstracts, pp 1655-1658.

Tyler K. 1994. Modelling heterogeneities in fluvial domains: a review of the influence on production profiles. In: J.M. Yarus and R.L. Chambers (eds) stochastic Modelling and Geostatistics. *AAPG Computer Applications in Geology* **3**, 77-89.

Van Oort E. 1994. A novel technique for the investigation of drilling fuild induced borehole instability in shales. 94th SPE/ISRM Rock mechanics in Petroleum Engineering Conference, Delft, The Netherlands, SPE 28064.

Vandenbroucke M. 2003. Kerogen from types to models of chemical structure. Oil & Gas Science Technology. *Revue de l'Institut Français du Pétrole* **58**, 243-269.

Vernik L. and Nur A. 1994. Ultrasonic velocity and anisotropy of hydrocarbon source rocks. *Geophysics* **57**, 727–735.

Watts G.F. 1996. Reservoir monitoring of the Magnus field through 4D time-lapse seismic analysis. *Petroleum Geoscience* **2**, 361-372.

Weber K. 1982. Influence of common sedimentary structures on fluid flow in reservoir models. *Journal of Petroleum Technology* **6**, 665-72.

White C. and Barton M. 1999. Translating outcrop data to flow models, with application to the Ferron sandstone. *SPE Reservoir Evaluation & Engineering* **3**, 341.

Whyatt M., Bowen J.M. and Rhodes D.N. 1992. The Nelson Field: a successful application of a development geoseismic model in North Sea exploration. *Geological Society Special Publication* **67**, 283-305.

Wiggins M. and Startzman R. 1990. An approach to reservoir management. 65th SPE Annual Technical Conference, New Orleans, Louisiana, USA, SPE 20747.

Wong R.C.K. 1996. Behaviour of water-jet mined caverns in oil sand and shale. *Canadian Geotechnical Journal* **33**, 610-617.

Yang Y. and Aplin A.C. 2007. Permeability and petrophysical properties of 30 natural mudstones. *Journal of Geophysical Research* **112**, B03206.

Zeito G. 1965. Interbedding of shale breaks and reservoir heterogeneities. *Journal of Petreoleum Technology* **17**, 1223-1228.

Zaske J., Pickles C., and Bagala S. 2009. Geophysical challenges at the HP/HT Erskine field, North Sea" presented at the HPHT Arena 2009 workshop, Aberdeen, UK.